

Ultra Low Power FM-UWB Transceiver for High-Density Wireless Sensor Networks

THÈSE N° 8399 (2018)

PRÉSENTÉE LE 9 MARS 2018

À LA FACULTÉ DES SCIENCES ET TECHNIQUES DE L'INGÉNIEUR
LABORATOIRE DE CIRCUITS INTÉGRÉS
PROGRAMME DOCTORAL EN MICROSYSTÈMES ET MICROÉLECTRONIQUE

ÉCOLE POLYTECHNIQUE FÉDÉRALE DE LAUSANNE

POUR L'OBTENTION DU GRADE DE DOCTEUR ÈS SCIENCES

PAR

Vladimir KOPTA

acceptée sur proposition du jury:

Prof. H. Shea, président du jury
Prof. C. Enz, directeur de thèse
Dr J. Farserotu, rapporteur
Prof. J. Long, rapporteur
Prof. Q. Huang, rapporteur



ÉCOLE POLYTECHNIQUE
FÉDÉRALE DE LAUSANNE

Suisse
2018

Acknowledgements

First and foremost, I would like to express my sincere gratitude to Prof. Christian Enz, it was his enthusiasm and encouragement that inspired me to pursue a Ph.D. degree in the first place. His continuous guidance and support over the past few years helped me expand my knowledge in the area of analog and RF IC design, and motivated me to push myself and aim for the highest goals.

I would then like to thank Dr. Alain-Serge Porret and Mr. Nicolas Raemy of CSEM for providing me with the opportunity to conduct my studies in an industrial environment and participate in projects beyond the scope of this thesis. In addition, I must also thank the whole RF and analog design team for their selfless help with all the problems I encountered. Mr. Erwan Le Roux, Dr. Franz Pengg, Dr. David Barras (now with 3dB Access), Dr. Alexandre Vouilloz, Dr. David Ruffieux, Dr. Nicola Scolari, Mr. Pascal Persechini, Dr. Camillo Salazar and Mr. Ernesto Perez have always been there to provide useful advice and help improve my work. In addition, I would also like to thank Mr. Ricardo Caseiro and Mr. Cedric Monneron for all the help with the layout design, Mr. Daniel Sigg for the support with CAD tools, and Mr. Pierre-Alain Beuchat, Mr. Yann Liechti and Mr. César Henzelin for the PCB design and help in the laboratory. Finally, I would like to thank Dr. Dragan Manić for taking care of all the logistics regarding tape-outs, but also for his company during numerous lunch breaks.

I further thank Dr. John Farserotu, who led the *WiseSkin* project, for the fruitful discussions that inspired my work and for all the motivation to develop my ideas and bring them to life. My thanks also go to other members of the *WiseSkin* team: Prof. Decotignie, Prof. Lacour, Dr. Claudio Bruschini, Dr. Christian Antfolk, Dr. Eleni Daskalaki, Dr. Hadrien Michaud, Camilo Rojas and Huaiqi Huang for their hard work and effort, and for making the collaboration on this project a truly pleasant experience. In addition, my gratitude also goes to Dr. Oleksandr Vorobyov for his contribution to the work on wireless powering and the antenna design.

I would also like to express my gratitude to Prof. Herbert Shea, Prof. Qiuting Huang and Prof. John Long for being part of my jury, taking their valuable time to read and evaluate my thesis, and for providing useful comments and remarks about my work.

Particular thanks go to all my colleagues from ICLAB, current and former, for making these past few years a delightful and memorable experience. I must first thank Raghavasimhan Thirunarayanan for everything he taught me during the first few years of my studies. I would then like to express my sincerest thanks to Anurag, Maria-Anna, Alessandro, Farzan, Arnout,

Acknowledgements

Mattia, Nino, Vincent, Jérémy, Chunmin, Francesco and Raffaele first for all the fun conversations during coffee breaks, but also for many discussions on somewhat more serious technical topics.

I am also thankful to all the friends I met in Switzerland for distracting me from work and helping me remember that there is life outside of EPFL. In order of appearance, I would like to thank: Vladan, Mare, Baki, Velja, Džoni, Čojba, Mića, Dionisije, Marija and Josipa.

Finally, I am grateful to my girlfriend Aurélie for being supportive and patient with me, and my family, my sister Maja and my parents Vera and Aleksandar, for inspiring me to pursue a career in engineering and always being there for me.

Neuchâtel, 2018

Vladimir Kopta

Abstract

The *WiseSkin* project aims to provide a non-invasive solution for restoration of a natural sense of touch to persons using prosthetic limbs. Although there are functional myoelectric prostheses available today, their use remains limited due to a lack of sensory function in the prosthesis. By embedding sensor nodes into the silicone coating of the prosthesis, which acts as a sensory skin, *WiseSkin* targets to provide improved gripping, manipulation and mobility for amputees. Flexibility, freedom of movement and comfort demand unobtrusive, highly miniaturized, low-power sensing capabilities built into the artificial skin, which is then integrated with a sensory feedback system. Wireless communication between the sensor nodes provides more flexibility, better scalability and robustness compared to a wired solution, and is therefore a preferred approach for *WiseSkin*. Design of an RF transceiver tailored for the specific needs of *WiseSkin* is the topic of this work.

The properties of FM ultra-wide band (FM-UWB) modulation make it a good candidate for High-Density Wireless Sensor Networks (HD-WSN). Transceiver simplicity and robustness to frequency offsets enable ultra-low power consumption and a high degree of integration, thereby reducing the size and cost of the node. Furthermore, FM-UWB is robust against narrow-band interferers and can support multiple users operating simultaneously in the same band, providing reliable communication and useful options for high-level protocol optimization.

The proposed FM-UWB receivers take advantage of short range to reduce power consumption, and exploit robustness of this wideband modulation scheme. The LNA, which is usually identified as the biggest consumer, is removed and signal is directly converted to dc, where amplification and demodulation are performed. Owing to the signal bandwidth of 500 MHz, relatively large frequency offset and phase noise can be tolerated, and a low-power, free-running ring oscillator can be used to generate the LO signal, allowing to achieve overall power reduction. The receiver is therefore referred to as an “approximate zero-IF” receiver. To compensate for the LO offset, all of the stages following the mixers provide higher bandwidth than necessary, and the ring oscillator is periodically calibrated to keep the offset within defined limits. Two receiver architectures are studied. The first one performs quadrature downconversion, and owing to the demodulator linearity, provides the multi-user capability. In the second receiver, quadrature demodulation is replaced by the single-ended one. Due to the nature of the demodulator, sensitivity degrades, and multiple FM-UWB signals cannot be

Abstract

resolved, but the consumption is almost halved compared to the first receiver. The proposed approach is verified through two integrations, both in a standard 65 nm bulk CMOS process. In the first run, a standalone quadrature receiver was integrated (with the second FSK demodulation and baseband off-chip). Power consumption of 423 μW was measured, while achieving -70 dBm sensitivity. Good narrow-band interference rejection and multi-user capability with up to 4 FM-UWB channels could be achieved. In the second run, a full transceiver is integrated, with both quadrature and single-ended receivers and a transmitter, all sharing a single IO pad, without the need for any external passive components or switches. The quadrature receiver, with on-chip baseband processing and multi-user support, in this case consumes 550 μW , with a sensitivity of -68 dBm. The low power receiver consumes 267 μW , and provides -57 dBm sensitivity, at a single FM-UWB channel. The implemented transmitter transmits a 100 kb/s FM-UWB signal at -11.4 dBm, while drawing 583 μW from the 1 V supply. The on-chip clock recovery allows reference frequency offset of up to ± 8000 ppm. Since state of the art on-chip RC oscillators can provide accuracy below ± 2100 ppm across the temperature range of interest, the implemented transceiver demonstrates the feasibility of a fully integrated FM-UWB radio with no need for a quartz reference or any external components. In addition, the transceiver can tolerate up to 3 dBm narrow-band interferer at 2.4 GHz. Such a strong signal can be used to remotely power the sensor nodes inside the artificial skin and enable a truly wireless *WiseSkin* solution.

Key words: ultra-wideband, low power, wireless communication, RF, transceiver, UWB, frequency modulation, FM-UWB, FDMA, WSN, WBAN, power harvesting

Résumé

Le projet WiseSkin vise à développer une solution non-invasive pour redonner aux amputés utilisant des prothèses la sensation naturelle du toucher. Bien que des prothèses myoélectrique existent aujourd'hui, l'absence de fonction sensorielle limite leur utilisation. En intégrant des nœuds de capteurs dans le revêtement en silicone de la prothèse qui fait office de peau artificielle, WiseSkin vise à améliorer la manipulation, la mobilité et la préhension de la main artificielle. Flexibilité, liberté de mouvement et confort nécessitent des moyens de détection discrets, hautement miniaturisés et à faible consommation qui peuvent être intégrés dans la peau artificielle et faire partie d'un système de rétroaction sensorielle. Par rapport à une communication filaire, la communication sans fil apporte plus de flexibilité, une meilleure évolutivité et une robustesse améliorée, ce qui en fait la solution préférée. La conception d'un émetteur-récepteur RF adapté aux besoins particuliers de WiseSkin est le sujet de ce travail.

Les propriétés de la modulation de fréquence à bande ultra-large (FM-UWB) en font une bonne candidate pour les réseaux de capteurs sans fil à haute densité (HD-WSN). La simplicité de l'émetteur-récepteur ainsi que la robustesse contre les offsets de fréquence permettent une consommation d'énergie très faible et un fort degré d'intégration, permettant ainsi de réduire la taille et le prix des nœuds de capteurs. Par ailleurs, étant donné que la FM-UWB est résistante aux interférences à bande étroite et permet à plusieurs utilisateurs de communiquer dans la même bande simultanément, elle garantit une communication fiable et fournit des options intéressantes pour l'optimisation du protocole à haut niveau.

Les récepteurs FM-UWB proposés ici profitent de la courte distance entre les nœuds pour réduire la consommation tout en exploitant la robustesse de cette modulation. Ceci permet d'éliminer l'amplificateur à faible bruit qui est un des plus grand consommateur d'énergie. Le signal RF d'entrée est alors directement converti à une fréquence nul par un mélangeur, et ensuite amplifié et démodulé. Grâce à la largeur du signal de 500 MHz, l'offset de fréquence et le bruit de phase peuvent être tolérés, permettant ainsi d'utiliser un oscillateur en anneau pour générer la porteuse (LO) et ainsi réduire la consommation. Le récepteur est donc nommé récepteur à fréquence intermédiaire environ égale à zéro (AZ-IF). Pour compenser l'offset de fréquence, tous les étages suivant le mélangeur ont une bande passante élargie et l'oscillateur est périodiquement calibré pour maintenir la fréquence dans les limites désirées. Deux architectures de récepteurs sont étudiées. La première effectue une conversion en quadrature, qui grâce à la linéarité du démodulateur, permet de distinguer les différents signaux

Résumé

FM-UWB. Dans la deuxième architecture, la conversion en quadrature est remplacée par une conversion directe sans quadrature. A cause de la nature de ce récepteur, la sensibilité est réduite et le récepteur n'est plus capable de distinguer les signaux multiples à l'entrée, mais la consommation est réduite de moitié par rapport à la première architecture.

Deux circuits intégrés ont été fabriqués dans une technologie CMOS 65 nm standard pour démontrer la validité de l'approche proposée. Seul le récepteur à conversion en quadrature a été intégré sur la première puce (avec la partie bande de base et le deuxième démodulateur FSK à l'extérieur). La consommation mesurée est de $423 \mu\text{W}$ pour une sensibilité de -70 dBm . De plus, une bonne robustesse contre les interférences à bande étroite a été démontrée jusqu'à 4 canaux FM-UWB parallèles. La deuxième puce contient l'émetteur-récepteur complet, avec les deux types de récepteurs (à conversion en quadrature et sans quadrature) partageant une seule entrée/sortie avec le transmetteur, permettant ainsi d'éliminer tous les composants externes, comme par exemple le commutateur ou les composants passifs. Le récepteur à conversion en quadrature, avec la partie bande de base et le support de communications multi-utilisateur consomme $550 \mu\text{W}$, pour une sensibilité de -68 dBm . Le récepteur sans quadrature consomme $267 \mu\text{W}$ avec une sensibilité de -57 dBm pour un seul canal FM-UWB. Le transmetteur transmet un signal à 100 kb/s , avec une puissance de -11.4 dBm tout en consommant $583 \mu\text{W}$ avec une tension d'alimentation de 1 V . Le circuit de récupération d'horloge tolère un décalage de fréquence allant jusqu'à $\pm 8000 \text{ ppm}$. Etant donné que les oscillateurs RC de référence ont une précision de $\pm 2100 \text{ ppm}$ pour la gamme de température visée, l'émetteur-récepteur fabriqué ici démontre la faisabilité d'une radio FM-UWB complètement intégrée ne nécessitant aucun composant externe ni cristal de quartz. Par ailleurs, l'émetteur-récepteur peut tolérer des interférences à bande étroite d'une puissance allant jusqu'à 3 dBm à 2.4 GHz . Un signal aussi puissant pourrait d'ailleurs être utilisé pour alimenter les nœuds de capteurs dans la peau artificielle sans contact, permettant une solution WiseSkin complètement sans fils.

Mots clés : bande ultra-large, faible consommation, communication sans fil, RF, émetteur-récepteur, UWB, modulation de fréquence, FM-UWB, FDMA, WSN, WBAN, récupération d'énergie

Contents

Acknowledgements	i
Abstract (English/Français)	iii
List of figures	xi
List of tables	xv
1 Introduction	1
1.1 The <i>WiseSkin</i> Project	2
1.1.1 Miniature Sensing Module	4
1.1.2 Tactile Display	4
1.1.3 Power Distribution	6
1.1.4 Wireless Communication	7
1.2 Low Power Wireless Communications - the Overview	7
1.3 Dissertation Scope and Organization	10
References	11
2 FM-UWB as a Low-Power, Robust Modulation Scheme	13
2.1 Principles of FM-UWB	14
2.1.1 FM-UWB Modulation	14
2.1.2 Multi-User Communication and Narrowband Interference	17
2.1.3 Beyond standard FM-UWB	23
2.2 State-of-the-Art FM-UWB Transceivers	25
2.2.1 FM-UWB Receivers	26
2.2.2 FM-UWB Transmitters	29
2.2.3 FM-UWB against IR-UWB and Narrowband Receivers	31
2.3 Summary	34
References	35
3 Reducing the Power of FM-UWB receivers: the Approximate Zero IF Architecture	39
3.1 The Uncertain IF Architecture	40
3.2 The Approximate Zero IF Receiver with Quadrature Downconversion	41
3.3 The Approximate Zero IF Receiver with Single-Ended Downconversion	47
3.4 Receiver Sensitivity Estimation	51

Contents

3.5	Summary	53
	References	54
4	Quadrature Approximate Zero-IF FM-UWB Receiver	55
4.1	Receiver Architecture	55
4.2	Circuit Implementation	57
4.2.1	RF Frontend	57
4.2.2	IF Amplifier	59
4.2.3	LO Generation and Calibration	62
4.2.4	FM Demodulator	65
4.2.5	LF Amplifier and Output Buffer	67
4.2.6	Current Reference PTAT Circuit	68
4.3	Measurement Results	69
4.3.1	General Receiver Measurements	69
4.3.2	Single User Measurements	70
4.3.3	Multi-User Measurements	77
4.3.4	Multi-Channel Transmission Measurements	78
4.4	Summary	80
	References	81
5	FM-UWB Transceiver	83
5.1	Transceiver Architecture	83
5.2	Transmitter Implementation	85
5.2.1	Sub-Carrier Synthesis	86
5.2.2	DCO Digital to Analog Converters	87
5.2.3	DCO	88
5.2.4	Preamplifier and Power Amplifier	91
5.3	Receiver Implementation	95
5.3.1	RF Frontend	95
5.3.2	IF Amplifiers	96
5.3.3	Receiver DCO	98
5.3.4	Demodulator	100
5.3.5	N-Path Channel Filter	102
5.3.6	LF Amplifier and Comparator	106
5.3.7	FSK Demodulator and Clock Recovery	109
5.3.8	SAR FLL Calibration	111
5.3.9	Clock Reference	113
5.4	Measurement Results	114
5.4.1	Transmitter Measurements	114
5.4.2	Receiver Measurements	121
5.5	Summary	131
	References	132

6 Efficient Contactless Waveguide Power Transfer	135
6.1 Wireless Power Transfer	136
6.2 System Description	137
6.3 Antenna Design	139
6.4 Measurement Results	140
6.5 Summary	144
References	144
7 Conclusion	147
7.1 Summary of Achievements	148
7.2 Future Work	150
References	151
Curriculum Vitae	153

List of Figures

1.1	The <i>WiseSkin</i> concept.	2
1.2	The <i>WiseSkin</i> sensor node.	4
1.3	The concept of tactile feedback.	5
1.4	Conceptual view of the skin (a) and one of the <i>WiseSkin</i> prototypes (b) from [8].	6
2.1	Principle of FM-UWB signal modulation.	14
2.2	Wideband FM demodulator.	15
2.3	Comparison of standard orthogonal FSK and FM-UWB modulation.	17
2.4	FM-UWB multi-user communication.	19
2.5	FSK sub-channel frequency allocation and limits due to distortion.	21
2.6	ACPR for filtered and non-filtered FSK signal, as a function of channel separation (100 kb/s data rate, modulation index 1).	22
2.7	FM-UWB multi-channel broadcast.	24
2.8	Example of transmission on two channels, time domain sub-carrier signal (a) and transmitted signal spectrum (b).	24
2.9	FM-UWB receiver architectures reported in the literature.	26
2.10	Frequency-to-amplitude conversion characteristic of reported FM demodulators.	27
2.11	FM-UWB transmitters and receivers, evolution of power consumption. Type of demodulator used in each receiver is indicated on the graph.	34
3.1	Principle of operation of the uncertain IF receiver.	40
3.2	Block diagram of approximate zero IF receiver with IQ downconversion.	42
3.3	Principle of operation of approximate zero IF receiver with IQ downconversion.	43
3.4	Normalized fundamental C_1 and second harmonic amplitude C_2 at the output of the demodulator vs. the offset frequency. First harmonic is proportional to conversion gain. Four curves are plotted for four different values of the demodulator bandwidth (or equivalently different values of the delay τ).	45
3.5	Coefficient C_{MU} (a) and correction factor $ C_1 ^2/C_{MU}$ for SIR (b) as functions of the frequency offset. Four curves correspond to three different values of the demodulator bandwidth (or equivalently values of the delay τ).	47
3.6	Block diagram of approximate zero IF receiver with single-ended downconversion.	48
3.7	Principle of operation of the approximate zero IF receiver with single-ended downconversion.	49

List of Figures

3.8	Normalized fundamental C_1 and second harmonic amplitude C_2 at the output of the demodulator.	50
3.9	Simulated and calculated BER curves for the approximate zero IF receiver. . . .	51
3.10	Simulated and calculated BER curves with and without frequency offset for the approximate zero-IF receiver with quadrature downconversion (a) and single-ended downconversion (b).	53
4.1	Receiver block diagram.	56
4.2	Schematic of the LNA/Mixer.	58
4.3	Schematic of the IF amplifier, and the equivalent small-signal schematic of half circuit.	60
4.4	Simulated conversion gain and noise figure of the RF and IF stages.	61
4.5	Simplified schematic of the quadrature DCO.	62
4.6	Simulated frequency and current consumption of the DCO.	63
4.7	Schematic of the frequency divider.	63
4.8	Schematic of the buffer between the DCO and the frequency divider.	64
4.9	Frequency divider, waveforms at different points.	64
4.10	Schematic of the wideband FM demodulator.	66
4.11	Wideband FM demodulator, input and output waveforms.	67
4.12	Schematic of the output buffer.	68
4.13	Schematic of the PTAT current reference.	69
4.14	Die photograph.	69
4.15	Measured S_{11} parameter for different values of input capacitance.	70
4.16	Measured frequency and current consumption of the DCO	71
4.17	Measurement setup	71
4.18	Measured BER curves for different carrier offset.	72
4.19	Measured demodulator output waveform for different carrier frequency offsets	73
4.20	BER curves for different data rates.	74
4.21	BER curves for different modulation order.	75
4.22	Spectrum of the demodulated sub-carrier signal.	75
4.23	Sensitivity as a function of in-band interferer power.	76
4.24	BER curves for 2 FM-UWB users and varying input level between the two users.	76
4.25	BER curves for different number of FM-UWB users.	77
4.26	Spectrum of the demodulated sub-carrier signal, in different multi-user scenarios.	78
4.27	BER curves for different number of broadcast sub-channels.	79
4.28	Spectrum of the transmitted signal, for the standard FM-UWB and MC FM-UWB	79
4.29	Demodulated signal spectrum, with and without spacing between adjacent sub-channels	80
5.1	Top-level block diagram of implemented transceiver.	84
5.2	Block diagram of the implemented transmitter.	85
5.3	Digital sub-carrier synthesizer.	86
5.4	Static DCO current DAC.	87

5.5	Dynamic DCO current steering DAC.	88
5.6	Dynamic DAC test output buffer.	89
5.7	Transmitter DCO with buffers.	89
5.8	Schematic of the frequency divider buffer.	90
5.9	Simulated DCO frequency, current consumption and output voltage amplitude.	90
5.10	Preamplifier and power amplifier schematic.	92
5.11	Simulated S_{11} parameter at the RF IO.	92
5.12	Simulated power amplifier output power (a), consumption (b) and efficiency (c) including the preamplifier.	94
5.13	MU receiver LNA/mixer schematic.	95
5.14	LP receiver LNA/mixer schematic.	96
5.15	IFA schematic of MU and LP receiver.	97
5.16	Simulated characteristics of the LP and MU Rx frontend.	98
5.17	LP receiver DCO schematic.	99
5.18	LP receiver DCO simulated frequency, current consumption and output voltage.	100
5.19	MU receiver demodulator schematic.	101
5.20	LP receiver demodulator schematic.	101
5.21	LP receiver demodulator input and output waveforms.	102
5.22	Band-pass N-path filter schematic.	103
5.23	Transconductor of the N-path filter.	104
5.24	Non-overlapping clock phases used to drive switches and the differential switch-capacitor array.	105
5.25	Non-overlapping clock generator.	105
5.26	Transfer function of the N-path filter.	106
5.27	Schematic of the second order cell of the LP filter and half circuit small signal schematic.	107
5.28	Simulated frequency characteristic of the MU and LP receiver LFA.	108
5.29	Comparator schematic.	108
5.30	Block diagram of the FSK demodulator and clock recovery circuit.	109
5.31	Simulated signals of the FSK demodulator and clock recovery circuit.	110
5.32	SAR FLL block diagram.	112
5.33	Example measured SAR FLL calibration cycle.	112
5.34	Principle of clock generation and distribution.	113
5.35	SEM die photograph of the transceiver.	115
5.36	Measured sub-carrier DAC output (a) and measured frequency deviation of the transmitted signal (b).	116
5.37	Frequency and power consumption of the transmit DCO.	117
5.38	Phase noise of the transmit DCO at 4 GHz.	117
5.39	Measured power amplifier output power (a), consumption (b) and efficiency (c) including the preamplifier.	118
5.40	Transmitted FM-UWB signal spectrum.	119
5.41	Transmit power vs. transmitter power consumption.	120

List of Figures

5.42 Measured S_{11} parameter in transmit and receive mode.	120
5.43 Measured frequency and power consumption of the MU Rx DCO.	121
5.44 Measured frequency and power consumption of the LP Rx DCO.	121
5.45 N-path filter measured characteristic for center frequency of 1.25 MHz.	122
5.46 Demodulated signal spectrum before and after N-path filter.	123
5.47 Test setup used for transceiver characterization.	124
5.48 Single user BER of the MU Rx with internal and external demodulator at 100 kb/s.	125
5.49 Single user BER of the LP Rx with internal and external demodulator at 100 kb/s.	126
5.50 Measurement setup and comparison of transmit and received bits.	127
5.51 Sensitivity degradation due to the presence of an in-band interferer.	127
5.52 Sensitivity degradation due to the presence of an out of band interferer at 2.4 GHz.	128
5.53 BER for a fixed input signal level with varying reference clock frequency.	128
5.54 Measured BER curves for multiple FM-UWB users of same power level, demodulated with external (a) and internal (b) demodulator.	129
5.55 Measured BER curves for two FM-UWB users of different power levels, demodulated with external (a) and internal (b) demodulator.	130
6.1 General concept of a sensor node powered through wires (a) and a sensor node powered via RF energy, harvested from a master or powering node (b). RF energy is distributed via the flexible waveguide.	137
6.2 3D model of the designed antenna.	139
6.3 Model used for antenna optimization.	140
6.4 Simulated antenna S_{11} parameter, antenna is placed between the two metal layers.	140
6.5 Manufactured antenna with a μ FL connector.	141
6.6 Examples of the used waveguide samples, 275 mm long waveguide (up) and the same waveguide with a cut in the middle (down).	141
6.7 Test setup with the VNA and the implemented waveguide prototype.	142
6.8 S-parameters for different antenna distances: (a) S_{11} and (b) S_{21}	143
6.9 Reported efficiency of implemented rectifiers and rectennas at 2.4 GHz [18].	144
7.1 Power consumption evolution of implemented FM-UWB transmitters and receivers.	148
7.2 Power consumption vs. sensitivity of implemented FM-UWB receivers.	149

List of Tables

2.1	Performance summary of state-of-the-art FM-UWB receivers	29
2.2	Performance summary of state-of-the-art FM-UWB transmitters	31
2.3	Performance summary of IR-UWB receivers	32
2.4	Performance summary of narrowband receivers	33
4.1	Power consumption breakdown	71
4.2	Comparison with the state-of-the-art receivers	80
5.1	Transmitter power consumption breakdown	121
5.2	MU receiver power consumption breakdown	123
5.3	LP receiver power consumption breakdown	124
5.4	Comparison with the state-of-the-art transceivers	132
6.1	Available output power	143

1 Introduction

Advances in the fields of micro-electro-mechanical systems (MEMS), wireless communications and microelectronics have enabled ever more powerful, miniaturized devices capable of sensing, processing and communicating the data. These devices fueled the rapid expansion of wireless sensor networks (WSN) in domains and applications such as environmental monitoring, infrastructure monitoring, transport, retail, healthcare and others. Furthermore, they opened door to realizing a vision of the internet of things (IoT), i.e., a widespread network of interconnected objects capable of not only sensing the world around them, but also interacting with it, with the ultimate goal of improving the quality of our daily lives.

Electronics, combined with advanced biological and biomedical technology, paved the road to new solutions such as smart materials. These solutions, based on sensor networks, could find use in health and safety applications (e.g., prosthetics, handling hazardous substances etc.) as well as tactile robotics. The *WiseSkin* Nano-Tera project aims to develop a smart material that could restore a natural sense of touch to persons who have lost a limb and are using prosthesis. This material can be seen as a network, consisting of a potentially very large number of sensor devices, capable of communicating among each other and conveying the information from the skin to the central processing unit in charge of stimulating the patient and restoring the natural sensation of touch. The *WiseSkin* tactile skin for prosthetics is the main application and motivation behind this work. The core of the work focuses on a hardware implementation of a radio optimized for use in short range wireless sensor networks.

With the IoT and wireless sensor networks in focus, the reduction of size and power of the sensor nodes has been an important research topic over the past few years. Size of the node is usually directly proportional to its price, which is one of the main driving forces behind the effort to reduce it, especially when a large number of nodes are needed. In addition, in medical applications, where nodes may need to be placed on or inside the human body, size plays a crucial role as the nodes must not interfere with patient's movement and should

have a minimal impact on his life. By lowering power consumption of nodes one can either extend the autonomy, which is a paramount when talking about remote battery powered sensor nodes (e.g., environmental monitoring in isolated locations), or implanted devices, or use a smaller battery with lower capacity, again allowing to make it smaller. Eventually, as the consumption continues to decrease, it might become possible to fully power sensor nodes with energy harvested from the environment. With the wireless transceiver as the key component of the node, and the main bottleneck, a lot of effort has been directed towards improving its characteristics. Today's devices have already come a long way, and are capable of lasting for years using just a small battery, but as more and more demanding applications appear, such as *WiseSkin*, further enhancements are necessary.

1.1 The *WiseSkin* Project

The loss of a hand or a limb is a catastrophic event with major implications on the quality of life and daily activities of the person. Although various different types of prostheses have been made, their capabilities to this date remain limited. Sophisticated limb manipulation requires a complex coordination between motor commands, performed motion and sensory feedback. Replacing a lost hand, therefore, remains a major challenge, that is still a topic of interest for both engineers and clinicians. The focus of the *WiseSkin* project [1] is on the sensory feedback, aiming to restore the sense of tactility to the amputees, however, the concepts developed here could also be applied to other fields of use such as robotics.

A natural sense of tactility is needed in order to provide sensory feedback that would then allow precise control of all types of myoelectric hand prostheses, but also the lower limb prostheses allowing, for example, to enhance balance. The concept of the *WiseSkin* solution is illustrated in Fig. 1.1. The touch information is recorded by sensor nodes and conveyed to the

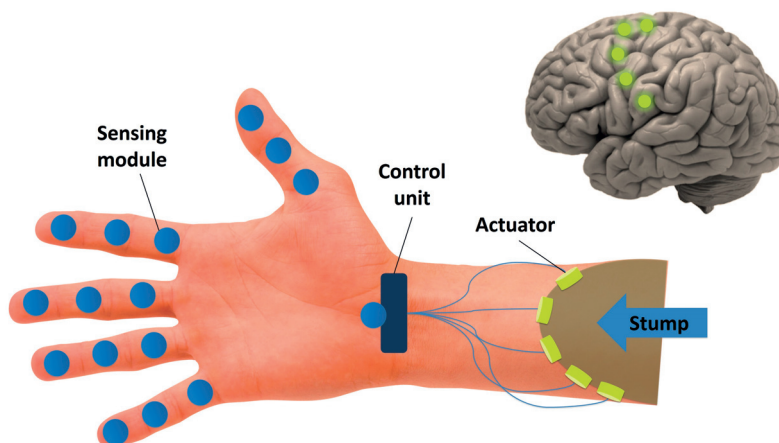


Figure 1.1: The *WiseSkin* concept.

control unit that processes the data and generates stimulation patterns for the tactile display. The tactile display then stimulates the patient's stump allowing him to perceive different objects and surfaces in contact with the prosthesis. Aside from providing sensory feedback, the *WiseSkin* solution should also help the patients to experience prosthesis as a part of their body, enhancing the feeling of body ownership and restoring a natural sense of touch, and allowing the patient to use the prosthesis without continuous visual monitoring.

The problem of restoring a sense of touch to a person using a prosthetic arm is complex and bears numerous difficulties. Within the scope of the *WiseSkin* project the aim is to create a kind of artificial skin, or a glove that would be used on top of a prosthetic arm (or possibly a leg) and behave much like the real skin. The sensors embedded in the skin would detect pressure when an object comes in contact with the prosthesis and convey this information to the patient. Ideally, the sensors would provide not only the data about the pressure, but also shear, providing for example the information on a slipping object. The information on temperature and humidity could be added in order to provide as realistic feeling as possible. Building all these capabilities into miniaturized sensor nodes becomes difficult. In addition, all the data from sensors must be delivered and processed in real time in order to provide a natural feeling and functional control of the artificial limb [2]. The solution is further constrained by the requirements for ease of use, freedom of movement and natural look, that impose highly miniaturized, unobtrusive and low power sensing capabilities. Although in some cases the minimum tactile capability might be restored with only one sensor per finger, many sensors of different types working together could be needed to enable a true natural feeling. For this reason the targeted solution must be scalable, and the communication between sensors is critical. For a small number of sensors, wired communication seems like a natural way to go, however, as this number increases, it becomes apparent that the wireless approach provides better scalability and more flexibility. Provided that it can handle the data capacity, and that the radio consumption does not add a significant load to the existing battery, a wireless solution also offers better reliability, ease of manufacturing and lower production cost. In that regard, the future goal would be to have fully wireless nodes, with the power either delivered without contact, or provided by means of energy harvesting. At the moment, however, a wired powering system is necessary, with wires capable of stretching and bending with the skin, without breaking or significantly increasing electrical resistance. Finally, a reactive, fast and low power sensor-to-person interface is essential, as a key part of the whole system.

The work within the *WiseSkin* project consisted of research in several different areas such as microelectronics, materials engineering, communications, human-machine interfaces etc. with the goal to push the forefront of available technologies. At the same time, a demonstrator showing the main concepts was developed using the commercially available components, that allowed for easier and more reliable system integration. The developed sensor node, that consists of a microcontroller unit (MCU), a pressure sensor and a radio with antenna is shown in Fig. 1.2. The existing technology allowed to integrate all the components on a rigid PCB, 17 mm long and 12 mm wide, allowing to place one node on each finger, but the solutions developed over the course of the project should allow further miniaturization and

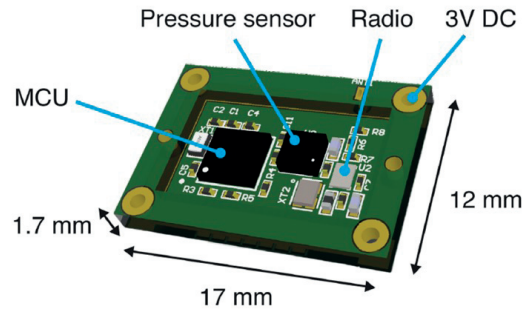


Figure 1.2: The WiseSkin sensor node.

higher degree of integration in the future. The research focused on four topics with particular challenges that will be discussed in the following text.

1.1.1 Miniature Sensing Module

Dexterous limb manipulation and gripping require detection of forces, torques, position and contact shape by miniature sensors embedded in the skin. The additional difficulty is that these sensors must endure frequent physical contact while still operating reliably, which is why durability and robustness are just as important as other sensor characteristics. Over the course of the *WiseSkin* project a fully soft solution based on integration of a gold strain gauge into the PDMS substrate was developed. Gauge is fabricated using Au-implantation through a microfabricated shadow mask. Measured performance indicated gauge factor (GF, ratio of relative change in resistance due to the mechanical strain) of 25, compared to thin film solutions with the GF of 2. A solution for large area tactile surfaces was explored as well, with the idea of developing a material with a low gauge factor, but that can withstand large mechanical strains without affecting its electrical properties [3].

For the *WiseSkin* prototype, the air pressure sensor LPS25H from ST Microelectronics was used [4]. The MEMS sensor, packaged together with the readout and calibration circuits, and a digital SPI interface, could easily be integrated into the sensor node. The sensor was encapsulated in the PDMS, effectively creating an air bubble at the sensor input. Applying pressure on top of the sensor node compresses air in the bubble, resulting in increased pressure that can be detected by the sensor. Once calibrated, the sensor could be used for touch detection with relatively good linearity.

1.1.2 Tactile Display

For the purpose of the *WiseSkin* project, idea is to use a non-invasive interface between the patient and the prosthesis. Unlike the approach from [2], where electrodes are directly connected to nerve endings, there is no need for complex surgery. Unfortunately, purely tactile, external stimulation is much more limiting in terms of patterns and motions that

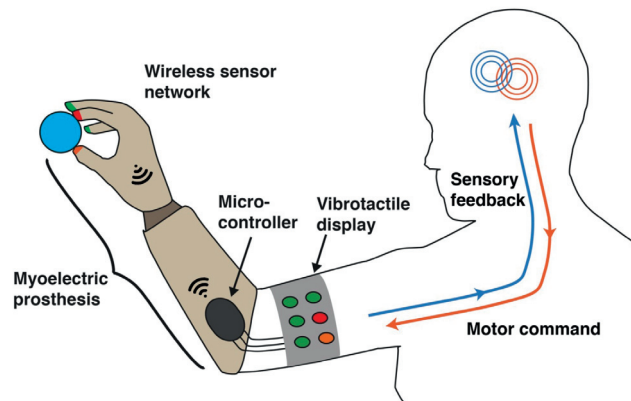


Figure 1.3: The concept of tactile feedback.

can be distinguished by the patient. On the other hand, the non-invasive approach greatly reduces the risk for the patient, simplifies the use of the prosthesis (for example, it can be freely removed when needed) and is generally more convenient.

The concept of the tactile sensory feedback is shown in Fig. 1.3, the tactile stimuli is conveyed from sensors on the artificial skin to the tactile display that stimulates the patient's stump. The solution relies on patient's "phantom map", that is the area on the remaining part of the arm where generated stimuli create the sensation of touching a part of the amputated hand. Depending on the location of the activated sensor and the pressure intensity, the tactile display unit should generate the corresponding stimulation pattern, inducing a physiologically natural perception of stimuli.

Different devices can be used to stimulate the phantom map, some examples include electrical devices, mechanotactile, vibrotactile, or devices using air pressure or temperature. Here, the choice was narrowed down to vibrotactile devices that produce vibrations of different frequency or intensity and mechanotactile devices that apply different levels of force to the skin [5, 6]. The difference between the two is in the latency, precision, human perception and control. The challenge is to produce a tactile display that can react quickly, without causing significant additional latency, and can create different patterns that represent different events. Furthermore, it must be flexible enough to adapt to each patient's phantom map, as this map changes significantly from one person to the other. Different machine learning algorithms can be applied to detect the phantom map distribution [7] and then adjust the tactile display for each case. Tests with amputees have shown the feasibility of the non-invasive approach, and have so far demonstrated the ability to distinguish different fingers by using mechanical (force and vibration) stimulation.

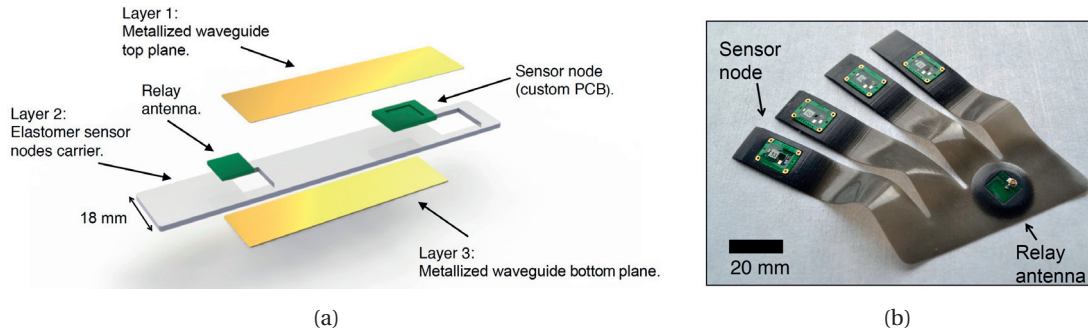


Figure 1.4: Conceptual view of the skin (a) and one of the WiseSkin prototypes (b) from [8]

1.1.3 Power Distribution

The original intent in the *WiseSkin* project was to use metallic wires on top of the flexible substrate to power the sensor nodes. These wires would have to be flexible and stretchable in order to conform to the shape of the skin. For example, during a grip the skin on the dorsal side of the hand stretches and the material used for the skin, together with the metallic layer, needs to stretch as well, without degrading the electrical performance.

Different approaches have been used in the past to enable stretchability of electronic conductors. Solid conductors can be made elastic by proper geometric design, for example meandering is one straight-forward way to achieve this. However, the elasticity is typically limited to one predefined direction. A different approach to stretchable electronics are the liquid metal conductors, which have good electrical performance, but are difficult to manufacture in a well controlled manner. A solution that resulted from the work on the *WiseSkin* was a combination of the two. A new class of biphasic solid-liquid conductors was invented, that kept the unhindered conductivity of the liquid solution and the ease of manufacturing of the solid conductors. The solution is based on a bilayer metallization sequence, starting with a thin layer of gold on top of the PDMS substrate followed by thermal evaporation of liquid gallium, that results in a thin film consisting of solid intermetallic alloy AuGa_2 forming a continuous network and dispersed bulges [9]. The solution achieved low sheet resistance of less than $1 \Omega/\square$, and gauge factor approximately equal to 1, meaning the resistance is practically unaffected by stretching.

The view of different layers and one of the prototypes are shown in Fig. 1.4. One issue that posed problems with prototypes was the contact between the stretchable wire and the rigid sensor node. These contacts would often break during experiments, disconnecting the supply line and detaching a node from the rest of the system. Instead of carefully engineering the contacts, and finding ways to provide a more reliable connection, a wireless powering approach is proposed in this work. Since the existing stretchable wires constitute a waveguide, the RF energy could be transferred from the source to the nodes without significant losses,

1.2. Low Power Wireless Communications - the Overview

therefore providing good energy efficiency. The proposed approach also simplifies the system, easing production and improving the system reliability.

1.1.4 Wireless Communication

Although more complex than wired communication, wireless communication offers better potential for scaling, flexibility and ease of manufacturing, and is a preferred solution from that perspective. In addition, wireless solution could be extended to other WSN applications where sensor nodes are battery powered. The wireless approach poses challenges with respect to low power consumption, latency and robustness. Compared to other parts of the system, such as the stimulation actuators, the existing Bluetooth radios already consume a very small amount of power, that does not pose a significant additional burden on the battery. Lowering the radio consumption could, however, allow to power the sensor nodes without wires, through energy harvesting, in the future. Latency is constrained by the requirement to provide a natural sense of touch, meaning that the information from the sensors must be conveyed to the stimulation module within several tens of milliseconds. The work on wireless communication is split into two parts, one that focuses on the optimization of radio, and another that targets protocol optimization.

For the implemented prototype with only 5 nodes, the amount of traffic and routing paths are not critical and there is no need for special techniques. These issues tend to become more important as the number of nodes grows, which is expected in the future. Thus need arises for a specific protocol that will provide the needed scalability, handle traffic surges and guarantee reliability. The developed protocol [10] uses two modes, a low-traffic mode optimized for power efficiency, and high-traffic mode that minimizes response time and is activated by an event such as detection of touch. The emphasis is on adaptability, capability to conform to different conditions and clever use of available resources. Instead of avoiding packet collisions (two transmitters sending data using the same channel) and wasting time and energy, the protocol leverages them by using constructive interference among different nodes, and in this way achieves state of the art performance.

Wireless transceiver designed for short range communications with a potentially large number of devices in a small area is the central topic of this dissertation and will be thoroughly addressed in the following chapters. A Bluetooth Low-Energy device developed by CSEM [11] was used for the *WiseSkin* prototype from Fig. 1.2. In the future, this radio should be replaced by a more optimal, ultra low power radio such as the one developed in this work, that leverages the short communication distance.

1.2 Low Power Wireless Communications - the Overview

Reducing the power consumption of radios has been a topic of research for quite a long time. In recent years, the search for energy efficient means of communication and constant effort

to lower the power consumption of wireless transceivers have been primarily driven by the growing popularity of the internet of things (IoT) [12]. First conceived by K. Ashton in 1999 in the context of supply chain management, the term internet of things has since spread to cover a wide range of applications such as healthcare, transport, environmental monitoring etc. For the worldwide network of interconnected objects to become a reality, different elements are needed, from sensors and low power communication devices, all the way to the data analytics and learning algorithms able to extract useful information from the huge amount of gathered data. Wireless sensor networks play a key role in the IoT vision. Finding ways to scale-up the number of connected devices, while reducing the power and coping with the increased interference, remains a difficult challenge. Although *WiseSkin* is a very particular application, a number of challenges are similar to those already present in WSNs developed for IoT. In that regard, some of the solutions can be borrowed from the IoT world, but also, the solutions developed specifically for the *WiseSkin* could find use in the broader WSN context.

Different approaches and different standards are used to connect various objects depending on specific limitations of the application. Perhaps the best known and the most widely used low power connection standard is the Bluetooth standard. It provides complete wireless connectivity services, not just wireless transport, and is commonly implemented in audio streaming, data transfer and broadcasting devices. Although initially designed for small networks consisting of up to seven peripherals connected to a master device (such as a computer, or a smart phone), Bluetooth has evolved over the years and now supports different network topologies with a much larger number of devices. It targets ranges from tens to hundreds of meters, and data rate in the order of 1 Mb/s. Another similar standard is the ZigBee or the IEEE 802.15.4, with the same communication distance and lower data rates that go up to 250 kb/s. Unlike Bluetooth, it targets mainly industrial applications, and therefore the emphasis is on security, robustness and scalability, providing support for high node counts. As of 2012, enhanced ZigBee specifications also include secured connectivity to batteryless devices, powered from energy sources like motion, light or vibration. For short range communication at distances of up to 10 cm, NFC is the most commonly used technology, however, due to the low frequency used, the coupling inductors tend to be quite large. At the other end of the spectrum are the ultra narrowband communication standards such as LoRa or Sigfox, targeting wide area networks (WAN) and connection over more than 5 km. They are specifically designed for low cost mobile devices, providing bidirectional mobile communication at data rates from just 10 b/s to 50 kb/s, which is suitable for low rate communication with sensors. In general, commercially available low power radios consume between 5 mW and 20 mW in receive state. Their consumption is usually limited by the receiver noise figure and linearity requirements. In transmit mode, consumption can vary anywhere between 5 mW and 200 mW, and is typically determined by the transmit signal power and the power amplifier efficiency. To minimize consumption and extend battery life, these devices are nearly always duty cycled, meaning that they sleep most of the time, and only wake up for a short period of time to receive or transmit a packet of data. This allows batteries to last for months or years instead of hours or days. Turning a node on less frequently results in decreased power consumption,

1.2. Low Power Wireless Communications - the Overview

however at the same time the minimum latency increases. This latency-power trade-off is a common characteristic of duty cycled systems.

A number of other protocols and standards exist, however, due to the specificity of the *WiseSkin* approach, there is currently no available solution adjusted for this case. Bluetooth or ZigBee transceivers could be used, but their performance surpasses the needs of *WiseSkin* in terms of sensitivity. Instead, a more optimal radio should trade the unnecessary sensitivity for power consumption. Existing short range solutions such as NFC or the RFID, need a relatively large coil, and are not suited from the size perspective. A custom radio is therefore required, tailored for the specific needs of *WiseSkin*, in order to achieve good overall performance, while maintaining small size and power consumption.

Aside from the widely used commercially available radios, a number of different technologies can be found in the literature. Different narrowband wake-up receivers can be found, reporting power consumption below 100 μ W, and some even going down to 100 nW. This is roughly 2-5 orders of magnitude below Bluetooth and ZigBee radios with peak consumption between 5 mW and 20 mW. The wake-up receivers are used to continuously listen and monitor the channel. Once the transmitted data is detected, they will turn on the main receiver in charge of data communication. The idea behind wake-up receivers is to break the latency-power trade-off that exists in duty-cycled systems. To achieve this their power consumption must be lower than the average consumption of standard receivers, which requires aggressive use of low power techniques. The achieved levels of power consumption come at a price in sensitivity, data-rate or interference rejection, and generally speaking the relatively limited capabilities of wake-up receivers.

An interesting technology from the *WiseSkin* viewpoint are the ultra wideband (UWB) radios. They are intended to provide robust and reliable communication while maintaining relatively low complexity and power consumption. Unfortunately, the UWB radios need wideband circuits, which typically require more power than the narrowband circuits of similar performance. For this reason, given the same sensitivity level, the UWB radios will always lag behind narrowband radios when it comes to power consumption. On the other hand, what they lose in sensitivity (or alternatively power) they gain elsewhere. The UWB radios are known to maintain good performance in channels with frequency selective fading, or in the presence of interferers. One of the interesting properties of the UWB radios is also the robustness against frequency offset. Due to large bandwidth of the transmit signal, a small error in frequency can be tolerated without a significant impact on the performance. The tolerable error is in fact several orders of magnitude higher than that of narrowband radios. For this reason frequency synthesis can be greatly simplified, allowing to avoid PLLs or similar power hungry blocks. In addition, a UWB radio could be implemented without the need for a reference oscillator with an external quartz crystal, and in that regards, it could offer a higher degree of integration and miniaturization than the narrowband radios. As a consequence, the size and cost of the sensor nodes can be reduced.

For the particular case of *WiseSkin*, robustness against fading, inherent resilience to interferers, tolerance to different receiver imperfections and high degree of integration, are all in favor of the UWB radio. Owing to the short distance between the adjacent sensor nodes, lower sensitivity, compared to narrowband radios with similar power consumption, can be tolerated. Two UWB schemes are dominantly used for low power applications, these are the impulse radio (IR) UWB and the frequency modulated (FM) UWB. Since the latter is known for its low complexity and lower peak power consumption it was chosen for implementation.

1.3 Dissertation Scope and Organization

As mentioned in the above sections, the goal of the work presented here is to reduce the power consumption of an FM-UWB transceiver, while aiming to reduce the number of external, off-chip components as much as possible. Different architectural and circuit techniques are employed to achieve this, and will be thoroughly discussed in the chapters to come. Aside from consumption, the transceiver is also designed to provide multi-user communication capability, allowing multiple transceivers to communicate simultaneously in the same frequency band. Such capability is extremely useful when the number of sensor nodes starts to grow, and allows better scalability and lower latency compared to systems that exploit only TDMA (Time Division Multiple Access).

Throughout the work conducted in this project, a somewhat unexpected discovery was made. Namely, the above mentioned stretchable power wires, initially intended for supplying power to the nodes, indeed act as a waveguide (see Fig. 1.4). Owing to the rather low loss of the structure, the power could be delivered to nodes "wirelessly" with a relatively high efficiency. Although the solution is not wireless, in the sense that metallic layers are still needed, it is contactless and enables better reliability and lower cost than the fully wired approach. However, in order to allow simultaneous communication and powering, the FM-UWB radio has to be capable to receive data in the presence of a strong interfering signal used to provide power.

The dissertation is organized as follows:

Chapter 2 explains the fundamentals of FM-UWB modulation and demodulation, with some possible directions for further development. The main reported receiver and transmitter architectures are presented, explained and compared to each other. Finally, FM-UWB receivers are compared to IR-UWB and ultra low-power narrowband receivers, and pros and cons of different approaches are highlighted and discussed.

Chapter 3 presents the two developed receiver architectures. The "approximate zero IF" (AZ-IF) receiver architecture is derived from the "uncertain IF" architecture, previously employed to reduce consumption of the narrowband wake-up radios. The principle of operation is demonstrated, and combined with system-level simulation in order to estimate the expected performance of the two receivers.

Chapter 4 describes the first implementation of the low power, quadrature approximate zero IF receiver. First, all the circuits are explained in detail together with the most important simulation results. Then the measurement results are reported. The receiver performance is characterized in different conditions, with narrowband and wideband interferers and using different variations of FM-UWB modulation, demonstrating in that way some of the interesting features of the FM-UWB approach.

Chapter 5 describes the implementation of the fully integrated, low power FM-UWB transceiver. Aside from the quadrature AZ-IF receiver, a single-ended receiver is added, providing a mode with even lower power consumption. As in the previous case, the two receivers are characterized under different operating conditions. In this case the emphasis is on robustness to narrowband interferers (allowing to power the node using a 2.4 GHz narrowband signal), and frequency offset tolerance. The implemented receiver is proven to tolerate clock offsets large enough to make use of an external quartz reference unnecessary, making it the first FM-UWB transceiver that can truly be implemented with no external components.

Chapter 6 is focused on wireless power transfer. First, a concept of powering sensor nodes through a flexible and stretchable waveguide is described, highlighting its benefits in the context of *WiseSkin*. As a proof of concept, measurements are conducted using simple waveguide samples, and a 2.4 GHz antenna designed for the initial *WiseSkin* prototype. The measured results are combined with the reported efficiencies of the state of the art rectennas to estimate the achievable efficiency of the proposed powering solution.

Chapter 7 concludes the dissertation, providing a summary of achieved results and contributions, and pointing to potential research topics for future work.

References

- [1] J. Farserotu, J. Baborowski, J. D. Decotignie, P. Dallemagne, C. Enz, F. Sebelius, B. Rosen, C. Antfolk, G. Lundborg, A. Björkman, T. Knieling, and P. Gulde, "Smart skin for tactile prosthetics," in *2012 6th International Symposium on Medical Information and Communication Technology (ISMICT)*, Mar. 2012, pp. 1–8.
- [2] S. Raspopovic, M. Capogrosso, F. M. Petrini, M. Bonizzato, J. Rigosa, G. Di Pino, J. Carpaneto, M. Controzzi, T. Boretius, E. Fernandez *et al.*, "Restoring natural sensory feedback in real-time bidirectional hand prostheses," *Science translational medicine*, vol. 6, no. 222, pp. 222ra19–222ra19, 2014.
- [3] A. P. Gerratt, H. O. Michaud, S. Gupta, and S. P. Lacour, "49-1: Invited paper: Large-area tactile skins prepared with thin-film technology," *SID Symposium Digest of Technical Papers*, vol. 47, no. 1, pp. 660–663, May 2016.
- [4] *LPS25H MEMS Pressure Sensor - Datasheet*, ST Microelectronics. [Online]. Available: <http://www.st.com/en/mems-and-sensors.html>
- [5] H. Huang, T. Li, C. Antfolk, C. Enz, J. Justiz, and V. M. Koch, "Experiment and investiga-

- tion of two types of vibrotactile devices,” in *2016 6th IEEE International Conference on Biomedical Robotics and Biomechatronics (BioRob)*, June 2016, pp. 1266–1271.
- [6] T. Li, H. Huang, J. Justiz, and V. M. Koch, “A miniature multimodal actuator for effective tactile feedback: Design and characterization,” *Procedia Engineering*, vol. 168, pp. 1547–1550, 2016.
- [7] H. Huang, T. Li, C. Bruschini, C. Enz, V. M. Koch, J. Justiz, and C. Antfolk, “Emg pattern recognition using decomposition techniques for constructing multiclass classifiers,” in *Biomedical Robotics and Biomechatronics (BioRob), 2016 6th IEEE International Conference on*. IEEE, June 2016, pp. 1296–1301.
- [8] H. Michaud, E. Daskalaki, J. Baborowski, O. Vorobyov, J. R. Farserotu, and S. P. Lacour, “Soft skin embedding and powering wireless tactile sensor nodes,” in *Nano-Tera Annual Plenary Meeting*, Apr. 2016.
- [9] A. Hirsch, H. O. Michaud, A. P. Gerratt, S. d. Mulatier, and S. P. Lacour, “Intrinsically stretchable biphasic (solid–liquid) thin metal films,” *Advanced Materials*, vol. 28, no. 22, pp. 4507–4512, June 2016.
- [10] C. Rojas and J. D. Decotignie, “Artificial skin for human prostheses, enabled through wireless sensor networks,” in *2017 IEEE 23rd International Conference on Embedded and Real-Time Computing Systems and Applications (RTCSA)*, Aug. 2017, pp. 1–8.
- [11] “CSEM scientific and technical report,” 2016.
- [12] J. Gubbi, R. Buyya, S. Marusic, and M. Palaniswami, “Internet of things (iot): A vision, architectural elements, and future directions,” *Future generation computer systems*, vol. 29, no. 7, pp. 1645–1660, 2013.

2 FM-UWB as a Low-Power, Robust Modulation Scheme

Ultra-wideband (UWB) systems were originally intended to provide robust, low-cost, low-complexity and low power wireless solutions for localization and communication. The first UWB systems were based on a time domain approach, they used a very short pulse to carry the information. Initially, they were used in radar systems, where pulse duration translated into spatial resolution. When used for communications, these pulses could be modulated using one of the standard approaches, most commonly the binary phase shift keying (BPSK) or pulse-position modulation (PPM). This was impulse radio (IR) UWB, and although it was able to provide robust, high-speed communication, it came at the price of circuit complexity and relatively high power consumption. The frequency-modulated (FM) UWB was developed as an easy to implement, complementary solution, preserving robustness and offering low to medium data rates. This analog spread spectrum technique is intended for short to medium range applications that require a reliable communication link, low cost and high degree of integration and miniaturization, and therefore perfectly fits the *WiseSkin* requirements.

This chapter begins by introducing the fundamentals of FM-UWB, explaining the modulation and demodulation principles and basic transmitter and receiver architectures. Then, the Gerrits' BER approximation is presented and extended to cases with multiple FM-UWB users and narrowband interferers. Finally, possible extensions of standard FM-UWB modulation are briefly discussed, highlighting its potential evolution. In the second part of this chapter, state of the art FM-UWB receivers and transmitters are discussed and analyzed, and a brief summary of their key characteristics is provided. They are also compared to narrowband and IR-UWB radios to point out the advantages and disadvantages of the FM-UWB modulation scheme.

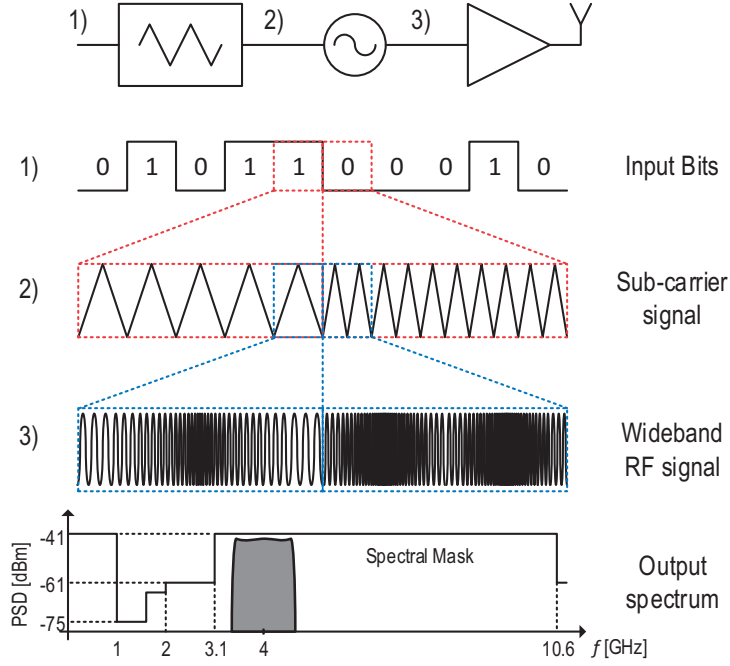


Figure 2.1: Principle of FM-UWB signal modulation.

2.1 Principles of FM-UWB

2.1.1 FM-UWB Modulation

The FM-UWB can be seen as an analog spread-spectrum technique. In its basic form it is a double FM modulation. A low modulation index FSK, called a sub-carrier, is followed by a high modulation index FM ($\beta \gg 1$) to achieve large bandwidth. The principle of FM-UWB modulation is shown in Fig. 2.1. The resulting FM-UWB signal can be represented as [1]:

$$s_{UWB}(t) = A \cos \left(\omega_c t + \Delta \omega \int_{-\infty}^t m(t) dt \right) = A \cos (\omega_c t + \phi(t)), \quad (2.1)$$

where ω_c is the center frequency, $\Delta \omega = 2\pi\Delta f$ is the frequency deviation and $m(t)$ is the normalized, FSK modulated sub-carrier. According to definition, to be considered UWB the signal must either exceed 500 MHz or 20 % of its center frequency. The bandwidth of the FM signal can be approximated using the Carson's rule [1]:

$$B_{FM} = 2f_m(\beta + 1) = 2(\Delta f + f_m). \quad (2.2)$$

In the above equation f_m is the maximum frequency in the FSK signal spectrum which depends on the sub-carrier center frequency f_{SC} and the data rate R , according to $f_m = f_{SC} + R$. Spectral properties of the FM-UWB signal depend on the sub-carrier waveform. For an FM signal with

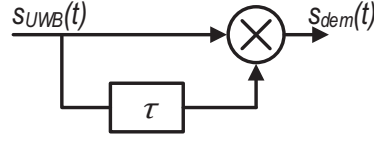


Figure 2.2: Wideband FM demodulator.

modulation index much larger than unity, quasi-stationary approximation is valid and the FM-UWB signal power spectral density (PSD) will be a function of the probability density function (PDF) p_m of $m(t)$ [2]:

$$S_{FM-UWB}(\omega) = \frac{\pi A^2}{2} \left[p_m \left(\frac{\omega - \omega_c}{\Delta\omega} \right) + p_m \left(\frac{\omega + \omega_c}{\Delta\omega} \right) \right]. \quad (2.3)$$

As long as the sub-carrier frequency is reasonably low (keeping the second FM modulation index high, $\beta \gg 1$), the FM-UWB spectrum will be largely determined by the sub-carrier waveform. For an ideal triangular sub-carrier the FM-UWB spectrum will be flat with a relatively steep roll-off. A steeper roll-off can be achieved using a sinusoidal sub-carrier, but this results in curved spectrum shape, with peaking at the edges of the band [3]. As a result the maximum transmit power must be lowered in order to comply with the spectral mask. At higher sub-carrier frequencies, or equivalently lower modulation index (practically $\beta < 20$) equation (2.3) is no longer valid, and good spectral properties of the FM-UWB signal are be lost.

Performance of the FM-UWB modulation can be studied using a wideband FM demodulator presented in Fig. 2.2. After multiplying the signal s_{UWB} with its delayed version and disregarding the high-frequency components, signal at the output of the demodulator will be given by [1]

$$s_{dem}(t) = \frac{A^2}{2} \cos(\omega_c \tau + \phi(t) - \phi(t - \tau)). \quad (2.4)$$

By choosing the time delay equal to an odd multiple N of the quarter period of the carrier center frequency $\tau = NT/4 = N\pi/2\omega_c$ ($N = 1, 3, 5, \dots$) equation (2.4) can be written in the following form:

$$s_{dem}(t) = (-1)^{(N+1)/2} \frac{A^2}{2} \sin(\phi(t) - \phi(t - \tau)) \quad (2.5)$$

$$= (-1)^{(N+1)/2} \frac{A^2}{2} \sin \left(\tau \frac{d\phi(t)}{dt} \right) \quad (2.6)$$

$$= (-1)^{(N+1)/2} \frac{A^2}{2} \sin \left(N \frac{\pi \Delta\omega}{2\omega_c} m(t) \right), \quad (2.7)$$

under the assumption that delay τ is much smaller than the period of the modulating fre-

Chapter 2. FM-UWB as a Low-Power, Robust Modulation Scheme

quency f_m . The bandwidth of the demodulator, herein defined as the frequency range over which the demodulator characteristic is monotonic, depends on N and is given by

$$B_{dem} = f_c \frac{2}{N}. \quad (2.8)$$

A small delay deviation results in offset between the demodulator center frequency and the FM-UWB signal center frequency. This offset will lead to a distortion of the output signal that is dependent on the bandwidth of the signal and the demodulator. It should be noted that the demodulated signal is proportional to the square of the input amplitude (as seen from equation 2.7). This results in expanded dynamic range of the demodulated signal, for example a 10 dB variation in the input amplitude causes 20 dB variation in the demodulated signal amplitude. Furthermore, the signal to noise ratio (SNR) at the demodulator output will be a non-linear function of the input SNR. Based on simplified analysis provided in [1] the SNR at the demodulator output is given by

$$\text{SNR}_{\text{out}} = \frac{B_{RF}}{B_{SC}} \frac{\text{SNR}_{\text{in}}^2}{1 + 4\text{SNR}_{\text{in}}}, \quad (2.9)$$

where SNR_{in} and SNR_{out} represent the signal to noise ratio at the input and the output of the demodulator, respectively. The ratio B_{RF}/B_{SC} is the ratio of the FM-UWB signal bandwidth and sub-carrier bandwidth, and can be seen as a kind of processing gain. The BER can then be calculated as shown in [1]

$$P_b = \frac{1}{2} \text{erfc} \left(\sqrt{\frac{\text{SNR}_{\text{out}}}{2}} \right). \quad (2.10)$$

The erfc function is defined as:

$$\text{erfc}(x) = \frac{2}{\sqrt{\pi}} \int_x^{\infty} e^{-t^2} dt. \quad (2.11)$$

A comparison between FM-UWB and FSK signals having equal power is given in Fig. 2.3. The ratio of energy per bit and noise power spectral density at the input E_b/N_0 is used instead of SNR_{in} in order to provide a fair comparison. This ratio is defined as

$$E_b/N_0 = \text{SNR}_{\text{in}} \frac{B_{RF}}{R}. \quad (2.12)$$

In the given example $B_{RF}=500$ MHz, the sub-carrier modulation index is $\beta_{sub}=0.5$ (the same modulation index is used for FSK) and R is the data rate. In terms of BER, the FM-UWB is clearly suboptimal compared to standard FSK modulation. This is not surprising considering that the larger signal bandwidth results in higher noise power, that ultimately lowers the input SNR. Part of the lost SNR will be recovered in the process of demodulation owing to the processing gain, however the BER degradation compared to the FSK remains notable. The gap between the two modulations decreases with increasing the FM-UWB data rate, and hence

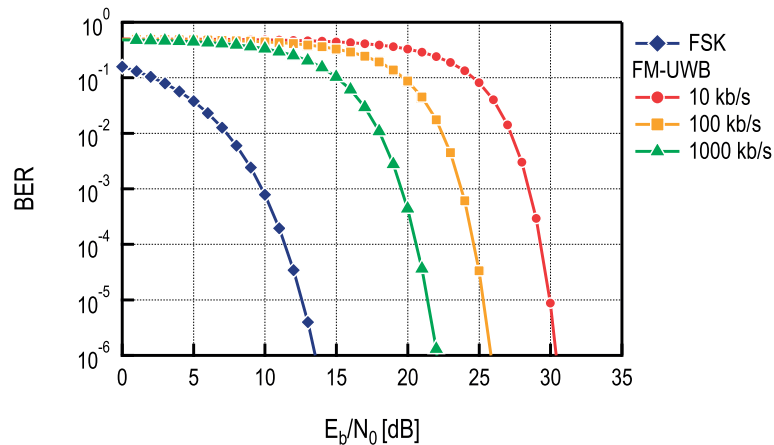


Figure 2.3: Comparison of standard orthogonal FSK and FM-UWB modulation.

higher data rates should yield better performance. However, higher data rates will also require higher sub-carrier frequencies, which results in loss of the spectral properties of the FM-UWB signal.

Compared to narrowband modulations, FM-UWB is clearly suboptimal in terms of sensitivity. There are however some benefits that are perhaps not apparent at a first glance. FM-UWB offers robustness against frequency selective fading and interferers. The behavior of FM-UWB signal in a multipath environment has been studied in [4]. It has been shown that even in severe environments performance degradation of FM-UWB is only minor. Owing to the fact that the signal is spread over a very large band, frequency selectivity is not as harmful as it is for narrowband signals (this can be seen as a kind of frequency diversity). The second benefit of using FM-UWB is its inherent robustness to narrowband interferers. Unlike narrowband systems that rely purely on filtering, the FM-UWB provides some inherent interferer rejection. This further implies that it does not require an increase of the receiver complexity or external filters to provide good performance, hence providing higher potential for miniaturization.

2.1.2 Multi-User Communication and Narrowband Interference

In a wireless sensor network, multiple nodes may need to communicate at the same time. One way to resolve this is the time-division multiple access (TDMA), that allocates time slots in which certain nodes can transmit or receive. This approach requires precise synchronization between the nodes, and as the number of nodes in the network grows, the latency increases quickly. Use of other techniques, such as frequency-division multiple-access (FDMA), where different frequencies are allocated to different users, may reduce the overall latency and synchronization requirements. This section studies the behavior of an FM-UWB system in the presence of multiple input signals and is mainly based on the approach presented in [1].

Suppose there are two signals present at the input of the wideband FM demodulator (Fig. 2.2)

$s_1(t)$ and $s_2(t)$. At the demodulator output the signal will be given by:

$$s_{dem} = s_1(t)s_1(t-\tau) + s_2(t)s_2(t-\tau) + s_1(t)s_2(t-\tau) + s_1(t-\tau)s_2(t). \quad (2.13)$$

Let us assume that the $s_1(t)$ is the FM-UWB signal and the $s_2(t)$ is a narrowband interferer. The component $s_1(t)s_1(t-\tau)$ corresponds to the demodulated sub-carrier. The component $s_2(t)s_2(t-\tau)$ is the FM demodulated narrowband signal. Since its bandwidth is rather small compared to the FM-UWB bandwidth, this component will be located close to dc and can easily be filtered out. It will therefore not influence the sensitivity of the receiver (at least in the ideal case). The last two terms in equation (2.13) constitute the residual signal that will pollute the useful signal [1]:

$$W(t) = s_1(t)s_2(t-\tau) + s_1(t-\tau)s_2(t) \quad (2.14)$$

The low-frequency terms of the residual signal $W(t)$ will fall within the sub-carrier band, effectively increasing the noise floor of the receiver and lowering sensitivity. Assuming the narrowband signal is located close to the FM-UWB signal center frequency, residual signal will be located at baseband frequencies from 0 to $B_{RF}/2$. If flat spectrum of the residual signal is further assumed, then the signal to interference ratio can be estimated as [1]:

$$\text{SIR} = 20 \log \left(\frac{A_1}{2A_2} \right) - 10 \log \left(\frac{B_{RF}}{2B_{SC}} \right), \quad (2.15)$$

where A_1 and A_2 are the amplitudes of the two input signals. Factor $B_{RF}/2B_{SC}$ is a result of sub-carrier filtering. Interestingly, the amount of interference rejection is proportional to the FM-UWB processing gain.

Multiple FM-UWB signals can be distinguished by assigning different sub-carrier frequencies to different users. This technique will be referred to as the sub-carrier FDMA (SC-FDMA). Assuming that the signals $s_1(t)$ and $s_2(t)$, from equation (2.13), are the two FM-UWB signals it is clear that the simultaneous demodulation of different FM-UWB signals is possible. The component $s_2(t)s_2(t-\tau)$ will in this case correspond to the second demodulated FM-UWB signal. As long as the sub-carrier frequency of the second signal is separated from the first, the two can be distinguished and demodulated separately. The principle of multi-user communications using the SC-FDMA is illustrated in Fig. 2.4. Multiple signals transmitted from different nodes can be demodulated either by a single node (for example gathering data from multiple sensors simultaneously), or by different nodes (e.g. to allow isolation of different parts of the network).

Just like in the case of the narrowband interferer residual signal will cause sensitivity degradation. Assuming two FM-UWB signals at the input, with aligned center frequencies, equa-

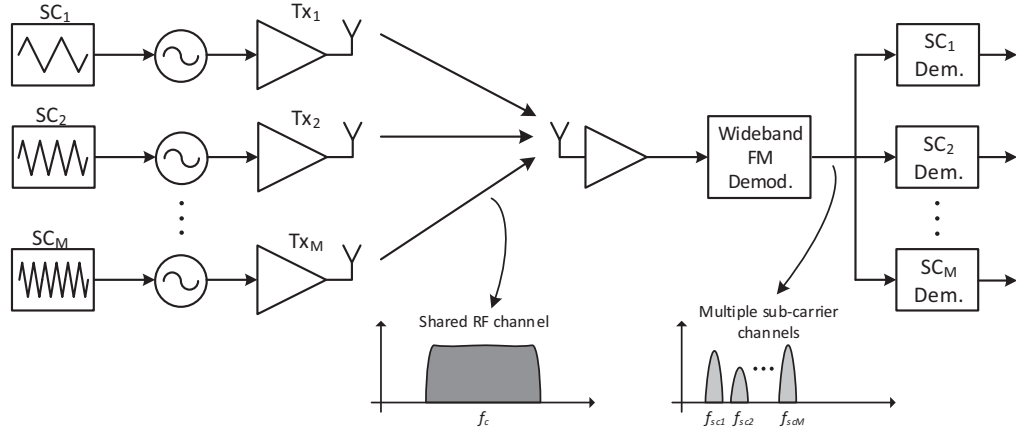


Figure 2.4: FM-UWB multi-user communication.

tion (2.14) can be written as:

$$W(t) = \frac{A_1 A_2}{2} \cos(\omega_c \tau + \phi_1(t) - \phi_2(t - \tau)) + \frac{A_1 A_2}{2} \cos(\omega_c \tau + \phi_2(t) - \phi_1(t - \tau)) \quad (2.16)$$

$$\approx (-1)^{(N+1)/2} A_1 A_2 \sin\left(\frac{\tau}{2} \left(\frac{d\phi_1(t)}{dt} - \frac{d\phi_2(t)}{dt}\right)\right) \cos(\phi_1(t) + \phi_2(t)) \quad (2.17)$$

$$= (-1)^{(N+1)/2} A_1 A_2 \sin\left(\frac{\Delta\omega\tau}{2} (m_1(t) - m_2(t))\right) \cos(\phi_1(t) + \phi_2(t)). \quad (2.18)$$

The residual signal is proportional to the difference of the two modulating signals multiplied by the factor $\cos(\phi_1(t) + \phi_2(t))$, which is a signal that occupies a bandwidth of $B_{RF} = 2\Delta f$. Again, assuming the spectrum of the residual signal is flat, signal-to-interference ratio can be estimated as [1]:

$$\text{SIR} = 20 \log\left(\frac{A_1}{2A_2}\right) - 10 \log\left(\frac{B_{RF}}{B_{SC}}\right). \quad (2.19)$$

The achievable BER is limited by the SIR. Increasing the number of users, or increasing the difference in power levels between the two users, reduce the SIR and could eventually prevent correct demodulation of the useful signal. The maximum required BER will ultimately limit the tolerable SIR, and subsequently, the number of users or the maximum acceptable power difference.

The analysis conducted by Gerrits in [1, 5] can be extended to the case of multiple FM-UWB users in the presence of noise. Assuming that the delay can be considered relatively small and that the noise autocorrelation function is $R_n(\tau) = 1$ for values of the delay $\tau = N\pi/2\omega_c$, the noise analysis can be simplified while maintaining good accuracy. The result reported in [6] can be generalized for the case of M FM-UWB users. Under the above assumptions the

demodulator output signal is given by

$$s_{dem} = (s_1 + s_2 + \dots + s_M + n)^2 \quad (2.20)$$

$$= \sum_{i=1}^M s_i^2 + 2 \sum_{i=1}^M \sum_{j=i+1}^M s_i s_j + \sum_{i=1}^M s_i n + n^2. \quad (2.21)$$

Terms of the form s_i^2 correspond to the demodulated sub-channel i . Terms of the form $2s_i s_j$, $i \neq j$, correspond to the interference among different FM-UWB signals, the number of these terms is $M(M-1)/2$. Finally, following the same reasoning as in [1, 5], and assuming that all the noise and interference terms are independent, the output signal to noise and interference ratio (SNIR) is given by

$$\text{SNIR}_{k,\text{out}} = \frac{B_{RF}}{B_{SC}} \frac{S_k^2}{N^2 + 4 \sum_{i=1}^M S_i N + 4 \sum_{i=1}^M \sum_{j=i+1}^M S_i S_j}, \quad (2.22)$$

where S_i corresponds to the input power of signal s_i and N is the input noise power. For a multi-user environment two cases are of particular importance:

1. Two FM-UWB users of different input power levels
2. M FM-UWB users of equal power levels

For the case of two users, equation (2.22) reduces to

$$\text{SNIR}_{1,\text{out}} = \frac{B_{RF}}{B_{SC}} \frac{S_1^2}{N^2 + 4S_1 N + 4S_2 N + 4S_1 S_2} \quad (2.23)$$

$$= \frac{B_{RF}}{B_{SC}} \frac{\text{SNR}_{1,\text{in}}^2}{1 + 4\text{SNR}_{1,\text{in}}(1 + \text{SIR}_{\text{in}}^{-1}) + 4\text{SNR}_{1,\text{in}}^2 \text{SIR}_{\text{in}}^{-1}}, \quad (2.24)$$

where $\text{SIR}_{\text{in}} = S_1/S_2$. Compared to equation (2.9) two additional terms exist that depend on the input signal to interferer ratio SIR_{in} . Furthermore, for increasing values of $\text{SNR}_{1,\text{in}}$ the output signal to noise and interference ratio $\text{SNIR}_{1,\text{out}}$, is no longer limited by noise, but solely by the interference and approaches

$$\text{SNIR}_{1,\text{out}} = \frac{B_{RF}}{B_{SC}} \frac{\text{SIR}_{\text{in}}}{4}, \text{ for } \text{SIR}_{\text{in}} \gg 1, \quad (2.25)$$

which is the limit from equation (2.19). As an example, consider that the FM-UWB signal is used with RF bandwidth $B_{RF} = 500$ MHz, using a 100 kb/s sub-carrier, with orthogonal FSK and a modulation index of 1 ($B_{SC} = 200$ kHz). The required SNIR for orthogonal FSK to achieve a BER of 10^{-3} is approximately 13 dB. The maximum difference in power levels between the two FM-UWB signals is then 21 dB.

For the case of M users of equal input power, $S_1 = S_2 = \dots = S_M = S$, the equation (2.22)

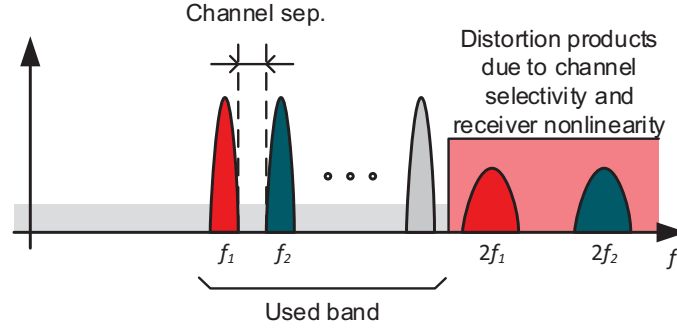


Figure 2.5: FSK sub-channel frequency allocation and limits due to distortion.

reduces to

$$\text{SNIR}_{\text{out}} = \frac{B_{RF}}{B_{SC}} \frac{S^2}{N^2 + 4MSN + 2M(M-1)S^2} \quad (2.26)$$

$$= \frac{B_{RF}}{B_{SC}} \frac{\text{SNR}_{\text{in}}^2}{1 + 4M\text{SNR}_{\text{in}} + 2M(M-1)\text{SNR}_{\text{in}}^2} \quad (2.27)$$

Again, if the signal power is sufficiently higher than the noise power, the output SNIR_{out} becomes a function of FM-UWB signal bandwidth and the number of users:

$$\text{SNIR}_{\text{out}} = \frac{1}{2M(M-1)} \frac{B_{RF}}{B_{SC}}, \text{ for } \text{SNR}_{\text{in}} \gg 1, \quad (2.28)$$

The above equation can be used to determine the maximum achievable number of users, for a given minimum required signal to noise and distortion ratio. For example, assuming the same system parameters as above ($B_{RF} = 500$ MHz, $R = 100$ kb/s, $B_{SC} = 200$ kHz), the maximum number of equal power users is 16. In both described cases FM-UWB signal bandwidth can be increased in order to increase the achievable SNIR_{out} .

The limits predicted by equations (2.25) and (2.28) assume an ideal system since they only take into account a limited number of effects. In practical systems, these limits are upper bounds and will be difficult to achieve. The above analysis only considers an ideal AWGN channel, with a perfectly flat frequency characteristic. In reality, this will never be the case. Part of the channel transfer function will come from the transmitter and receiver, and part will come from the wireless channel (multi-path propagation). Intuitively, one can see the FM-UWB signal as a carrier that slowly moves across a broad frequency range. Since the equivalent channel transfer function is not constant, the amplitude will vary with the instantaneous carrier frequency. Assuming that the channel does not change with time, amplitude will be a periodic function, with the period of the sub-carrier. Even if the wideband FM demodulator is perfect, these amplitude variations will result in the appearance of harmonics. Aside from the channel transfer function, the harmonics will also appear as a product of non-linearities in the receiver chain. Finally, these harmonics will limit the useful sub-carrier band to one octave. If $f_{SC, \text{min}}$ is the minimum sub-carrier frequency, then spectrum above $2f_{SC, \text{min}}$ will

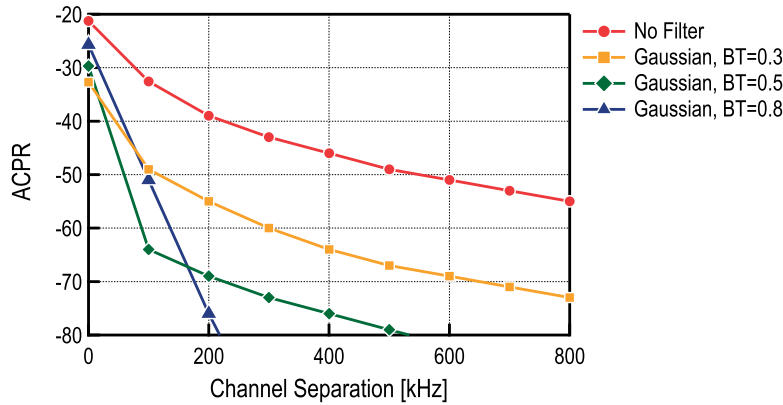


Figure 2.6: ACPR for filtered and non-filtered FSK signal, as a function of channel separation (100 kb/s data rate, modulation index 1).

be corrupted by the second and higher order components. The quality of any useful signal at frequencies above $2f_{SC,min}$ would, therefore, be degraded by the harmonics of other sub-carriers, preventing correct demodulation (Fig. 2.5). With one octave limit for the sub-carrier band, the lowest sub-carrier frequency $f_{SC,min} = 1$ MHz, and 200 kHz wide FSK channels, the number of sub-carrier channels that can be accommodated is 5. This number can be increased by increasing $f_{SC,min}$. In principle, the effect of channel transfer function can be canceled out by equalization of the input FM-UWB signal. However, equalization techniques are complex, they would drastically increase power consumption of the receiver, and as such are not suited for low power systems.

In the previous example, it was assumed that the FSK channels can be placed adjacent to each other. This is impractical for two reasons. The first reason is that the undesired channels must be filtered out before the final FSK demodulation. Because of the finite quality factor of the filter, some spacing must be introduced between the channels. The second reason is interference among adjacent FSK channels. Theoretically the spectrum of the FSK signal is infinitely wide. Although largest portion of the channel power is located inside the band defined by Carson’s rule, part of the spectrum will leak to side channels and interfere with adjacent users. This effect is quantified by the adjacent channel power ratio (ACPR), and is defined as the ratio of the power inside the channel to the power in the adjacent channel. The ACPR generally depends on the type of modulation, pulse shaping filter and transmitter non-linearity. In the case of FSK modulation, typically Gaussian pulse shaping is used. The shape of the Gaussian pulse is determined by the bandwidth-time (BT) parameter, defined as the ratio between the 3 dB filter bandwidth and data rate. Decreasing the BT parameter results in more compact spectrum, but increases the inter-symbol interference as the pulse duration increases (over several bit periods). ACPR as a function of channel separation, for different values of the BT parameter, is given in Fig. 2.6. Although filtering can be used to reduce interference, this was rarely done in reported FM-UWB implementations. The reason is that it adds complexity on both transmitter and receiver sides, and since multi-user communication

with FM-UWB has rarely been explored it was not needed. Interference among channels can always be decreased by increasing the channel separation, but this also reduces the number of available FSK channels. For a system with $B_{RF} = 500$ MHz, $R = 100$ kb/s, $B_{SC} = 200$ kHz, the required SNIR of the FSK signal to achieve a BER of 10^{-3} is 13 dB. If a channel separation of 100 kHz is used, with no filtering, then the adjacent channel power can be at most 20 dB above than the desired channel power. This will correspond to 10 dB difference in power between the two FM-UWB signals. For this particular case, it is the ACPR that will limit the maximum tolerable power difference between the two users and not the interference from the residual signal (equation (2.25))

Additional constraints may come from the receiver non-linearity and limited dynamic range. Due to the quadratic demodulator characteristic, the dynamic range requirements are higher for the circuits following the wideband FM demodulator. If one of the FSK signals is sufficiently strong it may saturate the circuits causing suppression of weaker FSK signals (FM capture effect). Since there is typically a trade-off between power and dynamic range in amplifiers, a larger acceptable power difference between the received signals will come at the cost of increased power consumption.

Different choice with respect to the system parameters leads to different performance in terms of complexity, sensitivity, data rate, number of channels and power consumption. By modifying the RF bandwidth, sub-carrier frequencies, dynamic range etc., it is possible to perform various trade-offs and to optimize the FM-UWB transceiver according to the specific needs of the system.

2.1.3 Beyond standard FM-UWB

The FM-UWB modulation was originally intended as double FM modulation, where a low modulation index FSK is followed by a large modulation index FM. It is an optional mode in the IEEE 802.15.6 standard for wireless body area networks [7]. According to the UWB PHY specifications, two modulations are supported; IR-UWB as mandatory and FM-UWB as an optional mode. For FM-UWB, the data rate is set to 250 kb/s, using a continuous phase (CP) FSK modulation, centered at 1.5 MHz, with a frequency deviation of 250 kHz. A Gaussian filter is used for pulse shaping with the BT parameter set to 0.8. For the sub-carrier waveform, either a triangular, a sawtooth, or a sine waveforms are allowed.

Strict standard definitions do not allow different sub-carrier frequencies, higher or lower data rates, or multi-user communication. The lack of flexibility limits the use of FM-UWB in WBAN applications, and does not allow FM-UWB to reach its full potential. In general, the sub-carrier modulation does not need to be limited to 250 kb/s 2-FSK. Speed and modulation order could be modified according to the channel conditions (a less frequency selective channel allows higher data rates). A transmitter implementing a data rate of 1 Mb/s has been reported in [8], that demonstrates the feasibility of moving to higher data rates. Furthermore, higher order FSK can be explored such as 4-FSK and 8-FSK, allowing to further boost communication

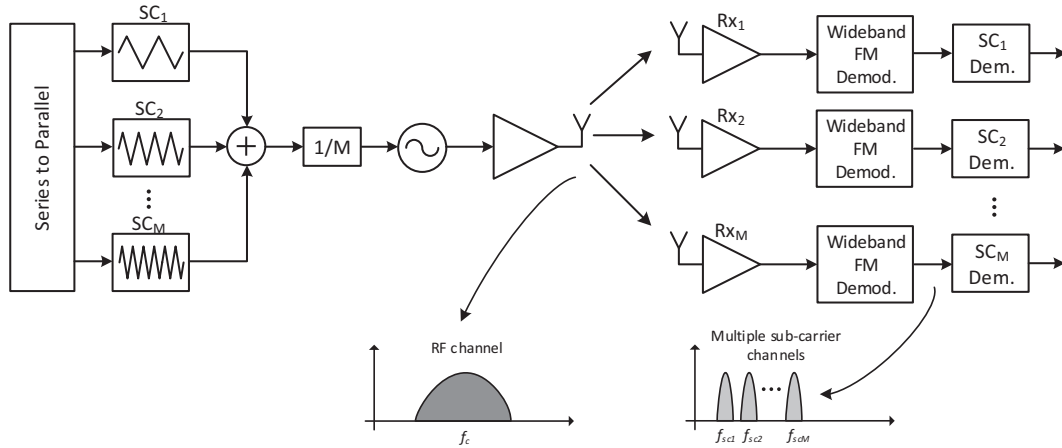


Figure 2.7: FM-UWB multi-channel broadcast.

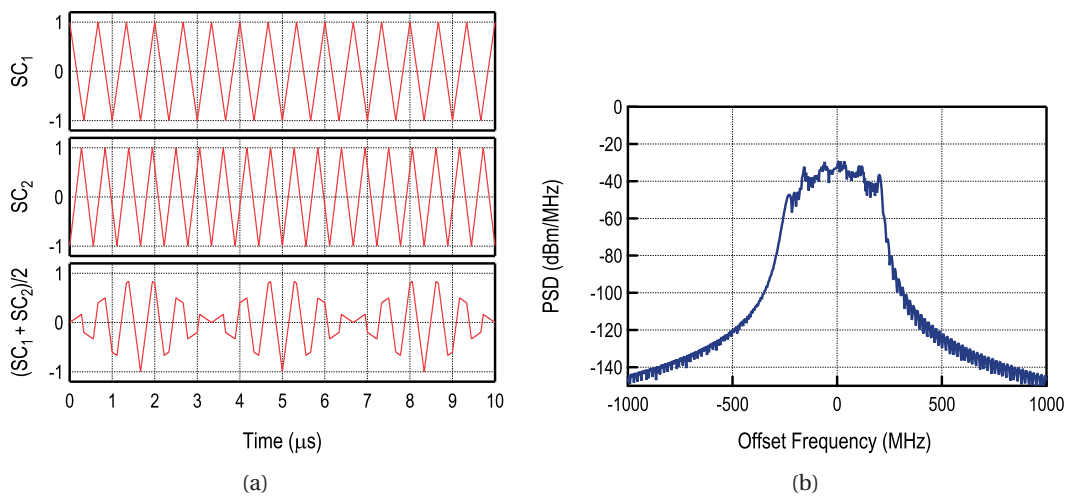


Figure 2.8: Example of transmission on two channels, time domain sub-carrier signal (a) and transmitted signal spectrum (b).

speed. One such transmitter is reported in [9]. Finally, it would also be possible to use PSK modulations without affecting the good spectral properties of FM-UWB. Other variations are possible, and one example is the Chirp-UWB (C-UWB) modulation [10], that is a trade-off between FM-UWB and IR-UWB. Instead of continuous frequency sweep, a single up or down chirp is transmitted depending on the input bit. The duration of the chirp is much lower than the symbol duration and allows duty cycling of the transceiver at a symbol level, thus saving power. At the same time the duration of the pulse is much longer than in the case of IR-UWB and does not require precise synchronization. One downside of C-UWB is that the good spectral properties of the FM-UWB signal are lost.

A minor modification of a standard FM-UWB signal can be used to enable simultaneous

transmission on multiple sub-channels. Instead of using a single FSK sub-channel, multiple sub-channels can be summed, and the resulting signal used to modulate the RF carrier. This would allow a single transmitter to transmit different messages to multiple receivers at the same time. The concept is shown in Fig. 2.7. In order to preserve the same frequency deviation, if M sub-channels are used, sub-carrier signals are scaled by a factor $1/M$. The example for two sub-carriers is shown in Fig. 2.8. Unfortunately, the flat spectrum of the transmitted signal is lost and, as a consequence, transmit power will have to be decreased in order to maintain the signal below the spectral mask defined for the UWB band. The spectrum will take the shape of the PDF of the modulating signal (as shown by equation (2.3)) which is in this case an average of the two sub-carrier signals, and is no longer a triangular waveform. The exact shape of the resulting sum of sub-carrier signals will depend on the number of sub-channels, their frequencies and initial phases. The BER calculation can be extended to the case of M sub-channels. The only difference compared to standard FM-UWB is that the power of each channel is scaled by M . This is equivalent to reducing the RF bandwidth by the same factor and hence the SNR_{in} will be scaled as well. Equation (2.9) can then be modified accordingly to estimate the output SNR:

$$\text{SNR}_{\text{out}} = \frac{B_{RF}}{B_{SC}} \frac{\text{SNR}_{\text{in}}^2 / M^2}{1 + 4\text{SNR}_{\text{in}} / M}. \quad (2.29)$$

The probability of error is then calculated in the same way as for the single user case. One advantage of the proposed modification compared to the described multi-user scheme is that a larger number of channels can be used in the same bandwidth. If orthogonal sub-carrier frequencies are used, there will be no interference between the channels on the receiver side (in that sense the proposed scheme resembles OFDM). In the multi-user case, transmitters would have to be perfectly synchronized to preserve orthogonality, which is practically impossible, and as a result produces interference among different users. The only way to solve this is to separate and filter out the unwanted channels.

An existing degree of freedom in the proposed modulation technique is the sub-channels scaling. If different receivers are located at different distances from the transmitting node, the received power, and subsequently the BER, may vary. This can be circumvented by using a different scaling factor for each of the channels. Smaller scaling factor could be assigned to more distant receivers, in order to improve the BER on their sub-channels. As long as the sum off all scaling factors is 1, the maximum frequency deviation will remain the same, maintaining the signal spectrum within the defined limits.

2.2 State-of-the-Art FM-UWB Transceivers

One of the main advantages of the FM-UWB is the simplicity of the transceiver architecture, which offers a low power consumption and a high degree of integration. Different transmitter and receiver implementations have been presented in the literature. They will be discussed in the following paragraphs, with a focus on both architecture and circuit level techniques.

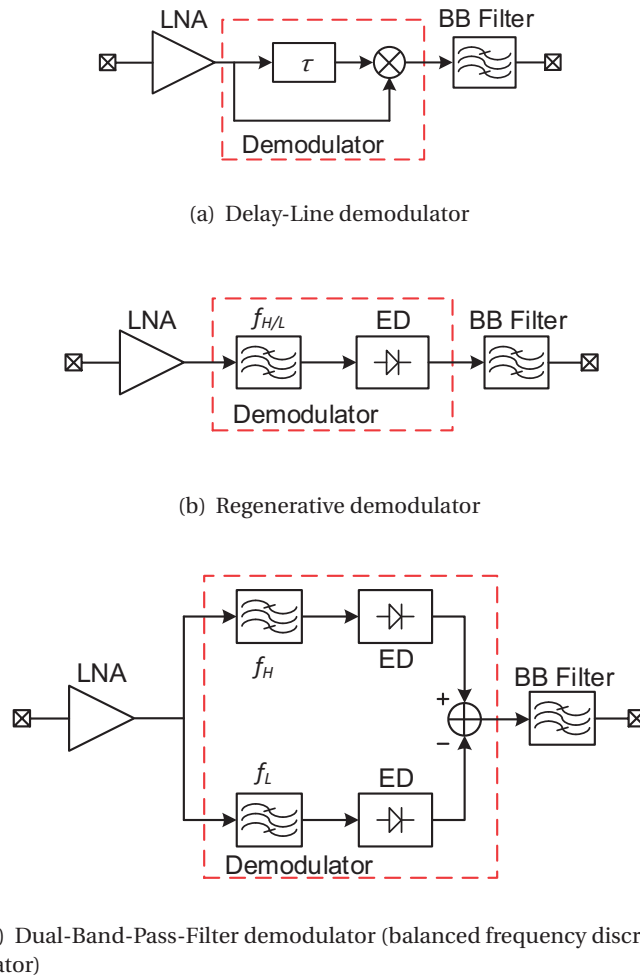


Figure 2.9: FM-UWB receiver architectures reported in the literature.

Finally, FM-UWB will be compared to state of the art narrow-band and IR-UWB receivers, to gain insight into some of the advantages and drawbacks of the chosen modulation scheme.

2.2.1 FM-UWB Receivers

Different FM-UWB receiver architectures found in the literature are presented in Fig. 2.9. The originally proposed wideband FM demodulator based on a delay line demodulator is depicted in Fig. 2.9(a). Two other implementations are based on an FM discriminator, they rely on filtering to convert the input FM signal into an amplitude modulated (AM) signal. Conversion characteristics of all the demodulators are shown in Fig. 2.10.

The FM-AM characteristic of the delay line demodulator was studied in the previous section (equation (2.7)). The output AM signal will be a sine function of the input frequency. It can be seen that the choice of delay is a trade-off between the conversion gain and the bandwidth

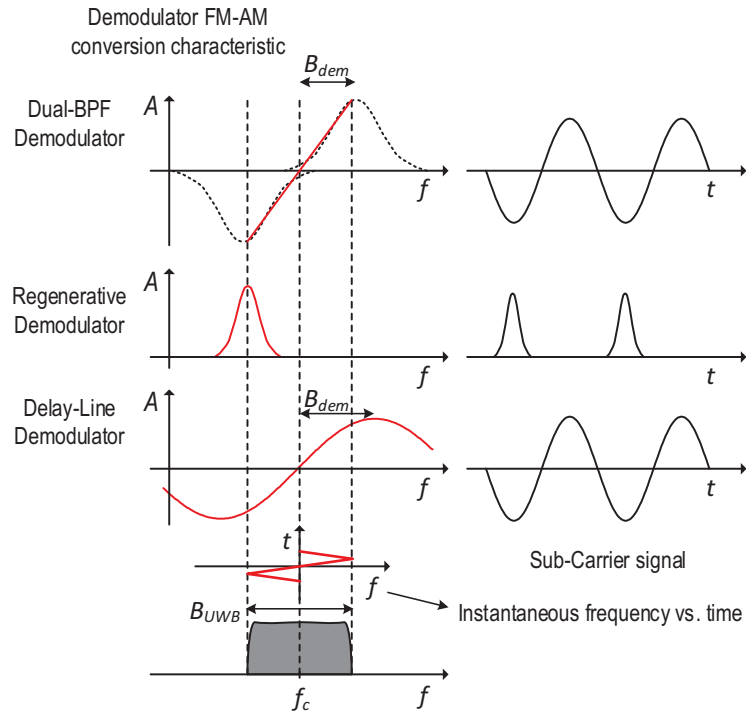


Figure 2.10: Frequency-to-amplitude conversion characteristic of reported FM demodulators.

of the demodulator. Decreasing delay leads to lower conversion gain, but also increases the useful frequency range. In addition, this delay is constrained to a discrete set of values and must be equal to an odd multiple of the quarter period of the carrier frequency. It must be determined precisely in order to avoid frequency offset. In practice, a small offset will always be present as a result of process variation, however since the transmitted signal is at least 500 MHz wide, this offset should not have a major impact on the receiver performance. The first fully integrated FM-UWB receiver based on a DL demodulator was described in [11]. It achieves a sensitivity of -88 dBm while consuming 9.4 mW. The demodulator itself consumes around 5.8 mW, and the additional 3.6 mW are used by the LNA.

An LNA that provides high gain across a large bandwidth inevitably requires more power compared to a narrowband LNA. In order to reduce the power consumption, a narrow-band regenerative receiver was proposed in [12]. This approach allows for preservation of high gain and relatively good noise figure, while minimizing the power consumption. The high-Q filtering is in fact implemented in the LNA and its center frequency corresponds to either the highest or the lowest frequency of the FM-UWB signal. The band-pass filter behaves as a frequency discriminator that converts the input FM signal into an AM signal, that is then converted to IF using an envelope detector. Due to the high-Q factor of the filter that results in a very nonlinear FM-AM conversion characteristic, the demodulated signal will be a train of pulses whose frequency corresponds to the sub-carrier frequency (Figure 2.10). The receiver

from [12] consumes 2.2 mW while achieving -84 dBm sensitivity. A later implementation presented in [13] introduced several improvements at the circuit level (most notably current reuse among several blocks) which resulted in power consumption of only 560 μ W and only a slight reduction of sensitivity. Although the regenerative receiver achieved significant power savings, there are some downsides to this architecture. Narrow-band interferer rejection mostly relies on the high-Q input filtering. If the interferer falls inside the pass-band it could easily saturate the stages following the LNA and prevent reception. Indeed, such a scenario could be avoided by introducing the on-chip tuning circuit that could shift the filter center frequency, but this adds complexity to the system. The second downside comes from the nonlinear FM-AM conversion. If several FM-UWB signals were to occupy the same RF band, the weaker signals would be attenuated in the nonlinear conversion process, which would prevent correct demodulation. This is known as the capture effect [14], and limits the regenerative receiver to cases where only one FM-UWB signal is transmitted in the given RF band.

In an attempt to improve the linearity of the regenerative demodulator, a modified architecture was proposed in [15]. Instead of using just one band-pass filter, a second branch was added (Figure 2.9(c)), resulting in a Dual Band-Pass Filter (DBPF) demodulator, otherwise known as a balanced frequency discriminator. The two filters are tuned to the highest and the lowest frequency in the FM-UWB signal spectrum, they are followed by the two envelope detectors that remove the RF carrier from the signal, and the difference of the two IF signals finally yields the demodulated sub-carrier. The equivalent linearized characteristic is shown in Figure 2.10. Compared to the original regenerative receiver, the Q-factor of the two filters can be lowered, which allows some power savings per filter, but the two still consume more than the single filter from [13]. The dominant source of power consumption remains the wideband LNA, that must provide equal gain over the entire band in the DBPF receiver. The two architectures perfectly illustrate the trade-off between linearity and power consumption in FM-UWB receivers. The implementation from [15] consumed 3.8 mW, and achieved -78 dBm of sensitivity. The same architecture was reused in [10] for demodulation of a Chirp-UWB signal, where symbol-level duty-cycling of the receiver was used to bring down the average power consumption to 0.6 mW. The DBPF receiver exhibits better narrow-band interferer rejection compared to a standard regenerative receiver and should perform better in scenarios with multiple FM-UWB users, although such capability was not confirmed by measurements.

A performance summary of different FM-UWB receivers is given in Table 2.1. Each of the proposed architectures has its own advantages and disadvantages. Receiver from [11] generally has the best performance but is also the most power hungry. The regenerative receiver can provide a very low power consumption while maintaining good sensitivity, but at the cost of linearity. A trade-off between linearity and interference rejection on one side, and power consumption on the other, is demonstrated with the balanced frequency discriminator from [15]. One thing that is in common for all the architectures is that the largest contributors to the power consumption are the RF blocks, mainly the LNA. Therefore, one approach to decreasing consumption would be to minimize the number of RF blocks, or to completely remove them if

Table 2.1: Performance summary of state-of-the-art FM-UWB receivers

Reference	[11]	[16, 12]	[17]	[15]	[10]	[18, 13]
Year	2009	2010	2012	2013	2014	2014
Demodulator	RF-DL	Reg	RF-DL	DBPF	DBPF	Regen.
Frequency [GHz]	7.5	3.75	3.8	3.75	8	4
Power cons. [mW]	9.4	2.2	7.2	3.8	0.6/4*	0.58
Supply [V]	1.8	1	1.6	1	1	1
Data rate [kb/s]	50	100	50	100	1000	100
Sensitivity [dBm]	-88	-84	-70	-78	-76	-80.5
NB SIR [dB]	-25	-30	-	-23	-	-18
SC-FDMA	Yes	No	-	No	No	No
Efficiency [n]/b]	188	2.2	144	38	1	5.8
Tech. node [nm]	250	90	180	65	65	90

* Power consumption is 0.6 mW with duty-cycling and 4 mW without duty-cycling.

possible. This approach will be studied in the following chapters.

2.2.2 FM-UWB Transmitters

Unlike the FM-UWB receivers, the architecture of FM-UWB transmitters has remained unchanged over the past several years. Considering its simplicity (Figure 2.1) it is clear that there is not a lot of potential for improvement at the architectural level. In fact, the reduction of power on the transmitter side is mainly a result of improvements at the circuit level. Every FM-UWB transmitter consists of three blocks, the sub-carrier generator, the VCO (sometimes as a part of a PLL or an FLL) and a power amplifier (PA).

The sub-carrier generator synthesizes the triangular waveform that is used to drive the VCO. As the sub-carrier frequencies are rather low (typically 1-2 MHz) this block does not contribute significantly to the overall transmitter consumption. One way to implement it is a Direct Digital Synthesis (DDS) as described in [19]. The advantages of digital implementation are the simple and precise frequency control without the need for calibration. The drawback of the fully digital approach becomes apparent at higher data rates, where higher sub-carrier frequencies are needed. In [8] 51 MHz sub-carrier frequency is used. Since roughly 20 points per period are needed to generate a reliable sub-carrier waveform, a DDS would need to operate at a clock speed of more than 1 GHz, which would be difficult to implement and would consume a significant amount of power. Instead, a relaxation oscillator is used within a PLL, a simpler and lower power solution in this case. Another interesting approach that leads to a very low power consumption is a free-running relaxation oscillator that is periodically calibrated using an FLL [20]. In this case, a digital frequency control is provided through a capacitor bank, however this approach is usually not precise enough if multiple sub-carrier channels are to be used. Additionally, it might occupy a larger area due to the size of capacitors needed at the frequency of interest.

The two main parts of the FM-UWB transmitter that essentially determine its power consumption are the VCO and the PA. In the case where transmitted power is 10 dBm or more, the transmitter efficiency was dominated by the PA, however at lower output powers, such as -10 dBm the contribution of the VCO becomes quite significant. In some of the earlier implementations, the RF carrier was synthesized using an LC VCO within a PLL [21, 8]. To decrease power, the frequency synthesizer is duty cycled, making the frequency dividers active for only 10 % of the time. Although this allowed some savings, the power consumption was still on the order of 10 mW. A significant improvement was made when the LC oscillator was replaced with a ring oscillator [20, 9]. This was possible owing to the loose phase noise constraints of the FM-UWB modulation. Additionally, instead of the quasi-continuous PLL, an FLL calibration loop was used [20]. Since the FM-UWB spectrum is very wide, the center frequency can deviate slightly without a major impact on performance and it does not need to be monitored continuously. Therefore, once calibrated, the VCO can operate in a free running manner until temperature or some other external factor causes a significant frequency shift. Since these external processes are usually slow, calibration only needs to be done once in a few hours or days, which makes the average power consumption of such an FLL practically negligible. The described approach led to the first sub-milliwatt FM-UWB transmitter [20]. The next step in reducing the VCO consumption was reducing the frequency of oscillation. Since an N -stage ring oscillator produces N equally spaced phases, these phases can be combined to produce a frequency that is N times higher [22]. It is then possible to use a ring oscillator that works at a frequency that is N times lower than the carrier center frequency. The approach was demonstrated in [22] and used for the FM-UWB transmitter in [13] to reduce the power consumption down to 0.63 mW. A three-stage ring was used that oscillated at one third of the carrier frequency, which resulted in the VCO power consumption of less than 90 μ W.

Even though the VCO cannot be neglected, the PA remains the most power-hungry block in the system. The key to further reducing the power consumption of an FM-UWB transmitter is an efficient power amplifier. However, design of an integrated PA for such a low power and wide band poses a number of challenges. In standard narrow-band applications targeting 10 dBm output power or more, the most efficient approach is to use a switching PA such as class D or E. The first problem with class E is that the output matching network is set to a very narrow range of frequencies and achieving good efficiency over a large band would be impossible. Second problem with switching amplifiers is that their efficiency is directly related to the on-resistance of the switch, which dictates the minimum size of the output transistor. In addition, the PA must be driven by a square wave with very sharp transitions to minimize the turn-on time of the switch. The two requirements impose very hard constraints, resulting in power dissipation in the driving circuits that is comparable to that of the PA. Therefore, when the driving circuit is also accounted for, switching PAs seem not to be the best solution. The linear power amplifiers, classes A, AB, B and C, do not achieve as high efficiency, but their driving requirements are also lower. Moving from class A to class C operation, the maximum attainable efficiency increases, but the power gain decreases and larger driving signal is necessary, thus again shifting the burden from the PA to the driver. A good compromise is the class AB that attains

Table 2.2: Performance summary of state-of-the-art FM-UWB transmitters

Reference	[21]	[8]	[20]	[17]	[9]	[10]	[18, 13]
Year	2010	2011	2011	2012	2013	2014	2015
SC Modulation	2-FSK	2-FSK	2-FSK	2-FSK	8-FSK	2-FSK	2-FSK
Frequency [GHz]	3.8	3.8	4	3.8	3.75	8	4
Bandwidth [MHz]	600	700	500	560	500	500	500
Power cons. [mW]	9.6	18.2*	0.9	8.7	1.14	3.5**	0.63
Supply [V]	1.6	1.6	1	1.6	1	1	1
Data rate [kb/s]	10	1000	100	50	750	1000	100
Out. power [dBm]	-14.5***	-12.8	-10.2	-13.7	-14	-11***	-10.1
Efficiency [nJ/b]	960	18.2*	9	174	1.5	0.39	3.1
Tech. node [nm]	180	180	90	180	65	65	90

* Excluding the output PA.

** In continuous mode, 0.39 mW with duty cycling.

*** Estimated from figure.

decent efficiency and does not need a rail-to-rail input signal. In fact, all of the transmitters reported in [20, 9, 13], which achieve the lowest power consumption reported so far, use a complementary class AB power amplifier.

For linear PAs in general, optimal efficiency is obtained when the output voltage swing is maximized. In case of a complementary class AB or B amplifier, maximum output voltage swing is equal to the supply voltage. The load resistance seen from the power amplifier, must therefore be chosen such as to provide the desired output power. The problem with low power transmission is that the value of the optimal load resistance is relatively high. As a consequence a large transformation ratio of the matching network is needed, which then increases the losses in the network. One way to solve this problem would be to reduce the supply voltage. However, such an approach would require another circuit (a DC-DC converter) that would lower the voltage to the desired level. This would not only increase complexity but also introduce its own losses and possibly require off-chip components. A better and simpler way is to apply current reuse technique demonstrated in [13], where the PA and the driver share the same current. Since the effective PA supply voltage is lower, there is no need for such a high transformation ratio of the matching network and, at the same time, the PA bias current is used to supply the driver. The efficiency of the transmitter can therefore be improved without any increase in complexity, which led to the current lowest power FM-UWB transmitter [18, 13], as shown in Table 2.2.

2.2.3 FM-UWB against IR-UWB and Narrowband Receivers

IR-UWB is a time domain approach to ultra-wideband communications. The IR-UWB uses pulses of very short duration to achieve the desired bandwidth, and the pulses are modulated using one of the standard digital modulations, such as on-off keying (OOK), pulse position

Chapter 2. FM-UWB as a Low-Power, Robust Modulation Scheme

modulation (PPM), PSK or FSK. Table 2.3 summarizes the performance of some of the IR-UWB receivers. Compared to FM-UWB, the IR-UWB is targeting higher data rates, typically above 1 Mb/s, and in some cases going up to 1 Gb/s, and as a result, it also achieves better efficiency. Energy per bit of FM-UWB receivers remains above 1 nJ/b, while some of the IR-UWB implementations achieve an improvement by an order of magnitude. At the same time IR-UWB receivers exhibit much higher power consumption, in some cases exceeding 100 mW. Another downside of IR-UWB is that the higher complexity usually typically results in larger silicon area and, also a more difficult, costly and time consuming implementation. This higher complexity is associated to synchronization difficulties inherent to IR-UWB. Short pulse duration means that precise synchronization is required to detect and demodulate pulses (especially in the case of PPM). This translates into a need for a precise frequency reference, and complex and power-hungry baseband signal processing, sometimes involving a digital signal processor (DSP). Since the targeted application doesn't require high data rates, and a highly integrated and miniaturized solution is preferred, FM-UWB has an advantage, even though it may not always be the most energy efficient solution.

Table 2.3: Performance summary of IR-UWB receivers

Reference	[23]	[24]	[25]	[26]	[27]	[28]
Year	2009	2008	2006	2010	2009	2013
Modulation	BPSK	BPSK	OOK	OOK	OOK	BPSK
Frequency [GHz]	8	4	4.1	4	3-9	2.4
Power cons. [mW]	4.3*	98	81	1.64	156	1.28*
Supply [V]	1.2	1.2	1.8	1	1	1.2
Data rate [Mb/s]	40	1000	200	1	50	12.5
Sensitivity [dBm]	-52	-41	-72	-60	-53	-16**
Efficiency [nJ/b]	0.11	0.98	0.4	1.64	3.12	0.012
Tech. node [nm]	130	65	180	130	90	180

* No LNA

** 50 mV input signal in 50 Ω system

Narrowband radios are widely used in WSN applications today. A wide variety of commercial Bluetooth, ZigBee and similar transceivers are readily available and can easily be integrated into sensor nodes. These kind of transceivers typically consume between 5 mW and 10 mW, provide data rates from 1 kb/s to 1 Mb/s and sensitivity varying from -80 dBm down to -100 dBm. To conserve power, the sensor nodes typically employ duty cycling, enabling autonomy on the order of one year (using for example a CR2032 battery, and a duty cycle roughly equal to 0.01). Although these radios could be used for the WiseSkin application, they are clearly not optimized for this case.

From the perspective of a short-range WSN, an interesting class of narrowband receivers are the “wake-up” (WU) receivers. The purpose of the wake-up receiver is to constantly listen, and then turn-on the main receiver once the wake-up message has been received (signifying

that there is data to be transmitted). The main idea behind the WU receiver is to break the power-latency trade-off in duty cycled networks. If a receiver in a WSN is periodically switched on, network latency will depend on the duty cycle. In order to decrease latency, duty cycle must be increased, hence increasing power consumption. Assuming an auxiliary receiver can be made, that consumes sufficiently low power, the main receiver could be turned on only when needed, allowing to reduce both latency and power consumption. State of the art WU receivers are shown in Tab. 2.4. Most WU receivers target data rates ranging from 10 kb/s to 100 kb/s, while achieving power consumption from 100 μ W to 100 nW. The complexity and architecture of these radios are quite different. Most of the sub-microwatt implementations are based on the use of an envelope detector with an external matching network. These are quite simple and have a limited scope of use. Some of the more sophisticated receivers provide interferer rejection and sensitivity comparable to standard Bluetooth receivers [29], but they are more power-hungry. Energy efficiency can vary depending on data rate, sensitivity and carrier frequency, but implementations achieving values below 1 nJ/b have been demonstrated.

Table 2.4: Performance summary of narrowband receivers

Reference	[30]	[31]	[29]	[32]	[33]	[34]
Year	2009	2012	2016	2014	2011	2013
Modulation	OOK	OOK	OOK	OOK	FSK	OOK
Frequency [GHz]	2	0.915	2.4	0.868	0.4	2.4
Power cons. [μ W]	52	0.98	99	3	44	0.116
Supply [V]	0.5	1.2	0.5	2.5	1	1.2
Data rate [kb/s]	100	100	50	0.064	200	12.5
Sensitivity [dBm]	-72	-41	-92	-83*	-70	-43.2
Efficiency [pJ/b]	520	0.98	1980	46.9	220	9.28
Tech. node [nm]	90	65	65	130	130	130

* Defined as 1 % missed wake-up events

Compared to FM-UWB, narrowband WU receivers clearly have the advantage when it comes to power consumption at comparable data rates and sensitivity levels (not taking into account fading and frequency selectivity). This is not surprising considering that FM-UWB receivers need to amplify and demodulate signal that is at least 500 MHz wide. The wideband amplifier that provides the same gain and noise figure will inevitably consume more than its narrowband equivalent. To make things worse, FM-UWB is inherently sub-optimal compared to the standard FSK (as shown in Fig. 2.3), and will provide higher BER for the same input signal power. However, FM-UWB provides other benefits that may not be apparent at first. It is inherently robust against interferers, unlike NB radios that need to rely on filtering. Owing to the spread spectrum, FM-UWB is also robust against frequency selective fading. Narrowband radios might be unable to establish a link due to a notch in the channel frequency characteristic, whereas the FM-UWB only suffers a minor performance degradation. Also, FM-UWB could provide support for multi-user communication at almost no increase in power consumption. Finally, FM-UWB has better potential for miniaturization, enabling implementations with

no off-chip components. Every narrowband radio needs a crystal oscillator to provide a precise frequency reference, and in most cases other off-chip components are needed to provide additional filtering, or output matching. Thanks to robustness to reference frequency offset, that partially comes from the large signal bandwidth, FM-UWB is capable of using an imprecise, on-chip reference oscillator, while still providing reliable communication. The combination of robustness, architecture simplicity and high degree of integration are, finally, the main arguments in favor of FM-UWB when compared to narrowband radios.

2.3 Summary

The first part of this above chapter describes the main principles of the FM-UWB modulation. Basic calculations related to the modulation technique are presented and extended to the cases with multiple users. The described techniques, such as multi-user communication and multi-channel transmission, can be used to optimize the system performance according to the specific needs. Different sub-channels can be used, trading data-rate per channel with the number of available sub-channels, depending on the number of nodes in the network and their purpose.

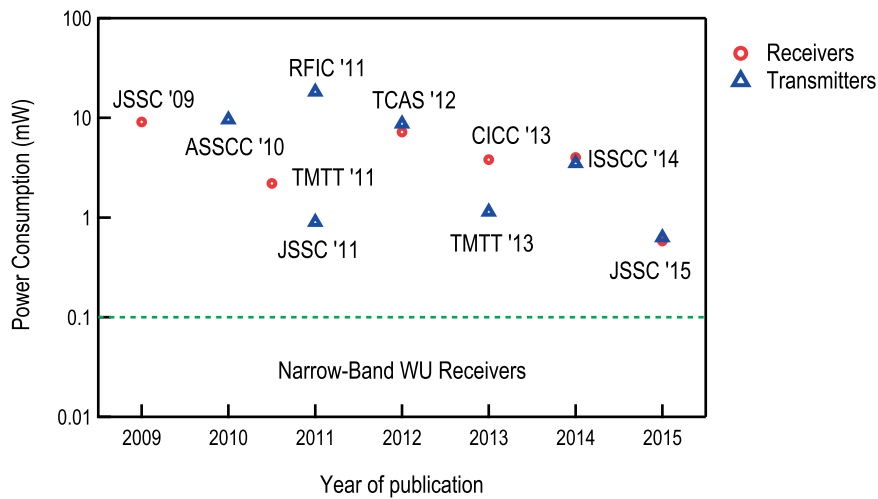


Figure 2.11: FM-UWB transmitters and receivers, evolution of power consumption. Type of demodulator used in each receiver is indicated on the graph.

In the second part of the chapter, the state of the art FM-UWB transceivers are discussed along with the the most important power reduction techniques reported in the literature. These techniques, combined with technology scaling, led to sub-milliwatt power consumption levels in today’s implementations. The evolution of power consumption over the past 8 years is illustrated in Figure 2.11 for both transmitters and receivers, from which a decrease by a factor of 20 can be observed. However, the narrow-band receivers still have the edge, at least with respect to power consumption. The proposed wake-up receivers found in literature consume from 100 μ W [29] all the way down to 100 nW [31]. FM-UWB can hardly compete with such low

levels, a simple consequence of the fact that wide-band circuits require more power to achieve the same performance in terms of gain and noise figure. On the other hand, the FM-UWB brings higher resilience to interferers, without off-chip components such as SAW filters, better performance in frequency selective channels and higher potential for miniaturization. All of these are very favorable capabilities that could assure a place for FM-UWB in short-range applications such as wireless body area networks.

References

- [1] J. F. M. Gerrits, M. H. L. Kouwenhoven, P. R. van der Meer, J. R. Farserotu, and J. R. Long, "Principles and Limitations of Ultra-wideband FM Communications Systems," *EURASIP J. Appl. Signal Process.*, vol. 2005, pp. 382–396, Jan. 2005.
- [2] M. Kouwenhoven, *High-Performance Frequency-Demodulation Systems*. Delft University Press, 1998.
- [3] N. Saputra and J. Long, *FM-UWB Transceivers for Autonomous Wireless Systems*, ser. River Publishers Series in Circuits and Systems. River Publishers, 2017.
- [4] J. F. M. Gerrits, J. Farserotu, and J. Long, "Multipath Behavior of FM-UWB Signals," in *IEEE International Conference on Ultra-Wideband, 2007. ICUWB 2007*, Sep. 2007, pp. 162–167.
- [5] —, "Multi-user capabilities of UWB-FM communications systems," in *IEEE International Conference on Ultra-Wideband*, Sep. 2005, pp. 1–6.
- [6] V. Kopta, J. Farserotu, and C. Enz, "FM-UWB: Towards a robust, low-power radio for body area networks," *Sensors*, vol. 17, no. 5, 2017.
- [7] *IEEE Standard for local and metropolitan area networks - Part 15.6: Body Area Networks*, 2012.
- [8] B. Zhou, H. Lv, M. Wang, J. Liu, W. Rhee, Y. Li, D. Kim, and Z. Wang, "A 1mb/s 3.2-4.4 ghz reconfigurable FM-UWB transmitter in 0.18 μm CMOS," in *2011 IEEE Radio Frequency Integrated Circuits Symposium (RFIC)*, Jun 2011, pp. 1–4.
- [9] F. Chen, Y. Li, D. Lin, H. Zhuo, W. Rhee, J. Kim, D. Kim, and Z. Wang, "A 1.14mw 750kb/s FM-UWB transmitter with 8-FSK subcarrier modulation," in *2013 IEEE Custom Integrated Circuits Conference (CICC)*, Sep. 2013, pp. 1–4.
- [10] F. Chen, Y. Li, D. Liu, W. Rhee, J. Kim, D. Kim, and Z. Wang, "9.3 A 1mw 1mb/s 7.75-to-8.25ghz chirp-UWB transceiver with low peak-power transmission and fast synchronization capability," in *Solid-State Circuits Conference Digest of Technical Papers (ISSCC), 2014 IEEE International*, Feb. 2014, pp. 162–163.
- [11] Y. Zhao, Y. Dong, J. F. M. Gerrits, G. van Veenendaal, J. Long, and J. Farserotu, "A Short Range, Low Data Rate, 7.2 GHz-7.7 GHz FM-UWB Receiver Front-End," *IEEE Journal of Solid-State Circuits*, vol. 44, no. 7, pp. 1872–1882, July 2009.
- [12] N. Saputra and J. Long, "A Short-Range Low Data-Rate Regenerative FM-UWB Receiver," *IEEE Transactions on Microwave Theory and Techniques*, vol. 59, no. 4, pp. 1131–1140, Apr. 2011.
- [13] N. Saputra and J. R. Long, "A Fully Integrated Wideband FM Transceiver for Low Data Rate Autonomous Systems," *IEEE Journal of Solid-State Circuits*, vol. 50, no. 5, pp. 1165–1175, May 2015.
- [14] K. Leentvaar and J. Flint, "The capture effect in FM receivers," *IEEE Transactions on Communications*, vol. 24, no. 5, pp. 531–539, May 1976.
- [15] F. Chen, W. Zhang, W. Rhee, J. Kim, D. Kim, and Z. Wang, "A 3.8-mW 3.5-4-GHz Regenerative FM-UWB Receiver With Enhanced Linearity by Utilizing a Wideband LNA and Dual Bandpass Filters," *IEEE Transactions on Microwave Theory and Techniques*, vol. 61, no. 9, pp. 3350–3359, Sep.

2013.

- [16] N. Saputra, J. R. Long, and J. J. Pekarik, "A 2.2 mW regenerative FM-UWB receiver in 65 nm CMOS," in *2010 IEEE Radio Frequency Integrated Circuits Symposium*, May 2010, pp. 193–196.
- [17] B. Zhou, J. Qiao, R. He, J. Liu, W. Zhang, H. Lv, W. Rhee, Y. Li, and Z. Wang, "A Gated FM-UWB System With Data-Driven Front-End Power Control," *IEEE Transactions on Circuits and Systems I: Regular Papers*, vol. 59, no. 6, pp. 1348–1358, June 2012.
- [18] N. Saputra, J. Long, and J. Pekarik, "A low-power digitally controlled wideband FM transceiver," in *2014 IEEE Radio Frequency Integrated Circuits Symposium*, June 2014, pp. 21–24.
- [19] P. Nilsson, J. F. M. Gerrits, and J. Yuan, "A Low Complexity DDS IC for FM-UWB Applications," in *2007 16th IST Mobile and Wireless Communications Summit*, July 2007, pp. 1–5.
- [20] N. Saputra and J. Long, "A Fully-Integrated, Short-Range, Low Data Rate FM-UWB Transmitter in 90 nm CMOS," *IEEE Journal of Solid-State Circuits*, vol. 46, no. 7, pp. 1627–1635, July 2011.
- [21] B. Zhou, R. He, J. Qiao, J. Liu, W. Rhee, and Z. Wang, "A low data rate FM-UWB transmitter with-based sub-carrier modulation and quasi-continuous frequency-locked loop," in *2010 IEEE Asian Solid-State Circuits Conference*, Nov. 2010, pp. 1–4.
- [22] J. Pandey and B. P. Otis, "A sub-100 μ W MICS/ISM band transmitter based on injection-locking and frequency multiplication," *IEEE Journal of Solid-State Circuits*, vol. 46, no. 5, pp. 1049–1058, May 2011.
- [23] M. Verhelst, N. V. Helleputte, G. Gielen, and W. Dehaene, "A reconfigurable, 0.13 μ m cmos 110pJ/pulse, fully integrated IR-UWB receiver for communication and sub-cm ranging," in *2009 IEEE International Solid-State Circuits Conference - Digest of Technical Papers*, Feb. 2009, pp. 250–251,251a.
- [24] A. Medi and W. Namgoong, "A high data-rate energy-efficient interference-tolerant fully integrated cmos frequency channelized uwb transceiver for impulse radio," *IEEE Journal of Solid-State Circuits*, vol. 43, no. 4, pp. 974–980, Apr. 2008.
- [25] Y. Zheng, Y. Tong, C. W. Ang, Y.-P. Xu, W. G. Yeoh, F. Lin, and R. Singh, "A CMOS carrier-less UWB transceiver for WPAN applications," in *2006 IEEE International Solid State Circuits Conference - Digest of Technical Papers*, Feb. 2006, pp. 378–387.
- [26] M. Crepaldi, C. Li, K. Dronson, J. Fernandes, and P. Kinget, "An ultra-low-power interference-robust IR-UWB transceiver chipset using self-synchronizing OOK modulation," in *2010 IEEE International Solid-State Circuits Conference - (ISSCC)*, Feb. 2010, pp. 226–227.
- [27] F. Zhang, A. Jha, R. Gharpurey, and P. Kinget, "An agile, ultra-wideband pulse radio transceiver with discrete-time wideband-IF," *IEEE Journal of Solid-State Circuits*, vol. 44, no. 5, pp. 1336–1351, May 2009.
- [28] L. Liu, T. Sakurai, and M. Takamiya, "A 1.28 mW 100 Mb/s impulse UWB receiver with charge-domain correlator and embedded sliding scheme for data synchronization," in *2009 Symposium on VLSI Circuits*, June 2009, pp. 146–147.
- [29] C. Salazar, A. Cathelin, A. Kaiser, and J. Rabaey, "A 2.4 ghz interferer-resilient wake-up receiver using a dual-if multi-stage n-path architecture," *IEEE Journal of Solid-State Circuits*, vol. 51, no. 9, pp. 2091–2105, Sep. 2016.
- [30] N. M. Pletcher, S. Gambini, and J. Rabaey, "A 52 μ W wake-up receiver with - 72 dBm sensitivity using an uncertain-IF architecture," *IEEE Journal of Solid-State Circuits*, vol. 44, no. 1, pp. 269–280, Jan. 2009.
- [31] N. E. Roberts and D. D. Wentzloff, "A 98nw wake-up radio for wireless body area networks," in *2012 IEEE Radio Frequency Integrated Circuits Symposium*, June 2012, pp. 373–376.
- [32] H. Milosiu, F. Oehler, M. Eppel, D. Frühsorger, S. Lensing, G. Popken, and T. Thönes, "A 3- μ w 868-mhz wake-up receiver with -83 dbm sensitivity and scalable data rate," in *2013 Proceedings of*

- the ESSCIRC (ESSCIRC)*, Sep. 2013, pp. 387–390.
- [33] J. Pandey, J. Shi, and B. Otis, “A 120 μw mics/ism-band fsk receiver with a 44 μw low-power mode based on injection-locking and 9x frequency multiplication,” in *2011 IEEE International Solid-State Circuits Conference*, Feb. 2011, pp. 460–462.
- [34] S. Oh, N. E. Roberts, and D. D. Wentzloff, “A 116nw multi-band wake-up receiver with 31-bit correlator and interference rejection,” in *Proceedings of the IEEE 2013 Custom Integrated Circuits Conference*, Sep. 2013, pp. 1–4.

3 Reducing the Power of FM-UWB receivers: the Approximate Zero IF Architecture

The primary goal of this work is to reduce the power consumption of an FM-UWB transceiver. In duty cycled wireless sensor networks the bottleneck is typically the receiver. This is because transmitters only need to be turned on when there is a need to transmit data. As a result their power consumption will only be a small fraction of the overall power consumed by the network. Receivers, on the other hand, need to capture the transmitted data and must therefore be turned on periodically to check whether data is being transmitted. This is why the power consumption of the network will almost entirely be determined by the receiver power consumption. Lowering the duty cycle ratio, or equivalently, increasing the duration of the period between the two on states of the receiver, can be used to bring down network power consumption, but it will also increase latency. In systems like *WiseSkin*, where sensors need to provide pressure information to the patient, latency constraints are imposed by the physiological characteristics of the human body. In order to provide a natural sense of touch, the delay from sensors to actuators must not be larger than the time it takes for neurons to convey information from the fingers to the brain. Once the maximum delay limit is reached the only way to reduce network power consumption is to reduce the consumption of the FM-UWB receiver.

Another property that could be of use in the receiver is the capability to handle multiple FM-UWB signals at the same time. This requirement comes from the fact that potentially a large number of sensor nodes may be located close to each other. Providing the multi-user capability would then allow to parallelize data transfer and decrease network delay. Normally, receivers with such capability need good linearity and dynamic range, which again come at the price of power consumption. Fortunately, since the distance between nodes is not large, and in the targeted application it is less than 1 m, sensitivity is not a limiting factor, and can in this case be sacrificed for the benefit of multi-user communication and energy efficiency.

This chapter describes the proposed architecture, intended to further reduce the power consumption of an FM-UWB receiver. Two architectures are explored, one that aims to provide the multi-user communication capability, and another that attempts to aggressively lower the power consumption, while essentially neglecting all other aspects.

Chapter 3. Reducing the Power of FM-UWB receivers: the Approximate Zero IF Architecture

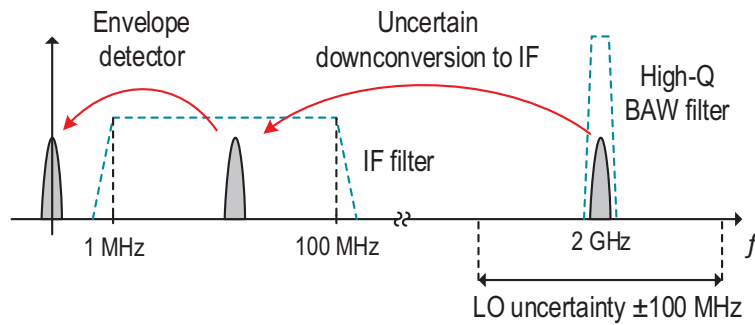


Figure 3.1: Principle of operation of the uncertain IF receiver.

3.1 The Uncertain IF Architecture

It is a common observation that in any type of circuits there is a correlation between the frequency of operation and power consumption. The simplest example is the CMOS logic gate, where it can be shown that the dynamic power consumption is proportional to the frequency of operation $P_{dyn} \propto fCV^2$. Similar conclusion holds for other types of circuits, for example, amplifiers typically need more power to achieve the same gain at higher frequencies (or to provide larger bandwidth). As a consequence, the most power-hungry blocks in the receivers are the ones that operate at RF. These are usually the Low Noise Amplifier (LNA), needed to provide a good noise figure, and the frequency synthesizer, where the dominant consumers are the voltage controlled oscillator and frequency dividers. A typical example could be the Bluetooth receiver presented in [2], where the LNA consumes around 25 % of the overall power, and 53 % of the power is used for the PLL, including the DCO.

Due to the large bandwidth of the FM-UWB signal, precise frequency synthesizers can be completely removed. Gain at high frequencies, however, remains a bottleneck. Consider the FM-UWB receiver from [3], where the LNA consumes 1.6 mW, or 73 % of the overall power consumption. A similar case is found in [4], where the LNA consumes 55 % of the entire receiver consumption. The preamplifier and the demodulator in the FM-UWB receiver from [5], both operating at RF, consume around 3 mA and 6 mA, respectively. Removing the LNA from the design, or loosening the specifications on RF gain and noise figure, could lead to significant power savings.

The opportunity to decrease power consumption by moving the gain stages from RF to IF was first recognized by Pletcher [6], who demonstrated this approach through the implementation of the “Uncertain IF” receiver. In this design the LNA is merged with the mixer into a single current reuse block, the active mixer. Combined with the external bulk acoustic wave (BAW) resonator, it provides the input matching, and converts the RF signal to IF, where the gain stages are located. The lack of voltage gain at RF simplifies the design and allows for low dc current of the active mixer. Although the power hungry LNA is eliminated from the design, the LO signal must now be generated in order to perform the downconversion. For the proposed design from [6] to be truly power efficient, the LO generator must consume sufficiently low power. A simple three-stage, CMOS ring oscillator used in this design consumes very little power and provides a rail to rail output signal, but this comes at a price. Ring oscillators are generally sensitive to changes in supply voltage and temperature, phase noise is relatively high compared to LC oscillators, and finally the output frequency is rather unstable and tends

3.2. The Approximate Zero IF Receiver with Quadrature Downconversion

to drift with time. This is the key point of the architecture from [6]. Instead of using a PLL to stabilize the oscillator frequency, the IF amplifier bandwidth is increased to allow for LO frequency offset. Hence the name “uncertain IF” receiver is used. The described principle is illustrated in Fig. 3.1. The designed oscillator generates the LO signal that remains within the ± 100 MHz range from the center frequency. To account for this offset, the IF amplifier is designed with a bandwidth of 100 MHz, assuring that the downconverted signal falls inside the desired band. Using 100 MHz amplifiers to amplify a signal with 10 kHz bandwidth is a necessary overhead, but still results in less power consumed than if a PLL were used to generate the LO signal. The oscillator, however, does need to be calibrated periodically to compensate for the drift due to temperature or supply voltage variation, and maintain the LO frequency within the defined limits. Owing to the fact that these changes are slow, the calibration will only be done once in a few hours, resulting in a negligible overhead in terms of power consumption. The final stage of the receiver is the envelope detector that demodulates the transmitted OOK (on-off keying) signal. It should still be noted that a relatively good noise performance in this case was achieved using a narrowband BAW filter that is precisely tuned to the frequency of the transmitted signal. Finally, the receiver from [6] reached a power consumption of only $50 \mu\text{W}$, for an input signal at 2 GHz, and is still among the lowest consuming narrowband receivers in the literature today.

The same principle can be applied to the FM-UWB signal. Instead of implementing the wideband amplifiers at RF, the input signal is directly downconverted to zero center frequency using an active mixer (LNA and mixer stack), allowing amplification and processing to be done at low frequencies. Since the LO signal is generated using an imprecise ring oscillator, a certain frequency offset will always be present between the LO signal and the center frequency of the input signal. Hence, the proposed receiver is referred to as the “Approximate Zero IF” receiver. The aforementioned offset should be relatively small compared to the 500 MHz wide input signal, and so the necessary overhead, i.e. larger bandwidth of the IF amplifiers and the demodulator, will be relatively small. Moving the main gain stages from RF to IF results in higher noise figure (NF) of the receiver chain. Since only a limited amount of gain is available at high frequencies, noise of the IF stages will contribute more significantly to the overall noise figure. At the same time, the power consumed by the IF amplifiers can now be greatly reduced since they operate at low frequencies instead of RF, and the same overall gain comes at a lower price.

3.2 The Approximate Zero IF Receiver with Quadrature Downconversion

The first proposed receiver architecture is based on a delay line demodulator described in the previous chapter. This demodulator has already been used in some receiver implementations [5, 7]. In its original form it operates directly at RF, and the delay needs to be tuned precisely to the signal center frequency. The demodulator can be moved from RF to baseband, without changing its functionality, if two signal branches are used with a 90° phase shift between them [8]. The two signals can easily be generated by using quadrature LO signals for downconversion.

The proposed receiver architecture is shown in Fig. 3.2. Some of the blocks that will be present in the actual implementation are omitted for clarity, and to emphasize functionality. The input signal is directly converted to zero frequency by the mixer. Since a ring oscillator will be used to generate the LO signal, some frequency offset will always be present, meaning that the downconverted signal will never be precisely centered at zero, and the architecture is therefore named the “Approximate Zero IF” architecture. The downconverted signal will then be amplified by the IF amplifiers. In Fig. 3.2 only

Chapter 3. Reducing the Power of FM-UWB receivers: the Approximate Zero IF Architecture

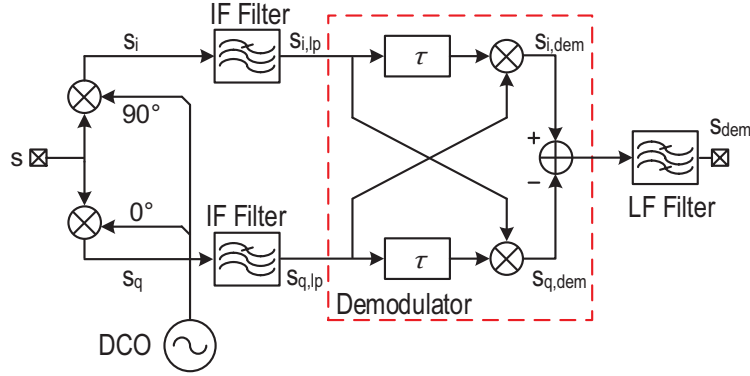


Figure 3.2: Block diagram of approximate zero IF receiver with IQ downconversion.

filters are shown to emphasize limited bandwidth of the IF path. In this work a 500 MHz wide FM-UWB signal is used. After downconversion the signal would ideally occupy frequencies from zero to 250 MHz. Accounting for a frequency offset of ± 50 MHz, 300 MHz should be sufficient for the bandwidth of the IF path. The case remains the same with the demodulator bandwidth. It needs to be larger in order to accommodate the input signal with a frequency offset.

The principle of operation of the demodulator can be described through the following mathematical model. The simple calculation presented here follows the approach from [9], extending it to account for the LO frequency offset. The aim of the calculation is to explain the principle of operation and provide insights into the main trade-offs when choosing the delay of the demodulator, which is the main design parameter in this case and determines the bandwidth of the demodulator. The FM-UWB signal at the input of the receiver can be represented as

$$s(t) = A \cos(\omega_c t + \phi(t)), \quad (3.1)$$

where $\omega_c = 2\pi f_c$ is the carrier center frequency of the signal and $\phi(t)$ is the time varying phase, which is the integral of the sub-carrier wave (usually a periodic triangular or sine signal):

$$\phi(t) = \Delta\omega \int_{-\infty}^t m(t) dt. \quad (3.2)$$

The sub-carrier wave $m(t)$ is normalized to the interval $[-1,1]$, and $\Delta\omega$ is the frequency deviation corresponding to half of the FM-UWB signal bandwidth $\Delta\omega = 2\pi\Delta f = \pi B_{UWB}$. The signal is first converted to baseband, such that the signals in the in-phase and quadrature branches are given by

$$s_i(t) = A \cos(\omega_c t + \phi(t)) \cos(\omega_{osc} t) \quad (3.3)$$

$$s_q(t) = A \cos(\omega_c t + \phi(t)) \sin(\omega_{osc} t) \quad (3.4)$$

where the conversion gain of the mixer is assumed to be unity for simplicity. Note that since the carrier frequency ω_c does not correspond ideally to the locally generated frequency ω_{osc} , there will be a residual term after mixing that is equal to the difference of the two frequencies. The two filtered,

3.2. The Approximate Zero IF Receiver with Quadrature Downconversion

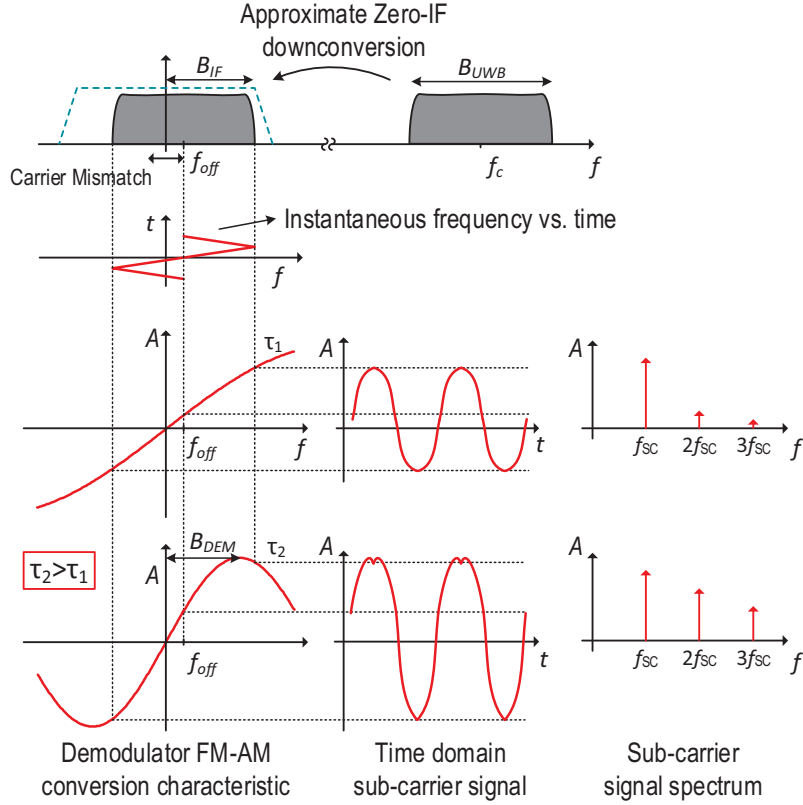


Figure 3.3: Principle of operation of approximate zero IF receiver with IQ downconversion.

downconverted components at the demodulator input are:

$$s_{i,lp}(t) = \frac{A}{2} \cos(\omega_{off} t + \phi(t)) \quad (3.5)$$

$$s_{q,lp}(t) = -\frac{A}{2} \sin(\omega_{off} t + \phi(t)) \quad (3.6)$$

where $\omega_{off} = 2\pi f_{off} = \omega_c - \omega_{osc}$ is the frequency offset of the LO signal. The two quadrature signals are then multiplied with the delayed copy of each other in the process of demodulation. The signals at the output of the two demodulator mixers are:

$$s_{i,dem}(t) = -\frac{A^2}{4} \cos(\omega_{off}(t - \tau) + \phi(t - \tau)) \sin(\omega_{off} t + \phi(t)) \quad (3.7)$$

$$s_{q,dem}(t) = -\frac{A^2}{4} \cos(\omega_{off} t + \phi(t)) \sin(\omega_{off}(t - \tau) + \phi(t - \tau)). \quad (3.8)$$

Finally, the difference of $s_{i,dem}(t)$ and $s_{q,dem}(t)$ results in the following signal:

$$s_{dem}(t) = \frac{A^2}{4} \sin(\omega_{off} \tau + \phi(t) - \phi(t - \tau)). \quad (3.9)$$

Following the same approach as in [9], assuming time interval τ is small enough that $\phi(t)$ does not

Chapter 3. Reducing the Power of FM-UWB receivers: the Approximate Zero IF Architecture

change too significantly, equation (3.9) can then be approximated by

$$s_{dem}(t) \approx \frac{A^2}{4} \sin(\omega_{off}\tau + \tau \frac{d\phi(t)}{dt}) \quad (3.10)$$

$$= \frac{A^2}{4} \sin(\omega_{off}\tau + \tau \Delta\omega m(t)), \quad (3.11)$$

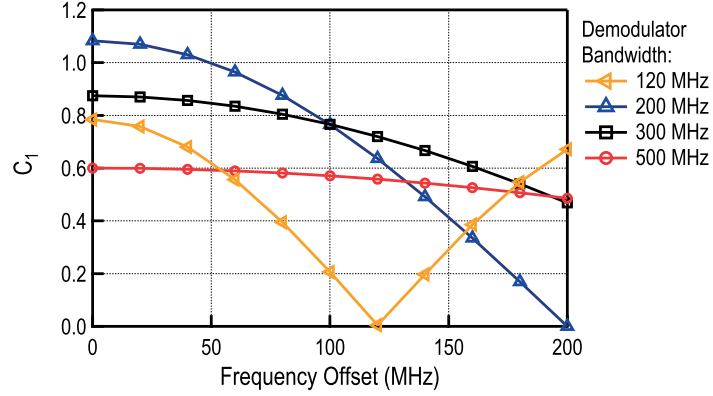
which in fact corresponds to the demodulated signal. The last equation reveals the sinusoidal FM-AM characteristic of the demodulator, showing that it, in fact, acts as a baseband equivalent of the RF delay line demodulator. The illustration of the demodulation principle and the equivalent demodulator characteristic are given in Fig. 3.3. The shape of the output demodulated signal is shown for two different values of the delay, assuming that a certain frequency offset is present in the LO signal. The amplitude and the shape of the demodulated signal depend on the demodulator delay τ and the frequency offset f_{off} , as illustrated in Fig. 3.3. The demodulator bandwidth can be defined as the monotonic part of the characteristic, i.e. $\tau \times B_{DEM} = \pi/2$. Increasing the delay results in decreased demodulator bandwidth, which increases the amplitude, but also distorts the output signal. Note that unlike with the RF delay line demodulator, the delay τ is no longer related to the input signal center frequency. Ideally, in the case of the RF delay line demodulator, τ should be equal to the integer multiple of the quarter period of the center frequency $NT/4$. Any deviation of τ results in mismatch between the demodulator center frequency and the signal center frequency. The end effect is equivalent to the LO frequency offset in the approximate zero IF receiver.

The conversion gain is defined as the ratio of the fundamental amplitude of the demodulated signal and the amplitude of the signal at the demodulator input:

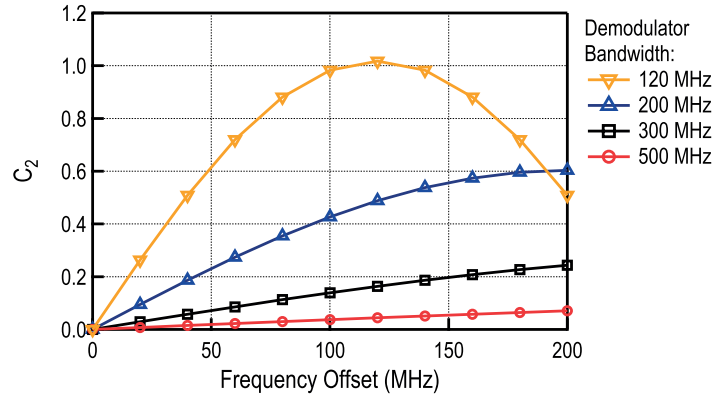
$$G_{conv} = \frac{A_{(1)}}{A/2} = \frac{C_1 A^2/4}{A/2} = \frac{A}{2} C_1. \quad (3.12)$$

The coefficient C_1 corresponds to the fundamental component of the demodulated signal normalized to $A^2/4$ and accounts for the non-linear characteristic of the demodulator. This coefficient will depend on τ and f_{off} . Assuming a triangular sub-carrier wave, C_1 and C_2 (normalized second harmonic amplitude) are calculated and plotted in Fig. 3.4 as functions of the frequency offset, for several different values of the delay τ . These graphs show the trade-off between the distortion and the conversion gain mentioned above. Choosing larger τ , such that the demodulator bandwidth is smaller than the signal bandwidth, for example $B_{dem} = 200$ MHz, will indeed result in a higher gain, but will also make it more sensitive to the carrier offset. For the value of τ selected to provide 500 MHz bandwidth, the conversion gain is practically half of that obtained for $B_{DEM} = 200$ MHz, but remains almost constant even for a very high carrier offset. The conversion gain remains the same for both noise and signal at the input, and in that sense doesn't affect the SNR. However, in a practical realization the demodulator itself will generate noise, and with this noise taken into account higher conversion gain will yield a higher output SNR. It should also be noted that a high demodulator bandwidth (together with IF bandwidth B_{IF}) also results in a higher noise bandwidth, which combined with lower gain inevitably leads to a degradation of sensitivity. Looking at the second harmonic, the increase of distortion that comes with the decrease of bandwidth becomes evident. In the ideal case, with no carrier offset, the second harmonic will be zero. However, for the proposed receiver architecture this will never be the case and the amplitude of the second harmonic will depend on offset and demodulator delay. Finally as a compromise between the gain, sensitivity to frequency offset and distortion, a bandwidth of 300 MHz can be chosen for the demodulator implementation and the same value should be used for the bandwidth of the preceding IF amplifiers.

3.2. The Approximate Zero IF Receiver with Quadrature Downconversion



(a)



(b)

Figure 3.4: Normalized fundamental C_1 and second harmonic amplitude C_2 at the output of the demodulator vs. the offset frequency. First harmonic is proportional to conversion gain. Four curves are plotted for four different values of the demodulator bandwidth (or equivalently different values of the delay τ).

The proposed demodulator can be used to simultaneously demodulate two or more FM-UWB signals. If an additional FM-UWB signal, occupying the same RF bandwidth but using a different sub-carrier frequency, is present at the input of the receiver, the signals in the I and Q branches are given by

$$s_{i,lp} = \frac{A_1}{2} \cos(\omega_{off}\tau + \phi_1(t)) + \frac{A_2}{2} \cos(\omega_{off}\tau + \phi_2(t)) \quad (3.13)$$

$$s_{q,lp} = -\frac{A_1}{2} \sin(\omega_{off}\tau + \phi_1(t)) - \frac{A_2}{2} \sin(\omega_{off}\tau + \phi_2(t)). \quad (3.14)$$

Following the same steps as in the above calculation the demodulated signal can then be derived as

$$s_{dem} = \frac{A_1^2}{4} \sin(\omega_{off}\tau + \tau \frac{d\phi_1(t)}{dt}) + \frac{A_2^2}{4} \sin(\omega_{off}\tau + \tau \frac{d\phi_2(t)}{dt}) + W(t). \quad (3.15)$$

Aside from the first two terms, which represent the two demodulated signals, an additional term, $W(t)$ appears. This term corresponds to the intermodulation product of the two FM-UWB signals. The effect

Chapter 3. Reducing the Power of FM-UWB receivers: the Approximate Zero IF Architecture

is the same as for the case of the RF delay line demodulator, where the additional term corrupts the two useful signals and limits the achievable BER. Fortunately, as will be shown, this term will be spread across a large frequency, allowing to filter out most of it in the baseband. The $W(t)$ term is given by

$$W(t) = \frac{A_1 A_2}{4} \sin(\omega_{off} \tau + \phi_1(t) - \phi_2(t - \tau)) + \frac{A_1 A_2}{4} \sin(\omega_{off} \tau + \phi_2(t) - \phi_1(t - \tau)). \quad (3.16)$$

Using the same approximation as in the single-user case, assuming τ is very small $W(t)$ can be rewritten as

$$W(t) \approx \frac{A_1 A_2}{4} \sin\left(\omega_{off} \tau + \frac{\tau}{2} \frac{d\phi_1(t)}{dt} + \frac{\tau}{2} \frac{d\phi_2(t)}{dt}\right) \sin(\phi_1(t) + \phi_2(t)) \quad (3.17)$$

$$= \frac{A_1 A_2}{2} \sin\left(\omega_{off} \tau + \frac{\tau \Delta\omega}{2} (m_1(t) + m_2(t))\right) \sin\left(\Delta\omega \int_{-\infty}^t (m_1(t) - m_2(t)) dt\right) \quad (3.18)$$

$$= \frac{A_1 A_2}{4} w(t). \quad (3.19)$$

The intermodulation product $W(t)$ consists of two factors. The first one, proportional to the sum of the two sub-carrier signals, is the slow-varying envelope. Clearly the shape of the envelope will depend on the demodulator delay τ , and the frequency offset f_{off} , and therefore these two parameters will affect the average power of the intermodulation product. The second factor is spread from 0 to $2\Delta\omega$, which is equal to the signal bandwidth B_{UWB} , with the instantaneous frequency that is proportional to the difference of the two sub-carrier signals. Since the intermodulation product is spread over a very wide band, only a small fraction of its power will fall into the useful sub-carrier band B_{SC} . The effect of inter-user interference will be similar to the elevated noise floor at the output of the receiver. This results in a degradation of sensitivity as either the number of users or the power of additional users increase. For a given targeted bit error rate, interference among users will ultimately limit the number of users or the difference in power levels between the two FM-UWB signals that can be handled at the same time.

The average power of the intermodulation product can be calculated as

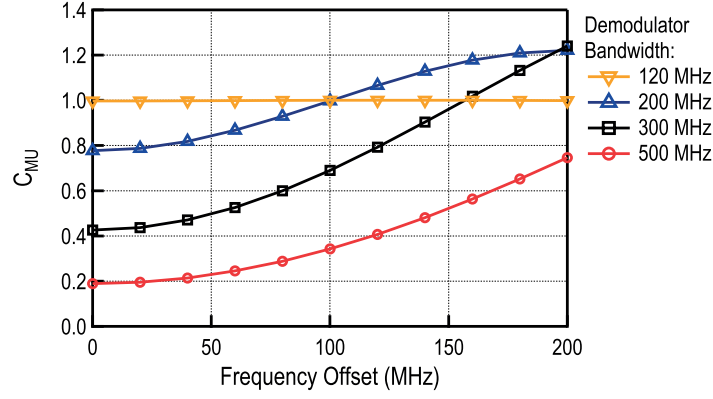
$$\overline{W(t)^2} = \frac{A_1^2 A_2^2}{16} \overline{w(t)^2} = \frac{A_1^2 A_2^2}{16} C_{MU} \quad (3.20)$$

Factor C_{MU} is the normalized average power of the intermodulation product and depends on τ and f_{off} . It is calculated for two triangular sub-carrier waves and presented in Fig. 3.5(a). The decrease of the demodulator bandwidth (increase of τ) in this case leads to increased power of the intermodulation product. Making the approximation that the spectrum of $W(t)$ is flat across the entire band [9], the output signal-to-interference ratio (SIR) can be calculated as

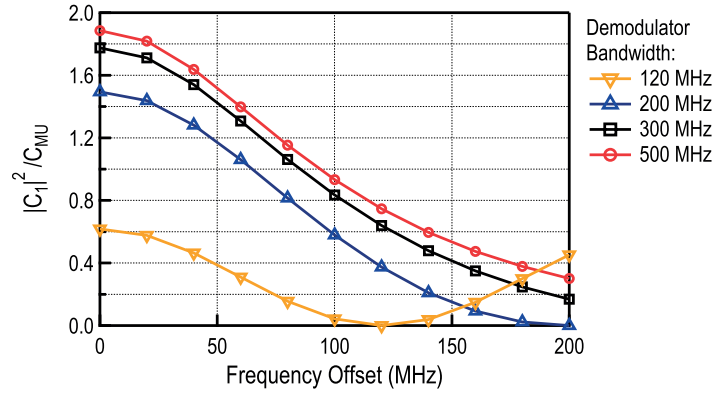
$$SIR_{out} = 10 \log_{10} \left(\frac{A_1^2 |C_1|^2 B_{UWB}}{A_2^2 C_{MU} B_{SC}} \right), \quad (3.21)$$

where factor $|C_1|^2 / C_{MU}$ is added to the original formula from [9] to account for the frequency offset [10]. Fig. 3.5(b) shows how this factor changes with the frequency offset for different demodulator bandwidths. As expected the best result is obtained for the highest demodulator bandwidth. The difference is, however, not too significant compared to the case with 300 MHz bandwidth. At the same time, extending the demodulator bandwidth also requires the extension of the IF amplifier bandwidth,

3.3. The Approximate Zero IF Receiver with Single-Ended Downconversion



(a)



(b)

Figure 3.5: Coefficient C_{MU} (a) and correction factor $|C_1|^2 / C_{MU}$ for SIR (b) as functions of the frequency offset. Four curves correspond to three different values of the demodulator bandwidth (or equivalently values of the delay τ).

which finally leads to increased power consumption. For this reason 300 MHz is chosen as a good trade-off between power and distortion and is the bandwidth that will be used in the receiver implementation described in the following chapter.

3.3 The Approximate Zero IF Receiver with Single-Ended Downconversion

As a general rule, quadrature downconversion is needed in direct downconversion receivers, otherwise part of the information will be lost, and it will be impossible to recover the data. However, because of the properties of the FM-UWB signal, transmitted bits can be recovered even if the signal is directly converted to zero using only a single branch. Shift to a single-ended receiver architecture enables some power savings. First of all, only one IF amplifier can be used, allowing to halve the power of the IF stages. In addition, the simplified FM demodulator should also allow some savings compared to

Chapter 3. Reducing the Power of FM-UWB receivers: the Approximate Zero IF Architecture

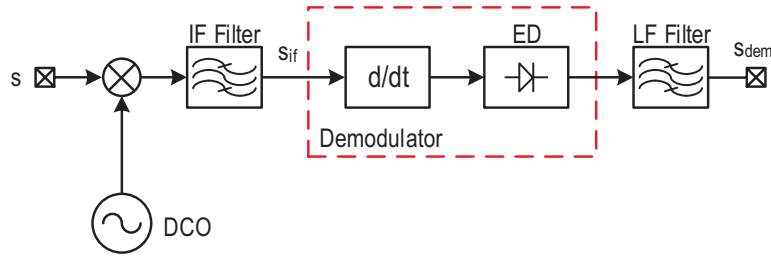


Figure 3.6: Block diagram of approximate zero IF receiver with single-ended downconversion.

the IQ delay line demodulator. Finally, the most important savings come from the DCO. Quadrature demodulation requires quadrature LO generation that tends to be power costly. Using a single-ended oscillator simplifies the circuit and allows to reduce power by a factor of more than 2 for the same oscillation frequency.

The operation of the demodulator can be explained using a simplified receiver model, presented in Fig. 3.6. Like in the previous case the input FM-UWB signal can be represented as

$$s(t) = A \cos(\omega_c t + \phi(t)), \quad (3.22)$$

where $\phi(t)$ is again the integral of the sub-carrier wave, and ω_c is the center frequency. After downconversion, the signal at the mixer output is given by

$$s_{mix}(t) = k A \cos(\omega_c t + \phi(t) + \phi_0) \cos(\omega_{osc} t) \quad (3.23)$$

The IF low-pass filter removes all the high frequency components, resulting in the signal at the filter output given by

$$s_{if}(t) = \frac{A}{2} \cos(\omega_{off} t + \phi(t)), \quad (3.24)$$

where ω_{off} is the offset frequency, that is equal to the difference of the LO frequency and the signal center frequency. The following stage, a differentiator, converts the FM signal into an AM signal given by

$$\frac{ds_{if}(t)}{dt} = \frac{A}{2} \sin(\omega_{off} t + \phi(t)) \left(\omega_{off} \tau_0 + \tau_0 \frac{d\phi(t)}{dt} \right), \quad (3.25)$$

where τ_0 is the time constant of the differentiator. The resulting signal is then demodulated using the envelope detector. Here, an ideal square law envelope detector is assumed, resulting in the output signal given by

$$\begin{aligned} s_{dem}(t) &= \frac{A^2}{4} \sin^2(\omega_{off} t + \phi(t)) \left(\omega_{off} \tau_0 + \tau_0 \frac{d\phi(t)}{dt} \right)^2 \\ &= \frac{A^2}{8} (1 - \cos(2\omega_{off} t + 2\phi(t))) \left(\omega_{off} \tau_0 + \tau_0 \frac{d\phi(t)}{dt} \right)^2 \end{aligned} \quad (3.26)$$

The low-pass filter following the envelope detector will practically remove the fast changing component

3.3. The Approximate Zero IF Receiver with Single-Ended Downconversion

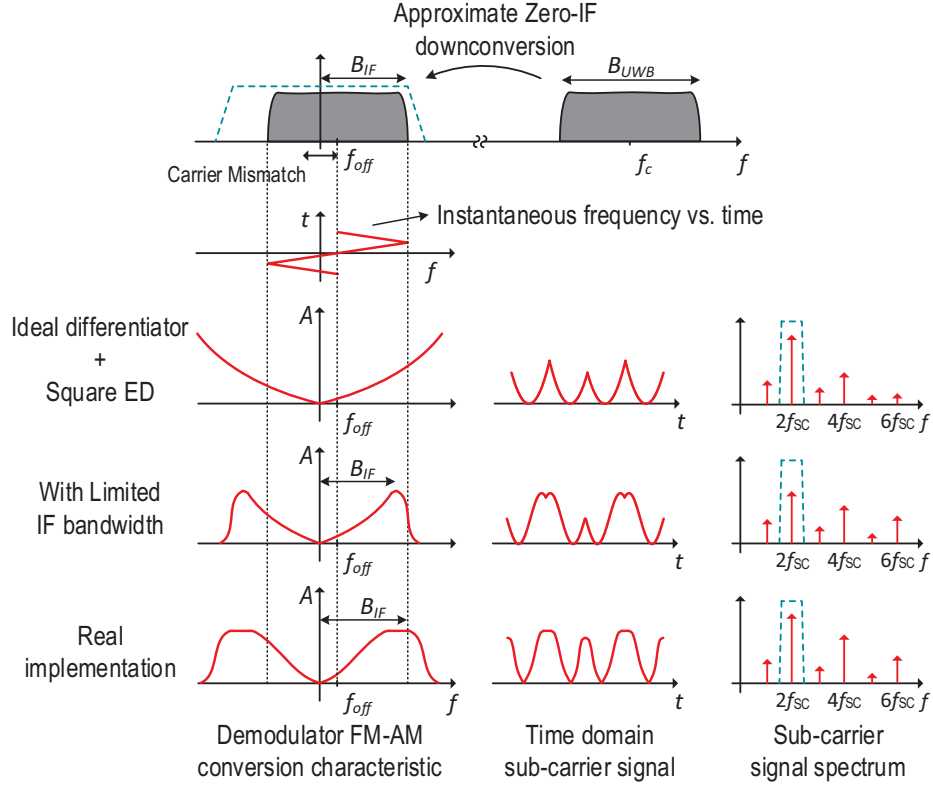


Figure 3.7: Principle of operation of the approximate zero IF receiver with single-ended downconversion.

$\cos(2\omega_{off}t + 2\phi(t))$, resulting in the signal at the filter output given by

$$s_{dem}(t) = \frac{A^2}{8} \left(\omega_{off}\tau_0 + \tau_0 \frac{d\phi(t)}{dt} \right)^2. \quad (3.27)$$

For simplicity, let us assume that the sub-carrier signal is a sine wave. The demodulated signal is then

$$s_{dem}(t) = \frac{A^2}{8} (\omega_{off}\tau_0 + \Delta\omega\tau_0 \sin(\omega_{sc}t))^2 \quad (3.28)$$

$$= \frac{A^2}{8} \tau_0^2 (\omega_{off}^2 + 2\omega_{off}\Delta\omega \sin(\omega_{sc}t) + \Delta\omega^2 \sin^2(\omega_{sc}t)) \quad (3.29)$$

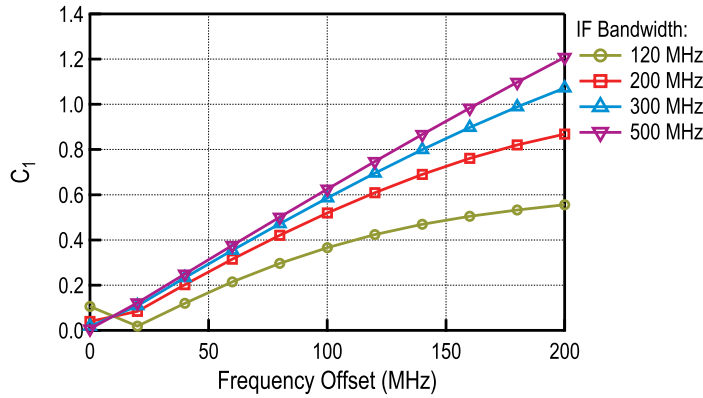
$$= \frac{A^2}{8} \tau_0^2 \left(\omega_{off}^2 + 2\omega_{off}\Delta\omega \sin(\omega_{sc}t) + \Delta\omega^2 \left(\frac{1}{2} - \frac{1}{2} \cos(2\omega_{sc}t) \right) \right). \quad (3.30)$$

In the ideal case the offset frequency is zero, $\omega_{off} = 0$, and the only remaining useful term is the term at twice the sub-carrier frequency

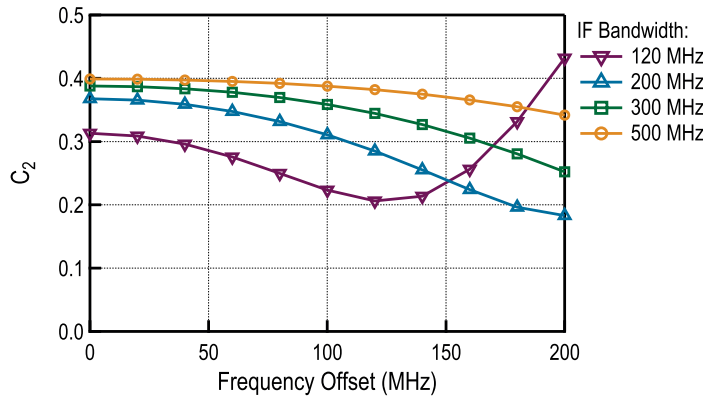
$$s_{dem,2}(t) = \frac{A^2}{16} \Delta\omega^2 \tau_0^2 \cos(2\omega_{sc}t). \quad (3.31)$$

The demodulation can now be performed using this signal. The same conclusion holds for the triangular wave since it can be represented by the Fourier series, in which case again, the second harmonic of the

Chapter 3. Reducing the Power of FM-UWB receivers: the Approximate Zero IF Architecture



(a)



(b)

Figure 3.8: Normalized fundamental C_1 and second harmonic amplitude C_2 at the output of the demodulator.

demodulated sub-carrier wave can be used for the final FSK demodulation. Interestingly, if an ideal differentiator is used and if infinite IF bandwidth is assumed, the amplitude of the second harmonic will be independent of the frequency offset. The first harmonic will appear with the increase of the frequency offset, however in this case, this component can be filtered out by the LF band-pass filter.

The principle of the single-ended baseband FM demodulator is shown in Fig. 3.7. In the derivation, an ideal differentiator was used and infinite IF bandwidth was assumed. In a realistic implementation the IF bandwidth will affect the useful signal and will cause the second harmonic of the demodulated signal (used for demodulation) to decrease with frequency offset. Also, the ideal differentiator, used for derivation, will be replaced by a lossy (non-zero dc gain) first order high-pass filter. This filter will have a certain cut-off frequency after which the transfer function flattens. The equivalent FM-AM characteristic should finally resemble the characteristic at the bottom of the Fig. 3.7.

The first and second harmonic of the demodulated signal are plotted in Fig. 3.8 as functions of the offset frequency. The calculation is done for a triangular sub-carrier signal with varying IF bandwidth. As explained previously, the first harmonic is close to zero for small frequency offsets, and increases as the offset increases. The second harmonic (useful part of the signal), decreases with the frequency

offset. This decrease is purely a consequence of the limited demodulator bandwidth, since the second harmonic after a perfect square law envelope detector remains constant regardless of the offset. The amplitude of the second harmonic shows less variation with the frequency offset as the IF bandwidth increases. Ideally, the IF bandwidth should then be extended to get the best performance, however this again requires more power for the IF amplifiers, and in the receiver implementation a bandwidth of 300 MHz will be used as a good trade-off.

3.4 Receiver Sensitivity Estimation

The first step in estimating the receiver sensitivity is to find the output BER as a function of the SNR at the receiver input. For the approximate zero IF receiver with quadrature demodulation, the FM-AM conversion characteristic is equivalent to the one of the RF delay line demodulator. The only difference between the two is that the demodulator is located at the baseband instead of RF. The expectation is then that the BER performance of the two receivers remains the same, meaning that the same approximation can be used to estimate the BER. The hypothesis is verified using the high-level model corresponding to the one shown in Fig. 3.2. A bandwidth of 300 MHz was used for the IF filters, and 2 MHz for the LF filter that filters the demodulated FSK signal. The bandwidth of the demodulator is chosen larger than the IF bandwidth and is set to approximately 350 MHz. The simulation results are compared to the Gerrits' approximation [9] in Fig. 3.9. The simulation points match well with the calculated curve, validating the use of Gerrits' approximation for the proposed quadrature receiver.

In the case of the single-ended receiver architecture, the Gerrits' approximation no longer holds in its original form. However, looking at the receiver structure, after the squaring operation of the envelope detector, the same products appear as in the case of the delay line demodulator. In principle the same approach can be used as in [9], with the difference that the useful signal amplitude is half of the one in the case of the delay line demodulator. The resulting output SNR is then given by

$$\text{SNR}_{\text{out}} = \frac{B_{RF}}{B_{SC}} \frac{(\text{SNR}_{\text{in}}/4)^2}{1 + \text{SNR}_{\text{in}}}. \quad (3.32)$$

The rest of the calculation remains the same as for the delay line demodulator. The resulting calculated BER curve is shifted by approximately 6 dB compared to the BER of the quadrature receiver. This is

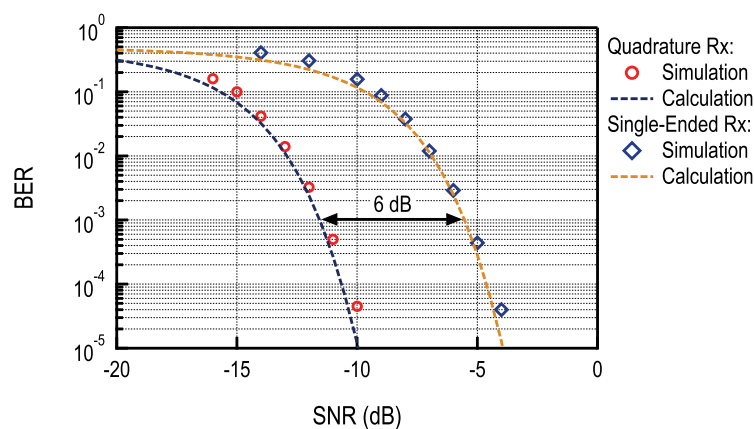


Figure 3.9: Simulated and calculated BER curves for the approximate zero IF receiver.

Chapter 3. Reducing the Power of FM-UWB receivers: the Approximate Zero IF Architecture

the price paid for the simplified receiver architecture. The calculated BER curve is compared to the simulated points in Fig. 3.9. The used model corresponds to the block diagram of Fig. 3.6. The IF bandwidth of 300 MHz was used in the simulation, and a high-pass filter with a cut-of frequency of 300 MHz replaced the differentiator. Such implementation should roughly correspond to the actual implementation of the single-ended receiver.

The two BER curves provide the information on the minimum SNR needed at the receiver input in order to achieve the desired BER. Typically, for low power wireless receivers a BER of 10^{-3} is taken as the reference point. The sensitivity of the receiver is then defined as the signal level at the receiver input needed to achieve this BER. To calculate this sensitivity, the noise power at the receiver input must first be calculated. The equivalent input referred noise of the receiver in dBm is given by

$$N = 10\log(kTB_{UWB}/1\text{ mW}) + NF, \quad (3.33)$$

where NF is the noise figure of the receiver, and $10\log(kTB_{UWB}/1\text{ mW})$ is the thermal noise power in dBm at the receiver input at a temperature of $T = 25^\circ\text{C}$. The used FM-UWB signal bandwidth is $B_{UWB}=500\text{ MHz}$. Considering that the main target is to lower the receiver power consumption and that the LNA will be either completely removed, or have very limited performance, relatively high noise figure of the receiver should be accounted for. In [6] the total noise figure of the active mixer and the IF amplifiers is 23 dB. The high noise figure is a consequence of the mixer first architecture and low power gain of the first stage, which results in significant contribution from the IF amplifier. For this design, a 20 dB noise figure will be assumed in order to calculate the achievable sensitivity of the FM-UWB receiver. The sensitivity is then calculated as

$$S_{in} = 10\log(kTB_{UWB}/1\text{ mW}) + NF + \text{SNR}_{min}. \quad (3.34)$$

For the quadrature receiver minimum input $\text{SNR}_{min}=-11.5\text{ dB}$, which results in a receiver sensitivity of around $S_{in}=-78.5\text{ dBm}$. For the single-ended receiver the minimum input SNR is approximately 6 dB higher, which results in sensitivity of $S_{in}=-72.5\text{ dBm}$. Achievable sensitivity, although low compared to typical narrowband receivers that achieve levels lower than -90 dBm (for example, typical Bluetooth receivers), is sufficient for communication in body area networks at distances below 1 m. The presented calculation and simulation are valid in an ideal case, where the LO frequency is perfectly aligned with the center frequency of the FM-UWB signal. Since the idea behind power reduction is to use a low quality oscillator whose frequency might drift with time, the sensitivity degradation due to frequency offset should be estimated as well. This is done using the same high-level model, and the results are presented in Fig. 3.10

The 50 MHz offset is taken as a maximum offset that should be tolerated, and the LO frequency must be maintained within these limits. In the practical implementation this will be achieved using a calibration FLL loop that is periodically turned on (e.g. by a microcontroller when temperature exceeds certain limits). The sensitivity degradation for a 50 MHz frequency offset and for the receiver with quadrature downconversion is reported in Fig. 3.10(a). As can be seen, this degradation is below 1 dB, confirming empirically the initial hypothesis that the frequency offset does not cause a major sensitivity degradation. In the case of the receiver with single-ended downconversion this degradation amounts to around 1.6 dB, as seen in Fig. 3.10(b) showing that the simplified architecture is slightly more susceptible to frequency offsets.

It should be noted here that the given calculation and simulation models only account for a noise source at the input of the receiver. The separate contributions of receiver blocks are accounted for through the

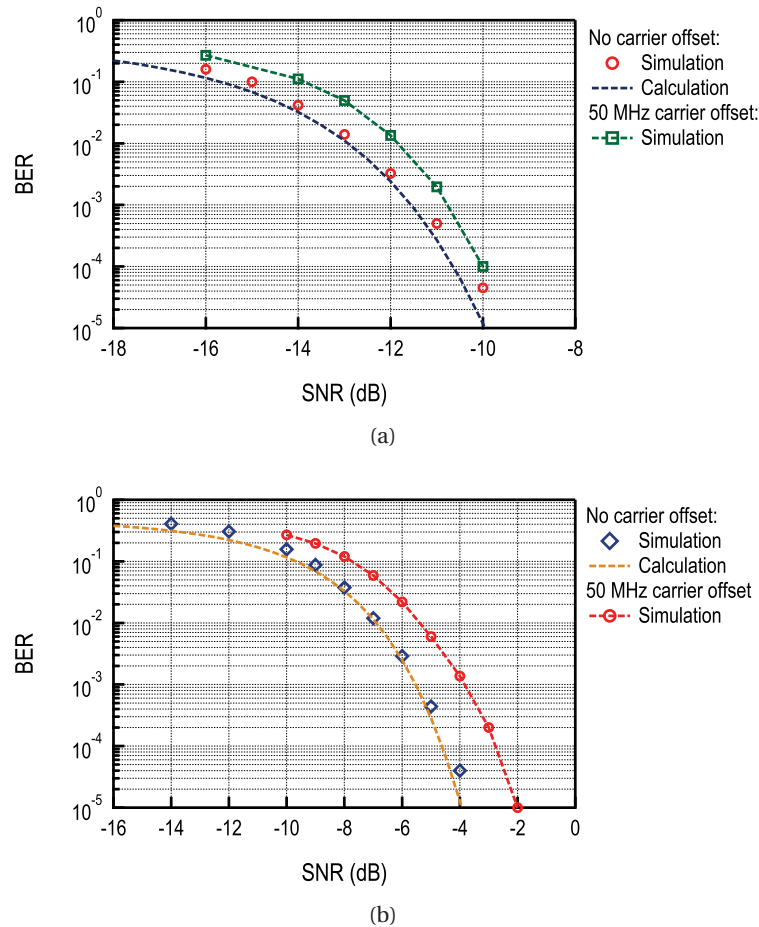


Figure 3.10: Simulated and calculated BER curves with and without frequency offset for the approximate zero-IF receiver with quadrature downconversion (a) and single-ended downconversion (b).

noise figure, however what is not accounted for is the noise generated by the FM demodulator (delay line demodulator for the quadrature, and envelope detector for the single-ended receiver). Due to the nonlinear nature of FM demodulators, the output noise will be depend on the input signal level. In order for the presented sensitivity estimation to be valid, the noise of this block must be negligible compared to the noise from other sources. This requirement is simply achieved by increasing the gain of the stages preceding the demodulator, and it is in fact this requirement that sets a limit for the combined gain of the LNA, mixer and the IF amplifier.

3.5 Summary

This chapter presents the general approach to receiver power reduction through use of “uncertain IF” and “approximate zero IF” architectures. The main idea is to loosen constraints on RF stages, that usually consume the most power, and shift the burden to IF where high gain comes at a lower price in terms of power. Two different receiver architectures are proposed. The quadrature approximate zero IF receiver targets to reduce consumption, but also to provide enough linearity to support multi-user

Chapter 3. Reducing the Power of FM-UWB receivers: the Approximate Zero IF Architecture

communication. Potential to parallelize communication through sub-carrier FDMA, on top of existing TDMA could bring both latency and power savings at a network level. The second architecture, the single-ended FM-UWB receiver architecture, aims solely to reduce power consumption. The used approach sacrifices all other performance aspects in order to provide the lowest possible consumption level, and could be used when there is no need for SC-FDMA. The analysis of the two architectures is presented, providing some insight into the key points and the principle of operation, together with a short sensitivity analysis that estimates the achievable receiver performance.

The implementation of the concepts presented here is the subject of the following chapters. First, the quadrature approximate zero IF FM-UWB receiver is implemented and characterized standalone. Then, in the second iteration, a full transceiver is integrated. Both receiver are placed on the same die, with the idea to use the single-ended FM-UWB receiver as a low power mode.

References

- [1] J. Farserotu, J. Baborowski, J. D. Decotignie, P. Dallemagne, C. Enz, F. Sebelius, B. Rosen, C. Antfolk, G. Lundborg, A. Björkman, T. Knieling, and P. Gulde, "Smart skin for tactile prosthetics," in *2012 6th International Symposium on Medical Information and Communication Technology (ISMICT)*, Mar. 2012, pp. 1–8.
- [2] A. Sai, H. Okuni, T. T. Ta, S. Kondo, T. Tokairin, M. Furuta, and T. Itakura, "A 5.5 mW ADPLL-based receiver with a hybrid loop interference rejection for BLE application in 65 nm CMOS," *IEEE Journal of Solid-State Circuits*, vol. 51, no. 12, pp. 3125–3136, Dec. 2016.
- [3] N. Saputra and J. R. Long, "A short-range low data-rate regenerative FM-UWB receiver," *IEEE Transactions on Microwave Theory and Techniques*, vol. 59, no. 4, pp. 1131–1140, Apr. 2011.
- [4] F. Chen, W. Zhang, W. Rhee, J. Kim, D. Kim, and Z. Wang, "A 3.8-mW 3.5-4-GHz regenerative FM-UWB receiver with enhanced linearity by utilizing a wideband LNA and dual bandpass filters," *IEEE Transactions on Microwave Theory and Techniques*, vol. 61, no. 9, pp. 3350–3359, Sep. 2013.
- [5] Y. Zhao, Y. Dong, J. F. M. Gerrits, G. van Veenendaal, J. Long, and J. Farserotu, "A short range, low data rate, 7.2 GHz-7.7 GHz FM-UWB receiver front-end," *IEEE Journal of Solid-State Circuits*, vol. 44, no. 7, pp. 1872–1882, July 2009.
- [6] N. M. Pletcher, S. Gambini, and J. Rabaey, "A 52 μ W wake-up receiver with - 72 dBm sensitivity using an uncertain-IF architecture," *IEEE Journal of Solid-State Circuits*, vol. 44, no. 1, pp. 269–280, Jan. 2009.
- [7] J. Gerrits, J. Farserotu, and J. Long, "A wideband FM demodulator for a low-complexity FM-UWB receiver," in *The 9th European Conference on Wireless Technology, 2006*, Sep. 2006, pp. 99–102.
- [8] M. Kouwenhoven, *High-Performance Frequency-Demodulation Systems*. Delft University Press, 1998.
- [9] J. F. M. Gerrits, M. H. L. Kouwenhoven, P. R. van der Meer, J. R. Farserotu, and J. R. Long, "Principles and limitations of ultra-wideband FM communications systems," *EURASIP J. Appl. Signal Process.*, vol. 2005, pp. 382–396, Jan. 2005.
- [10] V. Kopta, D. Barras, and C. C. Enz, "An approximate zero IF FM-UWB receiver for high density wireless sensor networks," *IEEE Transactions on Microwave Theory and Techniques*, vol. 65, no. 2, pp. 374–385, Feb. 2017.

4 Quadrature Approximate Zero-IF FM-UWB Receiver

The previous chapters explained the basics of FM-UWB modulation, discussed the existing state of the art and introduced two new architectures for an FM-UWB receiver. The concept of the proposed approximate zero-IF architecture with quadrature downconversion is brought to life in this chapter. The work is mainly oriented towards exploiting the short communication range, in order to lower power consumption of the receiver, but also to provide means to efficiently communicate as the number of sensor nodes in the network scales up. This is achieved through the use of the sub-carrier FDMA, that allows to distinguish multiple FM-UWB signals sharing the same RF band.

The chapter starts by introducing the top-level architecture of the integrated receiver. The following section deals with the details of circuit design, focusing on the key approaches and techniques used to reduce the power consumption of the most important circuits. Measurements of the implemented receiver are presented in Section 4.3. Beyond the intended data rate of 100 kb/s, the receiver is characterized in additional scenarios (higher speed, M-FSK modulation, multi-channel transmission) showing the true potential of the FM-UWB modulation. Finally, the chapter is concluded with a summary of achieved results and a comparison with similar receivers from the literature.

4.1 Receiver Architecture

The aim of this work is to reduce power of the FM-UWB receivers beyond the current state of the art while preserving the demodulator linearity and multi-user communication capability. As the LNA and other blocks operating at RF have been shown to consume the most power in previously implemented receivers, the strategy here is to first downconvert the signal to baseband, and then perform all the processing at low frequencies. Since power consumption in all of these blocks typically increases with frequency, moving them to baseband should result in significant power savings.

An oscillator, that was not needed in previous FM-UWB receiver implementations, is now necessary to generate the LO signal. Only if the LO can be implemented with a reasonable power budget can the approximate zero-IF architecture lower the overall consumption. Fortunately, ring oscillators in deep sub-micron technology nodes are known to consume very little and can be used here for such

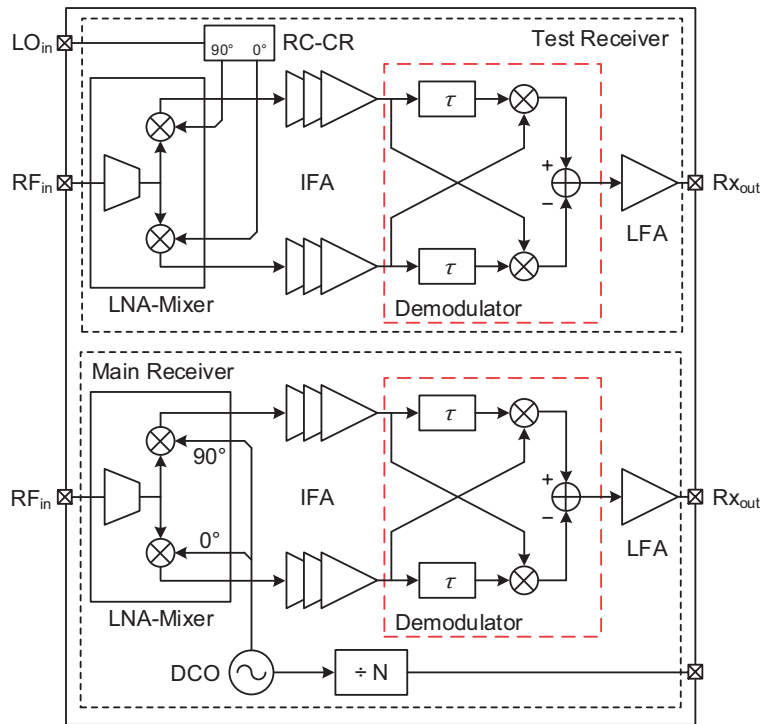


Figure 4.1: Receiver block diagram.

LO generation. The downside of using a low power ring oscillator is its high phase-noise, unstable oscillation frequency and high susceptibility to environmental changes. Ring oscillators are almost exclusively used in closed loop systems such as PLLs, where the oscillator is locked to a reference frequency, and all the aforementioned problems disappear. However, a PLL would require frequency dividers and these would add a significant contribution to the receiver power consumption. Instead of implementing a PLL, a free-running oscillator is used for this implementation and owing to the large FM-UWB signal bandwidth, some of the issues, such as phase noise, are circumvented. Frequency dividers are still needed, but they are used as part of the FLL calibration loop and are turned on only when calibration is necessary. That is mostly to compensate for frequency drift due to temperature or supply voltage variations. Fortunately, since these changes are slow and the calibration is not needed very often, the FLL calibration circuits will not pose a significant overhead to the receiver consumption.

The high-level block diagram of the implemented receiver is shown in Fig. 4.1, with the main receiver at the bottom and the test receiver at the top. The two receivers are implemented in order to assess the performance loss due to the on-chip, low power ring oscillator. They are identical in all aspects except for the LO. The main receiver uses the ring oscillator, whereas the test receiver uses an external signal to drive the mixer. Since this is a direct conversion receiver, quadrature LO signals are generally needed to perform correct demodulation. In the main receiver these are generated directly by the ring (multiple stages produce different phases, as will be shown later), while the test receiver uses an RC-CR network to provide quadrature signals, allowing to reduce the number of input pads. The difference in performance between the two receivers will be reported in the measurement section.

As already mentioned, the idea is to reduce power consumption by removing the RF blocks. It can be seen in Fig. 4.1 that the LNA is still present, however in this implementation it is simply a transconductance amplifier that converts the input voltage into current that is then downconverted by the mixer. The two can also be regarded as an active mixer with an input matching network. Since this is practically a mixer-first receiver the noise figure will be higher compared to a more standard approach with the LNA in front, but this remains an acceptable price for the achieved power savings. The main gain stages are placed at baseband (here referred to as IF amplifiers), allowing to achieve higher gain at lower power. Since the oscillation frequency of the ring oscillator is not stable, the bandwidth of these amplifiers is increased to account for a ± 50 MHz carrier frequency offset. Instead of 250 MHz that would normally be sufficient to amplify a downconverted 500 MHz wide signal, the bandwidth of IF amplifiers is extended to 300 MHz. The IQ delay line demodulator is a modified version of the demodulator from [1], adjusted for baseband operation, as described in the previous chapter.

The receiver presented here only implements the first FM demodulation. The resulting demodulated sub-carrier signal is buffered and is available at the receiver output. This signal is then converted to digital domain using an ADC, allowing the further data processing to be conducted off-line. The second FSK demodulation, and all the additional baseband processing (e.g. channel filtering) is implemented in software, allowing to measure BER performance of the receiver. It should be noted that this idealized approach yields a somewhat better performance than otherwise achievable with a low-power hardware implementation, but can nevertheless be used to assess performance of the integrated blocks. All of the implemented circuits can be controlled through an SPI bus, allowing to tune the bias current, resonance frequency, gain and bandwidth of different blocks and switch them on or off. Details of circuit implementation are given in the following section.

4.2 Circuit Implementation

4.2.1 RF Frontend

The LNA and the mixer, shown in Fig 4.2, are stacked in order to save power. The circuit can also be seen as an active mixer with the input matching network. An active mixer is chosen for downconversion because unlike a passive mixer, it provides voltage gain and does not require a rail to rail LO swing, preventing excessive consumption in the LO buffers. The used LO swing is around 300 mV peak to peak (single-ended), which is sufficient for the chosen circuit topology. Increasing the swing to 1 V, would result in an increase of the LO buffer power consumption by more than a factor of 9 (proportional to V_{LO}^2), hence justifying the choice of an active mixer. The transistor M_1 acts as a main transconductance stage, that converts the input voltage into current before the downconversion. Center-tapped symmetric inductor L_1 acts as a transformer and boosts the equivalent transconductance of transistor M_1 [2, 3], without the increase of power consumption, making this approach ideal for a low power design. Disregarding capacitor C_T for the moment, and assuming C_2 is large enough to be considered as a short circuit at the frequencies of interest, the equivalent transconductance seen from the gate of M_1 is given by

$$G_{m,eq} = \frac{\Delta I_1}{\Delta V_G} = \frac{(k+1)G_{m1}}{1 + j\omega L G_{m1}(1 - k^2)}, \quad (4.1)$$

where k is the transformer coupling coefficient. As k approaches 1 (ideal transformer) the equivalent transconductance becomes purely real and equal to $2G_{m1}$. It has been shown that, for the same current

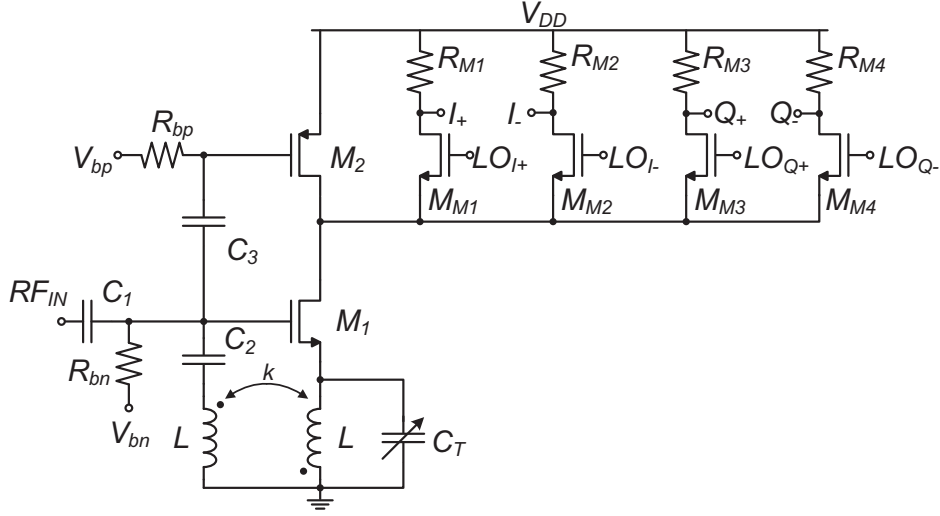


Figure 4.2: Schematic of the LNA/Mixer.

consumption, this approach achieves higher gain and larger bandwidth compared to the standard inductively degenerated LNA [3].

It was shown in [2] that the input impedance of the transformer feedback LNA is given by (assuming C_2 is large, $C_{GS} \ll C_1$, $k = 1$, $C_T = 0$ and $\omega^2 L^2 G_{m1}^2 \gg 1$)

$$Z_{in} \approx \frac{1}{j\omega C_1} + j\omega L + 2\omega^2 L^2 G_{m1}. \quad (4.2)$$

Resonance frequency is then $\omega_0^2 = 1/LC_1$. In this design tuning capacitor C_T is added to provide capability to tune the resonance frequency and to compensate for small component variations. With C_T the expression of the input impedance becomes:

$$Z_{in} \approx \frac{1}{j\omega C_1} + j\omega L \frac{1 - \omega^2 LC_T(2 - k^2)}{1 - 2\omega^2 LC_T} + \omega^2 L^2 G_{m1} k(1 + k) \frac{1 - \omega^2 LC_T(1 - k)}{1 - 2\omega^2 LC_T}. \quad (4.3)$$

In the above expression it is assumed that $C_T \ll C_1$, which means that close to resonance $\omega^2 LC_T < 1$. Assuming $k = 1$ 4.3 can be further simplified to:

$$Z_{in} \approx \frac{1}{j\omega C_1} + j\omega L \frac{1 - \omega^2 LC_T}{1 - 2\omega^2 LC_T} + \frac{2\omega^2 L^2 G_{m1}}{1 - 2\omega^2 LC_T}, \quad (4.4)$$

which shows that the resonance frequency is now a function of C_T . Unfortunately, C_T also affects the real part of the input impedance, however it is still possible to achieve good matching and roughly 10% tuning range of the resonance frequency.

A common problem in active mixers is that the bias current required by the transconductance M_1 and switching transistors M_{M1-4} is not the same. Bias current of M_1 is set by the input matching condition and the desired voltage gain. Voltage gain of the active mixer is proportional to the product

of the transconductance and the load resistance $G_{m1}R_{M1-4}$. At the same time, the dc point of the output voltage and the LO feedthrough ($I_{+/-}$ and $Q_{+/-}$ outputs) are dependent on the product of the bias current and load resistance $I_b R_{M1-4}$. Increasing the voltage gain, either through G_{m1} (and consequently I_b) or through R_{M1-4} lowers the output bias voltage and increases the LO feedthrough. To add a degree of freedom and break this dependence, “current stealing” technique can be used. This is accomplished using the transistor M_2 , that sinks part of the M_1 bias current. In this way mixer bias current can be set independently of the M_1 bias current, allowing to break the dependence between the voltage gain on one side and dc bias and LO feedthrough on the other. As a consequence, load resistor values can be increased to maximize voltage gain without causing excessive LO feedthrough. In addition to current stealing, since the gate of M_2 is connected to the LNA input through a large capacitor C_3 , it also contributes to the overall transconductance, further increasing voltage gain. The approach is similar to the complementary LNA presented in [4], with the difference that the bias currents of M_1 and M_2 are not the same. The addition of M_2 has some downsides in a practical implementation. More complex layout of the LNA will result in increased parasitics, and more importantly drain capacitance of M_2 will be added to the parasitic capacitance at the mixer input, effectively reducing bandwidth of the RF front-end. To compensate for the added capacitance, the equivalent input resistance of the mixer can be reduced by increasing the size of the switching transistors M_{M1-4} , but this comes at price of increasing the load of the LO buffers.

In this design resistors R_{M1-4} can be switched between 22k Ω and 14k Ω and provide two gain steps for the mixer. Since the voltage gain is obtained entirely at baseband frequencies, after mixing, it comes at a lower cost in terms of power, and eliminates the need for a resonant load, thereby saving silicon area. Achieved voltage gain is around 15 dB over a 600 MHz bandwidth, for the maximum gain setting. Simulated current consumption is 70 μ A from a 1 V supply. The input referred 1 dB compression point of the RF frontend is at -19 dBm. The price to be paid for low power consumption is elevated noise figure, which in this case is 15 dB according to simulations (this is including the LNA and the mixer). Even though it is higher than the typical values found in standard receiver implementations, it is still acceptable for communication over short distances.

4.2.2 IF Amplifier

The mixer is followed by the I and Q IF amplifiers that provide most of the voltage gain. Each IF amplifier is a cascade of three modified CMOS Cherry-Hooper (CH) amplifiers shown in Fig. 4.3. The basic concepts that come from [5] were further developed in [6], where emitter-follower was introduced in the feedback, and the first CMOS version was presented in [7]. A CH amplifier is a feedback amplifier with a second order transfer function. Compared to a cascade of standard differential pairs, feedback amplifiers offer larger bandwidth for the same power consumption. This is why these amplifiers were originally used for high data rate optical receivers, targeting bandwidths of more than 1 GHz. In this case, the design was optimized for 300 MHz bandwidth and low power consumption. By controlling the Q-factor of the transfer function, behavior close to the edge of the pass-band can be controlled. In this particular case peaking was used to compensate for the slight drop in the LNA/mixer conversion gain close to the band edges and provide a relatively flat overall gain characteristic.

The small-signal schematic of the half-circuit is given in Fig. 4.3. Capacitors C_1 and C_2 are a combination of gate capacitance (in the case of C_2 this would be the gate capacitance of the following stage) and layout parasitics. Capacitance C_z introduces a zero in the transfer characteristic, and is used to prevent offset accumulation in the IF amplifiers. Although, strictly speaking, the downconverted FM-UWB

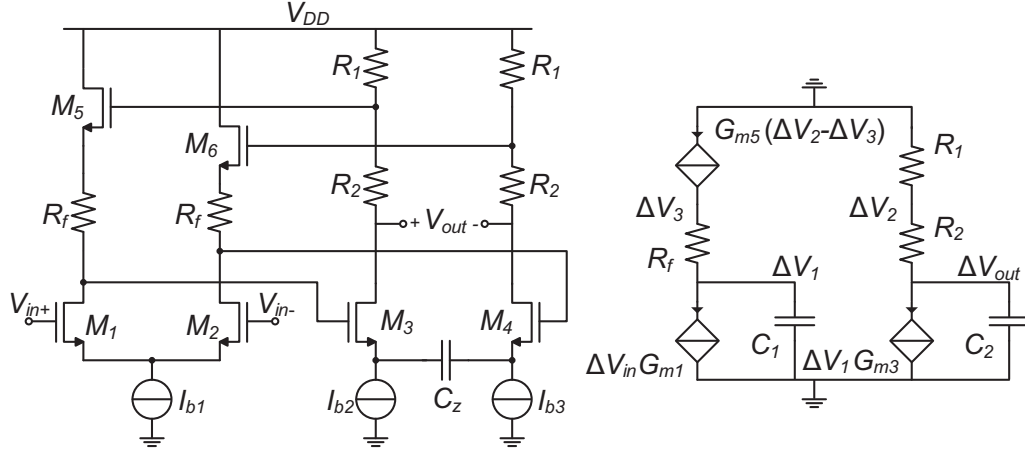


Figure 4.3: Schematic of the IF amplifier, and the equivalent small-signal schematic of half circuit.

signal occupies frequencies from 0 to 250 MHz, a zero in the transfer function will not affect the performance of the demodulator as long as this zero is low compared to the signal bandwidth. In this case the zero is placed around 1 MHz, and since it will not affect the behavior in the pass-band it is not considered in the small-signal analysis. Gain in the pass-band is given by [7]

$$A_{v0} = \frac{G_{m1}(R_1 + R_2)(1/G_{m5} + R_f)}{(1/G_{m3} + R_1)}. \quad (4.5)$$

Assuming $G_{m5}R_f \gg 1$ and $G_{m3}R_1 \gg 1$ the above expression reduces to

$$A_{v0} \approx \frac{G_{m1}(R_1 + R_2)R_f}{R_1}. \quad (4.6)$$

As the voltage gain is a function of the ratio of the two load resistors R_1 and R_2 , gain switching can be implemented by switching the value of R_2 . The second order transfer function of the CH amplifier is given by

$$A_v(s) = \frac{G_{m1}G_{m3}(R_1 + R_2)(1 + G_{m5}R_f)}{G_{m5}(1 + G_{m3}R_1) + s(C_1(1 + G_{m5}R_f) + G_{m5}C_2(R_1 + R_2)) + s^2C_1C_2(R_1 + R_2)(1 + G_{m5}R_f)}. \quad (4.7)$$

Again, assuming the transconductances are high enough that $G_{m5}R_f \gg 1$ and $G_{m3}R_1 \gg 1$ leads to the simplification of the expression that reduces to

$$A_v(s) = \frac{G_{m1}G_{m3}(R_1 + R_2)R_f}{G_{m3}R_1 + s(C_1R_f + C_2(R_1 + R_2)) + s^2C_1C_2(R_1 + R_2)R_f}. \quad (4.8)$$

Capacitors C_1 and C_2 are determined by the size of the differential pair transistors and the layout parasitics. Gain, bandwidth and Q-factor of the amplifier transfer function are then set by the resistances of R_1 , R_2 and R_f , which can be used as design parameters.

Simulated gain of the standalone LNA/mixer, and the LNA/mixer together with IF amplifiers is shown in Fig. 4.4(a). Overall gain of all the stages preceding the FM demodulator is around 53 dB, with

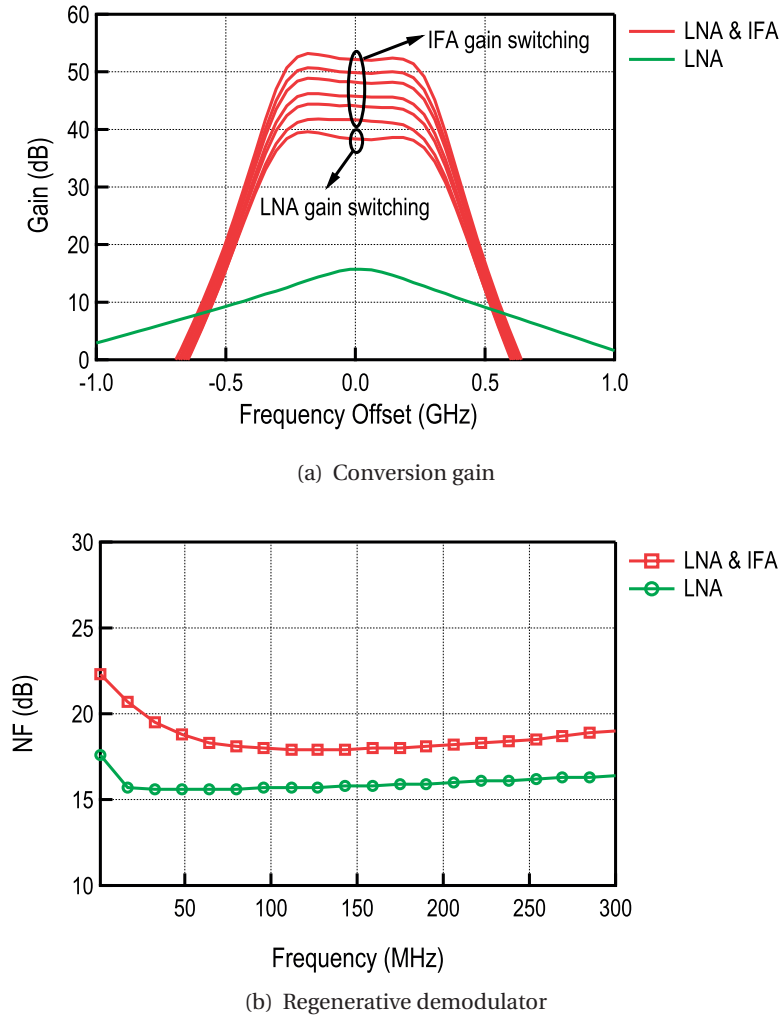


Figure 4.4: Simulated conversion gain and noise figure of the RF and IF stages.

approximately 38 dB provided by the IF amplifier. Each CH amplifier cell requires $20\ \mu\text{A}$ of current, which results in $120\ \mu\text{A}$ consumed by the I and Q IF amplifier chains. Equivalent 6th order filtering characteristic provides the attenuation of 32 dB at an offset frequency of 500 MHz. Gain control is implemented through switching of R_2 , that can take one of the values $6\ \text{k}\Omega$, $18\ \text{k}\Omega$ and $30\ \text{k}\Omega$, while $R_1 = 24\ \text{k}\Omega$. With three cascaded stages, the designed IF amplifier provides 6 different gain levels and one additional level is provided by switching the mixer load resistors R_{M1-4} . Different gain levels can be seen in Fig. 4.4(a). Fig. 4.4(b) shows the simulated noise figure of the standalone RF frontend and of the RF frontend and the IF amplifiers together. The RF frontend provides around 15 dB of voltage gain, however the power remains low. This is a consequence of low bias current of the LNA/mixer, that results in a low value of transconductance. As a result the noise added by the IF amplifiers will increase the total noise figure by approximately 3 dB. The noise figure of the standalone IF amplifier is around 5 dB in the pass-band. Finally, even though the noise figure is higher compared to more conventional receiver implementations, the achieved levels still provide enough sensitivity for communication over short distances.

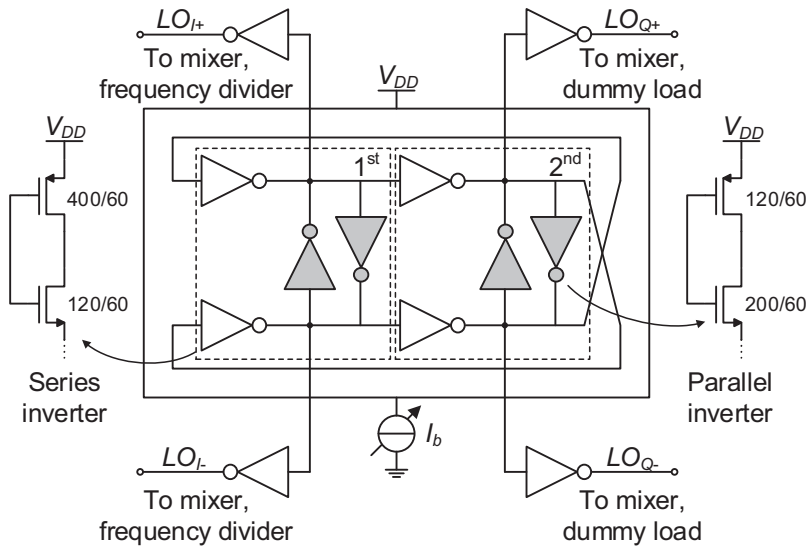


Figure 4.5: Simplified schematic of the quadrature DCO.

4.2.3 LO Generation and Calibration

The proposed receiver is intended for use in the lower part of the UWB band, targeting 500 MHz wide signal centered around 4 GHz. The emphasis of the work described here is on reducing the power consumption of the receiver, while still preserving the capability to operate in an environment where several FM-UWB transceivers might be communicating at the same time. The power reduction dominantly comes from the fact that the gain stages operate at low frequencies, while no voltage gain is provided at RF. However, such an approach can only be beneficial if the LO signal can be generated efficiently. Additional difficulty is the need for quadrature signals since a 90° shift is generally required for correct demodulation in a direct conversion (zero IF) receiver. Providing such signals at 4 GHz tends to be power costly. Fortunately, owing to the properties of FM-UWB and the chosen receiver architecture, the oscillator constraints are quite loose. Due to the large bandwidth of the FM-UWB signal, phase noise is not a major concern (-80 dBc at 10 MHz offset according to [8]) and no precise frequency generation is needed, and so a simple free-running ring oscillator can be used to provide carrier signals for downconversion. When it comes to power consumption, ring oscillators are advantageous compared to LC oscillators, as they benefit from technology scaling. Inductor quality factor, which is a limit to power consumption of integrated LC oscillators, remains constant and practically independent of technology. On the other hand, gate capacitance and interconnect parasitic capacitances, that determine consumption of ring oscillators, decrease with technology scaling. This enables the reduction of power consumption of the ring oscillator, making the proposed approach favorable for future implementations.

The oscillator schematic is shown in Fig. 4.5. A chain with an even number of inverters is needed to provide quadrature signal generation, however such a circuit would latch on its own. In order to prevent latching, and force a 180° shift parallel inverters are added between the corresponding nodes (grey inverters in Fig. 4.5). A different way to see the implemented oscillator would be as a pseudo-differential two stage ring oscillator, where each stage consists of four inverters and the differential mode is enforced by the parallel inverters [9, 10]. The two stages provide a 90° phase shift, and additional 180° shift is

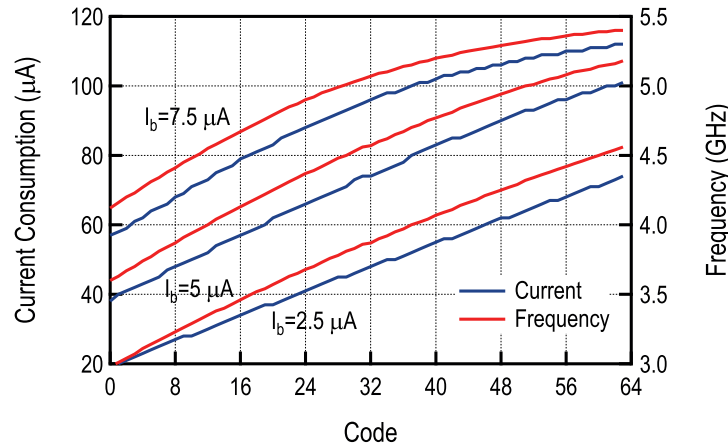


Figure 4.6: Simulated frequency and current consumption of the DCO.

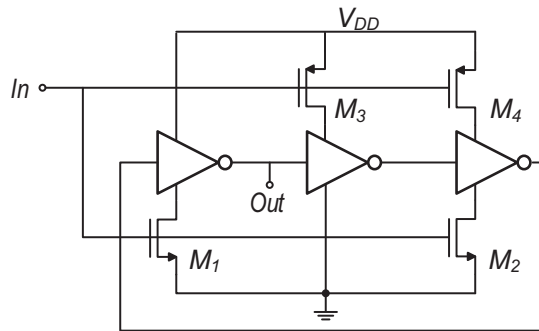


Figure 4.7: Schematic of the frequency divider.

provided by cross-coupling the stages assuring a reliable start-up. The series and parallel inverters are sized differently, W/L ratios in nm are shown in Fig. 4.5, dimensions were optimized for low power consumption. One of the difficulties in designing very low power ring oscillators is that capacitive load is dominantly determined by the capacitance of the interconnect wires, and is layout dependent. Careful layout design with several iterations is needed to minimize power consumption. Correct phase relations between different signals are guaranteed by symmetry, however a small quadrature error is present due to mismatch between transistors. The error will vary from die to die and according to Monte Carlo simulations their standard deviation is $\sigma_\phi = 2.6^\circ$. Frequency is controlled via supply current of the current starved CMOS inverters. All inverters share the same current source as this approach was proven to perform better than the solution with a separate current source for each inverter, or inverter pair [9].

Since process-voltage-temperature (PVT) variations can have a significant impact on the oscillation frequency, the digitally controlled oscillator (DCO) was designed to cover the frequency range from 3 GHz to 5 GHz, thus assuring that it can be tuned correctly under all conditions. A 6-bit current DAC is used to provide the supply current, resulting in less than 30 MHz frequency resolution. The frequency step is not constant due to non-linear characteristic of the DCO and decreases as the oscillation

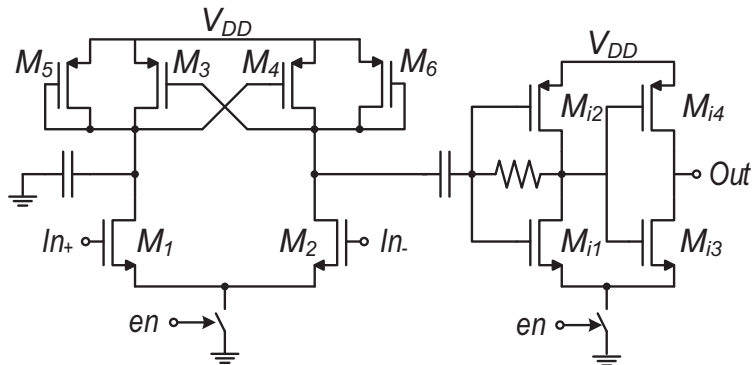


Figure 4.8: Schematic of the buffer between the DCO and the frequency divider.

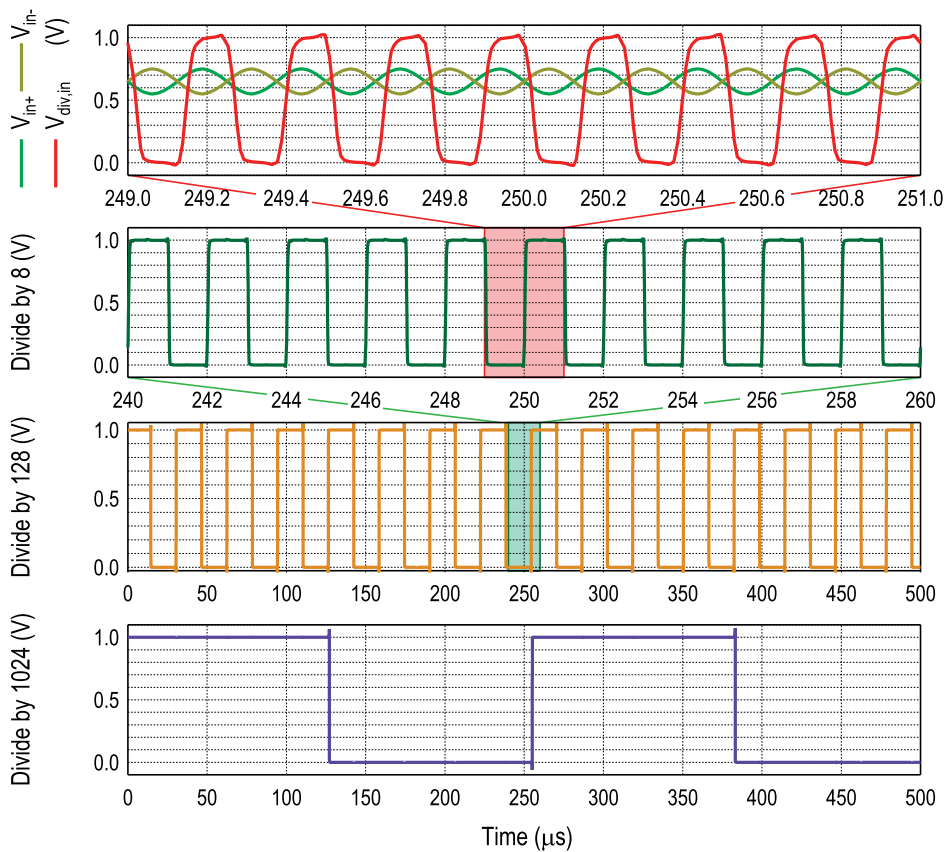


Figure 4.9: Frequency divider, waveforms at different points.

frequency increases. At 4 GHz the DCO produces a 300 mV peak-to-peak single-ended signal while consuming 140 μ A (including the buffers). Simulated oscillation frequency and current consumption of the DCO, as functions of input code, are shown in Fig. 4.6 for different DAC reference currents.

Since the oscillation frequency of the DCO is imprecise and prone to environment changes it must be calibrated periodically to assure correct operation (e.g. to compensate for temperature). Since environmental changes are slow, the calibration would only need to be done once in a few hours or potentially even days, meaning that the consumption of the calibration circuitry on average remains negligible compared to the receiver consumption. The calibration can be done using a frequency-locked loop (FLL) that is turned on as needed. The FLL was not integrated in this implementation, however it can be added externally using a microcontroller or an FPGA, and the available output from the on-chip frequency divider. A fixed ratio, integer frequency divider is implemented as a cascade of 10 divide-by-2 cells. By selecting outputs from different dividers, one of the four divide ratios 128, 256, 512 and 1024 can be selected as an output for calibration. Each cell is a simplified version of a dynamic 2/3 divider circuit described in [11]. It was designed to cover a somewhat larger range of frequencies than the DCO to assure reliable operation. Owing to the simplified structure, the circuit from Fig. 4.7 can work up to 6 GHz. Since the divider requires a rail-to-rail input signal, it is preceded by a buffer from Fig 4.8 that performs differential to single-ended conversion and amplifies the signal. The first stage of the buffer is a pseudo-differential amplifier that uses positive feedback to boost the gain. The positive feedback is implemented using the cross-coupled transistors M_3 and M_4 that provide a negative transconductance. This negative transconductance is used to minimize the equivalent output conductance of the amplifier and increase gain. The differential amplifier is followed by inverters that further amplify the LO signal and produce a rail-to-rail voltage at the output. The whole buffer consumes around $250\ \mu\text{W}$ at 4 GHz and its power consumption is proportional to the input frequency. Figure 4.9 shows simulated waveforms at the buffer input and output, and divider signals in different points. The whole divider chain consumes around $150\ \mu\text{W}$, and largest part of the consumption is coming from the first two stages that operate at the highest frequencies.

The frequency divider buffer itself is connected to the LO_{I+} and LO_{I-} outputs of the DCO buffers. Dummy load is added to LO_{Q+} and LO_{Q-} to prevent amplitude mismatch between the I and Q LO signals. Even though the DCO itself can produce a sufficiently large output amplitude, the four buffers (Fig. 4.5) need to be placed between the internal nodes of the DCO and the inputs of the mixer and divider. This is done to decouple the oscillation frequency from the mode of operation (reception or calibration). The input capacitance of the divider buffer varies with the bias current of the two input transistors, and is different in the on and off state. If these buffers were connected directly to the DCO, the change in load capacitance would cause a shift in frequency after calibration. In addition, the presence of DCO buffers reduces coupling between the external signal and the DCO, thus preventing the pulling effect (shift in frequency caused by external signal). The four buffer inverters consume around $80\ \mu\text{A}$, almost 60 % of the entire DCO consumption which is a significant but necessary overhead.

4.2.4 FM Demodulator

The implemented wideband FM demodulator is a modified version of the delay-line demodulator presented in [1]. In order to conserve power, the demodulator has been moved from RF to baseband, but it now requires quadrature inputs to perform correct FM demodulation. Additional benefit of moving the demodulator to baseband is that there is no need for precise delay generation, as it is no longer related to the input signal frequency. The only limit is coming from the demodulator bandwidth that is inversely proportional to the delay. The implemented delay-line demodulator is presented in Fig. 4.10. Two double-balanced Gilbert's mixers perform multiplication of the I and Q signals with their delayed copies. The output currents of the two cells are combined to implement subtraction and

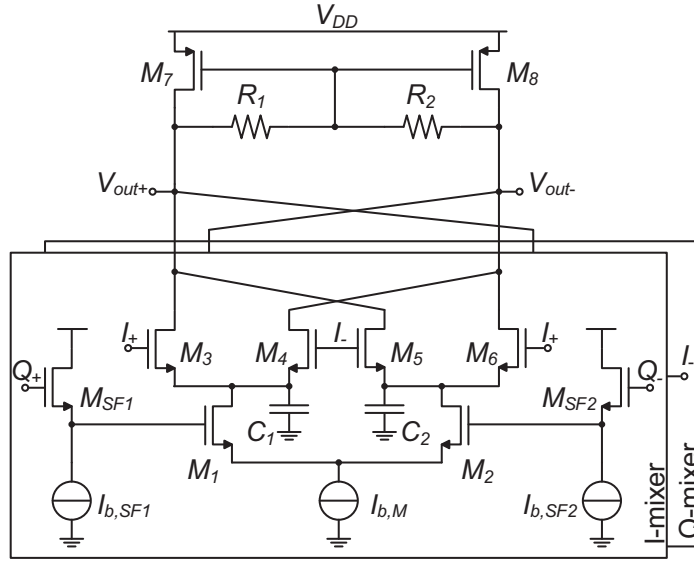


Figure 4.10: Schematic of the wideband FM demodulator.

produce the demodulated signal. Top inputs of Gilbert's mixer are connected directly to the outputs of the IF amplifier (gates of transistors M_{3-6}). Source followers are placed between the IF amplifier and bottom inputs (gates of transistors $M_{1,2}$) to provide a correct dc level of the input voltage. The delay path consists of source followers $M_{SF1,2}$ and bottom transistors of the Gilbert's mixer $M_{1,2}$. For a first order filter with a pole at ω_p it can be shown that the delay through the filter is equal to $1/\omega_p$, for a signal whose maximum frequency is sufficiently below the cut-off frequency. In this case the total delay is a sum of delays that come from two poles. First one is associated to the source follower and is given by

$$\tau_1 \approx \frac{C_{G1}}{G_{m,SF1}}, \quad (4.9)$$

where the capacitance C_{G1} accounts for the total capacitance seen at the gate of M_1 . Since M_1 is a relatively small transistor, parasitics will contribute a significant portion of the total load.

Due to the asymmetry of the double balanced mixer with respect to the two signal paths, some delay will inherently exist between the bottom and top inputs. This delay is caused by the pole that exists due to the parasitic capacitance at the drain of M_1 . To provide better control of the delay and reduce dependence on parasitics, an additional MOM (metal-oxide-metal) capacitor is added in this node ($C_{1,2}$), resulting in the delay that is given by

$$\tau_2 \approx \frac{C_1}{G_{m3} + G_{m4}}. \quad (4.10)$$

All the transistors in the FM demodulator are biased in weak inversion. Since the transconductance of each transistor is proportional to the bias current, delay of the demodulator can consequently be controlled by the bias currents $I_{b,SF}$ and $I_{b,M}$. Two bit control of the bias current is provided to allow delay tuning after production. Load resistors R_1 and R_2 can be switched between the two values to provide two gain settings. The FM demodulator input and output waveforms are shown in Fig. 4.11. The figure shows the input sub-carrier signal (top), the I and Q signals (middle) and the demodulated

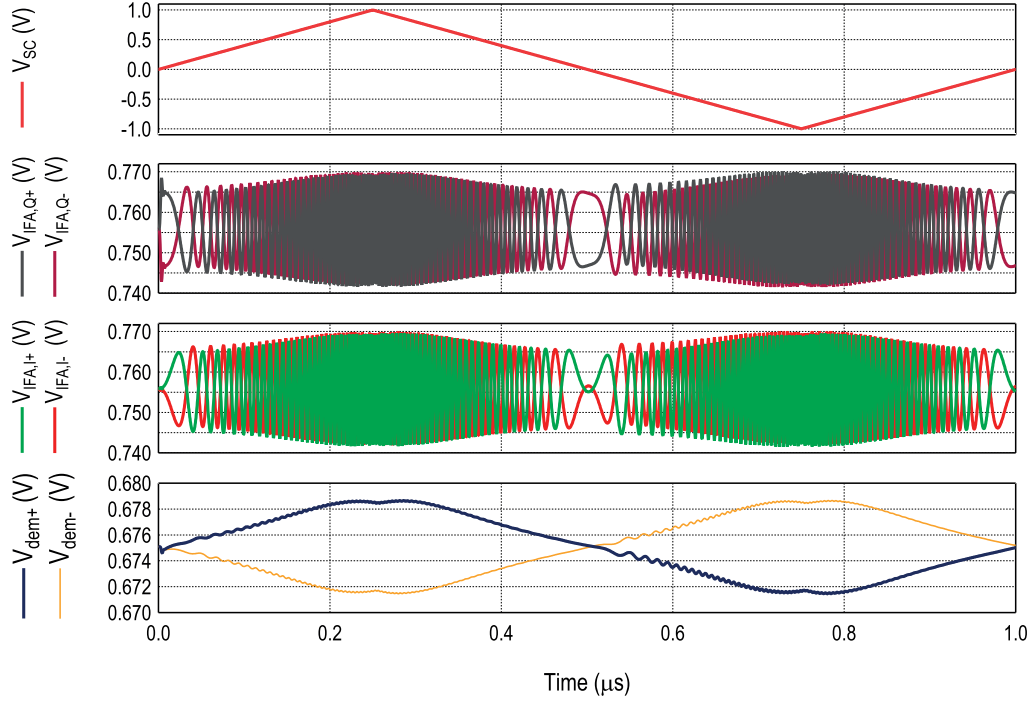


Figure 4.11: Wideband FM demodulator, input and output waveforms.

signal (bottom). A small distortion can be seen at the peak values of the demodulated signal. This is a result of the IF amplifier bandwidth, combined with the fact that delay decreases at higher frequencies.

The demodulator consumes only $25 \mu\text{W}$, mainly due to the fact that it operates at baseband. Compared with the demodulators from [12, 13], that require close to 6 mW , this is an improvement by two orders of magnitude, allowing significant power savings and still providing sufficient linearity to handle multiple input FM-UWB signals. Additionally, there is no need for inductors and no need for a complex passive network that provides a precise delay, thus resulting in area savings as well.

4.2.5 LF Amplifier and Output Buffer

For the targeted sensitivity levels, the signal amplitude at the output of the demodulator will be too low. Before it can be digitized and analyzed, the signal must be amplified and filtered. The two low-frequency (LF) amplifiers that follow the FM demodulator provide a band-pass characteristic from 1 MHz to 2.5 MHz and a maximum voltage gain of roughly 20 dB while consuming $15 \mu\text{A}$. As shown in Fig. 4.12, each stage is implemented as a fully differential amplifier with resistive source degeneration. Source degeneration provides better linearity, and more precise gain control. The gain of the amplifier is given by

$$A_v = -\frac{G_{m1}R_L}{1 + G_{m1}R_S/2} \approx -\frac{R_L}{R_S/2}. \quad (4.11)$$

The approximation is valid if $G_{m1}R_S/2 \gg 1$, in which case the gain is solely determined by the ratio of load and source resistors. Two bit gain control is provided, both R_L and R_S can be switched between

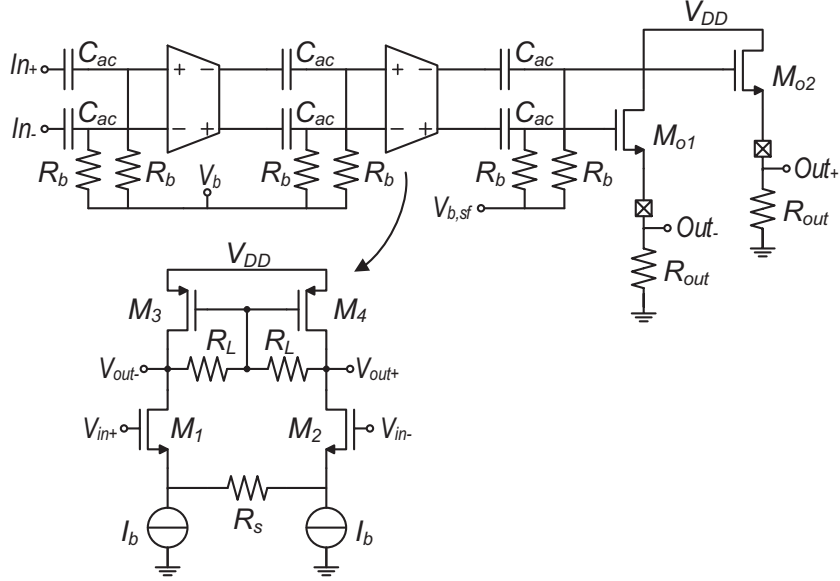


Figure 4.12: Schematic of the output buffer.

the two values. Since higher cut-off frequency is determined by R_L and the capacitance loading the amplifier output (gate capacitance of the following stage in series with C_{ac}), decreasing the gain also extends bandwidth. The lower cut-off frequency is determined by the elements of the ac coupling network as $1/R_b C_{ac}$.

Source followers M_{o1} and M_{o2} are placed at the output to provide a low impedance stage that drives the external circuits. They are design to drive a load of 10 pF, which corresponds to the capacitance of the oscilloscope probes or an external ADC, used to digitize the signal, although if necessary an additional external buffer can be added. External resistors define the bias current of the source followers, and can be chosen to have any value between 1 k Ω and 10 k Ω , while still providing sufficient bandwidth.

4.2.6 Current Reference PTAT Circuit

All the circuits described so far require a reference current that defines the bias point. All the reference currents are derived from a single current generated by the circuit from Fig. 4.13. The circuit provides a PTAT (proportional to absolute temperature) reference current and reuses the approach from [14]. It is a closed loop circuit made up of two current mirrors, a 1:1 current mirror M_5 - M_6 and a 1: K current mirror M_1 - M_2 . Transistors M_3 and M_4 are used as cascode transistors that define the drain voltage of M_1 and M_2 . The bias current is defined by the ratio of M_1 and M_2 , and since they are both biased in weak inversion the generated reference current I_{out} is be given by

$$I_{out} = \frac{U_T \ln K}{R}. \quad (4.12)$$

The output current is proportional to absolute temperature through thermal voltage $U_T = kT/q$. The generated current is used as a reference current for an array of current DACs that provide a reference

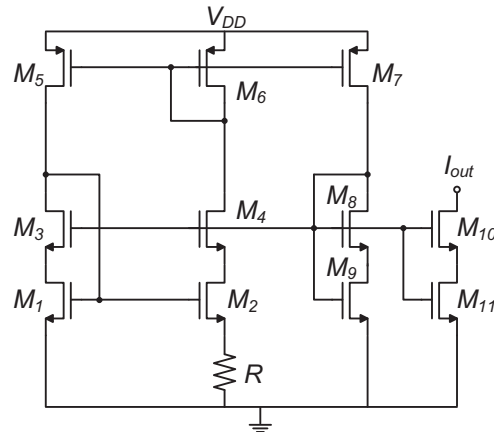


Figure 4.13: Schematic of the PTAT current reference.

current for each block of the system. Each of the reference currents can be digitally controlled with a resolution of $1.25 \mu\text{A}$, allowing some room for adjustment of the bias current after production.

4.3 Measurement Results

4.3.1 General Receiver Measurements

The proposed receiver was integrated in a standard 65 nm bulk CMOS process. The die photograph is presented in Fig. 4.14. The active area of the receiver is approximately 0.4 mm^2 , including roughly 450 pF of decoupling capacitance. The receiver only requires one inductor, with no additional off-chip components, which results in smaller area than most existing implementations. As already mentioned, for testing purposes two receivers were implemented on the same die. Rx1 is the main receiver that uses the ring oscillator described in the previous section to generate the quadrature LO signals. Rx2 is the test receiver that is identical to the first receiver except that it uses an externally generated LO signal. Two input pads are used for the differential LO, and the on-chip RC-CR network produces quadrature signals. The test receiver is integrated to serve as a reference that allows assessment of performance degradation due to a non-ideal locally generated carrier signal.

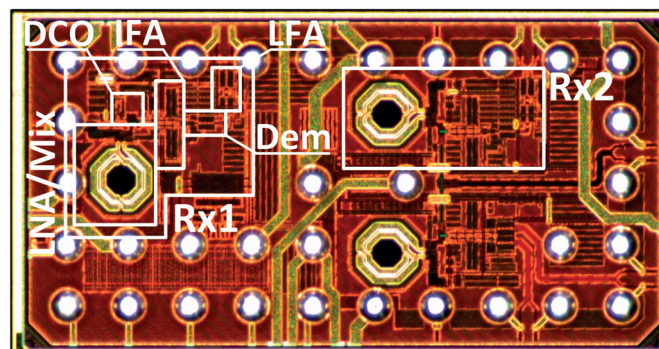


Figure 4.14: Die photograph.

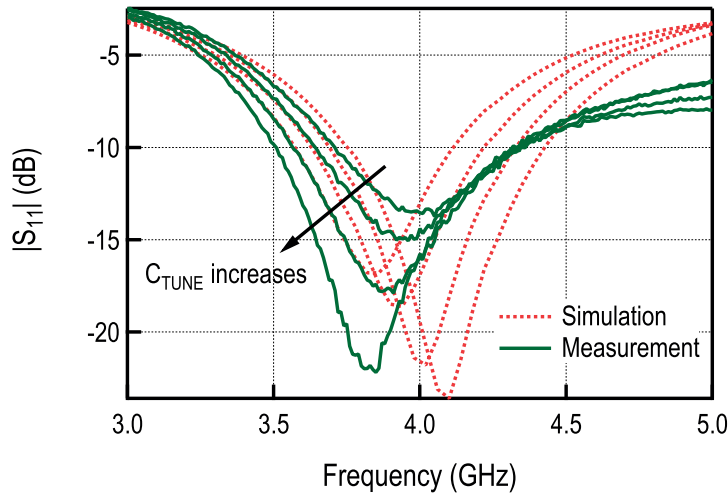


Figure 4.15: Measured S_{11} parameter for different values of input capacitance.

Figure 4.15 shows the simulated and measured S_{11} parameter of the receiver for different values of tuning capacitor C_T . A small difference in measured and simulated values is observed. The measurement was done on an FR4 test board with a 10 mm long 50 Ω coplanar waveguide between the pad and the connector. This line was not taken into account in the simulations and might be the cause of the shift in the resonance frequency. Nevertheless, the reflection coefficient is below -10 dB in the band of interest, providing sufficiently good matching.

The DCO frequency was measured using the on-chip frequency divider. As shown in Fig. 4.16 the oscillation frequency can be varied from 3.1 GHz to 4.7 GHz. At the same time the supply current of the DCO changes from 32 μA to 85 μA . At 4 GHz the DCO consumes around 60 μA , while the buffer consumes an additional 80 μA , a consequence of the fact that differential quadrature signals need to be buffered. Only one die measurement is presented here, however the frequency characteristic will vary significantly from one die to another as a result of process variation. Nevertheless, all of the measured dies covered the range from 3.6 GHz to 4.4 GHz and could be calibrated properly. In all cases the power consumption remains practically the same for the DCO oscillating at 4 GHz. A slightly non-linear behavior can be observed in the output frequency, which is of no significance in this case since the only requirement for the calibration loop is monotonicity, which is satisfied.

The proposed receiver consumes 423 μW of power from a 1 V supply. Power breakdown is shown in Table 4.1. The highest consumer is the DCO together with buffers, followed by the IF amplifiers and the LNA. The demodulator, with only 26 μW of power consumption consumes two orders of magnitude less power than the same type of demodulators implemented previously in [12, 13].

4.3.2 Single User Measurements

The test setup used for the bit error rate (BER) measurements is presented in Fig. 4.17. A random bit sequence is generated by software and mapped to the corresponding quadrature FM-UWB symbols. A 12 GS/s, 12-bit arbitrary waveform generator, M8190A was used to generate the baseband quadrature

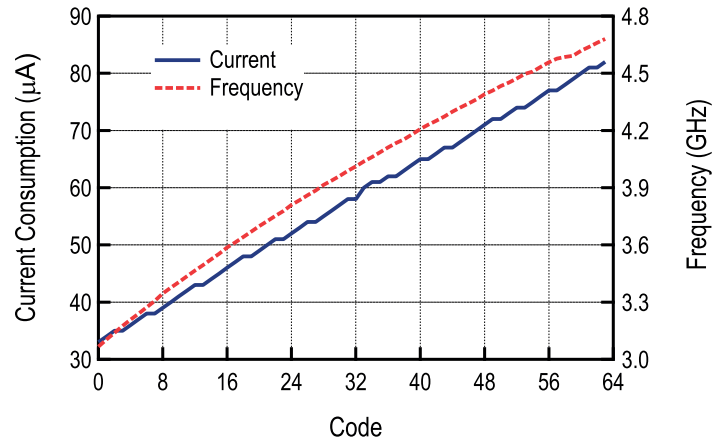


Figure 4.16: Measured frequency and current consumption of the DCO

Table 4.1: Power consumption breakdown

Block	Current cons. (µA)	Relative cons. (%)
LNA & mixer	91	21.5
DCO & buffers	140	33.1
IF amplifier	122	28.8
Demodulator	26	6.1
LF amplifier	15	3.5
Bias	29	6.9

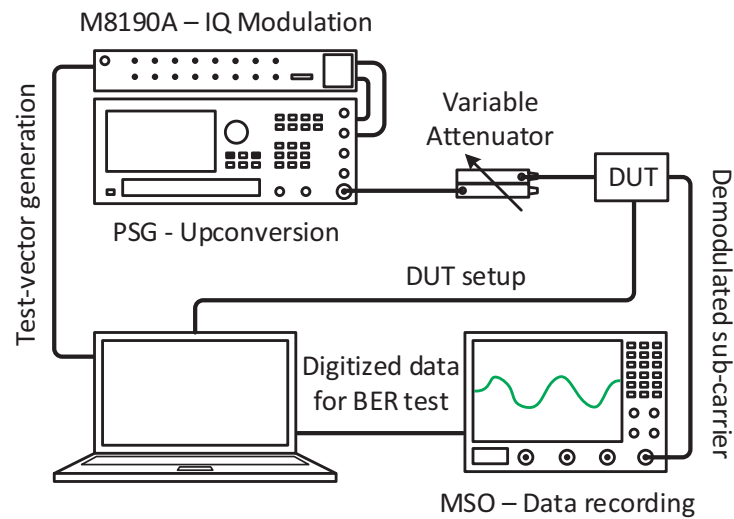
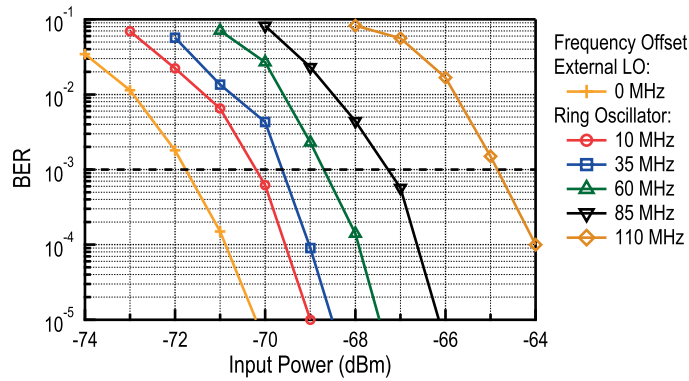
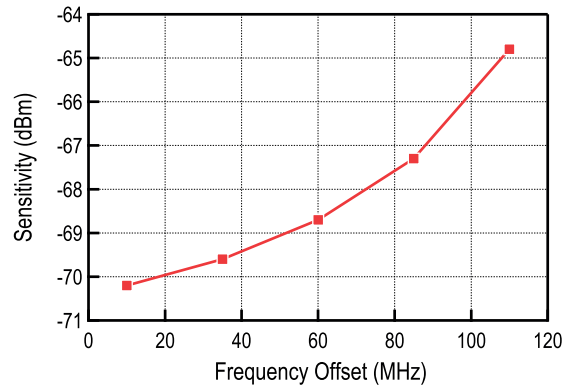


Figure 4.17: Measurement setup



(a) BER curves for different carrier offset



(b) Sensitivity vs. carrier frequency offset

Figure 4.18: Measured BER curves for different carrier offset.

FM-UWB signals. These signals are subsequently up-converted to 4 GHz by the Keysight PSG signal generator and used for receiver characterization. The flexibility provided by the M8190A allows to generate FM-UWB signal with different characteristics. Measurements with different data rates as well as with different modulation orders are reported in this section. The generator is also capable of producing different scenarios, that include multiple FM-UWB signals in the same RF band, but using different sub-carrier frequencies. The waveforms for different scenarios, as well as the test vectors for the BER measurements are generated using a PC. The same PC is then used to compare the original test vector with the demodulated data recorded by an oscilloscope, and finally produce the BER curves.

The on-chip demodulator performs the first, wideband FM demodulation, and provides the FSK sub-carrier at the output. The second FSK demodulation is performed by software. The receiver output signal is first recorded and digitized using the MSO oscilloscope (that acts as a 10 bit 20 MS/s ADC). The recorded vector is then demodulated using software. The FSK demodulator is implemented as a correlator, which is an optimal maximum-likelihood detector for this case.

As explained previously, two receivers were implemented on the same die in order to compare the receiver performance with the ideal LO and the integrated ring oscillator. Tests were performed using a nominal data rate of 100 kb/s, and the sub-carrier modulation index of 1, meaning that the frequency

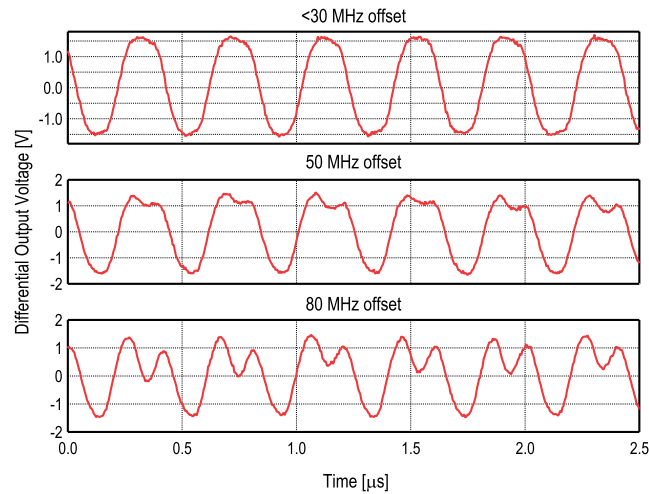


Figure 4.19: Measured demodulator output waveform for different carrier frequency offsets

deviation from center frequency is $\Delta f=50$ kHz. This is the minimum frequency deviation that preserves orthogonality between the two FSK frequencies for the case of non-coherent signaling. The BFSK sub-carrier signal is not filtered (no pulse shaping is applied), which simplifies the receiver implementation but causes higher ACLR. For this measurement the sub-carrier signal is centered at 1.55 MHz, resulting in two sub-carrier frequencies at 1.5 MHz and 1.6 MHz, although different center frequencies could have been used as well.

In all cases FSK frequencies are selected so as to have a continuous phase FSK signal. This is generally preferred in order to avoid discontinuities in the signal driving the VCO on the transmitter side, and is therefore used for testing. Sensitivity is defined as the input power that provides a BER of 10^{-3} . The result is shown in Fig. 4.18. Measured sensitivity of the receiver with an external LO signal is around -72 dBm. The approximate calculation presented by Gerrits in [1] suggests a sensitivity of -79 dBm for the noise figure of 18 dB. The difference is a result of imperfections present in the implemented receiver, most likely lower gain and increased noise figure of the RF frontend compared to the values obtained by simulation. The measured sensitivity with the internal ring oscillator is -70 dBm, a value approximately 2 dB worse than the sensitivity of the receiver with the external LO. This difference is a result of several factors. Firstly, due to the limited frequency resolution of the internal DCO, it can never be configured to generate the carrier at exactly 4 GHz, meaning that a slight frequency offset will always be present. In this case the minimum offset that could be achieved was 10 MHz. The second factor that deteriorates the sensitivity is the phase noise of the ring that after demodulation translates into the amplitude noise of the sub-carrier signal and degrades the SNR. The third factor is the amplitude of the LO signal. In the case of an external LO it was increased to provide the best achievable performance. The amplitude was set to 600 mV peak-to-peak at the receiver LO inputs, which results in approximately 420 mV after the RC-CR circuit. This value is larger than the simulated 300 mV peak-to-peak amplitude, that could be generated by the internal LO. The resulting difference is a small price to pay in order to reduce the power of the DCO, although it still remains the most power-hungry block in the receiver.

Additional degradation of sensitivity is expected as the frequency offset increases, as depicted in Fig. 4.18(b). Each BER curve was measured after incrementing the DCO control word, roughly corresponding to 25 MHz increase in frequency offset. As shown in the previous chapter, the demodulator conversion gain decreases with the increase of the frequency offset. This effect is further emphasized

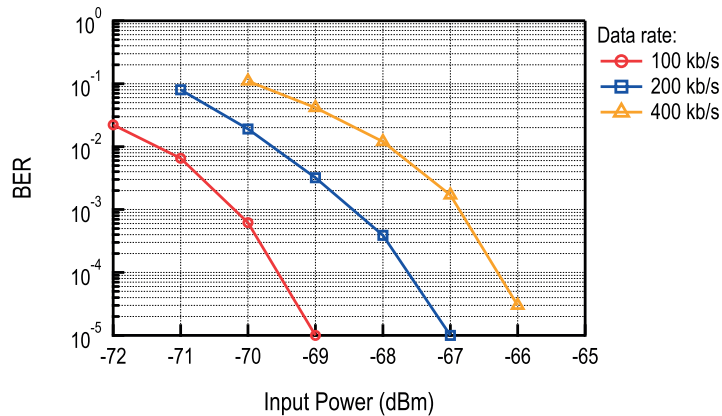


Figure 4.20: BER curves for different data rates.

by the finite bandwidth of the IF amplifier that attenuates the signal amplitude at the edges of the band for a frequency offset above 50 MHz. The effect can be observed in the output waveforms, shown in Fig. 4.19. As the frequency offset increases the demodulated signal further deviates from the sine wave, thus increasing the power contained in the higher harmonics. The final result is the sensitivity degradation of about 5 dB for the frequency offset of 110 MHz. Depending on the maximum sensitivity degradation that can be allowed, the maximum tolerable frequency offset can be defined, which then translates into the maximum period between the two calibrations and the power overhead due to calibration [15].

Although different receiver architectures have been explored, most of them focused only on standard 2-FSK sub-carrier modulation, targeting data rates of 100 kb/s and below. Transmitters proposing higher data rates and higher order M-FSK modulations have been implemented, but the full communication with one of the existing receivers has never been demonstrated. In principle, any kind of modulation can be combined with wideband FM modulation to produce the FM-UWB signal. The proposed receiver can then be used to perform the first FM demodulation, while the subsequent sub-carrier demodulation is performed digitally, by software. Two cases are of interest here, first is increasing data rate, and second is increasing the modulation order.

The BER curves for different data rates are shown in Fig. 4.21. In all cases orthogonal, continuous phase FSK modulation is used. Modulation index is kept constant at 1, meaning that the frequency deviation and the sub-carrier bandwidth increase proportionally to data rate. The limit for the implemented receiver is coming from the bandwidth of the LF amplifier that was intended for operation from 1 MHz to 2.2 MHz. It could easily be extended, at an almost negligible increase in power consumption, if higher data rates are needed. In this case the receiver is tested up to 400 kb/s. As expected, the sensitivity degrades as the data rate increases, but at a slower rate than in the case of narrow-band modulations, where doubling the data rate results in sensitivity shift of 3 dB. This is a consequence of the non-linear wideband FM demodulator characteristic and is typical for FM-UWB.

Measurements in Fig. 4.21 show symbol error rate (SER) results for different FSK modulation orders. The equivalent BER depends on the used coding scheme, and should always be better than the SER. Assuming the same equivalent data rate, increasing modulation order leads to better performance in terms of equivalent BER. This comes at a price of increased sub-carrier signal bandwidth, and demodulator complexity that grows exponentially with the number of bits per symbol. In the reported

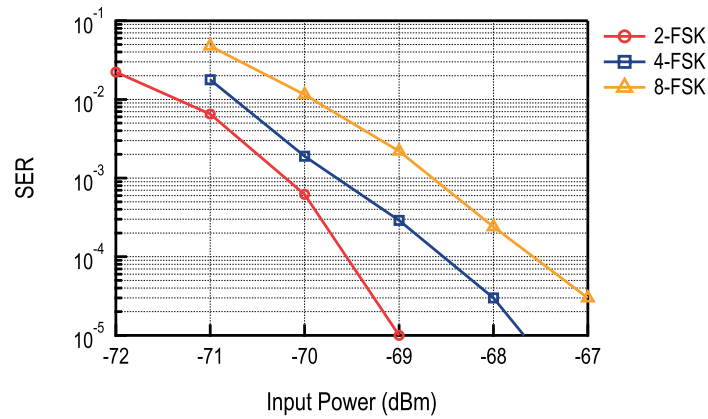


Figure 4.21: BER curves for different modulation order.

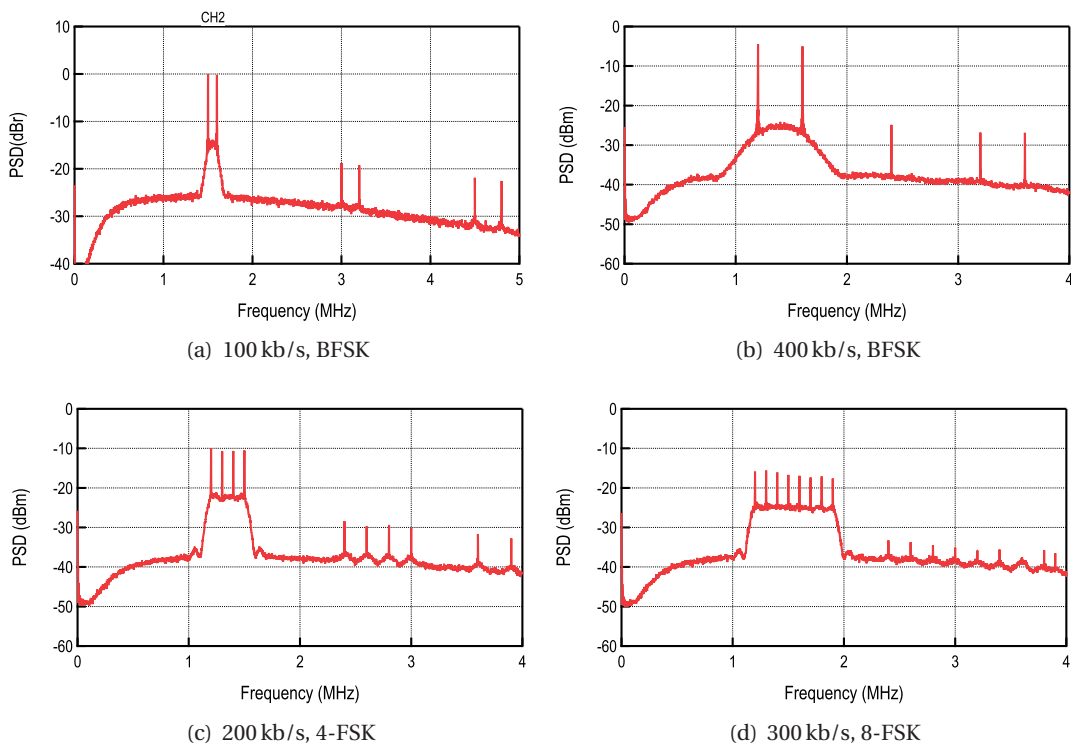


Figure 4.22: Spectrum of the demodulated sub-carrier signal.

measurements, the symbol rate is kept constant at 100 ksym/s, leading to 200 kb/s for 4-FSK and 300 kb/s for 8-FSK modulation. Figure 4.22 shows the sub-carrier spectrum at the output of the FM demodulator, shape and bandwidth depend on the modulation order and data-rate. In principle, the proposed FM-UWB receiver could use different modulations and data rates to conform to channel conditions (e.g. if path loss is low, higher throughput can be achieved) and available sub-carrier bandwidth, and optimize network performance.

The FM-UWB modulation scheme inherently provides some robustness against the narrow-band

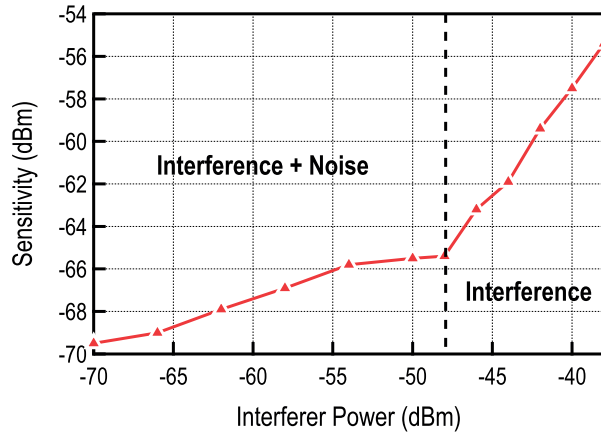


Figure 4.23: Sensitivity as a function of in-band interferer power.

interferers. In the process of demodulation the interferer itself is transformed into a dc component that can be filtered out. The cross product of the interferer and the FM-UWB signal results in a component that is spread over a large bandwidth and effectively increases the noise floor at the receiver output [1]. The performance of this receiver in the presence of a narrow-band interferer is shown in Fig. 4.23. Sensitivity slowly degrades with the increase of interferer power up to -48 dBm. After that point, the interference becomes the dominant factor that causes erroneous reception and sensitivity begins to degrade linearly with the interference power. The lowest SIR that can be tolerated by this receiver is -17 dB (at -48 dBm interferer power) for an interferer frequency offset of 100 MHz from the center frequency.

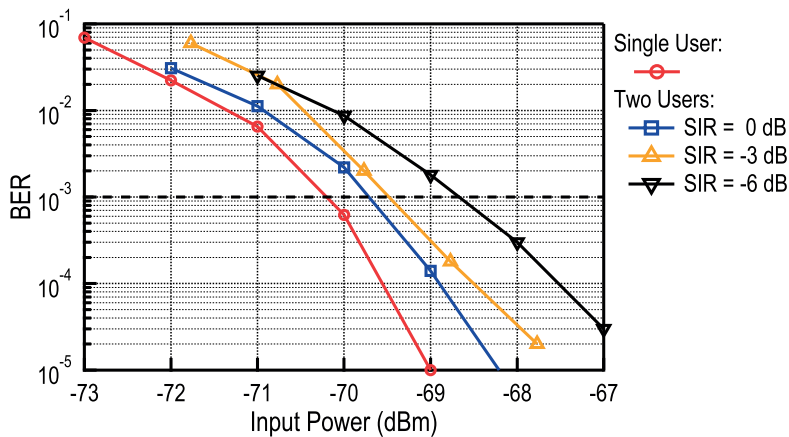


Figure 4.24: BER curves for 2 FM-UWB users and varying input level between the two users.

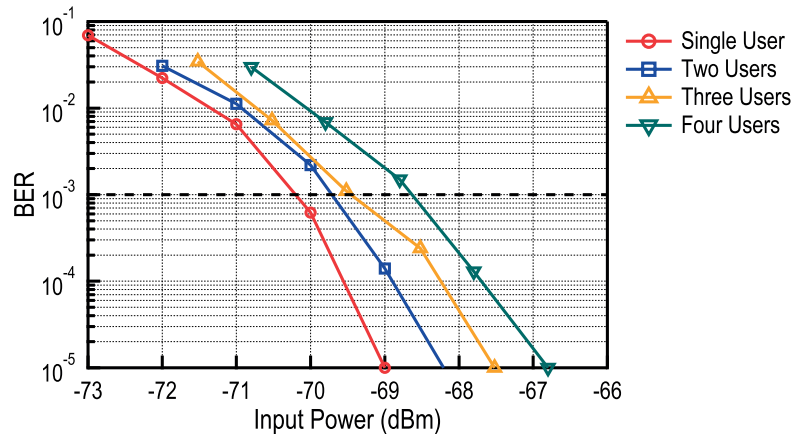


Figure 4.25: BER curves for different number of FM-UWB users.

4.3.3 Multi-User Measurements

As shown previously, multiple FM-UWB signals transmitted in the same RF band can be demodulated simultaneously as long as the sub-carrier frequencies are different. At the demodulator output FSK modulated useful components will be found along with the spread component that is a result of the cross product between two or more FM-UWB signals. Unlike the useful components that can be filtered out in the baseband, the spread component will always be present and will cause the degradation of sensitivity as the power or number of interfering FM-UWB signals increase. The BER curves in the case of two FM-UWB users are presented in Fig. 4.24. The measured sub-carrier channel is the same as in the single user case, centered at 1.55 MHz. Same parameters were used for both channels, 100 kb/s data rate and modulation index of 1, corresponding to sub-carrier bandwidth of 200 kHz. The interfering channel is centered at 1.25 MHz, which provides 100 kHz spacing between the two sub-carrier channels to avoid excessive ACPR. As expected, sensitivity decreases with the increasing power of the interfering FM-UWB signal. The quadratic characteristic of the the demodulator will cause the sensitivity degradation to occur quite rapidly. As an example, a 3 dB stronger interferer at the RF input results in 6 dB stronger FSK sub-carrier in the baseband. In order to tolerate significant difference of power levels, high dynamic range baseband circuitry would be needed together with sharp channel filtering. In this case, channel filtering is performed in the digital domain, using a band-pass FIR filter. Since the interfering signals are not filtered before the analog to digital conversion, receiver dynamic range is limited by the dynamic range of the output buffer. Instead of increasing the dynamic range of the receiver, which would inevitably result in increased power consumption, the problem could be approached at the protocol level by regulating the power on the transmitter side. For the case of HD-WSNs this approach should not carry too much overhead in terms of complexity as the nodes should not move significantly relatively to each other (in comparison with, for example, CDMA in the cellular network).

Just like the inter-user interference increases with the increasing power of the second FM-UWB signal, the increasing number of FM-UWB users will also increase the inter-user interference [16]. Figure 4.25 shows the scenario where the number of users increases from 1 to 4, while the power remains equal in all the channels. The increasing number of channels leads to degraded sensitivity and, just as in the previous case, requires larger dynamic range. Limiting factors to the number of channels, are sub-

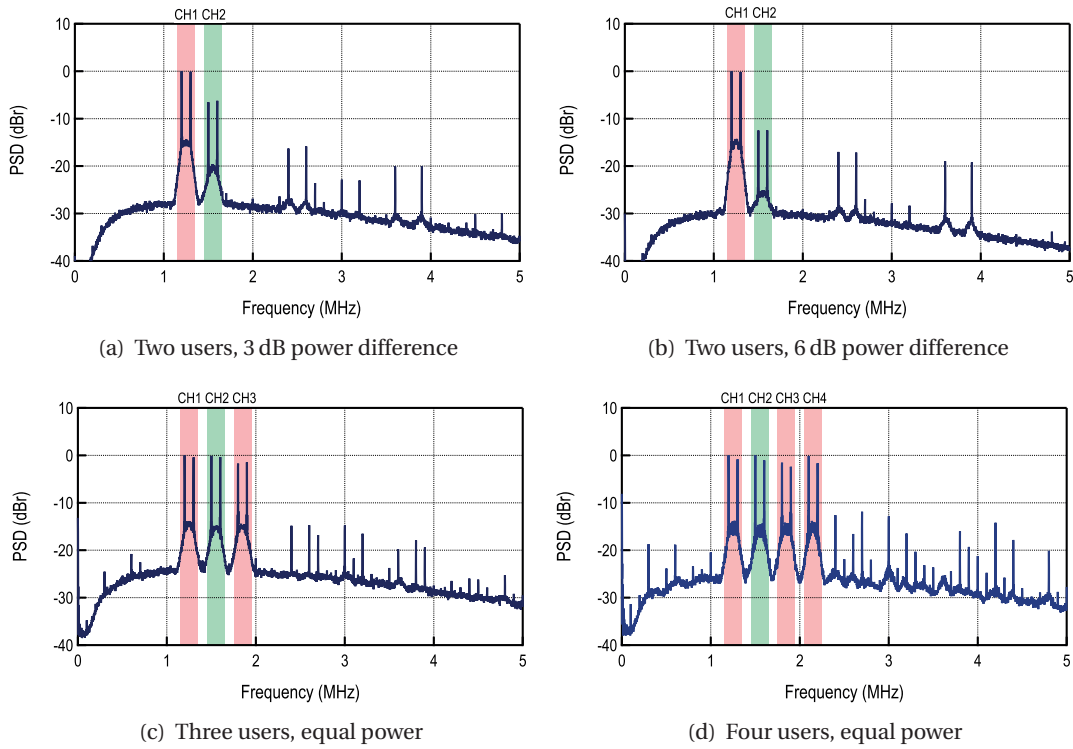


Figure 4.26: Spectrum of the demodulated sub-carrier signal, in different multi-user scenarios.

carrier frequencies, ACLR, channel separation, dynamic range, data rate and inter-user interference. For the given system parameters, 200 kHz wide channels with 100 kHz channel spacing, a maximum of four channels can be used if the lowest sub-carrier channel is located at 1.25 MHz. The demodulator output spectrum is presented in Fig. 4.26 for different multi-user scenarios. The measured channel (channel 2, centered at 1.55 MHz) is highlighted in green, and the interfering channels are highlighted in red. A different number of occupied channels can be observed in different figures. As suspected, it can be seen that the spectrum above 2.3 MHz is polluted by the harmonics of the sub-carrier signals and intermodulation products, thus preventing the placement of additional channels in this band. The harmonics that can be observed in Fig. 4.26 are a combined result of the IF amplifier bandwidth, demodulator bandwidth and the non-linearity of the output buffer.

4.3.4 Multi-Channel Transmission Measurements

The multi-channel (MC) transmission concept was also tested with the implemented receiver. The BER curves for different number of sub-channels are shown in Fig. 4.27. Compared to the case with multiple transmitters, a significant sensitivity loss can be observed. This is a consequence of scaling since the SNR of a single channel is proportional to $1/M^2$, where M is the number of sub-channels. Nevertheless, for short range applications, where distance between nodes does not exceed several meters, such as BAN, the proposed scheme could still be used and could be of particular interest when a large number of nodes are present and need to receive different data simultaneously. The transmitted spectrum is compared in Fig. 4.28 for the cases of a single FM-UWB signal and multiple sub-carrier FM-UWB signal. Since the modulating signal is no longer a triangular waveform, spectral flatness is lost.

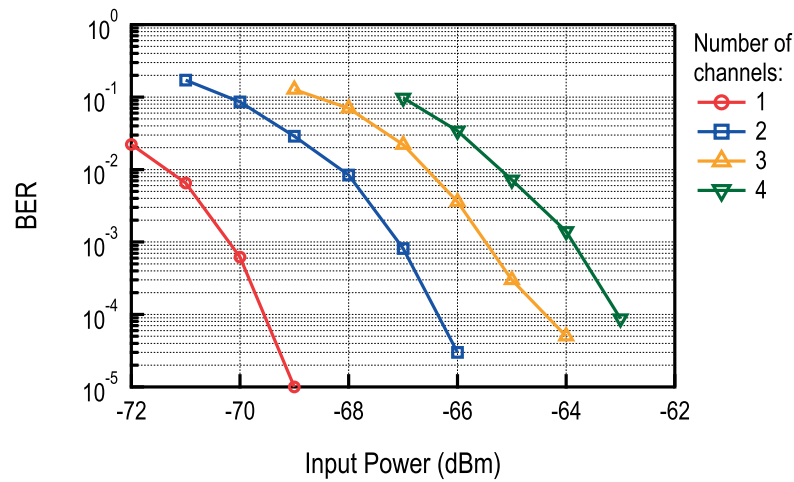


Figure 4.27: BER curves for different number of broadcast sub-channels.

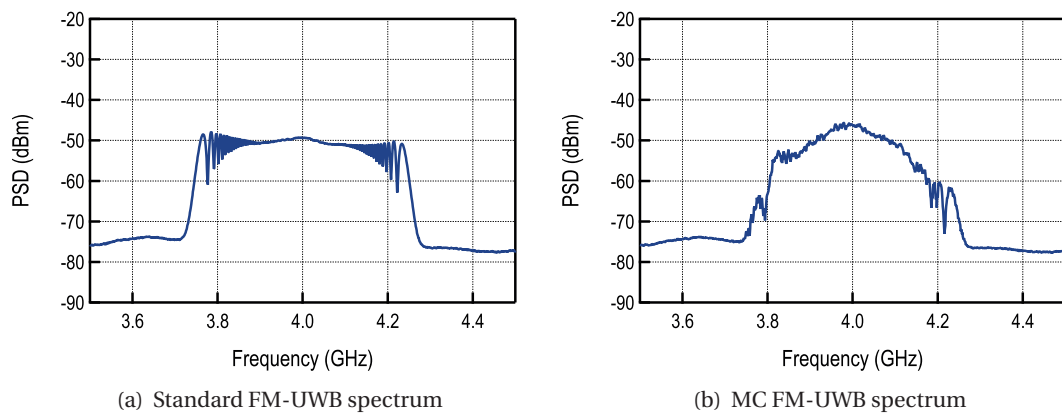


Figure 4.28: Spectrum of the transmitted signal, for the standard FM-UWB and MC FM-UWB

One important difference between SC-FDMA with multiple transmitters and a single transmitter is that, in the latter, sub-channels are perfectly synchronized. For multiple transmitters, even if the orthogonal frequencies are used for different sub-channels, the orthogonality is preserved only if symbols are perfectly synchronized. Since it is practically impossible to synchronize multiple transmitters, sub-channels must be separated and a channel filter is required. In the case of a single transmitter, the sub-channels remain perfectly orthogonal, so there is no need for separation, and hence more channels can be placed in the same sub-carrier band. As long as the orthogonality is maintained, this separation will not influence the BER. In that regard, the proposed FDMA scheme is similar to the Orthogonal Frequency Division Multiplexing (OFDM) combined with the FM-UWB spread spectrum technique. The spectrum of the demodulated sub-carrier signal with and without separation is shown in Fig. 4.29. Measured BER was not influenced by the channel separation.

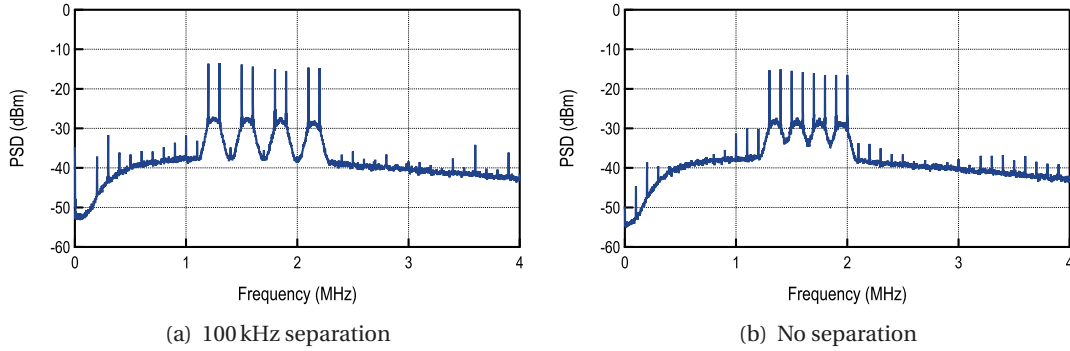


Figure 4.29: Demodulated signal spectrum, with and without spacing between adjacent sub-channels

4.4 Summary

The proposed receiver is compared to the State-of-the-Art receivers in Table 4.2. Of all the implemented FM-UWB receivers it consumes the lowest amount of power while still attaining sufficient sensitivity for short range communications in a HD-WSN. The delay-line demodulator based receivers from [13, 12] have an order of magnitude higher power consumption. The receiver in [17] achieves comparable consumption while providing better sensitivity. The low power consumption is obtained by using a narrow-band amplifier at the input. Since the demodulation is performed using a high-Q RF filter, with a very non-linear FM-AM conversion characteristic, it will not be possible to distinguish between different FM-UWB users. A modification of a regenerative receiver was proposed in [18] that uses two RF filter paths to achieve better linearity and loosen the Q constraints, but it consumes 3.8 mW. This receiver could potentially be utilized in a multi-user scenario, however this capability was not demonstrated. The same receiver architecture was used to demodulate a Chirp-UWB signal in [19]. Even though the receiver consumes a peak power of 4 mW, the average power is decreased to 0.6 mW by employing duty cycling. The receiver proposed here already consumes lower power in continuous operation, however, by applying the same duty-cycling technique its power consumption could be reduced below 200 μ W, which might be addressed in future research.

Table 4.2: Comparison with the state-of-the-art receivers

Parameter	[13]	[12]	[18]	[19]	[17]	This Work
SC-FDMA	Yes	Yes	-	No	No	Yes
Demodulator	DL	DL	Regen.	Regen.	Regen.	DL
Frequency	7.5 GHz	4 GHz	3.75 GHz	8 GHz	4 GHz	4 GHz
Power Conns.	9.1 mW	10 mW	3.8 mW	0.6 mW	580 μW	423 μW
Supply	1.8 V	2.5 V	1 V	1 V	1 V	1 V
Max. Data Rate	50 kb/s	62.5 kb/s	100 kb/s	1 Mb/s	100 kb/s	400 kb/s
Sensitivity	-88 dBm	-46 dBm	-78 dBm	-76 dBm	-80.5 dBm	-70 dBm
Efficiency	182 nJ/b	160 nJ/b	38 nJ/b	0.6 nJ/b	5.8 nJ/b	1.06 nJ/b
Technology	0.25 μ m	0.18 μ m	65 nm	65 nm	65 nm	65 nm
	BiCMOS	BiCMOS	CMOS	CMOS	CMOS	CMOS

Aside from the low power achieved, the proposed receiver offers the capability for several FM-UWB users to communicate in the same RF band at the same time. In an environment where a lot of nodes

need to operate in a small area, SC-FDMA can provide more flexibility for protocol optimization, and lead to lower latency by allowing multiple nodes to communicate at the same time. The only two other receiver implementations offering the same capability require an order of magnitude higher power, thus making the proposed receiver a better solution for the given scenario. In addition, the implemented receiver could support different data rates and different M-FSK modulations. With a flexible digital baseband it would be possible to dynamically adjust the number of channels and data rate per channel, allowing to further optimize network performance.

References

- [1] J. F. M. Gerrits, M. H. L. Kouwenhoven, P. R. van der Meer, J. R. Farserotu, and J. R. Long, "Principles and limitations of ultra-wideband FM communications systems," *EURASIP J. Appl. Signal Process.*, vol. 2005, pp. 382–396, Jan. 2005.
- [2] A. Shameli and P. Heydari, "A novel ultra-low power (ULP) low noise amplifier using differential inductor feedback," in *2006 Proceedings of the 32nd European Solid-State Circuits Conference*, Sept. 2006, pp. 352–355.
- [3] A. C. Heiberg, T. W. Brown, T. S. Fiez, and K. Mayaram, "A 250 mv, 352 μ W GPS receiver RF front-end in 130 nm CMOS," *IEEE Journal of Solid-State Circuits*, vol. 46, no. 4, pp. 938–949, April 2011.
- [4] T. Taris, J. Begueret, and Y. Deval, "A 60 μ W lna for 2.4 GHz wireless sensors network applications," in *2011 IEEE Radio Frequency Integrated Circuits Symposium*, June 2011, pp. 1–4.
- [5] E. M. Cherry and D. E. Hooper, "The design of wide-band transistor feedback amplifiers," *Electrical Engineers, Proceedings of the Institution of*, vol. 110, no. 2, pp. 375–389, Feb. 1963.
- [6] C. Holdenried, J. Haslett, and M. Lynch, "Analysis and design of HBT Cherry-Hooper amplifiers with emitter-follower feedback for optical communications," *IEEE Journal of Solid-State Circuits*, vol. 39, no. 11, pp. 1959–1967, Nov. 2004.
- [7] C. D. Holdenried, M. W. Lynch, and J. W. Haslett, "Modified CMOS Cherry-Hooper amplifiers with source follower feedback in 0.35 μ m technology," in *Solid-State Circuits Conference, 2003. ESSCIRC '03. Proceedings of the 29th European*, Sept. 2003, pp. 553–556.
- [8] N. Saputra and J. Long, "A Fully-Integrated, Short-Range, Low Data Rate FM-UWB Transmitter in 90 nm CMOS," *IEEE Journal of Solid-State Circuits*, vol. 46, no. 7, pp. 1627–1635, July 2011.
- [9] M. Grozing, B. Phillip, and M. Berroth, "CMOS ring oscillator with quadrature outputs and 100 MHz to 3.5 GHz tuning range," in *Solid-State Circuits Conference, 2003. ESSCIRC '03. Proceedings of the 29th European*, Sept. 2003, pp. 679–682.
- [10] E. J. Pankratz and E. Sanchez-Sinencio, "Multiloop high-power-supply-rejection quadrature ring oscillator," *IEEE Journal of Solid-State Circuits*, vol. 47, no. 9, pp. 2033–2048, Sept. 2012.
- [11] J. Chabloz, D. Ruffieux, and C. Enz, "A low-power programmable dynamic frequency divider," in *Solid-State Circuits Conference, 2008. ESSCIRC 2008. 34th European*, Sept. 2008, pp. 370–373.
- [12] J. Gerrits, J. Farserotu, and J. Long, "A wideband FM demodulator for a low-complexity FM-UWB receiver," in *The 9th European Conference on Wireless Technology, 2006*, Sept. 2006, pp. 99–102.
- [13] Y. Zhao, Y. Dong, J. F. M. Gerrits, G. van Veenendaal, J. Long, and J. Farserotu, "A short range, low data rate, 7.2 GHz-7.7 GHz FM-UWB receiver front-end," *IEEE Journal of Solid-State Circuits*, vol. 44, no. 7, pp. 1872–1882, July 2009.
- [14] E. A. Vittoz and O. Neyroud, "A low-voltage cmos bandgap reference," *IEEE Journal of Solid-State Circuits*, vol. 14, no. 3, pp. 573–579, June 1979.
- [15] N. Pletcher, S. Gambini, and J. Rabaey, "A 52 μ W wake-up receiver with 72 dBm sensitivity using an Uncertain-IF architecture," *IEEE Journal of Solid-State Circuits*, vol. 44, no. 1, pp. 269–280, Jan.

2009.

- [16] J. M. F. Gerrits, J. R. Farserotu, and J. R. Long, "Multi-user capabilities of UWBFM communications systems," in *2005 IEEE International Conference on Ultra-Wideband*, Sept. 2005.
- [17] N. Saputra, J. Long, and J. Pekarik, "A low-power digitally controlled wideband FM transceiver," in *2014 IEEE Radio Frequency Integrated Circuits Symposium*, June 2014, pp. 21–24.
- [18] F. Chen, W. Zhang, W. Rhee, J. Kim, D. Kim, and Z. Wang, "A 3.8-mW 3.5-4-GHz regenerative FM-UWB receiver with enhanced linearity by utilizing a wideband LNA and dual bandpass filters," *IEEE Transactions on Microwave Theory and Techniques*, vol. 61, no. 9, pp. 3350–3359, Sept. 2013.
- [19] F. Chen, Y. Li, D. Liu, W. Rhee, J. Kim, D. Kim, and Z. Wang, "A 1mW 1Mb/s 7.75-to-8.25GHz chirp-UWB transceiver with low peak-power transmission and fast synchronization capability," in *2014 IEEE International Solid-State Circuits Conference Digest of Technical Papers (ISSCC)*, Feb. 2014, pp. 162–163.
- [20] J. Farserotu, J. Baborowski, J. D. Decotignie, P. Dallemagne, C. Enz, F. Sebelius, B. Rosen, C. Antfolk, G. Lundborg, A. Björkman, T. Knieling, and P. Gulde, "Smart skin for tactile prosthetics," in *2012 6th International Symposium on Medical Information and Communication Technology (ISMICT)*, March 2012, pp. 1–8.
- [21] Y. Dong, Y. Zhao, J. F. M. Gerrits, G. van Veenendaal, and J. Long, "A 9 mW high band FM-UWB receiver front-end," in *Solid-State Circuits Conference, 2008. ESSCIRC 2008. 34th European*, Sept. 2008, pp. 302–305.
- [22] N. Saputra and J. R. Long, "A fully integrated wideband FM transceiver for low data rate autonomous systems," *IEEE Journal of Solid-State Circuits*, vol. 50, no. 5, pp. 1165–1175, May 2015.
- [23] —, "A short-range low data-rate regenerative FM-UWB receiver," *IEEE Transactions on Microwave Theory and Techniques*, vol. 59, no. 4, pp. 1131–1140, April 2011.
- [24] V. Kopta, D. Barras, and C. Enz, "A 420 μ W, 4 GHz approximate zero IF FM-UWB receiver for short-range communications," in *2016 IEEE Radio Frequency Integrated Circuits Symposium*, May 2016, pp. 218–221.
- [25] V. Kopta, D. Barras, and C. C. Enz, "An approximate zero IF FM-UWB receiver for high density wireless sensor networks," *IEEE Transactions on Microwave Theory and Techniques*, vol. 65, no. 2, pp. 374–385, Feb. 2017.

5 FM-UWB Transceiver

The previous chapter dealt in details with the implementation of the quadrature approximate zero-IF receiver. The next step is to integrate a full FM-UWB transceiver. Aside from the quadrature AZ-IF receiver, that provides the multi-user communication capability, the single-ended receiver is added, and can be used to reduce the power consumption of the transceiver when lower performance is acceptable. Furthermore, the integrated transceiver includes a baseband that performs the sub-carrier FSK demodulation and symbol clock recovery, and provides fully digital outputs that can be interfaced by an FPGA or a microcontroller. Although there are no major architectural innovation on the transmitter side, the clever use of circuit techniques provides means for some improvements compared to the state of the art in terms of power consumption and efficiency. The emphasis is on the fully integrated output matching network, that allows to use the same RF pad for both reception and transmission, eliminating the need for an external switch or any other passive components.

First, the top level architecture of the transceiver is described. Then, in the following section, the details of transmitter circuit implementation are given, followed by the circuit implementation of the two receivers in section 5.3. The results of transceiver characterization are presented in section 5.4, demonstrating the capabilities of the proposed approach with emphasis on robustness and low power consumption. Finally, the chapter is concluded with the summary of performance and comparison with the state of the art.

5.1 Transceiver Architecture

The implemented FM-UWB transceiver consists of two receivers and a transmitter (Fig. 5.1). Aside from low power consumption, the emphasis of this work is also on high level of integration and miniaturization, robustness to narrowband interferers and tolerance to reference frequency offset. A single RF pad is used as both receiver input and transmitter output, eliminating the need for an off-chip switch that was needed in all the previous implementations found in the literature. In addition, the matching network is fully integrated and no passive components need to be added externally.

Wires needed to provide power to sensor nodes in the *WiseSkin* system pose a reliability issue and

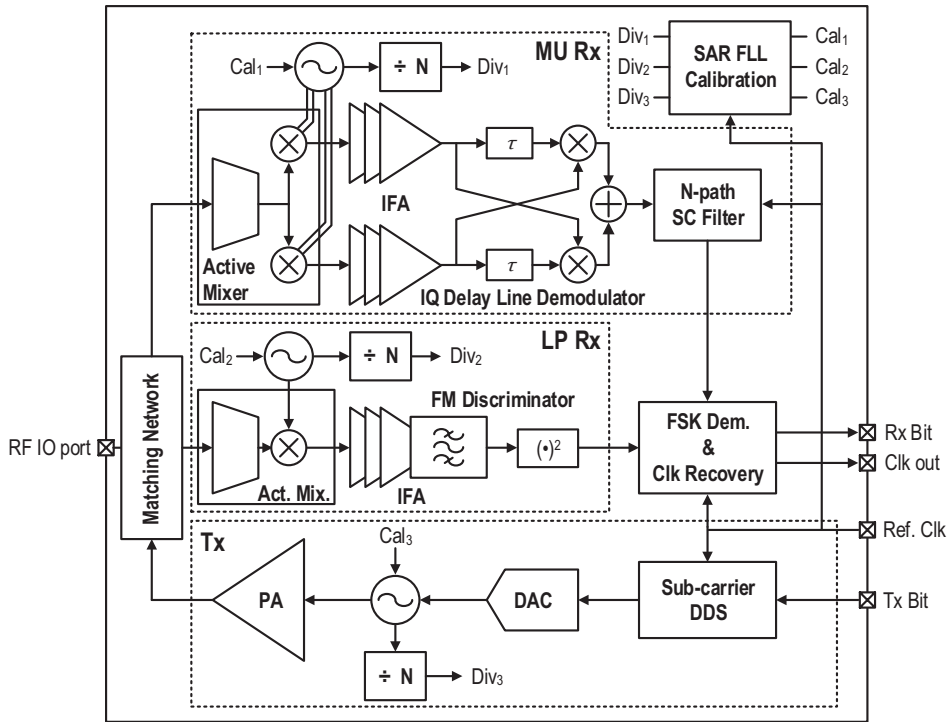


Figure 5.1: Top-level block diagram of implemented transceiver.

increase the cost and production complexity. The consumption of the FM-UWB is still not low enough to use some form of energy harvesting, however, a dedicated wireless powering system might be feasible. Power consumption below 1 mW is already good enough, provided that the FM-UWB transceiver can operate in the presence of a strong interfering signal intended to provide power. The coexistence of the powering and the communication signal would allow batteryless operation, as the two could be done simultaneously. Fortunately, the proposed architecture offers very good rejection of out of band interferers owing to the steep 6th order filtering characteristic of the IF amplifiers. In this case, a scenario is presented with a 2.4 GHz signal intended for providing power, demonstrating the capabilities of the proposed architecture.

Large signal bandwidth of the FM-UWB signal means that the transceiver inherently possesses some robustness against the RF carrier frequency offsets. In the baseband section of the receiver, a relatively small offset (e.g. less than 0.5 %) between the transmit and the receive symbol clock can be compensated using a simple clock recovery scheme. As a result, there is no need for a precise frequency reference in the system and no need for a crystal oscillator. Instead, an RC reference oscillator can be integrated on-chip and calibrated before use, allowing to completely remove all the external components.

Just like in the previous section, the LO signal is generated using ring oscillators. Owing to the loose phase noise constraints and the large signal bandwidth, such an approach is acceptable and is exploited to reduce the receiver power consumption. Normally, ring oscillators operate in a loop that stabilizes the oscillation frequency (PLL), however here they are used in a free-running mode so as to reduce the significant power overhead that would otherwise be present due to continuous operation of frequency

dividers. Instead, the oscillators are periodically calibrated using a successive approximation register (SAR) FLL, assuring that the frequency offset remains within the required limits.

The transmitter architecture is similar to other implementations found in literature. The sub-carrier signal is synthesized digitally, allowing easier control and switching of sub-carrier frequencies, as well as better precision compared to an analog solution with a capacitor bank. The sub-carrier signal is used to drive a current DAC that controls the DCO frequency, that finally produces the desired FM-UWB signal. The resulting signal is then amplified by the preamplifier (PPA) and the power amplifier (PA) before transmission.

The two implemented receivers are intended for two modes of operation. The multi-user (MU) receiver consumes more power and is capable of distinguishing multiple FM-UWB signals and providing SC-FDMA. Its purpose is to provide multiple channels and speed up communication when network traffic is high. It is based on the receiver described in the previous section with the addition of the channel filtering and baseband processing. The low power (LP) receiver provides a low power, low performance mode, that can be used when the network traffic is low and a single channel is sufficient. Instead of quadrature demodulation, it only uses a single branch, allowing to simplify the receiver architecture and save power. However, due to the non-linearity of the frequency-to-amplitude conversion characteristic of the demodulator, it cannot distinguish multiple channels allowing only a single FM-UWB user.

5.2 Transmitter Implementation

A more detailed block diagram of the transmitter is given in Fig. 5.2. The DCO is in fact driven by two DACs. The first one, referred to as the static DAC, only determines the highest frequency in the FM-UWB signal spectrum f_H . Its output remains constant during transmission. The second DAC, or the dynamic DAC, is driven by the digital sub-carrier signal and controls instantaneous frequency of the DCO, and hence all the modulation characteristics. Two DACs are calibrated prior to transmission using an on-chip SAR FLL. In the first step the static DAC is calibrated to set f_H . In the second step the dynamic DAC is calibrated to set the FM-UWB signal bandwidth. The third DAC is added for testing purposes. It is an exact copy of the dynamic DAC that provides the sub-carrier signal at its output, allowing to verify the correct operation of the SC-DDS and to measure the sub-carrier frequency.

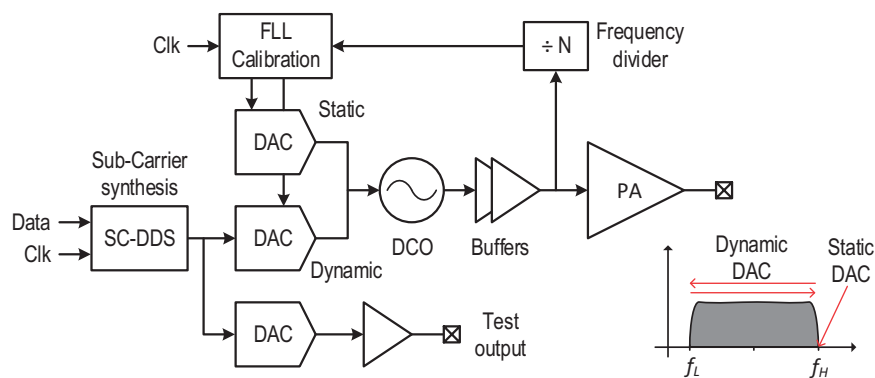


Figure 5.2: Block diagram of the implemented transmitter.

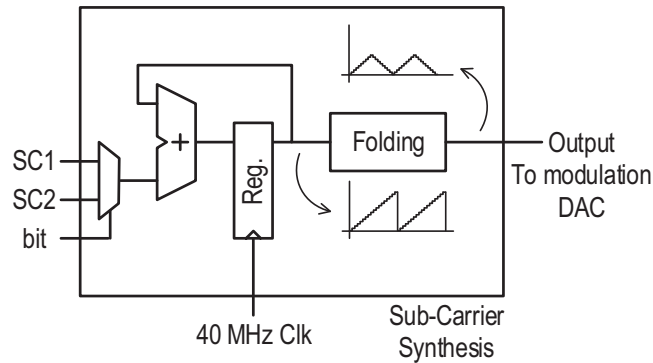


Figure 5.3: Digital sub-carrier synthesizer.

The DCO is separated from the PA and frequency dividers by buffers. These buffers prevent frequency pulling that might be caused by an outside signal, or by the change in capacitance value in the on and off state of the frequency divider. The frequency divider is implemented in the same way as in the receiver described in the previous chapter. It is a chain of ten divide-by-2 circuits from [1] that provide the signal for calibration. The divider buffer, that is needed to amplify the DCO signal and provide the rail-to-rail swing at its output, is adjusted here for a single-ended input.

5.2.1 Sub-Carrier Synthesis

The sub-carrier synthesizer is a fully digital block that provides a 6 bit value at its output. This implementation is following the principles described in [2] The sub-carrier signal is generated in two steps. First, an accumulator generates a saw-tooth waveform, and then in the second step this saw-tooth waveform is folded to produce a triangular waveform. The frequency of the sub-carrier is controlled by controlling the slope of the saw-tooth waveform, or equivalently the increment value of the accumulator (SC1 and SC2 in Fig. 5.3). The sub-carrier frequency is given by:

$$f_{sc} = f_{clk} \frac{M}{2^N}, \quad (5.1)$$

where f_{clk} is the input clock frequency, N is the number of bits of the accumulator, and M is the increment. Although only 6 bits are used to control the DAC, 16 bits are used for the accumulator to provide the needed frequency resolution. Nominal clock frequency is 40 MHz, which results in frequency resolution of approximately 600 Hz, which is more than enough to generate a 100 kb/s FSK signal with a modulation index of 1. No pulse shaping or filtering is used in this implementation. Compared to fully analog implementations, such as those described in [3, 4], DDS approach requires slightly more power. However, since the SC synthesizer consumption is typically small compared to other blocks in the transmitter, this overhead is negligible, and DDS provides better frequency precision (relative to the reference clock) and easier control, both highly desirable especially in a multi-user scenario.

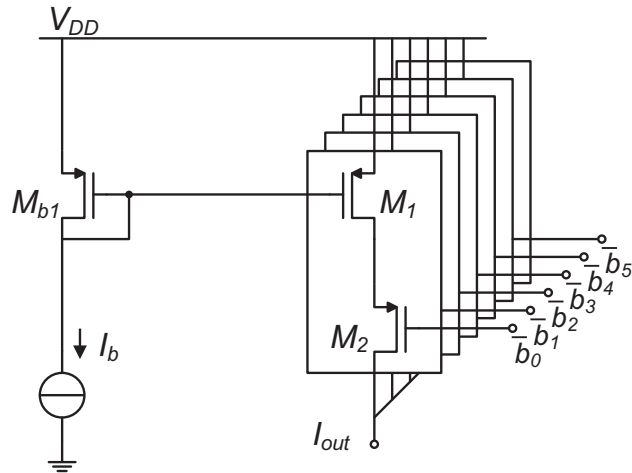


Figure 5.4: Static DCO current DAC.

5.2.2 DCO Digital to Analog Converters

Two current mode digital to analog converters are used to drive the current starved ring oscillator, as explained previously. The static DAC is used to set the high frequency of the FM-UWB signal f_H and the dynamic DAC is used to generate the FM-UWB modulation.

Static DAC is shown in Fig. 5.4. Digital control word can be either written manually, using the SPI bus, or a calibration loop can be used to set the register value. Once set, the control word remains constant throughout the transmission. Therefore, there are no specific constraints regarding speed or glitches, and a relatively simple solution can be used. Six bits (b_0 - b_5) control the binary weighted current mirror that provides the bias current of the ring oscillator. Although linearity is not paramount for the static DAC, a relatively good characteristic is obtained (as shown in Fig. 5.9). The only requirement of this DAC is monotonicity of the characteristic, that is needed to assure the proper functionality of the SAR FLL calibration scheme. Considering that only 6 bits are used, no special matching techniques are necessary to achieve the desired precision.

The dynamic DAC is shown in Fig. 5.5. This DAC is actually sinking current from the static DAC. As the value of the digital control word increases, so does the current, effectively reducing the bias current of the oscillator and consequently its frequency. This approach keeps current of the static source constant and provides the good linearity needed for FM-UWB signal generation. As opposed to the static DAC, cascode current mirror is used here, in order to provide better precision of the output current. The dynamic DAC is controlled by the digital sub-carrier signal, which means that it must operate at the clock frequency of 40 MHz, even though the sub-carrier frequency is below 2.5 MHz. For this reason, the current steering approach is used. In this way the bottom reference transistors M_3 and M_4 never switch off, and there is no additional delay coming from the time required for transistors to turn on (time it takes to charge gate capacitance through the bias transistors M_{b1} and M_{b2}). As a consequence, this technique produces smaller glitches at the output. A capacitor is placed at the output of the two DACs to filter the DCO current and avoid sharp pulses in DCO supply current.

Bandwidth of the FM-UWB signal is controlled using the reference current I_b . The sub-carrier DDS

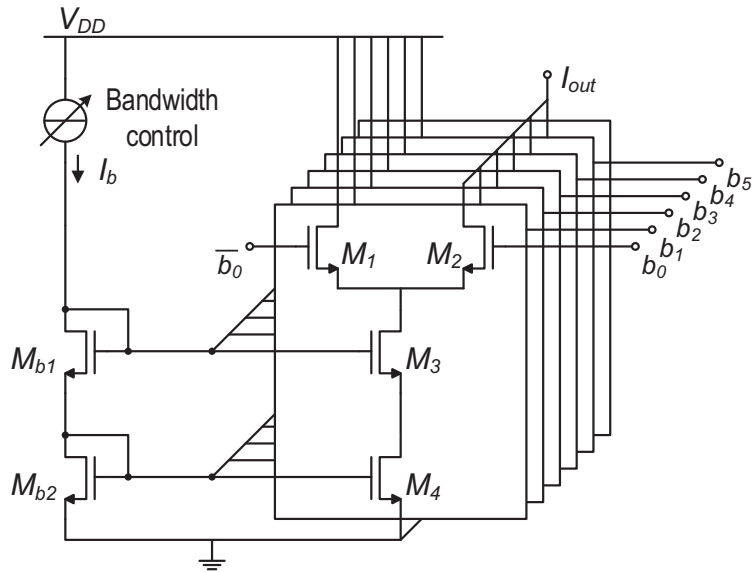


Figure 5.5: Dynamic DCO current steering DAC.

signal always produces a full scale DAC output (all 6 bits are used), and the reference current determines the maximum value of the current, and subsequently the lower frequency f_L . The reference current is generated using yet another current DAC (again static during transmission), with a 5 bit resolution. To calibrate the reference current, bits b_0 to b_5 are all set to '1', resulting in the maximum output current, and then the SAR FLL sets the control bits of the reference current DAC to provide the desired lower frequency f_L . In this way FM-UWB bandwidth is entirely decoupled from the sub-carrier generation.

As explained above, an exact replica of the dynamic DAC is added for testing. This DAC is driven from the same SC DDS circuit, and will add additional capacitive load to its output. However, since the consumption of the SC DDS remains negligible compared to the DCO and the PA, presence of the testing circuits will not have a significant impact on the overall power consumption. The test DAC drives a buffer that provides analog sub-carrier signal at its output. Resistor R_1 converts the DAC output current into the input voltage of the buffer. This buffer is shown in Fig. 5.6. Its main purpose is to verify the sub-carrier frequency. It consists of a resistively degenerated differential pair and a source follower that provides a low impedance output capable of driving a 10 pF capacitive load. Bias current and bandwidth of the source follower are set by the external resistor R_{ext} .

5.2.3 DCO

The implemented transmitter DCO is shown in Fig. 5.7. Since only a single-ended output is needed, the simplest topology, that consequently consumes the lowest amount of power for a given frequency of oscillation, is used. The three inverters of the ring oscillator are scaled progressively, with increasing transistor width from left to right (for both NMOS and PMOS). This was done to increase the driving capability of the inverter driving the buffer, without increasing the overall power consumption. A ring

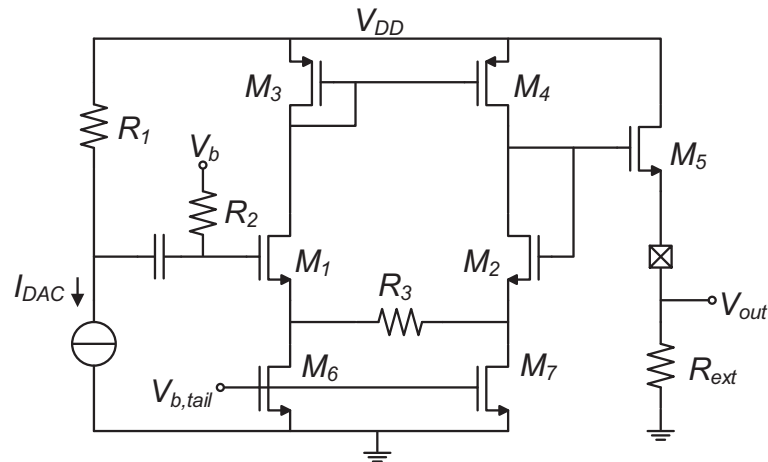


Figure 5.6: Dynamic DAC test output buffer.

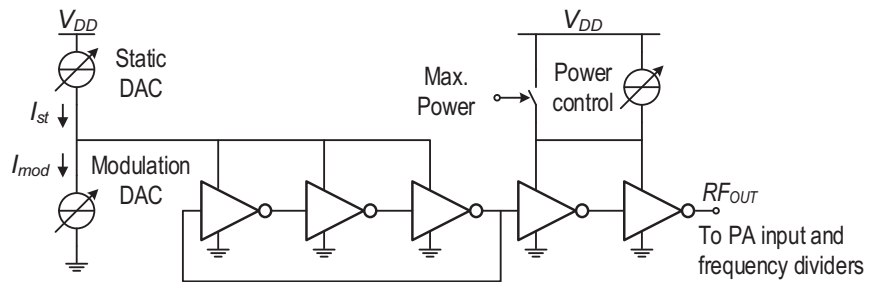


Figure 5.7: Transmitter DCO with buffers.

oscillator that is not fully symmetric, i.e. with different stages, generally exhibits higher phase noise [5]. However, in this case symmetry is already broken by the presence of the buffer, and phase noise is not a limiting factor due to the large signal bandwidth, allowing to concentrate on power reduction.

Buffers are placed between the DCO on one side and preamplifier and frequency divider driver on the other. Since the input capacitance of the driver changes in on and off state, buffer is needed to avoid frequency shift after calibration. In addition, it provides isolation in order to avoid frequency pulling if a strong external signal is present. The buffer inverters are current starved, allowing to control the output amplitude by controlling the supply current. There is also a possibility to bypass the current source and connect the buffers directly to the supply voltage, providing the maximum amplitude. Driver of the frequency divider (shown in Fig. 5.8) is needed to amplify the DCO output and provide a rail-to-rail signal. It is designed to provide a rail-to-rail signal for a minimum input amplitude of 10 mV, at 5.5 GHz. It consists of 5 inverter stages, two of which are self biased using a large resistor. Since the driver will be on only when calibration is needed it will not contribute significantly to the overall power consumption.

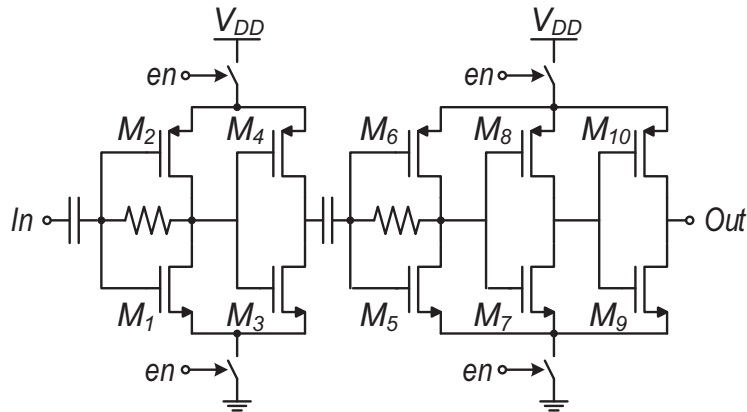


Figure 5.8: Schematic of the frequency divider buffer.

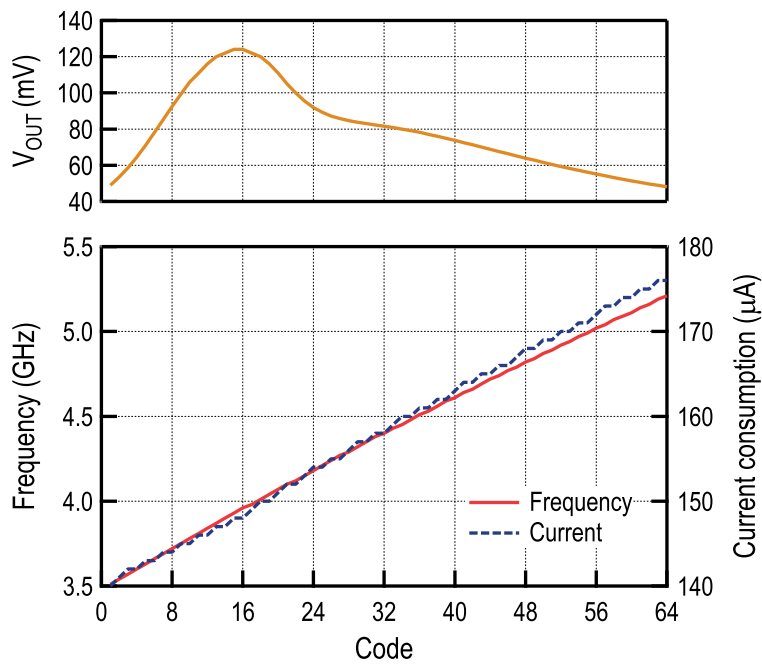


Figure 5.9: Simulated DCO frequency, current consumption and output voltage amplitude.

Figure 5.9 shows simulated frequency, current consumption and output amplitude of the designed DCO, including the two buffer inverters. Resonant load at the preamplifier input is used to boost the signal amplitude close to 4 GHz. The DCO covers the range from 3.5 GHz to 5.2 GHz, and with the 6 bit DAC, this results in frequency resolution of roughly 25 MHz. At 4 GHz, the DCO consumes 150 μW , for a 120 mV signal amplitude at the output. The linearity of the DCO is sufficient for the generation of the FM-UWB signal, and does not cause notable distortion in the output spectrum.

5.2.4 Preamplifier and Power Amplifier

The output stage of the transmitter consumes the largest portion of power and is therefore the most critical for the overall performance. As any other FM modulation, the FM-UWB is a constant envelope modulation, meaning that there is no need for use of special techniques such as outphasing, envelope elimination and restoration, adaptive biasing etc. However, low constraint in terms of output power (maximum output power is below -10 dBm), combined with large bandwidth of the FM-UWB signal, result in more complex output matching network, and consequently lower achievable efficiency.

Design of a power amplifier for low output power poses specific challenges, usually different than those seen in more common applications. Generally, for every power amplifier there is an optimal load impedance that results in highest efficiency for a given output power. Consider a PA that needs to provide 20 dBm output power. For a 50 Ω load this translates into a voltage swing of more than 6 V peak to peak. This becomes difficult to achieve in deep sub-micron technologies with a low supply voltage, and a matching network is required that will lower the load impedance to the optimal value, much smaller than 50 Ω . For the case of FM-UWB, the maximum output power is limited to -10 dBm, which translates into a 200 mV swing over a 50 Ω load. In this case the optimal impedance seen from the PA needs to be higher than the load, and the matching network instead needs to boost the load impedance to maximize efficiency. This adds different constraints and changes the design approach compared to the first case. The second important difference between the high and low power PA design is in the driving circuits. At 20 dBm output power, driving circuits will consume only a small portion of the overall power, and will not affect the efficiency significantly. They become much more important when the output power becomes comparable to the consumption of the driving circuit and may greatly affect the choice of the PA class of operation.

In most mid and high power applications, with a constant envelope modulation, class E PA is commonly used as the most efficient solution. To achieve high efficiency, such PA requires a matching network precisely tuned to a certain frequency. Achieving high efficiency over a wide bandwidth (500 MHz in this case) becomes a difficult task with class E. Additionally, class E and other switching PAs have very high driving requirements, which pose problems for the driving circuits at low output power levels. For proper class E operation the switch needs to be driven with a full swing rectangular signal, with very short transition times, in order to minimize switching losses. In addition, the efficiency of every switching PA is inversely proportional to the switch on resistance. This condition sets a limit to the minimum size of the PA transistor and consequently sets its input capacitance. Since the driver consumption is proportional to fCV_{DD}^2 , at 4 GHz and -10 dBm output power, it will become comparable to the PA consumption, resulting in significant overall efficiency penalty. For this reason, linear power amplifiers are a better choice for this application.

For the proper choice of a linear PA, its efficiency must be taken into account together with the needed input signal amplitude. Going from class A to class C, the conduction angle of the PA decreases, and the efficiency increases. However, to maintain the same output power, the input signal must increase its amplitude at lower conduction angles, thus imposing higher driving requirements. Higher input amplitude means higher preamplifier consumption (proportional to the square of the amplitude). A good trade-off between driving requirements and PA efficiency is a class AB amplifier and is therefore used in this design.

As explained previously, for -10 dBm output power and 1 V supply, optimal impedance seen from the PA is proportional to V_{DD}^2/P_{out} , which is in this case much larger than 50 Ω [6, 7]. The matching network that will implement this ratio is difficult to implement on chip due to the limited quality factor and

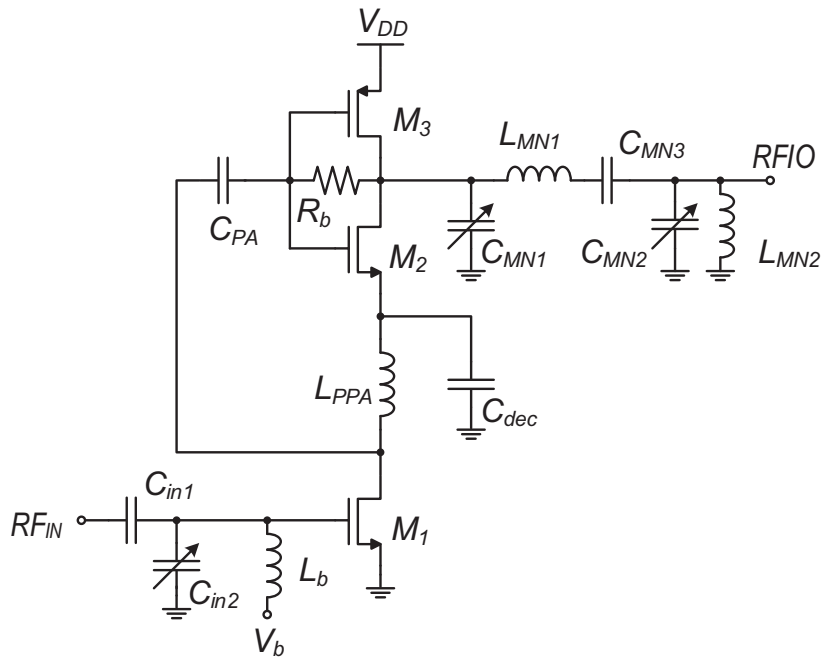


Figure 5.10: Preamplifier and power amplifier schematic.

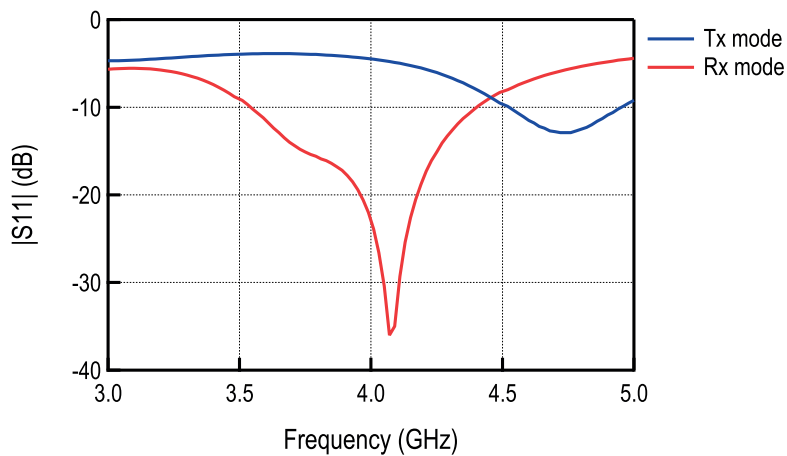


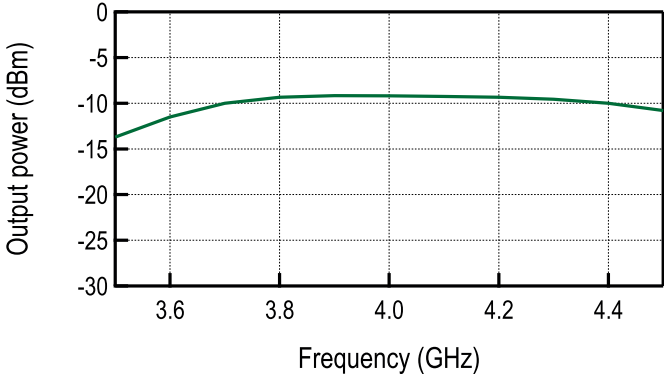
Figure 5.11: Simulated S_{11} parameter at the RF IO.

limited inductance value of the integrated inductors. The problem can be solved by lowering the supply voltage which consequently lowers the optimal impedance and the transformation ratio. Instead of using a separate circuit to lower the supply voltage (such as a DC-DC converter) preamplifier and the PA can be stacked (similarly to the approach from [3]). At the same time this simplifies the matching network, as the equivalent PA supply is reduced, and saves power since the preamplifier reuses the bias current of the PA.

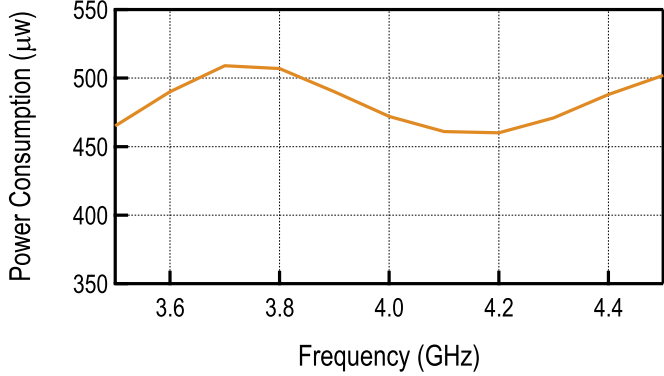
The designed output stage, with the preamplifier and the main PA is shown in Fig. 5.10. Capacitors C_{in1} and C_{in2} , together with the inductor L_{PPA} provide the resonant load for the DCO buffer in order to boost the amplitude around 4 GHz. Capacitor C_{in2} can be tuned to compensate for process variations. Bias current of the entire stage is determined by the bias point of the PPA transistor M_1 . Just like the main PA, the PPA is also biased in class AB. Output power can be controlled by controlling the bias point of M_1 . Filter that consists of the RF choke L_{PPA} and a decoupling capacitor C_{dec} provides a steady voltage at the source of M_2 . Depending on the bias current this voltage will vary from 0.3 V to 0.4 V, and is determined by the V_{GS} of M_2 and M_3 . The resonance frequency at the PPA output is determined by the L_{PPA} and the equivalent capacitance seen from the drain of M_1 , which is mainly determined by the C_{PA} and the gate capacitances of M_2 and M_3 . The two resonant frequencies at the input and output of the PPA are offset from 4 GHz in opposite directions in order to provide a relatively constant signal amplitude at the PA input over 500 MHz bandwidth. The main PA is a complementary class AB power amplifier. It is self biased via a 95 k Ω resistor R_b . The PA input amplitude above 250 mV in the desired band is enough to drive the class AB amplifier in saturation and provide a relatively good efficiency. Output matching network that consists of inductors $L_{MN1,2}$, and capacitors C_{MN1-3} transforms the output 50 Ω impedance into roughly 700 Ω over the entire band of operation, as seen from the PA output. This is enough to provide an almost rail to rail signal at the PA output (with respect to the PA supply, meaning from 0.3 V to 1 V), that minimizes power dissipation in the two output transistors.

The output matching network is designed together with the matching network of the two LNAs. To simplify the overall design procedure, the LNA is designed to present a capacitive load at the RF IO in the off state. The total capacitive load at the RF IO is determined by the pad capacitance and the two LNAs. Since matching requirements are not the same in the receive and transmit mode, the matching network must be able to adjust to both. This can be achieved by adjusting the capacitance of C_{MN1} and C_{MN2} . The value of C_{MN1} changes from 120 fF to 520 fF in transmit and receive mode. The C_{MN2} is actually set to 0 in the transmit mode. Generally the capacitance at this node (RF IO) should be minimized in order to maximize the efficiency. Inductor L_{MN2} is placed to partially compensate this capacitance and to extend the bandwidth. In the receive mode, the value of C_{MN2} increases to 600 fF. In the actual implementation 3 bits are used to control the two capacitors, the first bit switches from transmit to receive state, and the additional 2 bits allow some frequency tuning, that allows small modifications of the resonance frequencies once the chip is placed on a PCB. Simulated S_{11} parameter at the RF IO port is shown in Fig. 5.11 for the two modes of operation. It can be seen that in the transmit mode the reflection coefficient is quite high, around -5 dBm in the band of interest, and would not provide adequate matching to a 50 Ω antenna. Once the capacitors are switched, the input reflection coefficient drops below -10 dBm from 3.6 GHz to 4.35 GHz.

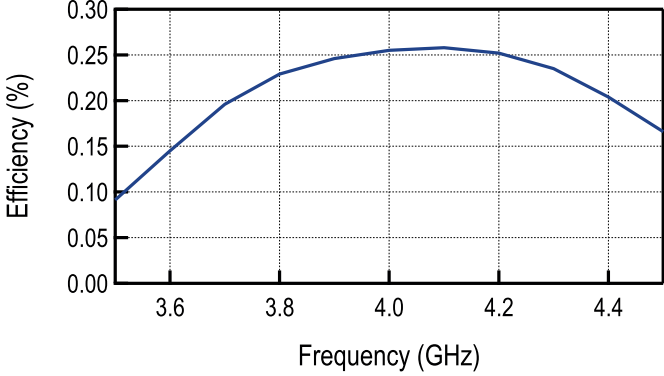
Simulated output power, power consumption and efficiency of the output stage are shown in Fig. 5.12. The shown characteristic of the PA is static in the sense that the signal frequency is constant. However, assuming a relatively slow moving FM-UWB carrier, the simulation should provide a good estimate of performance during transmission. The PA was designed to provide roughly constant output power over the desired frequency range of 500 MHz. The low equivalent Q factor of the output matching network results in lower peak efficiency of the amplifier, which is an inherent drawback of wideband power amplifiers, and the price to be paid for large signal bandwidth. As shown in Fig. 5.12(a) the simulated output power varies less than 1 dB between 3.7 GHz and 4.4 GHz, with an average output power around -9.4 dBm. This level is somewhat higher than the allowed power in the UWB band. The design is intentionally targeting a higher output power since the actual power level is expected to be lower than the one simulated. In the same band power consumption from a 1 V supply varies between 510 μ W and 460 μ W, with an average value of 481 μ W. The PA efficiency including the PPA is above



(a)



(b)



(c)

Figure 5.12: Simulated power amplifier output power (a), consumption (b) and efficiency (c) including the preamplifier.

20 % in the range of interest, with the average simulated efficiency of 24 %. With the reported results, the proposed transmitter should consume the lowest amount power of all the so far implemented FM-UWB transmitters.

5.3 Receiver Implementation

The two implemented receivers, MU and LP receiver will be described in detail here. The MU receiver is very similar to the receiver described in the previous chapter, only minor modifications are done at the circuit level. In the baseband, after the wideband FM demodulator, a channel filter and an FSK demodulator are added, so that the entire processing is now done on-chip. The same FSK demodulator is used by the LP receiver, however, in this case there is no need for the channel filter as only a single FM-UWB channel can be used.

5.3.1 RF Frontend

As in the previous case, the LNA and mixer are stacked (active mixer) to conserve power in both LP and MU receivers. The two schematics of the active mixer for the case of the MU receiver and the LP receiver are shown in Fig. 5.13 and Fig. 5.14 respectively. Again, a transformer based approach is used to boost the equivalent transconductance of the input transistor to approximately $2G_{m1}$. As opposed to the previous version, there is no complementary input transistor, only the NMOS is used, which simplifies the layout of the LNA and reduces parasitics, however, the output bias point and the LNA gain are no longer decoupled. Switch, sw_1 is placed to disconnect the transformer when transceiver is in the transmit mode. This is done to avoid the impact of the transformer to the PA output impedance and efficiency degradation. Resistors R_{M1-4} are fixed to $15\text{ k}\Omega$, no gain switching is present in this design, although G_{m1} can be varied by slightly tuning the bias current.

The LP RF frontend only has a single differential output, and therefore only needs one LO input. This allows to simplify the oscillator and save power in the the LO generation. Although a single LO signal is present, mixing is done using a current steering differential pair $M_{M1}-M_{M2}$, where gate of M_{M2} is

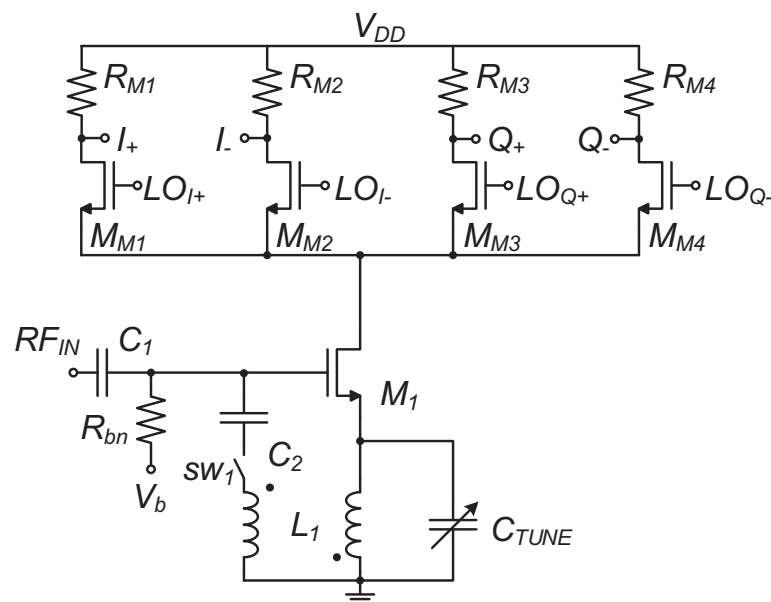


Figure 5.13: MU receiver LNA/mixer schematic.

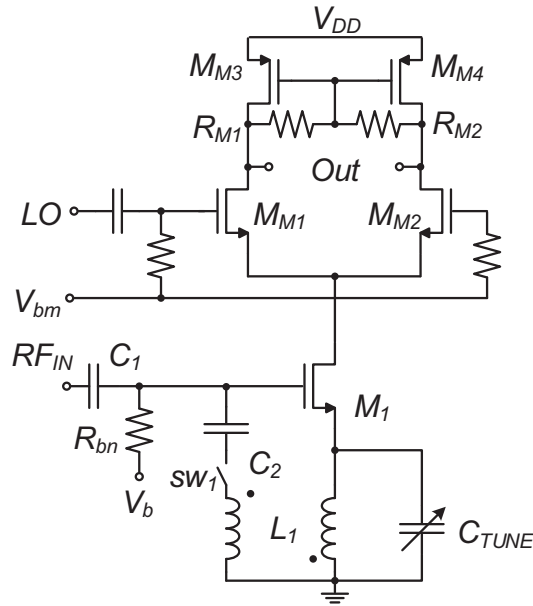


Figure 5.14: LP receiver LNA/mixer schematic.

connected to V_{bm} . Because a single-ended LO signal is used, voltage gain will be lower and noise figure will be higher compared to a case with a differential driving signal with the same amplitude. Load of the LP mixer is done using PMOS transistors M_{M3} and M_{M4} , that provide the output bias point and load resistors R_{M1} and R_{M2} that determine the output impedance, allowing some decoupling between the two.

Input matching network is implemented in the same way for both frontends. The input reflection coefficient is given in Fig. 5.11, and is the same for both (although there is a small difference in G_{m1}). The MU LNA/mixer provides 13 dB differential voltage gain, together with a noise figure of around 15 dB, while consuming 100 μ W. The LP LNA/mixer achieves 11 dB gain and 19 dB noise figure (it should be noted that a single ended LO signal of a lower amplitude is used) while consuming 70 μ W. In both MU and LP implementation the main source of noise is transistor M_1 . For both active mixers the input referred 1 dB compression point is around $P_{1dB} = -16$ dBm, and the third order intercept point is around $IIP_3 = -3$ dBm.

5.3.2 IF Amplifiers

A Cherry-Hooper amplifier described in the previous chapter was reused in this design. First difference that can be noticed compared to the previous design is that the capacitor C_1 , used to prevent offset propagation, is now placed in the source of the first differential pair. Second difference is that resistor R_f is now used to provide gain switching. It was established by simulation that additional parasitics due to switching circuitry at R_f have less impact on the amplifier bandwidth than was the case previously. A single gain control bit is provided per stage, resulting in 3 control bits for the 3 cascaded IF stages, that provide gain switching in roughly 5 dB steps. As in the previous case, lower gain setting slightly extends bandwidth.

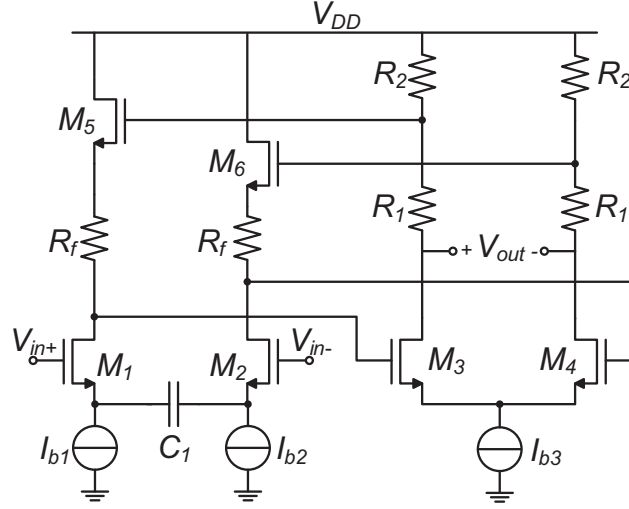


Figure 5.15: IFA schematic of MU and LP receiver.

Although, schematics of the two, LP and MU, IF amplifiers are identical, values of different circuit elements are different in order to conform to slightly different design requirements. Output resistors are slightly lower in the two last stages of the IF amplifier in order to cope with the higher capacitive load at this node. The capacitive load is mostly due to the buffers that precede the wideband FM demodulators. Additional difference exists in the LP IF amplifier and is concerning the capacitor C_1 . Namely, in the LP receiver case, the IF amplifier is also part of the FM demodulator, and acts as a frequency discriminator (performs FM-AM conversion). The high pass frequency characteristic needed for demodulation is implemented using a small capacitor C_1 . The zero and pole coming from this capacitor are given by

$$z \approx -\frac{1}{2C_1 R_{o,b}}, \quad p \approx -\frac{G_{m1}}{2C_1}, \quad (5.2)$$

where $R_{o,b}$ is the output resistance of the tail current source. The approximation is valid if $G_{m1} R_{o,b} \gg 1$. The cut-off frequency of the high-pass filter is determined by the M_1 transconductance and the source capacitor. This small capacitor of 200 fF is placed at the third stage of the IF amplifier. Large capacitors of 2.5 pF used for the first two stages provide cut-off frequency below 5 MHz and should not have a significant impact on demodulation. Finally, the chosen values result in a first order high pass characteristic with the cut-off frequency above 200 MHz.

Simulated characteristics of the implemented amplifiers are shown in Fig. 5.16. The high-pass characteristic of the IF amplifier in the LP receiver provides the FM-AM conversion before the envelope detector. In the pass band the IF amplifier provides more than 35 dB of gain, which together with the RF frontend results in the conversion gain of around 45 dB. The MU receiver IF amplifier provides around 40 dB gain, resulting in almost 50 dB conversion gain together with the RF frontend. Both amplifiers provide more than 300 MHz bandwidth, that should be enough to compensate for the ± 50 MHz carrier frequency offset. Sharp, 6th order filtering characteristic provides good rejection of out of band interferers. The total noise figure of all the stages preceding the demodulator is around 22 dB for the LP receiver and around 18 dB for the MU receiver. The limited gain of the LNA/mixer stage, results in increase of the noise figure due to the noise of the IF amplifiers. Higher noise in the LP IF amplifier

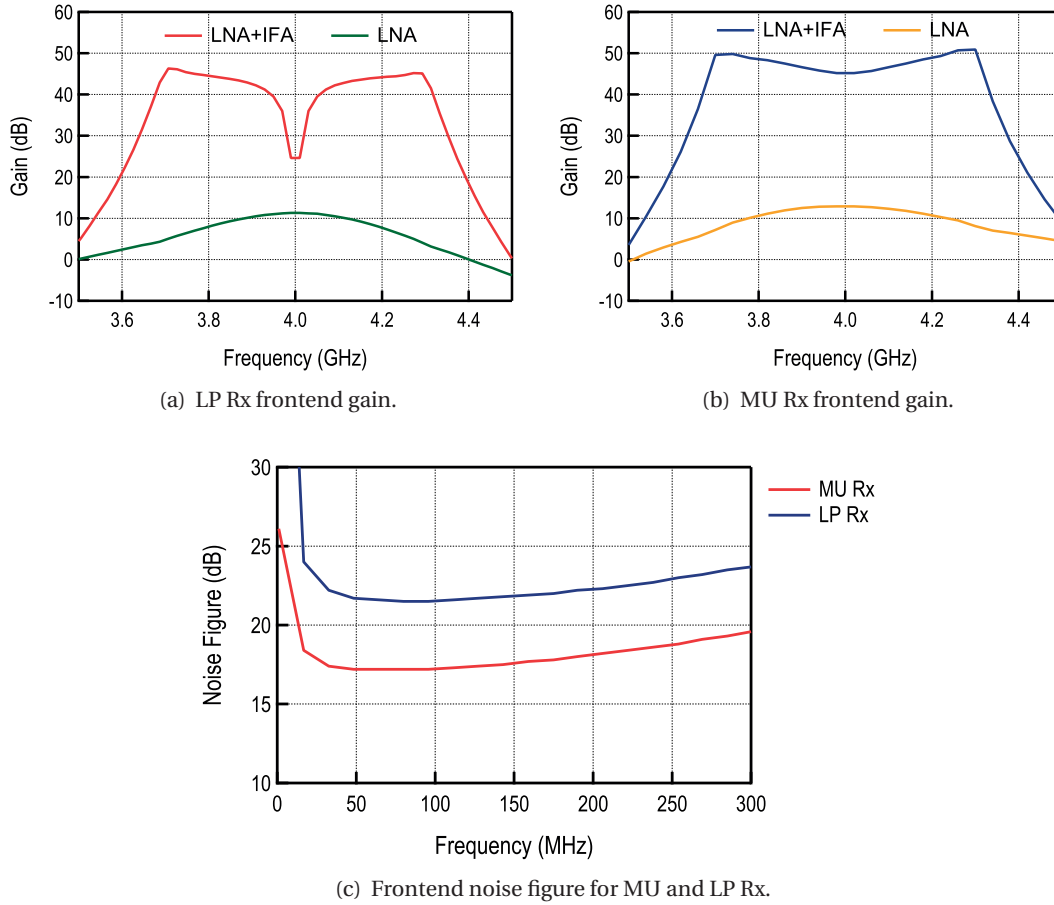


Figure 5.16: Simulated characteristics of the LP and MU Rx frontend.

is coming purely from the RF frontend. Together with the 6 dB difference in sensitivity, coming from the demodulator implementation, the 4 dB difference in noise figure should amount to roughly 10 dB difference in sensitivity between the two receivers. In this case this sensitivity loss is a price to pay for low power consumption. In both cases, a single IF stage consumes around $20 \mu\text{W}$, amounting to a total IF power consumption of $60 \mu\text{W}$ in the case of LP, and $120 \mu\text{W}$ in the case of MU receiver.

5.3.3 Receiver DCO

The quadrature DCO described in the previous chapter was reused in the MU receiver without any significant changes. Since the LP receiver does not require quadrature LO signals, a different DCO was designed, allowing to save power needed to generate the LO signal. Knowing that the DCO is one of the biggest consumers in the receiver, such approach allows to further reduce the overall power consumption of the LP receiver.

The implemented LP DCO is shown in Fig. 5.17. The architecture presented here uses the concept from [8] to lower the DCO consumption. The ring oscillator itself (transistors M_{7-11}) oscillates at one third of the desired frequency. The three phases ϕ_{1-3} are then combined using an edge combiner (transistors

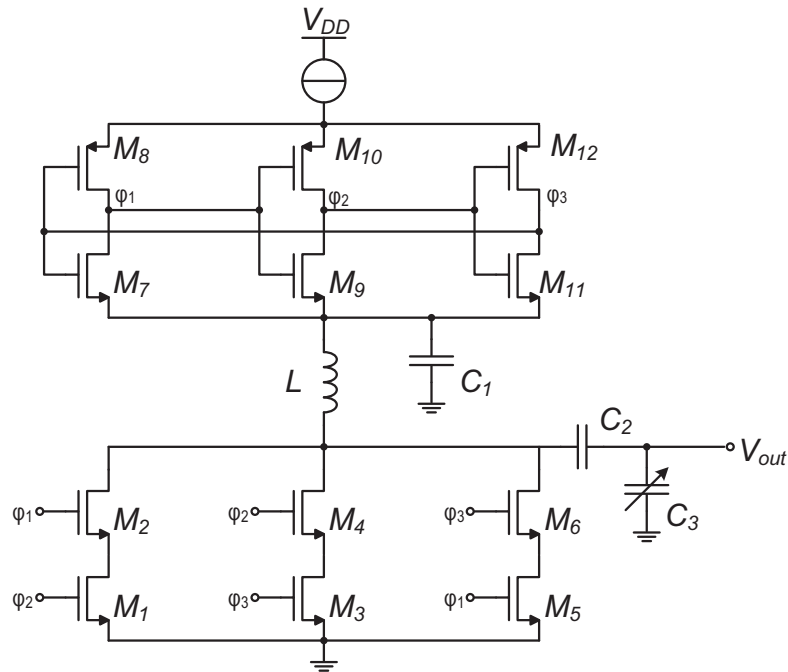


Figure 5.17: LP receiver DCO schematic.

M_{1-6}) in order to multiply the output frequency by 3. The oscillator and the edge combiner are stacked on top of each other and reuse the same current. The two stages are separated by an LC filter that provides a stable voltage for the source of the ring oscillator NMOS transistors on one side, and high impedance for the combiner output on the other. The stable source voltage sets at approximately 0.35 V and doesn't change significantly with the oscillation frequency. The resonance frequency at the edge combiner output is set by the values of the inductor L and the capacitor C_3 , and can be tuned by switching the capacitor bank C_3 . The edge combiner acts at the same time as the LO buffer in the sense that a change of the load capacitance at its output does not affect oscillation frequency (in the first order approximation). No additional buffers are added before the mixer and frequency divider input. Oscillation frequency is controlled via the supply current of the ring oscillator. One downside of the chosen DCO implementation is the fact that output amplitude and oscillation frequency cannot be set independently. The oscillator bias current, is at the same time bias current of the frequency tripler and therefore also sets the output amplitude. As a consequence, the output amplitude is lower than in the case of the MU oscillator resulting in lower mixer conversion gain and hence in a higher noise figure.

Simulation results of the designed oscillator-trippler are shown in Fig. 5.18. The oscillator covers a range from 3.5 GHz to 5 GHz, which for 6 control DCO bits corresponds to a resolution of around 25 MHz. At the same time power consumption varies from 57 μ W to 88 μ W. At 4 GHz the oscillator is expected to consume 65 μ W from a 1 V supply. At this power consumption the DCO output amplitude is equal to 85 mV. As it can be seen in Fig. 5.18, the amplitude is highly dependent on the resonance frequency of the output LC network, which was not the case in the MU DCO that provides almost constant amplitude over the entire frequency range. The tuning capability is added, in order to compensate for process variations and precisely tune the resonance frequency and maximize the output amplitude at 4 GHz

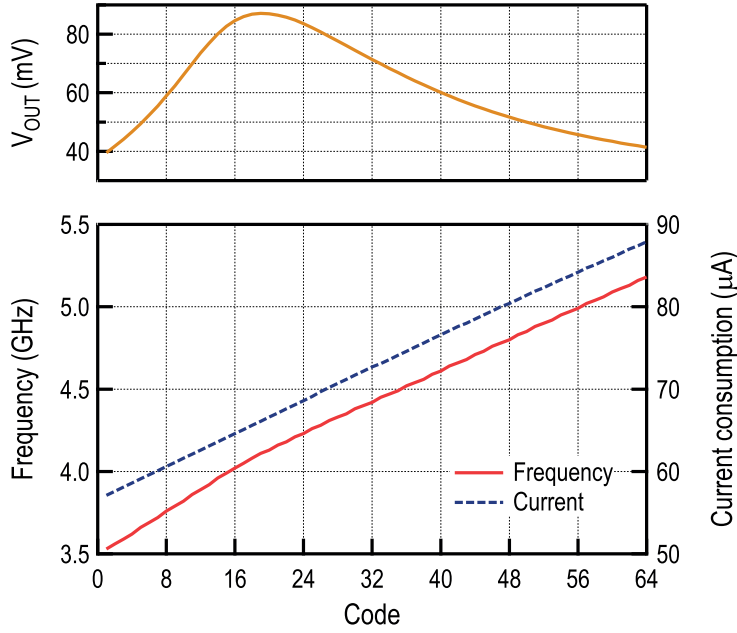


Figure 5.18: LP receiver DCO simulated frequency, current consumption and output voltage.

after production.

5.3.4 Demodulator

The demodulator of the MU receiver, shown in Fig. 5.19, is similar to the previously implemented demodulator. The only difference is the load of the double balanced mixer, that here has a band-pass characteristic instead of a low-pass characteristic. In principle, this should improve the suppression of narrowband interferers. After the first FM demodulation the narrowband interferer should be located at very low frequencies, determined by the signal bandwidth, that should be filtered out. Capacitor $C_4(5)$ attenuates components at frequencies higher than 2.5 MHz, and doesn't play a role below 1 MHz. Disregarding this capacitor the mixer load impedance is given by

$$Z_{out} = \frac{1}{G_{m7}} \frac{1 + 2sR_1C_3}{1 + 2sC_3/G_{m7}}. \quad (5.3)$$

At low frequencies, the mixer output impedance will be low, and equal to $1/G_{m7}$, thus attenuating potential interferers. At frequencies above the high-pass cut-off frequency $\omega_H = G_{m7}/2C_3$, the impedance seen from the mixer increases to R_1 , providing higher voltage gain.

The LP demodulator consists of the frequency discriminator and the envelope detector. The frequency discriminator is implemented as a high-pass filter and is a part of the IF amplifier. The envelope detector is shown in Fig. 5.20. The circuit is essentially a double balanced mixer, where the input signal is mixed with itself. To provide the two different bias points for the two mixer inputs, two different source followers were used. Source followers $M_{SF1,3}$ use native NMOS transistors with a 0 threshold voltage and drive the first mixer input (transistors M_{3-6}). Lower bias for the second mixer

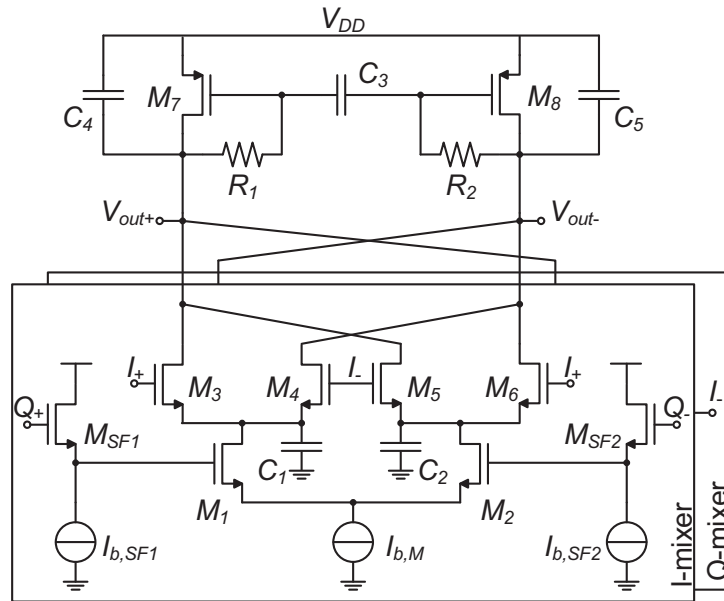


Figure 5.19: MU receiver demodulator schematic.

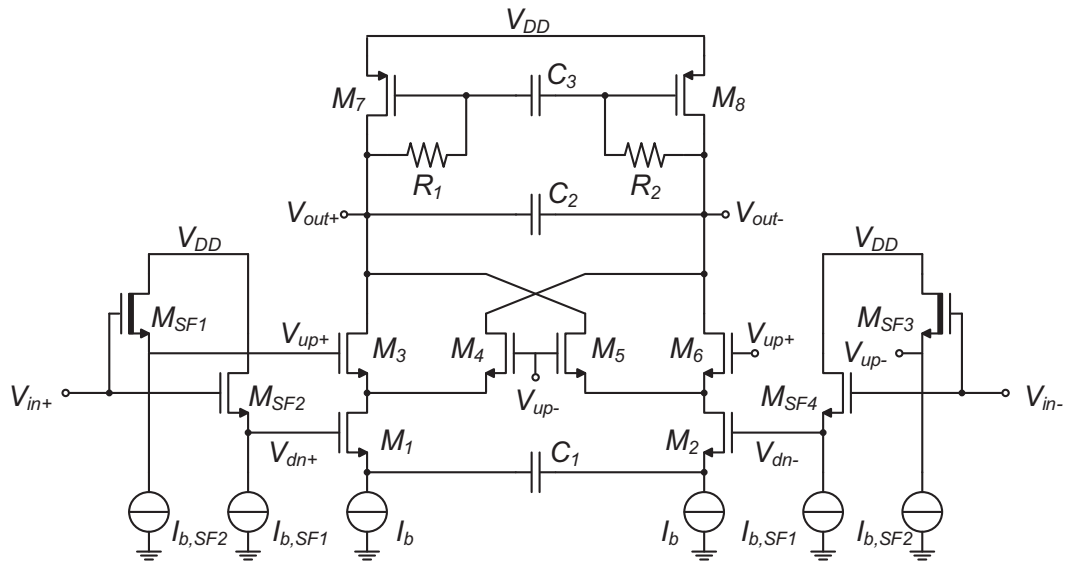


Figure 5.20: LP receiver demodulator schematic.

input (transistors $M_{1,2}$) is provided by the low threshold voltage devices $M_{SF2,4}$. The bias currents are the same for all the source follower stages. For the load of the mixer, the same approach is used as for the MU demodulator, with the difference that the pass-band is set from 2 MHz to 2.5 MHz. This is done because the LP demodulator doubles the frequency of the sub-carrier signal. Since the transmit SC channel is centered at 1.05 MHz, the received sub-carrier signal is located at 2.1 MHz.

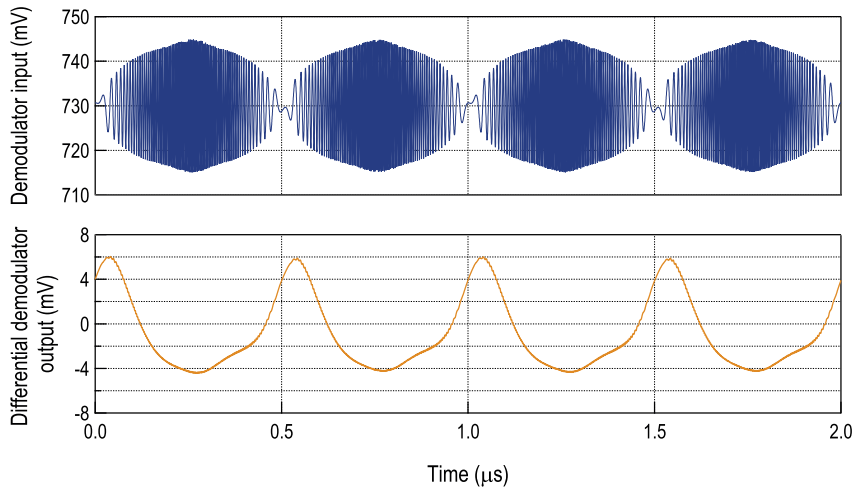


Figure 5.21: LP receiver demodulator input and output waveforms.

Simulated waveforms of the demodulator input and output signal are shown in Fig. 5.21. The effect of the high-pass characteristic of the IF amplifier can be observed in the input signal as the low frequency components are highly attenuated. After self mixing, the high frequency components disappear, and only envelope is left at the output. The output pulses appear at twice the transmitted SC frequency. After passing through the low-pass filter that follows the demodulator, higher components are attenuated and signal resembles a sine wave at the comparator input.

5.3.5 N-Path Channel Filter

The output of the first FM demodulator is the FSK modulated sub-carrier signal. Depending on whether one or many transmitters transmit simultaneously, there may be one or more sub-carrier signals present at the demodulator output. The purpose of the channel filter is to amplify the desired channel and filter out all the interfering sub-channels. As explained previously, the implemented receiver targets 4 sub-channels, each 200 kHz wide, with 300 kHz separation between adjacent channels. The implemented receiver is targeting a maximum of 10 dB difference in power levels between the two input FM-UWB signals. This translates into 20 dB difference in power of sub-channels after the first FM demodulator. To provide sufficient SNIR (signal to noise and interference ratio) before the FSK demodulation, the filter should attenuate the interfering sub-channels by 40 dB, thus providing the desired signal 20 dB stronger than the interferer. This chosen constraint is somewhat more stringent than necessary in order to provide margin for slight performance degradation compared to simulations. The filter should therefore provide a 200 kHz pass-band, and attenuation of 40 dB at 250 kHz away from the center frequency. Furthermore, the filter must be tunable from 1 MHz to 2.2 MHz in order to cover the entire sub-carrier range.

N-path filters seem like an excellent candidate for the given specification as they are known for their wide tuning range and high quality factor. The principle of N-path filters has been known for a long time [9], but they gained significant popularity in recent years as an alternative solution for high-Q RF filters that does not require off-chip passive components. Typical N-path filter consists of N parallel branches, each of them containing a switch and a capacitor in series. By driving the switches with N non-overlapping clock phases with frequency f_{ck} , the structure acts as a band-pass filter with a center

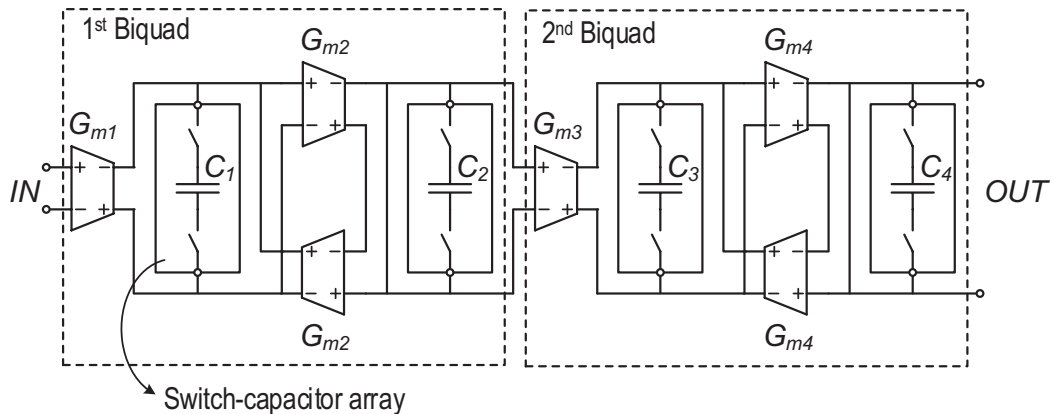


Figure 5.22: Band-pass N-path filter schematic.

frequency of f_{ck} . This can be seen as a low-pass to band-pass transformation of the filter made of the input resistance and the N aforementioned capacitors. The achievable Q-factor can be very high and is proportional to the RC constant, the number of phases used and the clock frequency [9, 10, 11]. There are some downsides to N-path filters, that are generally present in all sampling systems. First one is that the pass-band also appears at the integer multiples of the clock frequency. An improvement can be obtained by connecting the capacitors differentially, which removes all the even harmonics. The remaining harmonics still need to be filtered out by another filter following the N-path filter. The second downside is folding of signal and noise around frequencies that are multiples of Nf_{ck} (aliasing). This issue is typically solved by introducing an antialiasing filter that precedes the N-path filter, just like it is done with any sampling system (e.g. ADC). Fortunately, in this particular application noise is not an issue as this filter is close to the end of the receiving chain.

N-path filters have been used in many receivers, and have been proven to provide good linearity and interference rejection [12, 13, 14, 15]. However, in all these implementations N-path filters act as a high-Q second order filter, with a very narrow pass-band (relative to the center frequency). In this application, a relatively flat pass-band characteristic is required, along with a linear phase, in order to avoid distortion of the sub-carrier signal. Ideally, this requires translation of a higher order equivalent low-pass filter to the desired center frequency. The described design has been demonstrated for RF frequencies in [16, 17, 18], here it is reused and adapted for low frequency and low power operation.

The implemented N-path filter is presented in Fig. 5.22. It is immediately clear that if the switches are removed, the shown filter becomes a standard low-pass G_m -C filter. In fact, it was shown in [18] that by adding switches, and scaling the capacitor values by the number of phases, such that $C_x = C_{BBx}/N$, the low-pass characteristic translates into an equivalent band-pass characteristic. This characteristic will be affected by the non-idealities such as switch resistance and parasitic capacitance. The parasitic capacitances will result in slight asymmetry around the filter center frequency. It is possible to compensate for the effect of the parasitic capacitances by adding feed-forward capacitors [18]. In this case, it is not necessary to add the compensation capacitors as the parasitics are relatively small compared to the actual filter capacitors due to narrow filter bandwidth and low frequency of operation. Switch resistance affects the quality factor of the filter and limits the attenuation in the stop-band. This is an important problem at RF, as the filter is typically driven by a $50\ \Omega$ source, since

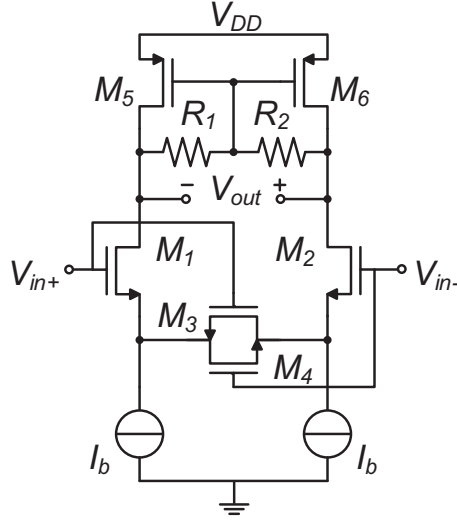


Figure 5.23: Transconductor of the N-path filter.

the maximum attenuation is limited to

$$A_{at,max} = \frac{2R_{sw}}{R_{in} + 2R_{sw}}, \quad (5.4)$$

where R_{in} is the source resistance, and R_{sw} is the switch resistance, factor 2 is present in differential implementation, since two switches are used. In order to achieve the desired attenuation, switch resistance must be sufficiently low (much smaller than $50\ \Omega$). This constraint will dictate the size of the switch and the driving requirements, and consequently power dissipation of the clock network. In this application, however, the filter is driven by an OTA with a high output resistance, on the order of $20\ \text{k}\Omega$, which enables use of relatively small switches, and low power consumption.

The filter design procedure is done in two steps. First, a low-pass equivalent filter is designed, with a $100\ \text{kHz}$ pass-band, and $40\ \text{dB}$ attenuation at $250\ \text{kHz}$. In the second step switches are added, and capacitors are scaled in order to obtain the desired $200\ \text{kHz}$ pass-band characteristic around the center frequency. In other applications it might also be necessary to add feed-forward capacitors to compensate for the parasitics. For this design it was determined that a 4th order, type 1 Chebychev transfer function satisfies the given specifications. Two biquadratic sections are used to implement the network with 4 poles p_{1-4} . The low-pass equivalent transfer function of each biquadratic section is given by

$$H(s) = \frac{H_0}{as^2 + bs + 1}, \quad (5.5)$$

$$H_0 = \frac{G_{m1}G_{m2}}{G_{m2}^2 + G_{o1}G_{o2}}, \quad a = \frac{C_1C_2}{G_{m2}^2 + G_{o1}G_{o2}}, \quad b = \frac{C_1G_{o2} + C_2G_{o1}}{G_{m2}^2 + G_{o1}G_{o2}}, \quad (5.6)$$

where G_{o1} is the output conductance at the output of G_{m1} , and G_{o2} is the output conductance at the input of G_{m3} . The active filter can also provide some voltage gain. Assuming that $G_{m1}G_{m2}/G_{o1}G_{o2} \gg 1$,

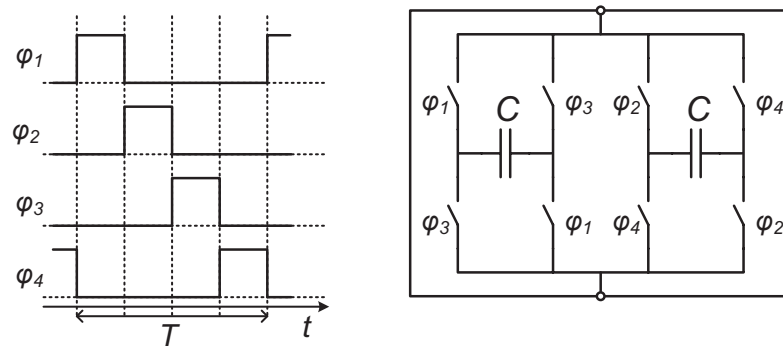


Figure 5.24: Non-overlapping clock phases used to drive switches and the differential switch-capacitor array.

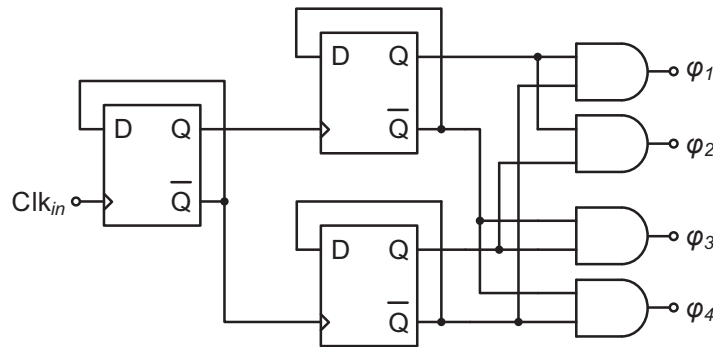


Figure 5.25: Non-overlapping clock generator.

gain can be approximated as $A_v = G_{m1}/G_{m2}$. Coefficients a and b are determined by the two poles

$$a = \frac{1}{p_1 p_2}, \quad b = \frac{p_1 + p_2}{p_1 p_2}, \quad (5.7)$$

for the first biquadratic section, and in the same way, using p_3 and p_4 , for the second biquadratic section. Once the coefficients a and b are set, parameters G_m , G_o and C must be chosen. The transconductances $G_{m1,2}$ are limited by the power consumption constraints that limit the bias current of each transconductor. Transconductors are implemented using a Krummenacher differential pair [19], as shown in Fig 5.23, in order to provide better linearity. Transistors of the differential pair are biased in weak inversion, with $\beta_1/\beta_3 = 2$, corresponding to the minimum ripple condition. With $4 \mu\text{A}$ per differential pair, the equivalent transconductance is set to $40 \mu\text{S}$. Output resistance of each cell (R_1 from Fig. 5.23), and capacitors $C_{1,2}$ are then determined to implement the desired transfer function. Finally, the chosen capacitance values are scaled by factor N , which corresponds to the number of phases.

In this design four phases are used. The driving signals, and the switched-capacitor array are shown in Fig. 5.24. Differentially connected capacitors cancel out the even harmonics. Using more phases would allow slightly better performance and less noise folding, but would increase the number of switches, and power consumption. Furthermore, four non-overlapping phases, can be generated using an input

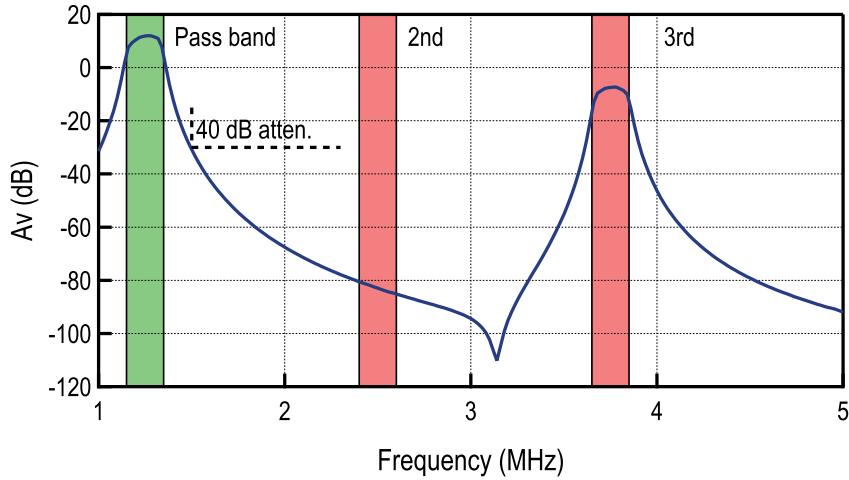


Figure 5.26: Transfer function of the N-path filter.

clock at four times the filter center frequency. In this case it is convenient since the same clock can be used by the FSK demodulator. The circuit that generates different phases ϕ_{1-4} is shown in Fig. 5.25. The three flip-flops divide the input clock by 4 and provide four equally spaced phases with a 50 % duty cycle. The desired waveforms are then produced by the four “and” gates.

Finally, the simulated filter characteristic is shown in Fig. 5.26. In the simulation, 5 MHz input clock is used, resulting in center frequency of 1.25 MHz. As explained previously, the differential capacitors cancel out all the even harmonics, and so the first higher order harmonic appears at 3.75 MHz. This is off-course the idealized case, and the attenuation of second harmonic will be limited by the component matching. Slight asymmetry around the center frequency can be observed, as expected, but in this case it does not cause severe distortion of the FSK signal. The filter center frequency can easily be tuned by adjusting the input clock frequency. Furthermore, bias currents of the transconductors can also be adjusted to modify the gain, filter bandwidth and attenuation in the stop-band.

5.3.6 LF Amplifier and Comparator

The low frequency (LF) amplifier, placed before the comparator, filters out high frequency noise, and amplifies the signal to the level needed by the comparator. The same architecture is used in both MU and LP receivers, with the pass-band adjusted to the desired frequency range. In the MU receiver, this filter also attenuates the 3rd harmonic of the N-path filter transfer function. A cascade of two fully differential amplifiers is used. A single amplifier cell is shown in Fig. 5.27, together with the small signal model of the half circuit. Each amplifier actually implements a 2nd order transfer function. The idea to use a negative resistance to implement the second order function was found in [20, 21]. This approach also allows a high quality factor, using a negative resistance that cancels out the real part of the output impedance, however, one must be careful to maintain the circuit stable and avoid oscillations. The voltage gain is given by

$$A_v(s) = \frac{s2C_1G_{m1}G_{m2}R_1}{(G_{m1} + s2C_1)(G_{m2} + s(2C_2 + 2R_1G_{m2}(C_3 - C_2)) + s^24C_2C_3R_1)} \quad (5.8)$$

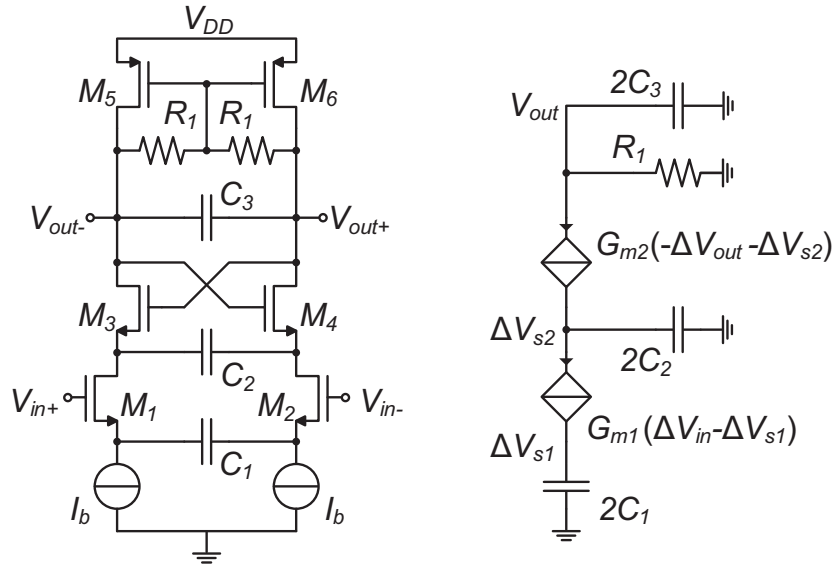


Figure 5.27: Schematic of the second order cell of the LP filter and half circuit small signal schematic.

The zero and pole created by C_1 provide the high-pass part of the characteristic that filters out flicker noise together with any low frequency components. The second factor in the denominator provides the 2nd order low-pass filtering. If the first real pole is sufficiently far from the two complex poles, gain in the pass band will be given by

$$A_{v,pb} \approx G_{m1} R_1. \quad (5.9)$$

For the two poles generated by this factor to be in the left half-plane, the coefficient with s must be positive. The circuit remains stable as long as $2C_2 + 2R_1 G_{m2}(C_3 - C_2) > 0$. This will be guaranteed if the capacitor C_3 is larger than the capacitor C_2 . Otherwise, given the sufficiently high bias current, and consequently the transconductance G_{m2} , the circuit might start to oscillate.

The simulated frequency characteristics of the two LF amplifiers are given in Fig. 5.28. The frequency band is selected based on the expected sub-carrier frequency. Since a larger band is needed for the MU receiver, in order to accommodate multiple SC channels, gain is slightly lower, around 25 dB in the pass-band, compared to approximately 32 dB in the LP receiver path. In this case linearity is not a concern, since only a single FSK signal is expected at the input (additional FSK signals should be removed by the preceding channel filter).

Comparator following the LF amplifier acts as a limiter and provides a rail-to-rail output signal that is needed for the digital FSK demodulator. The schematic of the comparator is shown in Fig. 5.29. It is designed to provide full swing for an input sine signal with a minimum differential amplitude of 20 mV at up to 5 MHz (which is above the needed range). The core of the comparator are transistors M_{1-6} . In order to provide better performance and avoid glitches due to noise, a small hysteresis is introduced in the comparator characteristic, on the order of 10 mV. This is done using the positive feedback transistors

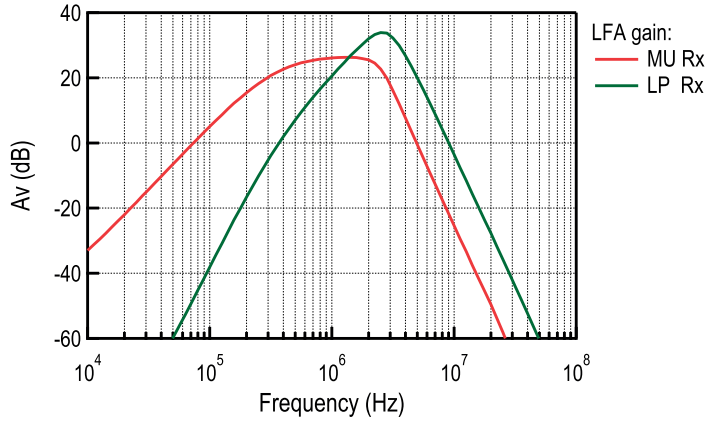


Figure 5.28: Simulated frequency characteristic of the MU and LP receiver LFA.

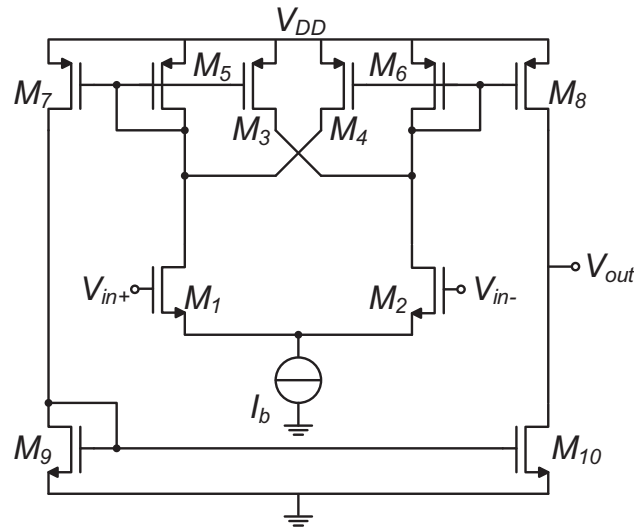


Figure 5.29: Comparator schematic.

M_3 and M_4 . Assuming the transistors are operating in weak inversion, the difference between the two threshold voltages is given by

$$\Delta V_{TH} = 2nU_T \ln k, \quad (5.10)$$

where factor k is defined as $k = \beta_3 / \beta_5 = \beta_4 / \beta_6$. Transistors M_{7-10} are added to provide a full swing output signal compatible with CMOS logic. The comparator consumes between $5 \mu\text{A}$ and $10 \mu\text{A}$, depending on the bias current setting. Since the expected input voltage amplitude is supposed to be larger than 20 mV , offset constraints are easily achievable and no calibration is necessary.

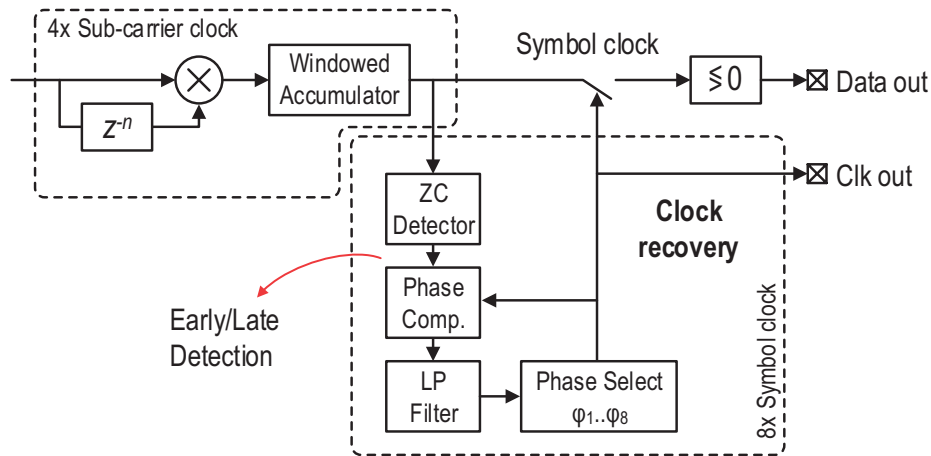


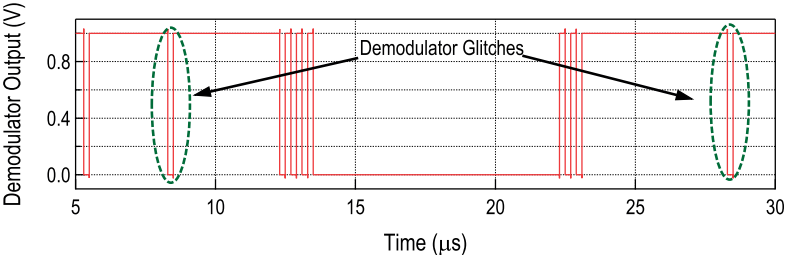
Figure 5.30: Block diagram of the FSK demodulator and clock recovery circuit.

5.3.7 FSK Demodulator and Clock Recovery

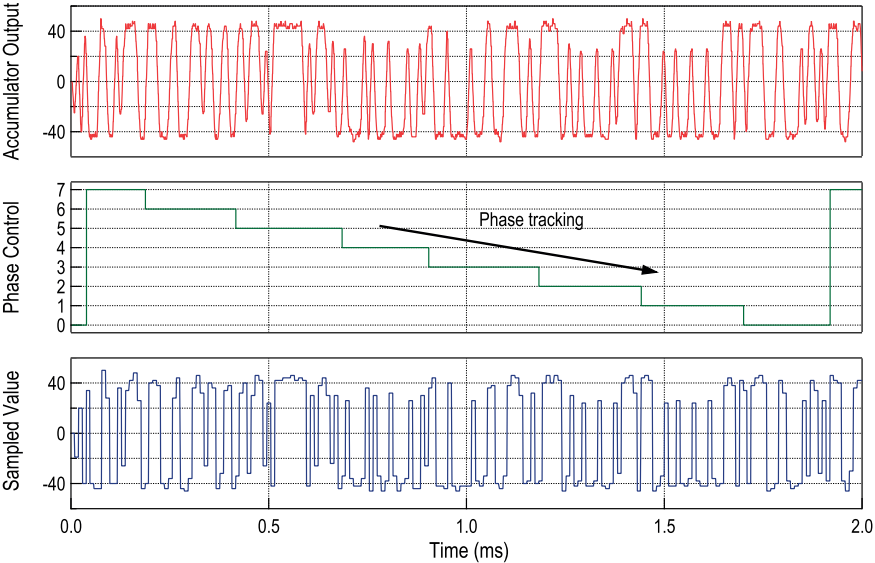
The last block in the system is the FSK demodulator, that is implemented together with the clock recovery circuit. The demodulator implemented here must be able to demodulate an FSK signal with the modulation index of 1, or equivalently 50 kHz frequency deviation at a data rate of 100 kb/s. The FSK demodulator reported in [3], is very simple, and consumes a small amount of power, but requires a large frequency deviation (250 kHz deviation was used). In this case, in order to support multiple sub-carrier channels, frequency deviation is limited to 50 kHz, and a different approach is needed.

The proposed demodulator, shown in Fig. 5.30 is a digital version of the delay line demodulator. The input signal is first sampled using a clock whose frequency is four times higher than the FSK signal center frequency. The same clock is used for the N-path channel filter. By adjusting the reference clock frequency, the corresponding sub-channel is selected. The sampled signal is then demodulated using a delay line and a “mixer”. Sampling the signal allows to implement the delay line as a chain of flip-flops controlled by the same reference clock. Delay can be configured easily by controlling the number of flip-flops in the signal path, which is simply achieved by configuring the multiplexers. This allows a more elegant control compared to analog solutions such as RC delay networks. An XOR gate plays the role equivalent to the mixer in the analog demodulator implementation. Depending on the delay, and whether the input frequency is higher or lower than the reference clock frequency, the output of the XOR gate will be '1' or '0'. Simulated signal at the FSK demodulator output is shown in Fig. 5.31(a). Since the output signal is not perfectly clean (even without the presence of noise), it cannot be simply sampled, instead it is first filtered using a windowed accumulator. In each clock cycle, the accumulator output is either incremented or decremented depending on the XOR output. The accumulator output is then used to make a decision for the output bit and to recover the symbol clock.

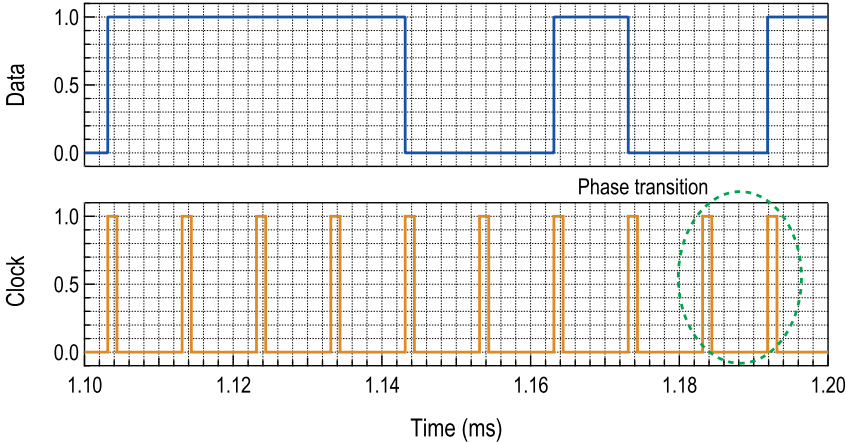
Clock recovery circuit is a necessary block in any receiver, and has a particularly important role here. As previously discussed, one of the good properties of FM-UWB is the inherent robustness to frequency offsets. Mismatch in carrier frequency of several megahertz, or even tens of megahertz will not cause a significant performance penalty. However, for the whole receiver chain to work properly, the baseband must also be able to tolerate a certain frequency offset. This is accomplished via a dedicated circuit that tracks the transmit symbol clock and adjusts the clock frequency on the receiver side. The amount of



(a) FSK demodulator output signal.



(b) Internal signals of the clock recovery circuit.



(c) Output signals.

Figure 5.31: Simulated signals of the FSK demodulator and clock recovery circuit.

frequency offset that must be tolerated depends on the implementation of the reference oscillator. One of the aims of this work is to demonstrate the feasibility of a fully integrated transceiver, which would include the reference oscillator. This also means removing the external crystal reference and minimizing the number of off-chip components. Unfortunately, the integrated RC oscillators cannot achieve the performance of a crystal oscillator, and the precision of the reference frequency will be much worse, in the order of thousands of ppm instead of tens of ppm. By using the FM-UWB, this relatively large frequency variation can be allowed, assuming that the clock recovery circuit can compensate the frequency offset between the transmitter and the receiver. Recent integrated RC oscillators achieve precision that is in the order of ± 2500 ppm across the designated temperature range [22, 23, 24, 25], which is a range that can be easily covered by the clock recovery circuit shown here.

The implemented clock recovery is based on a simple early/late zero crossing detection. The clock used for this circuit is derived from the reference clock, with the average frequency 8 times higher than the symbol rate, that is 800 kHz. This clock is then used to generate 8 different phases of the symbol clock, one of which is used to sample the accumulator output at a correct time instance. The clock recovery circuit determines which phase is used and works in the following way. First a zero crossing is detected from the accumulator output. In order to avoid false crossings due to noise, the circuit needs to detect a sufficient difference in levels between several consecutive samples. The phase comparator then determines whether the current zero crossing is early or late with respect to the currently selected clock phase. Depending on the number of clock cycles between the zero crossing and the reference, the corresponding value will be added to or subtracted from the register value of the LP filter (here the LP filter is simply implemented as an accumulator). Once the register value increases or decreases past a defined point, an up or down phase shift occurs. Depending on the frequency offset between the transmitter and the receiver, phase shifts will occur more or less often. As the phase changes, so does the average frequency of the receiver symbol clock. As long as the circuit is able to track symbols, this average frequency should correspond to the transmitter symbol clock frequency. The speed of the control loop can be controlled through the LP filter coefficient, that directly determines the filter bandwidth. Increasing the coefficient allows the loop to track larger difference in frequencies, but also makes it more prone to errors due to noise.

An example of the clock recovery circuit operation is given in Fig. 5.31(b). In this case the transmitter reference frequency is 2000 ppm faster compared to the reference on the receiver side. One can notice that the phase control signal constantly decreases (until 0 at which point it goes back to 7), which results in the average frequency of the symbol clock below the reference frequency. An example of the phase shift is shown in Fig. 5.31(b). In that particular time instance the instantaneous frequency of the symbol clock frequency drops to $7/8$ of the reference frequency during one cycle. The maximum theoretical frequency offset that can be tracked, assuming a phase shift occurs in every cycle, is $\pm 1/8$ of the reference frequency.

5.3.8 SAR FLL Calibration

Ring oscillators used to generate the LO signal in the receiver and the FM-UWB signal in the transmitter consume a small amount of power, but are sensitive to process, voltage and temperature variations. For that reason they need to be calibrated periodically to maintain frequency offset within certain limits. It was shown in the previous chapter that a relative frequency offset of ± 50 MHz between the receiver and transmitter causes only a minor performance degradation, and beyond that limit sensitivity decreases rapidly. Depending on the rate of environmental changes, the oscillators will need to be calibrated

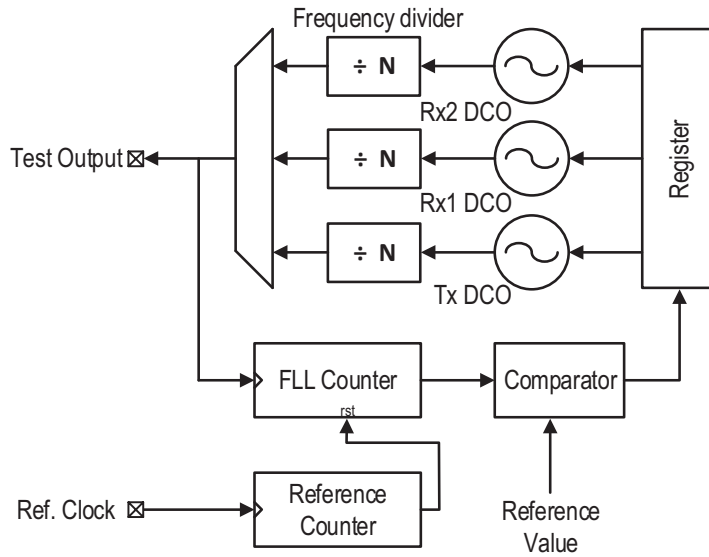


Figure 5.32: SAR FLL block diagram.

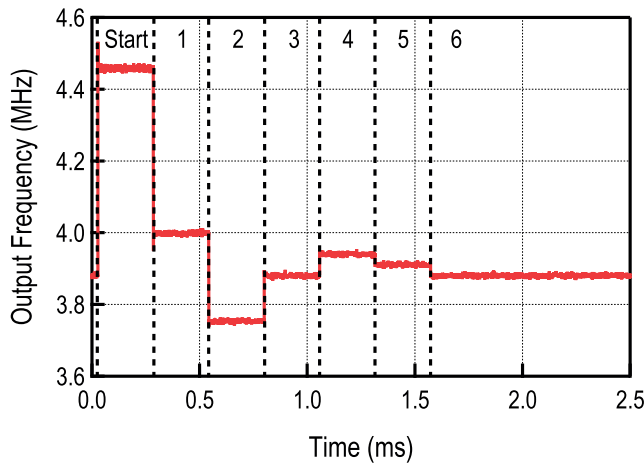


Figure 5.33: Example measured SAR FLL calibration cycle.

once every few hours, or potentially days.

Calibration is performed using an on-chip SAR FLL, shown in Fig. 5.32. Configuration of each oscillator is controlled using one of the two registers, one set manually by the SPI, and the other set by the calibration loop. The number of cycles for calibration is equal to the number of register bits used to set the DCO frequency. In each cycle one bit is set. Once the bit is set, the oscillator frequency is measured and compared to a reference value, if it is higher, the bit is set back to '0', otherwise it remains '1'. The DCO frequency is measured using two counters. The first counter counts the number of reference clock cycles up to value $N_{f,ref}$ that determines the duration of the measurement interval as $T_{ref}N_{f,ref}$. During that interval the second counter counts the number of cycles of the frequency divider output N_{cnt} . This value is then compared to the reference value N_{ref} in order to determine

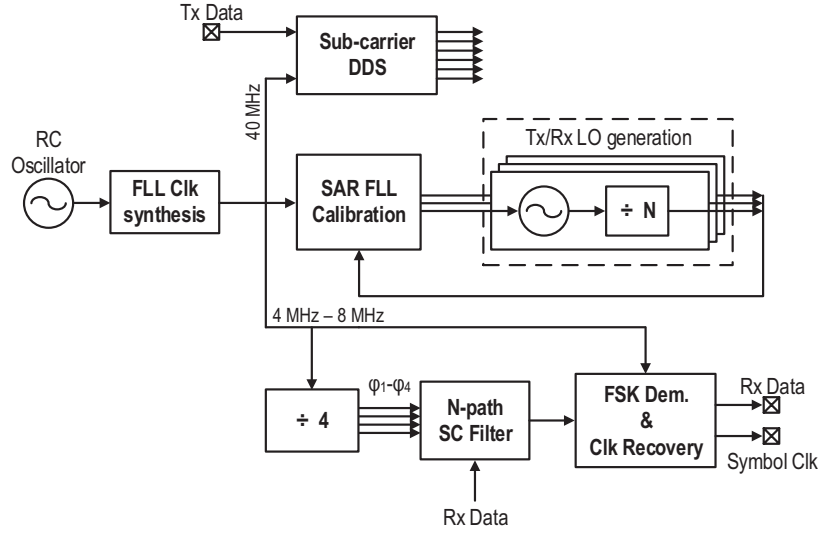


Figure 5.34: Principle of clock generation and distribution.

whether the corresponding bit should be '0' or '1'. Finally, assuming infinite resolution (number of bits or equivalently cycles), the frequency of the DCO after calibration will be given by

$$f_{DCO} = N_{div} f_{div} = N_{div} \frac{N_{ref}}{N_{f,ref}} f_{ref}, \quad (5.11)$$

where N_{div} is the frequency divider ratio (providing values between 128 and 1024) and f_{div} is the frequency at the divider output. In reality, the DCO configuration will produce the highest frequency that is still below the frequency given by equation 5.11. The frequency resolution of the FLL depends on the duration of the measurement interval and the division ratio $\Delta f = f_{ref} N_{div} / N_{f,ref}$. The only requirement here is to maintain the FLL resolution below the DCO resolution, that is in the order of 25 MHz.

An example of a measured calibration cycle is presented in Fig. 5.33. The measurement is done using the frequency divider output signal at the test port. For the shown measurement reference clock frequency is set to 4 MHz, and $N_{div} = 1024$, $N_{f,ref} = 1024$ and $N_{ref} = 1000$. After 6 steps of calibrations, 6 DCO control bits are set. The resulting output signal of the frequency divider is at 3.89 MHz, corresponding to the DCO frequency of 3.98 GHz, which is close enough to the ideal carrier frequency.

5.3.9 Clock Reference

The implemented FM-UWB transceiver does not contain an oscillator that would provide a frequency reference for other circuits (LO calibration, N-path filter, FSK demodulator etc.). Instead, the clock signal is generated externally using a signal generator, allowing to adapt to different modes of operation and test the functionality of the transceiver. Since one of the goals of this work is to show that an FM-UWB transceiver can be implemented without a precise, off-chip quartz resonator, one solution for derivation of all the necessary clock signals will be described here.

A simple RC oscillator could be used as a clock reference, similar to one of the solutions found in

[22, 23, 24, 25]. State of the art precision of 2500 ppm across the temperature range of interest is sufficient for the FM-UWB transceiver developed here. The FSK demodulator and the clock recovery circuit were designed to compensate the potential frequency offset. At RF this range translates into ± 10 MHz offset around the carrier frequency of 4 GHz, which is well below the targeted range of ± 50 MHz. The RC would simply provide the fixed reference clock signal, different frequencies needed for different circuits would be generated using a simple FLL or a DLL (delay locked loop). The block diagram of the conceptual solution with all the related sub-blocks is shown in Fig. 5.34.

For the SC-DDS, a clock frequency of at least 40 MHz is needed to provide a relatively good triangular signal. Higher frequencies should provide a better triangular waveform, but would also result in increased power consumption of this block. At the same time the FLL must be able to provide frequencies from 4 MHz to 8 MHz, as a reference for the N-path filter and the FSK demodulator. Luckily, the same frequency is used by both circuits. For the N-path filter, the clock is divided by 4 in order to generate the four non-overlapping phases at the sub-carrier center frequency. The symbol clock of approximately 100 kHz is derived from the input clock using a simple counter, and the clock recovery circuit assures that it tracks the symbol rate of the received signal. No particular constraints in terms of input frequency exist for the FLL calibration loop, the two configurable reference values (see Fig. 5.32) can always be set such that the DCO frequency is properly calibrated. The proposed clocking scheme can therefore be used to provide a reference to all the circuits in the system, demonstrating one way to implement a fully integrated FM-UWB transceiver.

5.4 Measurement Results

The proposed transceiver was integrated in a standard 65 nm bulk CMOS technology. The SEM die photograph is shown in Fig. 5.35. The die size is 2.25 mm by 2.25 mm, and roughly one third of it is the active area of the transceiver (including the decoupling capacitors). The remaining area is used for test circuits and decoupling capacitors. The transceiver layout is dominated by the inductors needed to provide input and output matching. Large inductor area makes routing more difficult and requires longer paths, that consequently add more parasitics at the transceiver IO. It should be noted here that standard TSMC inductors were used for the design. These inductors use only a single metal layer (the low resistance ultra-thick metal), and hence occupy a large area. The layout could be made more compact using smaller, more area efficient custom inductors, that would exploit additional available metal layers. The RF IO pad, used by the receivers and the transmitter, is marked in the figure. It is placed between the two ground pads, that are connected to the coplanar waveguide implemented on the PCB. Digital input and output pads, used for test and debug signals, clocks and input and output bits, are located on the side of the chip opposite to the RF IO pad and other sensitive analog signals in order to minimize coupling between strong digital signals and sensitive analog signals. Gold bumps, used for flip-chip bonding of the IC to the PCB, can also be seen in the Fig. 5.35.

5.4.1 Transmitter Measurements

The first block of the transmitter is the sub-carrier DDS. The static configuration that controls the two sub-carrier frequencies is loaded via the SPI, and the dynamic behavior of the circuit is controlled using the two inputs, the clock and the data input. The SC-DDS controls two current steering DACs, one that drives the DCO, and the other one that drives the test buffer. The output signal from the test buffer is presented in Fig. 5.36(a). The shown waveform corresponds to 2.1 MHz sub-carrier signal and 500 MHz

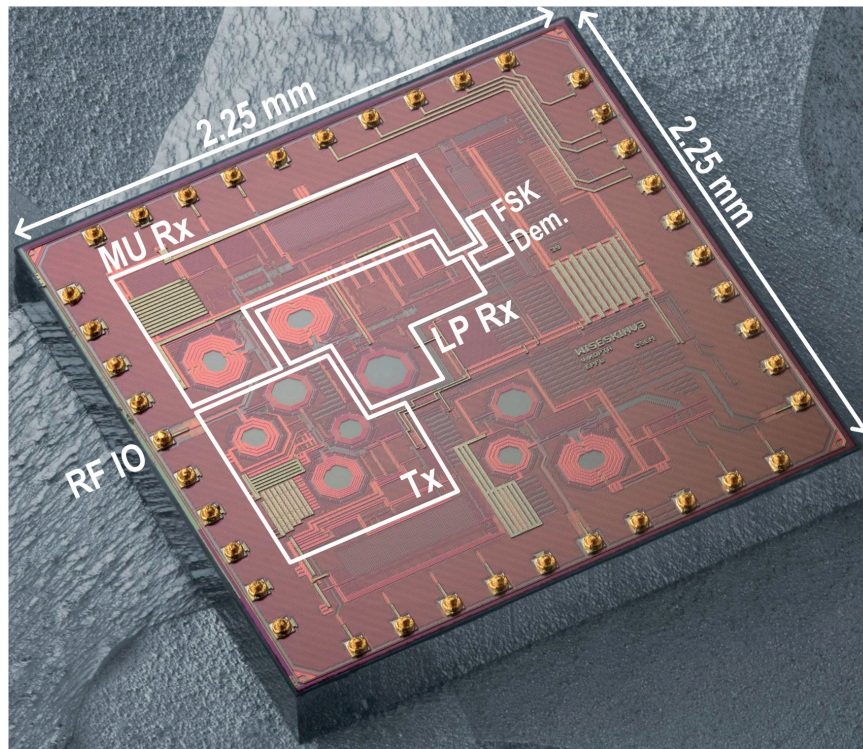


Figure 5.35: SEM die photograph of the transceiver.

wide FM-UWB signal. Deviation from the triangular waveform is a result of the limited bandwidth of the buffer. Sub-carrier waveform can also be obtained by directly measuring instantaneous frequency of the transmitted signal. The frequency measurement is done using the Keysight VSA application with the 8 GHz, MSO oscilloscope. The resulting waveform is depicted in Fig. 5.36(b). Due to large input bandwidth the resulting signal is relatively noisy, but still shows some of the properties of the generated SC signal. In the this case SC frequency is set to 4 MHz, which is in fact above the targeted SC frequency range. It can be seen in the figure that the output waveform deviates from a triangular close to the peaks. As a result the bandwidth of the output FM-UWB signal will be slightly lower than expected. This is a result of the low oversampling ratio (ratio between the clock frequency and the sub-carrier frequency f_{clk}/f_{SC}). In the presented example the oversampling ratio is 10, for a 40 MHz input clock. According to [2], a relatively good result is obtained for an oversampling ratio of around 20, which will be the case for the desired SC band (1.2 MHz-2.3 MHz).

Measured DCO frequency and power consumption are presented in Fig. 5.37. The DCO frequency can be varied from 3.5 GHz to 5.2 GHz and for this range the current consumption varies from 80 μA to 113 μA . This frequency tuning range is achieved using the static DAC that only sets the upper FM-UWB frequency. Dynamic modulation DAC then sinks the current from the static DAC to modulate the carrier frequency. The reported measurement is the consumption of the DCO alone, without the buffer consumption. For the nominal setting, the buffer consumes an additional 71 μA of current. By changing the buffer bias current, the DCO output amplitude can be adjusted, and the consumption can be varied from 48 μA to 94 μA . The input signal amplitude allows to control the output power and current consumption of the PA and PPA, and optimize the transmitter efficiency.

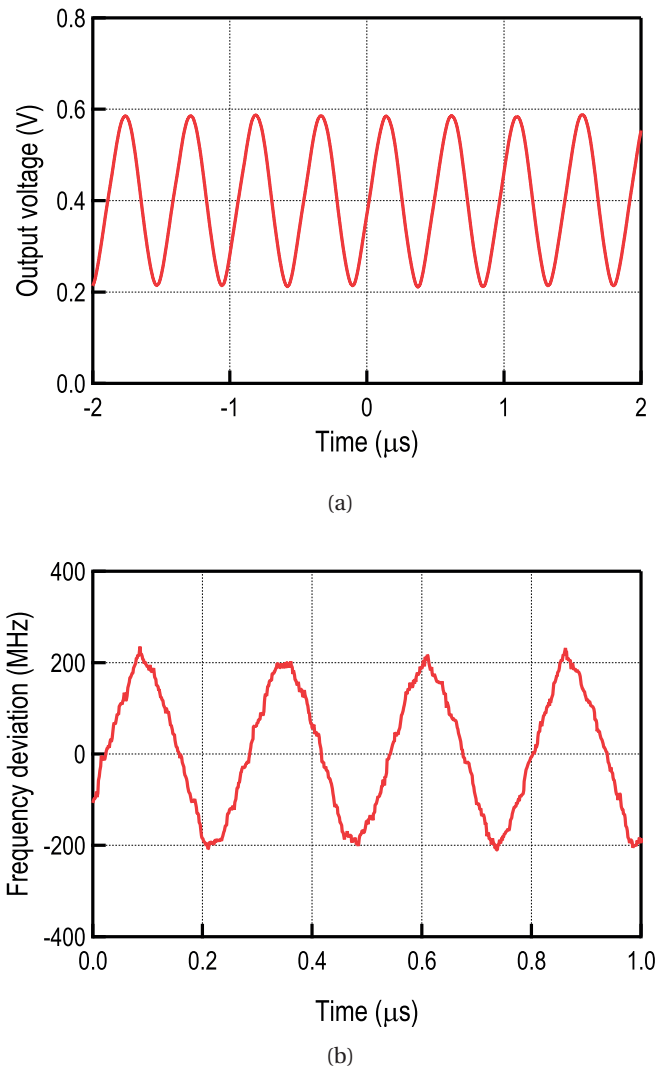


Figure 5.36: Measured sub-carrier DAC output (a) and measured frequency deviation of the transmitted signal (b).

Due to the large bandwidth, FM-UWB signal is inherently robust against carrier offsets. The same property allows it to tolerate relatively high levels of phase noise. It was shown in [3] that phase noise as high as -80 dBc/Hz, at 10 MHz away from the carrier, causes no significant performance degradation in terms of BER. This constraint is quite loose and permits the use of low quality ring oscillators for signal generation. For comparison, consider the Bluetooth standard that imposes a constraint of -102 dBc/Hz at 2.5 MHz [26], and consequently requires higher power consumption for carrier synthesis. The measured transmit oscillator phase noise, for the oscillation frequency of 4 GHz, is shown in Fig. 5.38. At 10 MHz away from the carrier, phase noise level is -98 dBc/Hz, which is considerably lower than the FM-UWB constraint. The phase noise was measured using the signal at the output of the frequency divider. A factor of $20 \log 1024$ was added to the measured phase noise to account for the division ratio of 1024. Noise coming from the dividers will add to the total phase noise at the output, however due to the already large phase noise of the ring oscillator it should not have a significant impact on the

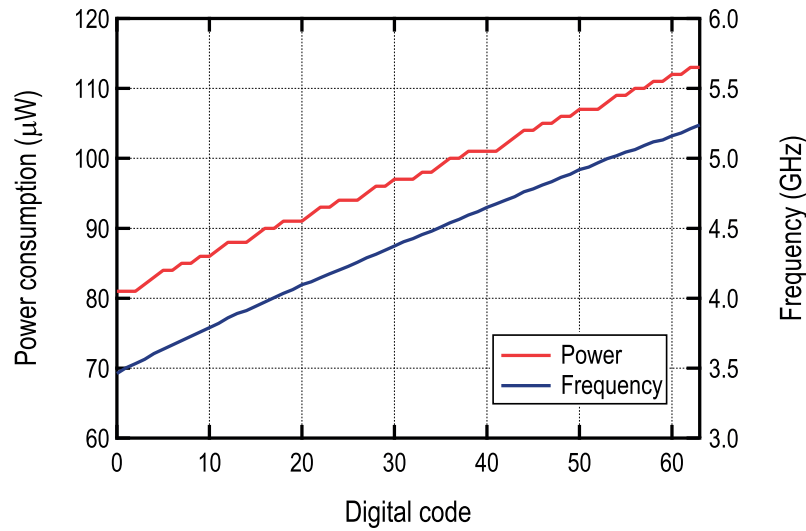


Figure 5.37: Frequency and power consumption of the transmit DCO.

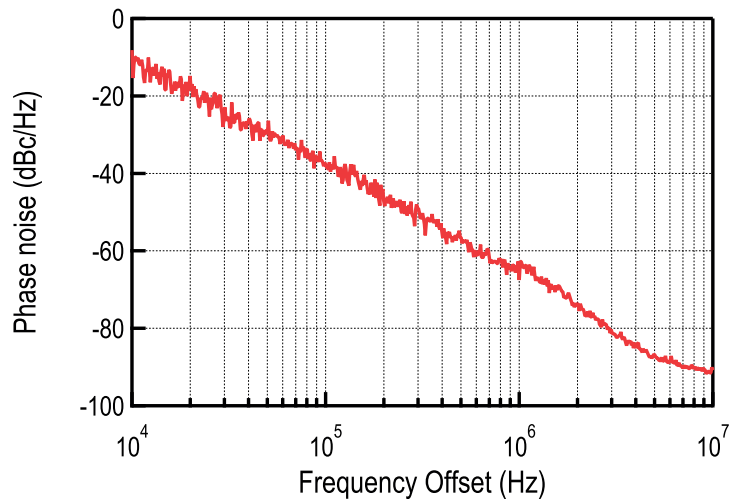
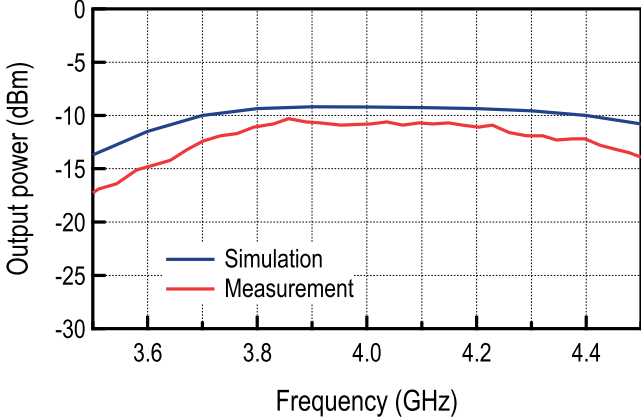


Figure 5.38: Phase noise of the transmit DCO at 4 GHz.

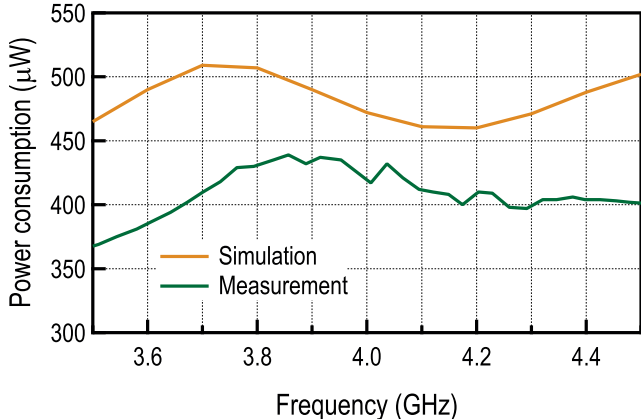
measured values.

The power amplifier and the output matching network were designed to provide good performance over the entire 500 MHz range. The idea is to achieve high average efficiency of the transmitter during wideband signal transmission, and not at a single frequency, which is usually the approach in narrowband systems. Static frequency characteristic of the PA and PPA stack is summarized in Fig. 5.39. The measurement is conducted using the DCO as the input signal source, since an external signal cannot be used. For this measurement the DCO is configured to produce a carrier signal at a single frequency. Due to high phase noise and unstable frequency of the ring oscillator, the result is likely worse than it would have been if a clean carrier signal were used.

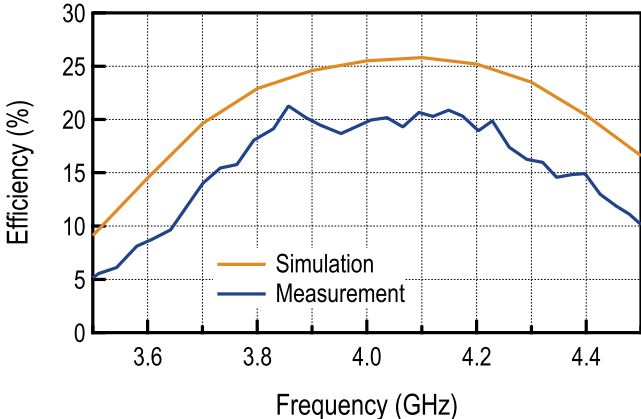
The measured output power of the transmitter is shown in Fig. 5.39(a). Compared to simulations,



(a)



(b)



(c)

Figure 5.39: Measured power amplifier output power (a), consumption (b) and efficiency (c) including the preamplifier.

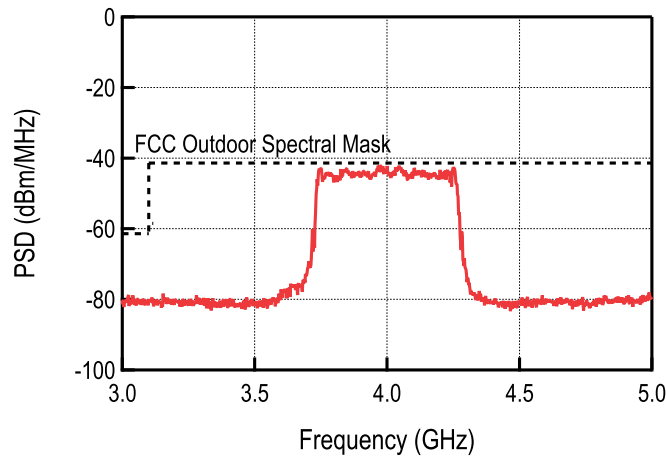


Figure 5.40: Transmitted FM-UWB signal spectrum.

the level is approximately 2 dB lower, with a somewhat smaller bandwidth. The discrepancy between the simulation and measurement is likely caused by the effects that were not taken into account in the simulation. A simplified model of the output pad and the interface towards the PCB were used, more accurate results would have been obtained by using a full 3D electromagnetic simulation. Nevertheless, the error remains within the expected limits of a few decibels. Fortunately, the impedance of the matching network also affects the power consumption. The fact that it slightly differs from the simulated values also results in decreased measured power consumption compared to the simulated one, as shown in Fig. 5.39(b). Lower output power, combined with lower power consumption, finally result in efficiency around 6 % lower than expected in simulations. As shown in Fig. 5.39(c) peak measured efficiency of the output stage (not including the DCO and the buffers) equals 21.3 %. In the largest part of the band efficiency stays around 20 %, and slowly drops close to the edges of the band, resulting in an average efficiency of around 18 %. The measured output power and efficiency of the implemented power amplifier are in line with the state of the art and exhibit similar performance as other implementations targeting low output power levels.

The spectrum of the transmitted signal is presented in Fig. 5.40. The shown spectrum is below the limit defined by the FCC spectral mask. Outdoor spectral mask is shown in this case, the only difference between the outdoor and the indoor mask being the attenuation outside the defined UWB band, which is more stringent for the outdoor mask. The transmit signal also satisfies the defined emission level between 0.96 GHz and 1.61 GHz, where maximum level set to -75 dBm/MHz (not shown in Fig. 5.40).

Figure 5.41 shows different output power levels and average transmitter power consumption, achievable using different transmitter configurations. Constant efficiency lines are provided to show the achievable efficiency at a given output power. In this case the whole transmitter is taken into account, including the DCO, buffers and SC-DDS (not just the PA and PPA). The shown output power levels are measured as integrated power across the transmit band during a single sub-carrier transmission. The output power level can be varied from -11.3 dBm down to -35 dBm, in steps that are smaller than 3 dB. This is done via the control of the DCO buffer strength (or equivalently PPA input signal amplitude), the PPA bias current and the matching network. The control of the output power can then be implemented using a look-up table in software. The ability to adjust the output power is useful for multi-user communication. For example if the two transmitting nodes are at different distances from the receiving node, the power

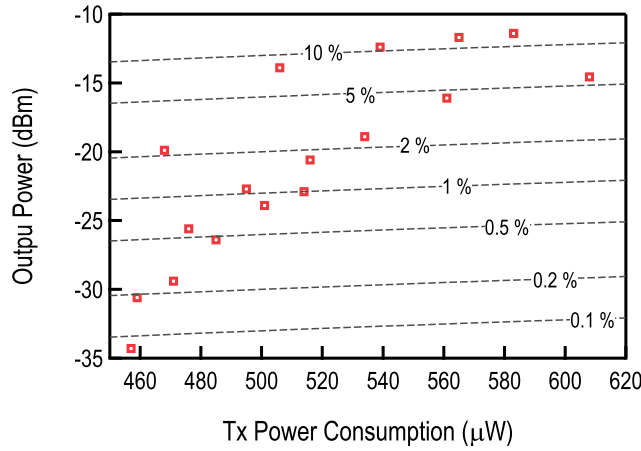


Figure 5.41: Transmit power vs. transmitter power consumption.

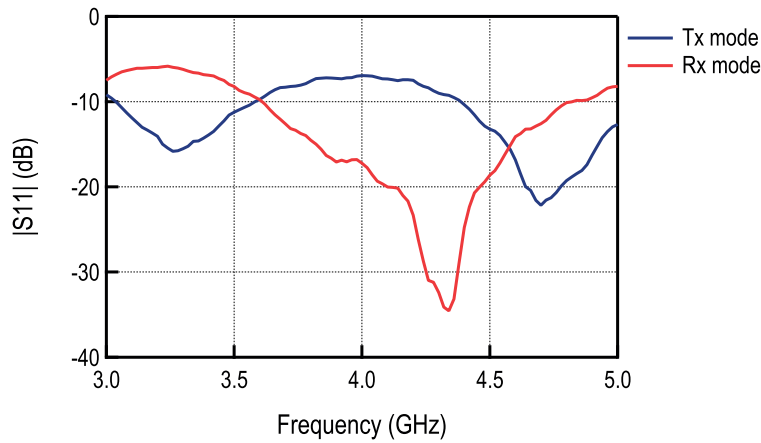


Figure 5.42: Measured S_{11} parameter in transmit and receive mode.

levels of the two signals will be different. In order to equalize power levels at the receiver, the closer transmitter can adjust its output power to avoid desensitizing the receiver.

Measured input S_{11} parameter is shown in Fig. 5.42. The measurement is done using the die bonded to the PCB, with a 1 cm long coplanar waveguide between the RF IO pad and the horizontal SMA connector. The lower values compared to the simulations are likely related to the PCB, since the connector and the transmission line were not taken into account. On the receiver side, the additional losses coming from the PCB actually improve the reflection coefficient, that is below -10 dB from 3.6 GHz to 4.75 GHz.

The power consumption breakdown of the transmitter is given in Table 5.1, for the transmitted power of -11.4 dBm. Almost 70% of the power is consumed by the output stage (PPA and PA). In order to improve the efficiency of the transmitter, this part should be carefully optimized in the future. The SC DDS consumption is practically negligible compared to other blocks, and so its implementation will have little impact on the overall performance. The DCO together with the buffers consume slightly less than 30%, thanks to the fact that there is no continuous time PLL or FLL controlling the output frequency.

Table 5.1: Transmitter power consumption breakdown

Block	Current cons. (μA)	Relative cons. (%)
PA+PPA	402	69.9
DCO	91	15.8
DCO Buffer	71	12.4
SC DDS	11	1.9
Total	575	100

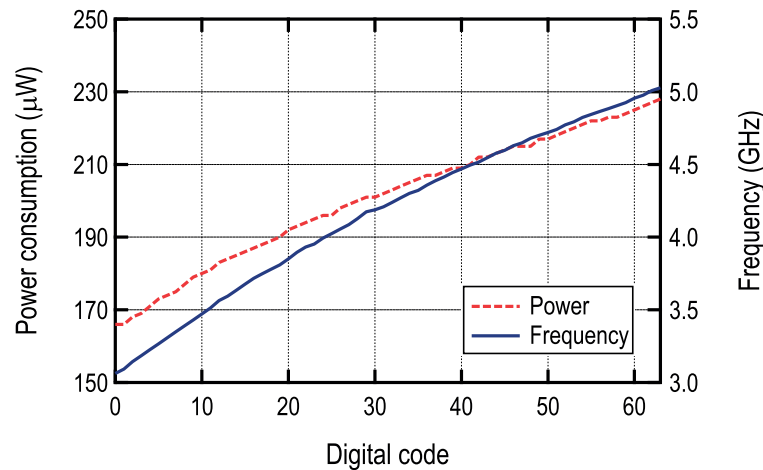


Figure 5.43: Measured frequency and power consumption of the MU Rx DCO.

5.4.2 Receiver Measurements

The two receivers are mainly characterized in terms of BER and sensitivity under different conditions. Unfortunately there is no way to access different internal points of the receiver and characterize each block separately. Addition of buffers that would allow this would result in increased capacitance in the corresponding nodes, which would consequently increase the receiver power consumption. The buffers and test outputs are therefore added only at lower frequencies where such capacitive load causes no significant problems.

The DCOs of the two receivers are the most important blocks in the chain, since without downconversion it will be impossible to perform demodulation. Just like with the transmitter DCO, the frequency dividers are added to provide information about the DCO frequency and to close the FLL calibration loop. Unlike the transmitter DCO, linearity of the frequency characteristic is not needed on the receiver side. What is important is its monotonicity, that ensures proper operation of the SAR FLL loop. The frequency and power consumption of each DCO are measured using the frequency dividers and a digital output buffer. The result for the MU receiver is shown in Fig. 5.43. The provided result also includes the four DCO buffers for quadrature LO signals. The oscillator frequency ranges from 3 GHz to 5 GHz, while power consumption changes from 166 μW to 228 μW . The resulting frequency resolution changes from 35 MHz to 20 MHz as the oscillation frequency increases. The same measurement for the LP receiver is given in Fig. 5.44. Again, measured power consumption includes the buffer, or in this case the frequency tripler, since it reuses the current from the oscillator. In this case, the output frequency takes values from 3.6 GHz to 5.25 GHz, while it consumes between 51 μW and 77 μW . Due to

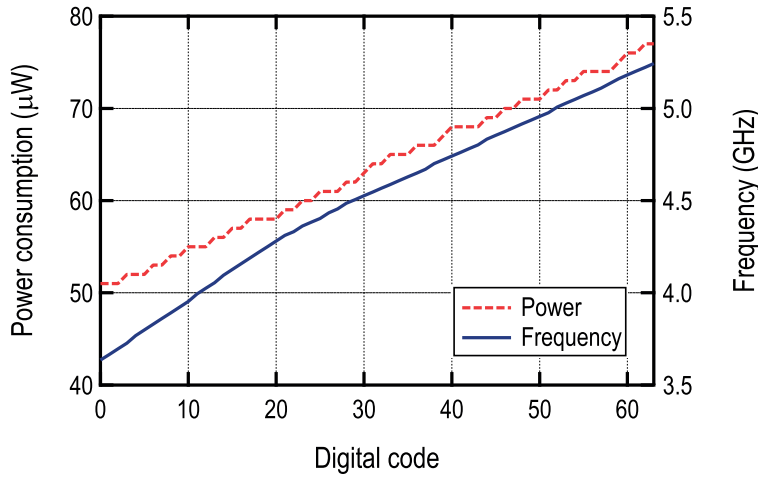


Figure 5.44: Measured frequency and power consumption of the LP Rx DCO.

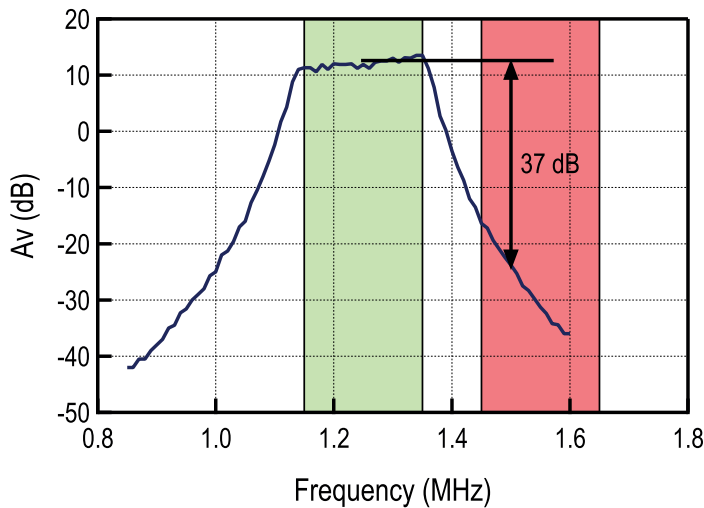


Figure 5.45: N-path filter measured characteristic for center frequency of 1.25 MHz.

nonlinear behavior of the oscillator, the frequency step reduces from around 30 MHz at the lower end, to 20 MHz at the high end.

Another block that can be measured standalone is the N-path filter. Figure 5.45 shows the voltage gain characteristic of the filter. Used input clock frequency is 5 MHz, which results in the filter center frequency of 1.25 MHz. For the given configuration, the filter provides 200 kHz of bandwidth, and attenuation of 37 dB at the frequency of the adjacent sub-carrier, which is 250 kHz away from the filter center frequency. As expected, the characteristic in the pass-band is not entirely flat. A small inclination appears as a result of parasitic capacitances in the layout, however, for this particular case the performance should not be affected. The purpose of the N-path filter is to remove the interfering sub-carrier channels. As a demonstration, the spectrum before and after the filter is shown in Fig. 5.46. Signal spectrum after the wideband FM demodulator is shown in top part of the figure. Four FM-UWB signals of equal power are present at the receiver input. After demodulation, four SC channels can be

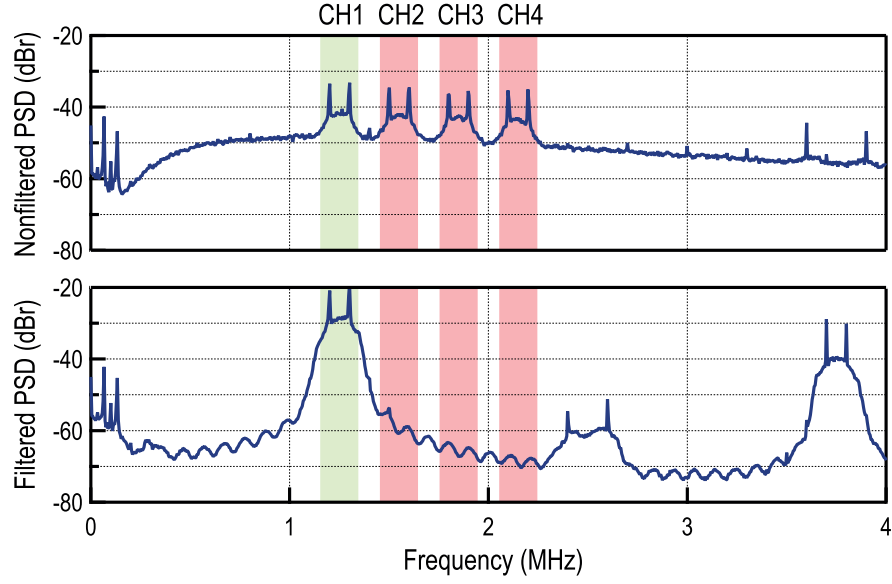


Figure 5.46: Demodulated signal spectrum before and after N-path filter.

Table 5.2: MU receiver power consumption breakdown

Block	Current cons. (μA)	Relative cons. (%)
LNA/Mixer	153	27.8
DCO	79	14.4
DCO Buffer	115	20.9
IFA	113	20.5
FM Demodulator	13	2.4
Channel filter	43	7.8
LFA	6	1.1
FSK Demodulator	8	1.5
Bias	20	3.6
Total	550	100

distinguished in the spectrum before filtering. After passing through the filter only channel 1 remains (bottom). Component at 3.75 MHz is a consequence of the sampled nature of the system. With the clock frequency of 1.25 MHz and 4 phases, the equivalent sample rate will be 5 MHz. Attenuated copy of the signal spectrum therefore appears at the frequency $(N - 1)f_{clk}$, where n is a number of phases, which is 3.75 MHz. Another visible component is the second harmonic of the SC channel at 2.5 MHz. This component is the combination of the output buffer non-linearity, and mismatch of the N-path filter. Ideally, second harmonic should be completely suppressed by the differential architecture of the N-path filter, however, in practice the amount of attenuation will be limited by matching.

Power consumption breakdown for the MU receiver is given in Table 5.2. As expected the highest amount of power is consumed by the high frequency blocks, the active mixer and the DCO, that together consume around 60% of the entire receiver consumption. The dominant consumer still remains the DCO, with buffers included, that consumes 194 μW . Among the low frequency blocks, notable amount of power is used for the N-path filter that provides sharp band-pass filtering. An overhead necessary

Table 5.3: LP receiver power consumption breakdown

Block	Current cons. (μA)	Relative cons. (%)
LNA/Mixer	103	38.6
DCO	53	19.9
IFA	46	17.2
FM Demodulator	23	8.6
LFA	11	4.1
FSK Demodulator	14	5.2
Bias	17	6.4
Total	267	100

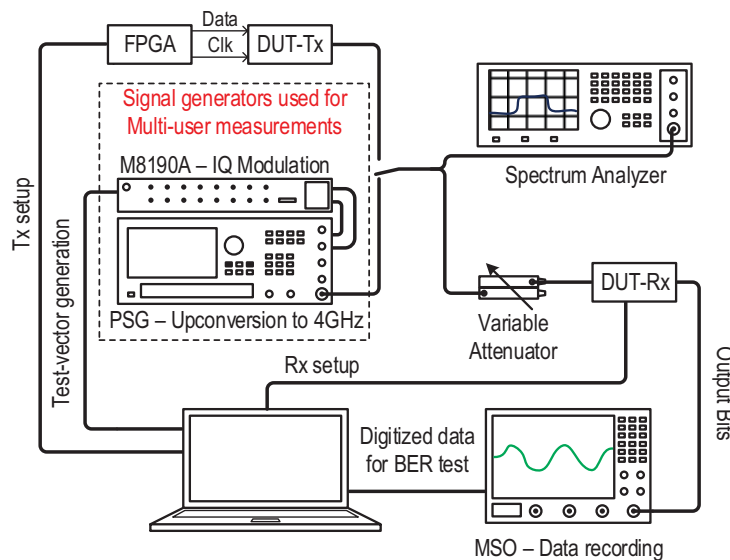


Figure 5.47: Test setup used for transceiver characterization.

to provide the multi-user capability. Finally, the total consumption of the MU receiver is $550 \mu\text{W}$. This is more than the receiver presented in the previous section, mainly due to the fact that the baseband processing is now placed on chip.

Power consumption breakdown for the LP receiver is given in Table 5.3. The strategy with power reduction is to reduce power of some of the main consumers from the MU receiver. Firstly, the DCO, that is now single-ended, consumes slightly more than one quarter of the MU DCO consumption, that is $53 \mu\text{W}$. One downside of the LP oscillator is the lower output amplitude that will affect the sensitivity. The active mixer, consumes a comparable amount of power, since the architecture is the same, with the only difference that a single differential signal is used at the output (there are no I and Q branches). A second significant power saving is coming from the IF amplifier. Since there is no need for two branches, in the LP receiver the consumption is practically halved compared to the MU receiver case. The IFA consumes $46 \mu\text{W}$ instead of $113 \mu\text{W}$ in the MU receiver. The total power consumption adds up to $267 \mu\text{W}$ for the whole LP receiver chain.

The measurement setup used for the BER measurements is shown in Fig. 5.47. The transmit bits

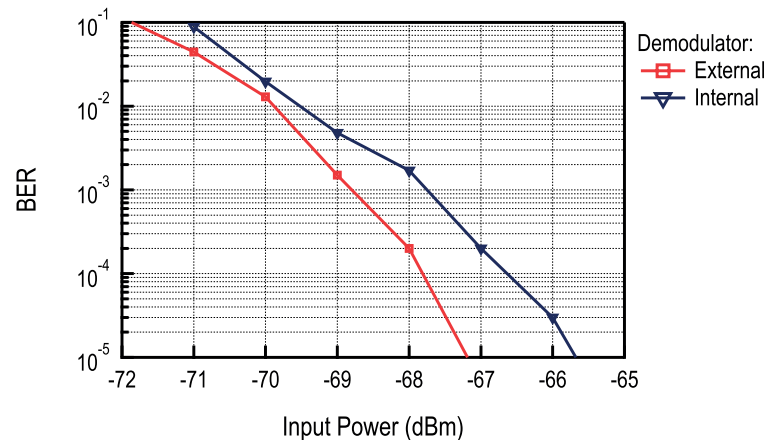


Figure 5.48: Single user BER of the MU Rx with internal and external demodulator at 100 kb/s.

and input vectors for signal generators are created using Matlab. A configured FPGA then provides clock and data inputs for the transmitter. The spectrum analyzer is used to verify that the proper signal is generated by the transmitter and to measure the signal level at the receiver input. Multi-user measurements are still done using the signal generators. This simplifies the setup and allows to precisely control the relative power levels of different FM-UWB signals. The M8190A AWG provides the quadrature baseband signals, which are then up-converted by the PSG. The MSO oscilloscope is used to capture data at the receiver output.

All the BER curves are measured in two ways, first using the offline data post processing, and then using the on-chip FSK demodulator. This allows to measure the loss of the on-chip FSK demodulator compared to the ideal demodulator implemented in software. For the offline BER measurement, the MSO acts as a 20 MS/s, 10 bit ADC that captures analog data after the wideband FM demodulator. This data is then processed using software. First, the desired channel is filtered using an FIR band-pass filter to remove any undesired adjacent sub-channels. Then it is passed through a correlator, that is an optimal detector for the orthogonal FSK modulation used. The output bits are then compared to the generated test vector. In the second measurement, that uses the on-chip FSK demodulator, digital outputs are available, logic analyzer is used to sample data on a rising edge of the recovered clock. It is worth mentioning that the second measurement takes significantly less time (and memory) since the number of samples is significantly lower and corresponds to the number of bits. In the first case 200 samples are captured per received bit in order to perform the demodulation in software. This corresponds to a sampling frequency roughly 10 times higher than the sub-carrier frequency.

The BER curves for the MU receiver and the single user case are presented in Fig. 5.48. The curves for both external (software) and internal demodulator are shown. In the case of the external demodulator the sensitivity is -69 dBm. The result is similar to the previous receiver implementation, with some losses due to a more complex input matching network. The internal demodulator adds 1 dB loss compared to the ideal software demodulator, resulting in a receiver sensitivity of -68 dBm. Accounting for approximately 2 dB loss due to a non-ideal LO, and 1 dB loss due to a non-ideal FSK demodulator, this is roughly 7 dB worse than the theoretical result.

The BER curves for the LP receiver in the single user case are presented in Fig. 5.49. Just like in the above case, both curves, for the external and internal demodulator, are shown. In the case of the external

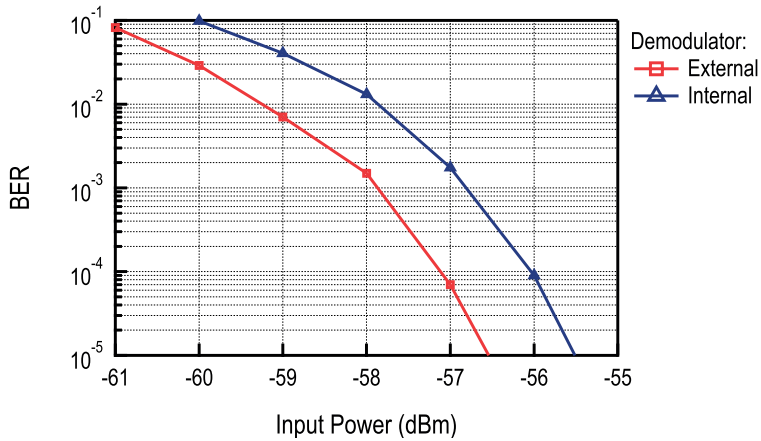


Figure 5.49: Single user BER of the LP Rx with internal and external demodulator at 100 kb/s.

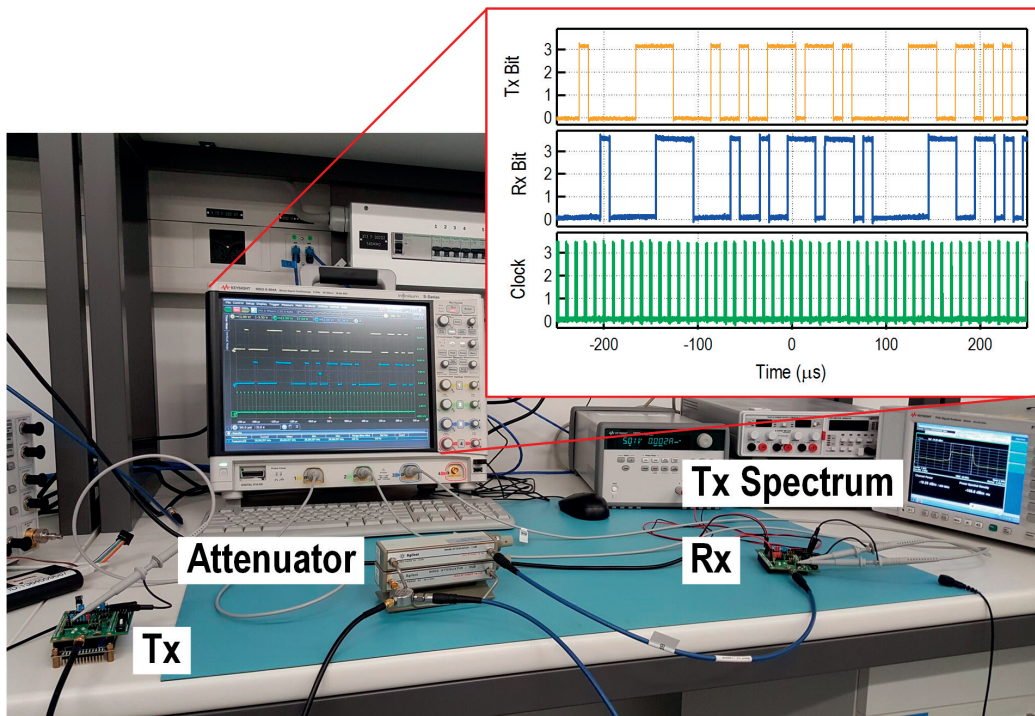


Figure 5.50: Measurement setup and comparison of transmit and received bits.

demodulator the sensitivity is -58 dBm. Accounting for the theoretical 6 dB difference in sensitivities between the two receivers, and higher noise figure of the LP receiver, the 11 dB degradation in sensitivity is expected. Compared to the theoretical sensitivity, same 7 dB degradation is observed as in the case of the MU receiver. This is the price to pay for lower power consumption of the LP receiver. Again, the simple, low power internal demodulator adds some loss, resulting in -57 dBm sensitivity of the LP receiver. Although sensitivity is relatively low compared to other FM-UWB receivers, it is still enough for short range communication in a WBAN, and the implemented receiver consumes the lowest amount of power among all the implementations reported in literature.

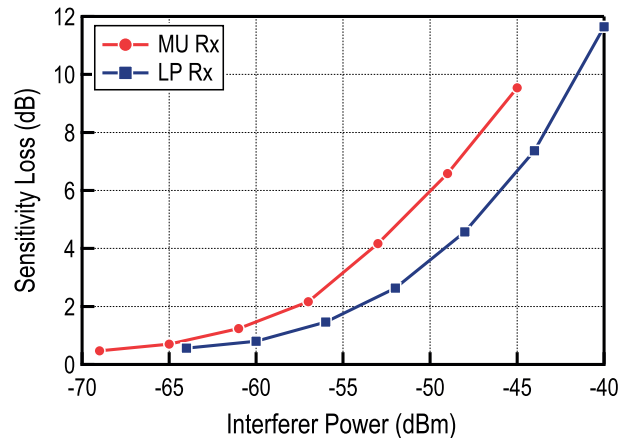


Figure 5.51: Sensitivity degradation due to the presence of an in-band interferer.

A photo of the measurement setup is shown in Fig. 5.50. Two boards can be seen in the figure, one is used as a transmitter and the other one as a receiver. The signal level on the receiver side is controlled using a configurable attenuator. Spectrum analyzer, showing the FM-UWB signal spectrum, is used to verify the proper operation of the transmitter and can be seen in the right part of the figure. In this case the oscilloscope is used to compare the transmitted and the received bits. The recording from the screen is shown clearly on the graph. Aside from the input and output data, the graph also shows the recovered clock used for sampling of the output data. A delay of approximately $20\mu\text{s}$ can be seen between the transmit and receive bit stream. In the shown example there are no errors present at the output.

The sensitivity of the receiver degrades in the presence of interferers. The behavior of the receiver is evaluated in the presence of a narrowband interferer inside and outside of the used FM-UWB band. The interferer is generated using a separate signal generator and the outputs are summed together using a power combiner. For the in-band interferer, a frequency of 4.1 GHz was chosen as the worst case. Placing the interferer close to the signal center frequency would attenuate it due to the high-pass characteristic of the IF amplifier, and placing it closer to edge of the band would again result in slightly lower IF gain due to the IFA low-pass behavior. The same frequency was used for both MU and LP receiver. The sensitivity degradation with the increase of interferer power is shown in Fig. 5.51. Assuming 3 dB sensitivity degradation is acceptable, the MU and LP receiver can tolerate up to -55 dBm and -52 dBm strong interferers respectively.

For the out of band interferer case, the frequency of 2.4 GHz was chosen. The reason is that the 2.4 GHz ISM band (industrial, scientific and medical) is commonly used by different short range BAN devices, and that this frequency could potentially be used to power the sensor nodes without contact. Within the scope of the WiseSkin project, sensor nodes are placed inside a flexible waveguide. This waveguide enables relatively low losses between different points and could allow efficient power transfer between the main node and the sensor nodes. Contactless powering would allow cheaper and easier manufacturing, and higher reliability of the WiseSkin solution. Details of the waveguide powering scheme are explained in the following chapter. Here the focus is on the receiver characterization, and so the aim is to evaluate what power level of the interferer can be tolerated at the receiver input. The sensitivity degradation in the presence of an out of band interferer is shown in Fig. 5.52. Assuming again

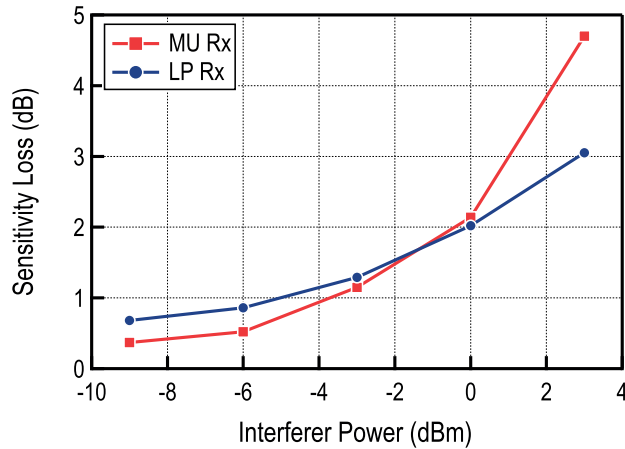


Figure 5.52: Sensitivity degradation due to the presence of an out of band interferer at 2.4 GHz.

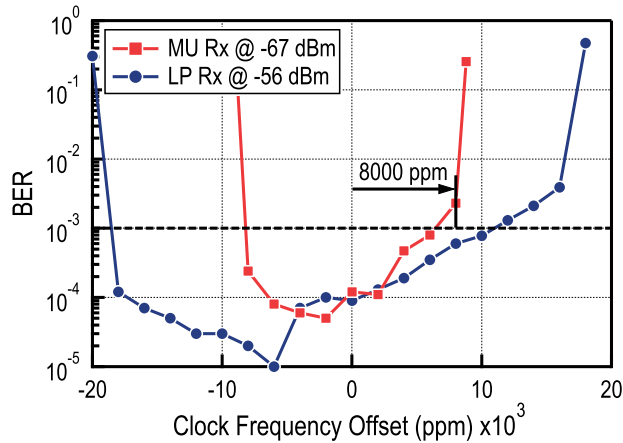


Figure 5.53: BER for a fixed input signal level with varying reference clock frequency.

3 dB sensitivity loss is acceptable, the MU receiver can tolerate 1 dBm interferer and the LP receiver can tolerate a 3 dBm interferer at 2.4 GHz. This is much higher than any other implementation and is due to the sharp filtering characteristic of the IF amplifier, that acts as a 6th order low pass filter. In most other implementations the interferer is only attenuated by the 2nd order LNA input matching network. This means that the proposed FM-UWB receivers can operate reliably next to any other device using the ISM band. Furthermore, the tolerable level of 1 dBm could be enough to supply power to the receiver. Assuming 50 % rectifier efficiency and 1 dBm power supplying signal, results in 630 μ W of available power, which is enough to power the transceiver in continuous mode of operation.

As discussed previously, FM-UWB is inherently robust against frequency offsets thanks to its large bandwidth. This is clear when it comes to tolerance to LO signal offset, however the property also applies to other parts of the system. After the wideband FM demodulation the sub-carrier channels are located between 1.2 MHz and 2.3 MHz. An offset of 1000 ppm translates into a maximum sub-carrier offset of 2.3 kHz, which would still not prevent correct FSK demodulation. For comparison, assume the same 1000 ppm offset is present in a Bluetooth transmitter that operates in the 2.4 GHz band. This

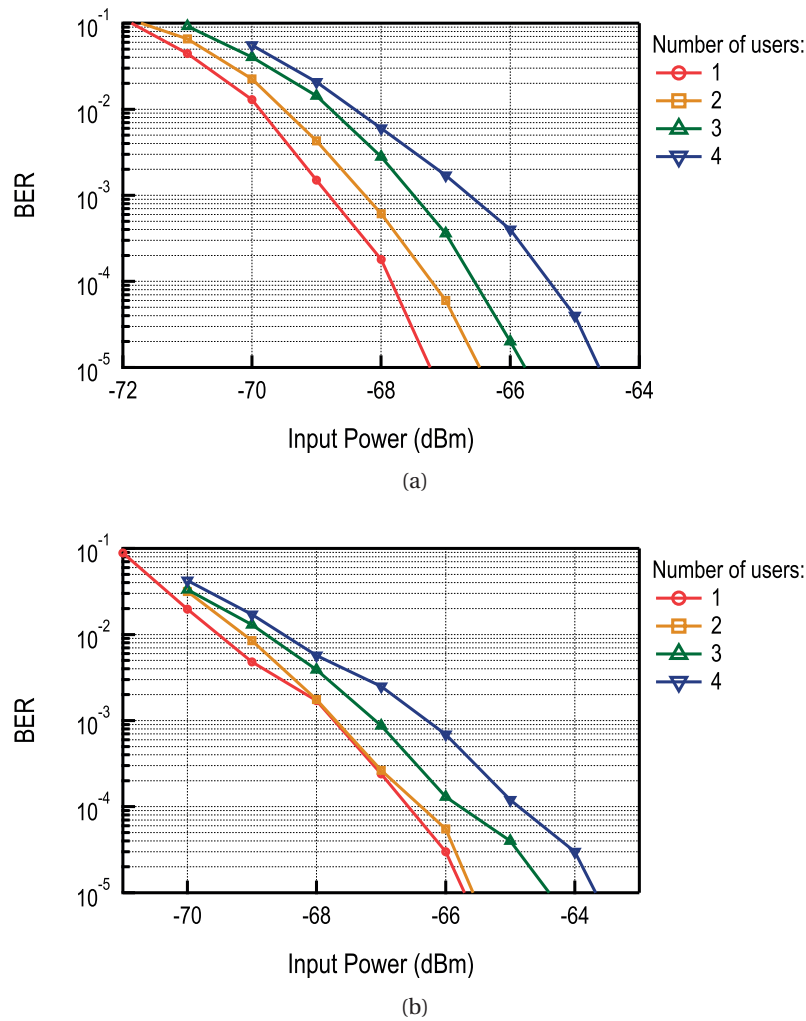


Figure 5.54: Measured BER curves for multiple FM-UWB users of same power level, demodulated with external (a) and internal (b) demodulator.

would roughly translate into an offset of 2.4 MHz, which is larger than a Bluetooth channel bandwidth. The example illustrates why an FM-UWB system has an advantage compared to typical narrowband systems. In fact, the FM-UWB receiver can tolerate a frequency offset much larger than 1000 ppm. Figure 5.53 shows the BER of the two receivers as a function of the receiver reference clock offset. The curves were measured at 1 dB below the sensitivity level, that is -67 dBm for the MU receiver and -56 dBm for the LP receiver. They show the amount of offset that can be tolerated before the sensitivity increases by 1 dB. Measurement was done with the fixed transmitter frequency reference and variable reference on the receiver side. Looking at the curves, two parts can be distinguished. The first is at relatively small offsets, where there is only a minor degradation in terms of BER. Then, it can be noticed that after offset increases beyond a certain point there is a sharp increase in BER. This is the region where clock recovery fails, and errors occur in sampling the decoded bits, which results in BER around 0.5. Interestingly, the LP receiver shows less degradation at higher offsets. The reason is that the sub-carrier frequency of the demodulated signal doubles after demodulation by the LP receiver. As a consequence the frequency deviation will be doubled and the FSK demodulator will be able to

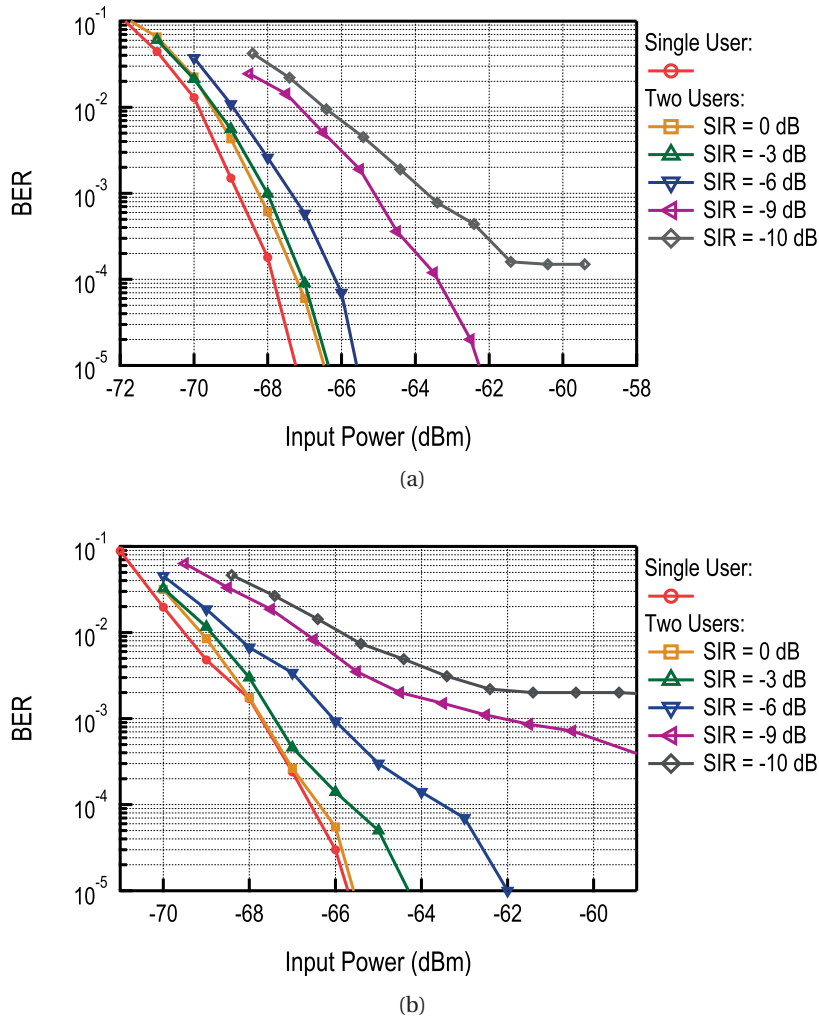


Figure 5.55: Measured BER curves for two FM-UWB users of different power levels, demodulated with external (a) and internal (b) demodulator.

operate more reliably at higher offsets. Both receivers are still able to perform reliable demodulation at offsets below 8000 ppm. This value is above the reported frequency deviation in state of the art on-chip reference oscillators. Therefore, the presented measurements clearly show that it is feasible to make a fully integrated FM-UWB transceiver, without external resonators for a reference clock.

The main advantage of the proposed MU receiver is the ability to distinguish multiple FM-UWB signals at the receiver input, provided that the sub-carrier frequencies are different. In the first scenario, multiple FM-UWB signals of equal power are present at the input. The measurement with the external demodulator is shown in Fig. 5.54(a), and the measurement with the internal FSK demodulator is shown in Fig. 5.54(b). The curves behave in a similar manner in both cases. As the number of users increases so does the inter-user interference and, as a result, the sensitivity degrades. In the case with 4 users a degradation of roughly 2 dB can be observed from the graph. As long as the power levels at the receiver input remain approximately equal, there will be no significant performance degradation. If several transmitting nodes are located at different distances from the receiving node, they can adjust

the their power levels so that the power at the receiver remains the same, and avoid the excessive sensitivity loss. This is the main reason why a transmitter that can adjust output power is useful for a HD-WSN.

A scenario with 2 users and a variable difference in power levels is shown in Fig. 5.55. Again, the inter-user interference increases with the increase in interferer power, and the resulting sensitivity degrades. With a sufficiently strong interferer at the input, the achievable SNIR after the first FM demodulation becomes limited by the interference, and the resulting BER curve flattens. The difference between the external and internal demodulation is clearly visible in Fig. 5.55(a) and Fig. 5.55(b). In both cases 10 dB stronger interferer results in a floor for the achievable BER. Since the external demodulator needs a 1 dB lower SNIR for the same performance, the BER curve flattens below $2 \cdot 10^{-4}$. In the case of the internal demodulator the curve flattens at $2 \cdot 10^{-3}$, and the desired sensitivity level remains unreachable. With the internal demodulator the receiver is capable of demodulating data if the difference of input levels is 9 dB or smaller. The limit is due to a combination of interference coming from the leakage of adjacent FSK sub-channels and cross modulation products between the two users in the process of the first FM demodulation.

5.5 Summary

A fully-integrated FM-UWB transceiver has been presented in this chapter. A single RF IO port is used, with an on-chip matching network, which eliminates the need for external passive components or switches. Two receivers provide two different modes of operation. The low power mode reduces the power consumption to 267 μ W, but only allows a single FM-UWB channel. To improve sensitivity and allow SC-FDMA, a MU receiver is used, that allows up to 4 FM-UWB transmitters to operate at the same time and in the same RF band. Inherent robustness against narrowband interferers, combined with sharp IF filtering, result in good in-band and out of band interferer rejection. This capability could allow to power the transceiver wirelessly using a 2.4 GHz narrowband signal. Finally, the transceiver is robust against reference clock offsets of up to 8000 ppm, effectively eliminating the need for an off-chip reference. Performance summary and comparison with the state of the art is given in Table 5.4.

The architecture of the implemented transmitter is very similar to the one from [3]. The solution from [3] uses a three stage DCO that generates one third of the carrier frequency. The three phases are combined using a frequency tripler that generates the FM-UWB signal. The tripler reuses the current of the power amplifier in order to minimize power consumption. One of the downsides of that approach is that the signal at one third of the frequency appears at the output together with its harmonics, which might violate the spectral mask. Second issue is that the tripler output power cannot be precisely controlled, which is a useful feature when a large number of nodes operate in a small area. In the proposed implementation this problem is solved by replacing the tripler with a class AB amplifier that drives the main PA. The output power can be regulated using the amplifier bias point, that also sets the bias of the main PA. In addition, the configurable buffer current, and matching network provide additional knobs for output power control, allowing steps smaller than 3 dB. The DCO directly produces the signal at 4 GHz, avoiding the problem with the spectral mask violation. The DCO together with buffers consumes slightly more than the DCO from [3], but this is compensated with a more efficient PA design, so that the overall transmitter consumption still improves.

The proposed receiver targets short range communication in a HD-WSN. Therefore, sensitivity constraint is not very stringent and emphasis is on reducing power and providing means for multi-user

Table 5.4: Comparison with the state-of-the-art transceivers

Parameter	[27] ⁽¹⁾⁽²⁾	[28]	[3]	This Work	
				LP	MU
Modulation	FM-UWB	Chirp-UWB	FM-UWB	FM-UWB	
Frequency	7.5 GHz	8 GHz	4 GHz	4 GHz	
Frequency deviation	25 kHz	-	250 kHz	50 kHz	
Receiver Cons.	9.1 mW	4/0.6 mW ⁽³⁾	580 μ W	267 μ W	550 μ W
Data Rate	50 kb/s	1 Mb/s	100 kb/s	100 kb/s	
FSK Sub-channels	2	No	No	No	4
SIR UWB	-	-	-	-	-9 dB
Matching Network	Ext.	Ext.	Ext.	Internal	
NB Interferer Power (in band)	-55 dBm	-	-52 dB ⁽⁴⁾	-52 dBm	-55 dBm
NB Interferer Power (@ 2.4 GHz)	-38 dBm @ 6 GHz	-	-38 dB ⁽⁴⁾	3 dBm	1 dBm
Ref. Clock Offset	-	-	-	8000 ppm	
Sensitivity	-88 dBm	-76 dBm	-80.5 dBm	-57 dBm	-68 dBm
Transmitter Cons.	-	2.8/0.42 mW ⁽³⁾	630 μ W	583 μ W	
Output Power	-	-	-12.8 dBm	-11.4 dBm	
Technology	0.25 μ m BiCMOS	65 nm	90 nm	65 nm	

⁽¹⁾Off-chip sub-carrier FSK demodulation ⁽²⁾Receiver only ⁽³⁾Without/with duty-cycling ⁽⁴⁾-70 dBm input signal power

communication. The receiver from [3] achieves very good sensitivity and low power consumption, but the demodulator characteristic is highly non-linear and it cannot support multiple sub-carrier channels. In addition it uses a frequency deviation of 250 kHz (or equivalently 500 kHz separation between the two sub-carrier frequencies), which allows for a simpler FSK demodulator implementation. In this work frequency deviation is reduced to 50 kHz in order to allow for multiple sub-carrier channels. A different demodulator implementation is necessary in order to demodulate an FSK signal with a modulation index of 1, which will consume slightly more power. Potential for multi-user communication with FM-UWB has been demonstrated before, for example, two different sub-carrier channels could be seen at the demodulator output from [27]. However, this implementation was only providing the first FM-UWB demodulation. The proposed receiver is the only fully integrated solution that provides support for multi-user communication. In addition, it also incorporates a clock recovery circuit that demonstrates the feasibility to integrate the full transceiver with no need for an off-chip crystal reference.

In this case there was no need for higher data rates, although it could be a topic of future research. Increasing data rate of the FM-UWB receiver would mainly require modifications in baseband, and so the overhead in terms of power consumption should remain very low. This should lead to a more efficient implementation, that could achieve even lower energy per bit. Multi-user communication could be explored further, combining either larger number of lower data rate channels, or fewer channels that provide higher data rates, depending on the needs of the specific application. Finally, there could be more room for improvements at the modulation level. The Chirp-UWB concept, that is positioned somewhere between the IR and FM UWB, provides higher data rates, without a significant increase in complexity, and symbol level duty cycling of the receiver provides very low power consumption. Similar modifications could be a topic of future research and could lead to different performance trade-offs.

References

- [1] J. Chabloz, D. Ruffieux, and C. Enz, "A low-power programmable dynamic frequency divider," in *Solid-State Circuits Conference, 2008. ESSCIRC 2008. 34th European*, Sep. 2008, pp. 370–373.
- [2] P. Nilsson, J. F. M. Gerrits, and J. Yuan, "A low complexity DDS IC for FM-UWB applications," in *2007 16th IST Mobile and Wireless Communications Summit*, July 2007, pp. 1–5.
- [3] N. Saputra and J. R. Long, "A fully integrated wideband FM transceiver for low data rate autonomous systems," *IEEE Journal of Solid-State Circuits*, vol. 50, no. 5, pp. 1165–1175, May 2015.
- [4] N. Saputra and J. Long, "A Fully-Integrated, Short-Range, Low Data Rate FM-UWB Transmitter in 90 nm CMOS," *IEEE Journal of Solid-State Circuits*, vol. 46, no. 7, pp. 1627–1635, July 2011.
- [5] A. Hajimiri, S. Limotyakis, and T. H. Lee, "Jitter and phase noise in ring oscillators," *IEEE Journal of Solid-State Circuits*, vol. 34, no. 6, pp. 790–804, Jun 1999.
- [6] P. Reynaert and M. Steyaert, *RF Power Amplifiers for Mobile Communications*, ser. Analog Circuits and Signal Processing. Springer Netherlands, 2006.
- [7] S. Cripps, *RF Power Amplifiers for Wireless Communications*, ser. Artech House microwave library. Artech House, 2006.
- [8] J. Pandey and B. P. Otis, "A sub-100 μ W microwatts band transmitter based on injection-locking and frequency multiplication," *IEEE Journal of Solid-State Circuits*, vol. 46, no. 5, pp. 1049–1058, May 2011.
- [9] L. E. Franks and I. W. Sandberg, "An alternative approach to the realization of network transfer functions: The N-path filter," *The Bell System Technical Journal*, vol. 39, no. 5, pp. 1321–1350, Sep. 1960.
- [10] A. Ghaffari, E. A. M. Klumperink, M. C. M. Soer, and B. Nauta, "Tunable high-Q n-path band-pass filters: Modeling and verification," *IEEE Journal of Solid-State Circuits*, vol. 46, no. 5, pp. 998–1010, May 2011.
- [11] M. C. M. Soer, E. A. M. Klumperink, P. T. de Boer, F. E. van Vliet, and B. Nauta, "Unified frequency-domain analysis of switched-series-RC passive mixers and samplers," *IEEE Transactions on Circuits and Systems I: Regular Papers*, vol. 57, no. 10, pp. 2618–2631, Oct. 2010.
- [12] A. Mirzaei, H. Darabi, and D. Murphy, "A low-power process-scalable super-heterodyne receiver with integrated high-Q filters," *IEEE Journal of Solid-State Circuits*, vol. 46, no. 12, pp. 2920–2932, Dec. 2011.
- [13] C. Salazar, A. Cathelin, A. Kaiser, and J. Rabaey, "A 2.4 GHz interferer-resilient wake-up receiver using a dual-IF multi-stage N-path architecture," *IEEE Journal of Solid-State Circuits*, vol. 51, no. 9, pp. 2091–2105, Sep. 2016.
- [14] C. Andrews and A. C. Molnar, "A passive mixer-first receiver with digitally controlled and widely tunable RF interface," *IEEE Journal of Solid-State Circuits*, vol. 45, no. 12, pp. 2696–2708, Dec. 2010.
- [15] D. Yang, C. Andrews, and A. Molnar, "Optimized design of n-phase passive mixer-first receivers in wideband operation," *IEEE Transactions on Circuits and Systems I: Regular Papers*, vol. 62, no. 11, pp. 2759–2770, Nov 2015.
- [16] M. Darvishi, R. van der Zee, E. A. M. Klumperink, and B. Nauta, "Widely tunable 4th order switched G_m -C band-pass filter based on N-path filters," *IEEE Journal of Solid-State Circuits*, vol. 47, no. 12, pp. 3105–3119, Dec. 2012.
- [17] M. Darvishi, R. v. d. Zee, and B. Nauta, "A 0.1-to-1.2 GHz tunable 6th-order N-path channel-select filter with 0.6 dB passband ripple and +7 dBm blocker tolerance," in *2013 IEEE International Solid-State Circuits Conference Digest of Technical Papers*, Feb 2013, pp. 172–173.
- [18] M. Darvishi, R. van der Zee, and B. Nauta, "Design of active N-path filters," *IEEE Journal of*

- Solid-State Circuits*, vol. 48, no. 12, pp. 2962–2976, Dec. 2013.
- [19] F. Krummenacher and N. Joehl, “A 4-MHz CMOS continuous-time filter with on-chip automatic tuning,” *IEEE Journal of Solid-State Circuits*, vol. 23, no. 3, pp. 750–758, June 1988.
- [20] S. D’Amico, M. D. Matteis, and A. Baschirotto, “A 6th-order 100 μ A 280 MHz source-follower-based single-loop continuous-time filter,” in *2008 IEEE International Solid-State Circuits Conference - Digest of Technical Papers*, Feb 2008, pp. 72–596.
- [21] S. D’Amico, M. Conta, and A. Baschirotto, “A 4.1-mW 10-MHz fourth-order source-follower-based continuous-time filter with 79-dB DR,” *IEEE Journal of Solid-State Circuits*, vol. 41, no. 12, pp. 2713–2719, Dec 2006.
- [22] D. Griffith, P. T. Røine, J. Murdock, and R. Smith, “17.8 a 190 nW 33 kHz RC oscillator with ± 0.21 % temperature stability and 4ppm long-term stability,” in *2014 IEEE International Solid-State Circuits Conference Digest of Technical Papers (ISSCC)*, Feb. 2014, pp. 300–301.
- [23] K. J. Hsiao, “A 32.4 ppm/ $^{\circ}$ c 3.2-1.6V self-chopped relaxation oscillator with adaptive supply generation,” in *2012 Symposium on VLSI Circuits (VLSIC)*, June 2012, pp. 14–15.
- [24] A. Paidimarri, D. Griffith, A. Wang, A. P. Chandrakasan, and G. Burra, “A 120 nW 18.5 kHz RC oscillator with comparator offset cancellation for ± 0.25 % temperature stability,” in *2013 IEEE International Solid-State Circuits Conference Digest of Technical Papers*, Feb. 2013, pp. 184–185.
- [25] T. Tokairin, K. Nose, K. Takeda, K. Noguchi, T. Maeda, K. Kawai, and M. Mizuno, “A 280 nW, 100 kHz, 1-cycle start-up time, on-chip CMOS relaxation oscillator employing a feedforward period control scheme,” in *2012 Symposium on VLSI Circuits (VLSIC)*, June 2012, pp. 16–17.
- [26] J. Masuch and M. Delgado-Restituto, “A 1.1-mW-RX -dBm Sensitivity CMOS Transceiver for Bluetooth Low Energy,” *IEEE Transactions on Microwave Theory and Techniques*, vol. 61, no. 4, pp. 1660–1673, Apr. 2013.
- [27] Y. Zhao, Y. Dong, J. F. M. Gerrits, G. van Veenendaal, J. Long, and J. Farserotu, “A short range, low data rate, 7.2 GHz-7.7 GHz FM-UWB receiver front-end,” *IEEE Journal of Solid-State Circuits*, vol. 44, no. 7, pp. 1872–1882, July 2009.
- [28] F. Chen, Y. Li, D. Liu, W. Rhee, J. Kim, D. Kim, and Z. Wang, “A 1mW 1Mb/s 7.75-to-8.25GHz chirp-UWB transceiver with low peak-power transmission and fast synchronization capability,” in *2014 IEEE International Solid-State Circuits Conference Digest of Technical Papers (ISSCC)*, Feb. 2014, pp. 162–163.
- [29] A. Ghaffari, E. Klumperink, and B. Nauta, “8-Path tunable RF notch filters for blocker suppression,” in *2012 IEEE International Solid-State Circuits Conference*, Feb. 2012, pp. 76–78.

6 Efficient Contactless Waveguide Power Transfer

Delivering power to *WiseSkin* sensor nodes requires particular attention. Even though the data is conveyed wirelessly, wires are still needed to provide power to the nodes. In order to allow for unobstructed movement of the prosthesis, power lines must be sufficiently thin, flexible and stretchable. One solution, developed over the course of the *WiseSkin* project, is to print a metallic grid on the skin substrate (typically PDMS) using stretchable biphasic thin metal films [1], and then connect sensor nodes to this grid. However, the rigid metallic connections between the elastic grid and the sensor nodes have been identified as a reliability issue, as over the extended period of use these wires would break. Contactless solution could improve the robustness of the *WiseSkin* sensor network, and is therefore preferred. In addition, such approach eases production, at the same time reducing cost, and allows easier replacement of sensor nodes in case of malfunction.

Wireless power transfer (WPT) takes place in any system where electrical energy is transmitted from a power source to an electrical load without interconnecting wires. With the development of electronics, short distance wireless power transmission has become popular in consumer and medical electronics [2]. In parallel, it has been shown that reasonable efficiency may be obtained at larger distances by using dedicated, highly directive antennas. Providing power without contact allows to preserve the freedom of movement and reduces the system price (by removing wires), but the benefits of WPT extend beyond cost and convenience. Certain conditions, environments, and applications are simply unsuitable for conventional wired sources of electricity. Our research interest lays in mid- and short-distance WPT systems, covering distances from a few centimeters to a few meters using guided electromagnetic waves at RF. Although *WiseSkin* is the primary targeted application, the use of such systems can be extended to smart materials, wearable devices and tactile robots.

The chapter begins with an introduction to the general concept of wireless power transfer. Then, the initial, wired and the proposed *WiseSkin* powering systems are described, explaining all the benefits of the WPT approach. Section 6.3 shows the antenna design, followed by the results of measurements with different waveguide samples and a summary of achieved results.

6.1 Wireless Power Transfer

The concept of wireless power transfer first appeared close to the end of the 19th century, when Tesla and Hertz demonstrated its feasibility. Today, WPT is still a topic of research and is used in systems where wires are impractical and limit the functionality of the device. Different types of WPT systems can be found in existing products and literature, and can be classified according to the distance and type of coupling used between the transmitter and the receiver.

Inductive coupling is typically used in short-range wireless power transmission for charging smartphones, smartwatches, tablets, or other devices. Two standards for short-range wireless charging have been adopted by the industry, the Qi and the AirFuel standard (which is a merger of former A4WP and PMA standards) [3, 4]. These wireless charging systems operate at low frequencies and are capable of providing high efficiency, but are limited to a few centimeters range and are usually sensitive to misalignment of the transmit and receive coil [5]. The misalignment issue can be solved either by guided positioning of the charged object (using e.g. a magnet), by moving the transmit coil, or by using an array of coils that detect the position of the object. Generally, a communication link is also established between the charger and the object. The two standards use different approaches. The Qi standard uses the existing inductive link to establish communication through load modulation, meaning that no additional hardware is needed, but communication might affect the charging efficiency. The AirFuel takes a different approach and uses a Bluetooth link, that is completely independent and does not affect WPT, but needs a separate antenna and dedicated hardware.

Dedicated WPT systems targeting large distances have also been implemented, but due to losses between the transmitter and receiver efficiency is typically much lower. The efficiency in these systems highly depends on antenna directivity and size, and is once again sensitive to misalignment [6]. Another approach that was explored in the literature was energy harvesting from available, widely spread sources (such as GSM for example) [7, 8, 9]. In this case, the devices are operating in the far field, and since much of the power is lost in free space, lower power levels are available at the receiver input. Low power levels usually result in low signal swing at the rectifier input and therefore lower efficiency. The main limit to rectenna efficiency at low power levels comes from the threshold voltage of the rectifier diodes [10], since this threshold is comparable to the input signal amplitude. Various approaches to improve performance have been proposed in literature, some focusing on the multi-band antenna design [11, 12] and others focusing on improving the matching network, the rectifier or the power management circuits [13, 14]. Effort has also been made towards integrating the rectifier in standard CMOS technologies. Different techniques have been proposed in order to compensate the threshold voltage of the MOS transistor [15, 16, 17] such as body biasing or clever interconnection techniques. However, the CMOS solutions are still unable to reach the efficiency achieved by using rectifiers with Schottky diodes [18]. To truly optimize efficiency, a co-design of the rectifier and antenna is needed [19]. These are usually referred to as the rectenna, and were invented by W.C. Brown in 1964. Due to the non-linearity of the rectifier circuit, impedance matching becomes a difficult problem. Because of the time-variant impedance seen from the antenna, the classical complex-conjugate matching approach cannot be used directly. Finally, low efficiency combined with low available input power result in systems that can only provide power on the order of microwatts [18].

The solution proposed here does not fit exactly into any of the described categories, but has similarities with each of them. In the *WiseSkin* case, the sensor nodes are usually located in the far field of the transmitting device, and in that sense the approach resembles far field RF energy harvesters. However, as shown in the following section, the two existing metallic layers constitute a waveguide and prevent

significant losses. This allows relatively high power levels at the sensor nodes, and consequently higher efficiency. In that regard the proposed system has more similarities with the short-range inductively coupled devices. Finally, the expected efficiency should be somewhere between the RF energy harvesters and the near field chargers.

6.2 System Description

Illustration of the original wired *WiseSkin* solution is presented in Fig. 6.1(a), showing the inner dielectric layer, the two metallization layers, the sensor node and the two wired connections to power and ground. The main source of unreliability is the interface between the stretchable metallic layers and the rigid sensor node, implemented on a standard FR4 PCB. During initial experiments with the artificial skin prototype, these wires would often break, thus completely disabling the sensor node. They are difficult to implement and effectively increase production cost and complexity of the system. Furthermore, once the wires are placed, the sensor node is fixed and cannot be easily replaced or moved to another location (ex. in case of malfunction). Assuming lower energy efficiency of the system can be tolerated, all of the mentioned issues can be solved by WPT.

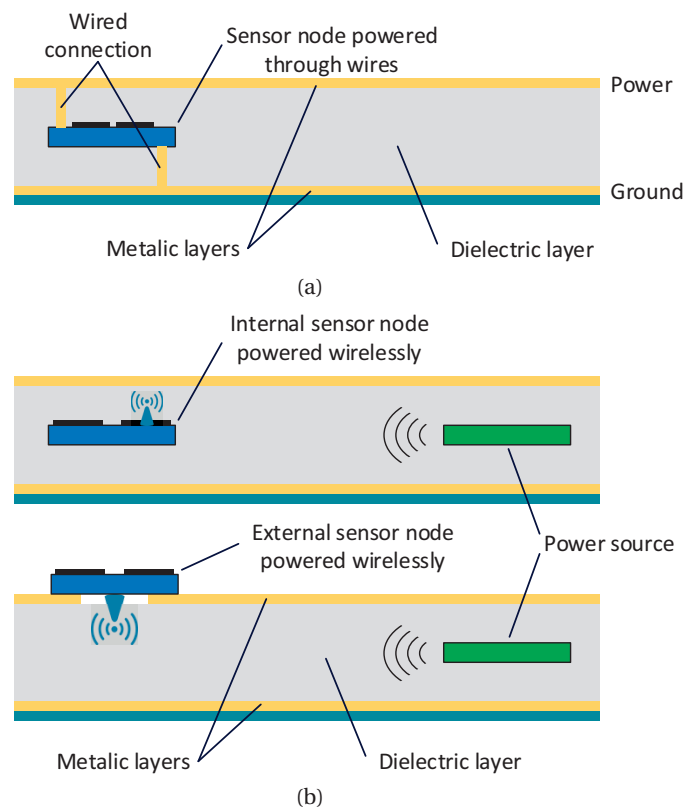


Figure 6.1: General concept of a sensor node powered through wires (a) and a sensor node powered via RF energy, harvested from a master or powering node (b). RF energy is distributed via the flexible waveguide.

Chapter 6. Efficient Contactless Waveguide Power Transfer

The proposed WPT system [20, 21] is shown in Fig 6.1(b). The system is wireless in the sense that there is no mechanical connection between the node and the metallic layers. However, the two metallic layers remain present, and together with the flexible middle layer (dielectric such as silicone, textile etc.) form a flexible and stretchable parallel plate waveguide. The power is distributed via the RF electromagnetic (EM) waves. The principle is similar to that of existing energy harvesters [18], with one important difference. Typically, these harvesters are designed to gather energy from EM waves already present in the air. Since most of the energy is lost in free space, input power levels are low and only modest efficiency can be achieved, unless a dedicated highly directive antenna is used. The proposed system exploits the existing waveguide to confine the transmitted energy and increase the overall efficiency by guiding the wave from the power source to the sensor node. Since relatively high input power levels are available (going up to 10 dBm), the rectifier converting the RF signal into dc power can operate in the high efficiency region, thus improving the overall system efficiency.

The general principle can be extended beyond the scope of the *WiseSkin* solution to different applications such as wearable electronics, health care or robotics [22]. Additionally, sensor nodes do not necessarily need to be placed inside the waveguide. They can also be placed on top of the artificial skin, in which case the slot in the metallic layer acts as an antenna. Depending on the application, a battery (or other means of storing the energy, such as supercapacitors) can be placed on the sensor node. This would allow to charge the nodes first, and then turn them on to collect data and transmit. This approach simplifies hardware since charging and communication occur in different time instants, but the battery increases size and cost of the node. Since in *WisesSkin*, the miniaturization of nodes is paramount, a solution without a battery is preferred. To enable batteryless operation, communication and powering need to coexist, meaning that the communication device needs to be able to operate in the presence of a strong interferer. Fortunately, the used FM-UWB modulation is inherently robust against narrowband interferers. As shown in the previous chapter, the two receivers can tolerate up to 3 dBm input signal at 2.4 GHz. Assuming the efficiency of the rectifier and the converter can be kept above 50 %, and with the sub-milliwatt consumption of the radio in mind, such signal could be used to power the sensor nodes. The described solution follows the approach of AirFuel, with completely separated powering and communication channel.

The proposed flexible waveguide structure confines and guides the electromagnetic power, enabling practical means of remote powering and batteryless operation of sensor or actuator nodes. The solution is contactless and wireless, and conformable to different surfaces as required by the application. The proposed solution offers the following benefits:

- Batteryless operation - allows smaller node footprint and a lower cost solution, but requires the communication and powering scheme to coexist.
- Increased robustness - no mechanical contacts or wires are needed for powering nor communication. Mechanical contacts are difficult to implement and could be the first source of failure. If power is provided wirelessly, even if the stretchable metallic layer is broken, the system remains functional and the loss in efficiency can be compensated by increasing the transmitted power, therefore improving reliability.
- Ease of manufacturing and lower cost - removal of the mechanical contacts eases manufacturing, thus also reducing cost and complexity.
- Configurability - assuming detachable layers can be produced, sensor and actuator devices may be placed at different locations within the flexible structure as they are not constrained

by wires or fixed connections. Furthermore this allows easier replacement of sensor nodes for maintenance, repair etc.

In this work the antenna and the waveguide are optimized for operation in the 2.4 GHz ISM band, although different bands can be used as well. Using higher frequencies leads to smaller antennas and further miniaturization of the sensor nodes. However, the efficiency of rectifiers, needed to convert the input RF signal into power, typically decreases at higher frequencies [18], leading to lower overall system efficiency. Additionally, the optimal frequency also depends on the thickness of the used material, which is constrained by other system parameters.

6.3 Antenna Design

The proposed antenna, shown in Fig. 6.2, is a compact capacitive loop solution optimized for integration into the PDMS (polydimethylsiloxane) structure with top and bottom metallization. As most miniature antenna solutions, the proposed antenna does not provide high bandwidth. However, it can be fairly easily tuned to the desired frequency, when all parameters are known. For example, by changing the feed location of the antenna, the resonance frequency will be smoothly shifted toward higher or lower frequency. Other parameters, like the antenna ground plane (GP) and the slot between the GP and the antenna element, can shift the antenna resonance frequency, as well as improve the antenna matching. The 10 mm by 10 mm antenna prototype is implemented on a 1.2 mm thick FR4 substrate.

The model for the antenna design and optimization through simulation is shown in Fig. 6.3 and consists of two elements. First is the PDMS structure represented by a 50 mm by 100 mm rectangular block with metallized top and bottom surfaces. These two plates constitute a parallel plate waveguide that guides RF waves to the sensor node. In the ideal case (infinite width and length) the waveguide properties are determined by its thickness and the dielectric constant and loss [23]. The second element is the antenna placed on one side of the PDMS block, close to the edge and in the middle between the top and bottom metallized layers. The model is used to assess the antenna matching in a simplified scenario that should correspond to the *WiseSkin* case. In reality the width and the length of the waveguide will vary and the shape will be more complex, in the particular case of *WiseSkin* corresponding to a human (or robotic) hand. In addition, the shape, particularly thickness, may change as the artificial skin moves, stretches and bends with the prosthetic arm. Finally, the full metal plate is just a representation of the real case, which should resemble a grid. However, as long as the holes in the grid are significantly

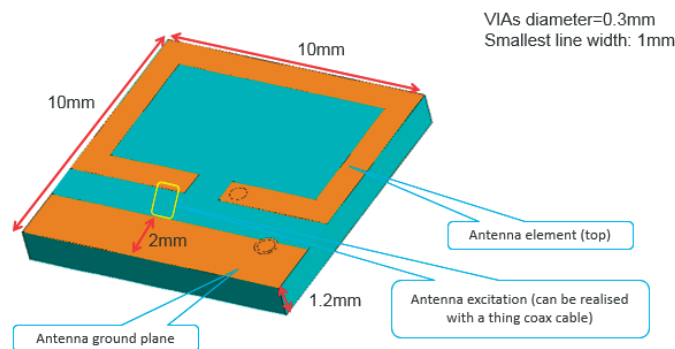


Figure 6.2: 3D model of the designed antenna.

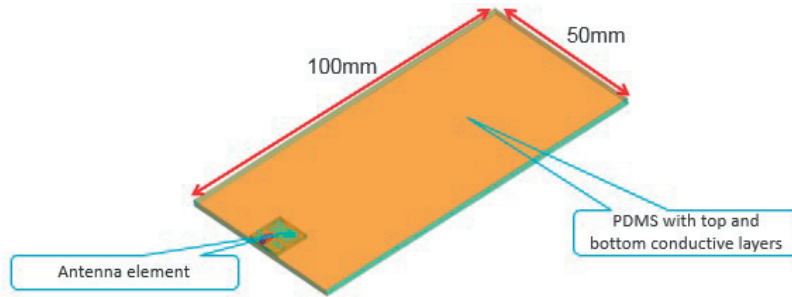


Figure 6.3: Model used for antenna optimization.

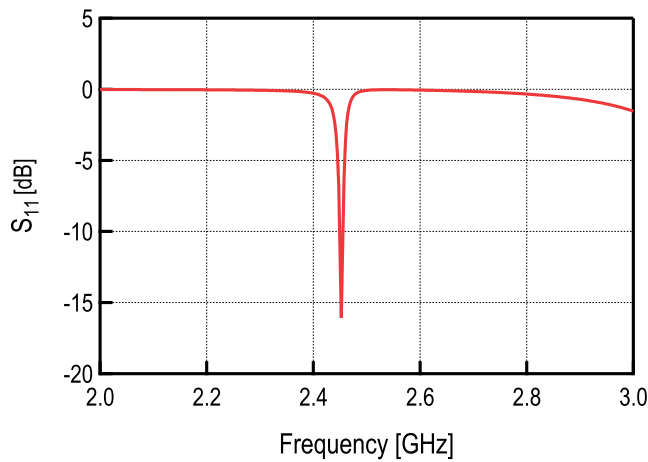


Figure 6.4: Simulated antenna S_{11} parameter, antenna is placed between the two metal layers.

smaller than the wavelength, and the thickness of the substrate sufficiently smaller than the other two dimensions, the presented model should be good enough to estimate the antenna performance. The simulated reflection coefficient is presented in Fig. 6.4, and shows that the antenna is matched at roughly 2.45 GHz.

6.4 Measurement Results

To assess the performance of the proposed power delivery system, several waveguide samples were used. A 125 mm thick PDMS sheet was used as the dielectric layer in all samples. To emulate the two metallic layers, conductive tape was placed on both sides of the PDMS, the width of the metallic trace is 16 mm. The used structure is shown in Fig. 6.6. Three samples of different lengths were used in order to measure performance for different distances between the transmit and the receive antenna: 60 mm, 120 mm and 275 mm. In addition, a second 275 mm long sample was used, with the top metallic layer cut in the middle (Fig 6.6). The cut is done in such a way that there is no electrical contact between the left and right part, but that the geometry of the waveguide remains preserved. This should correspond to the case where a fissure appears in the metallic layer of the skin (for example, as a result of a number of stretching cycles). The test setup is rather simple and consists of a two-port Vector Network Analyzer (VNA) connected to the measured sample using a miniature coaxial cable (μ FL). Ferrites are placed close to antenna connections to suppress common mode and radiation from the cables and parasitic

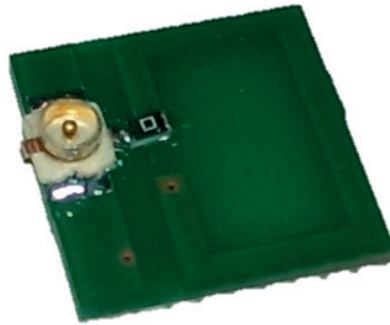


Figure 6.5: Manufactured antenna with a μ FL connector.

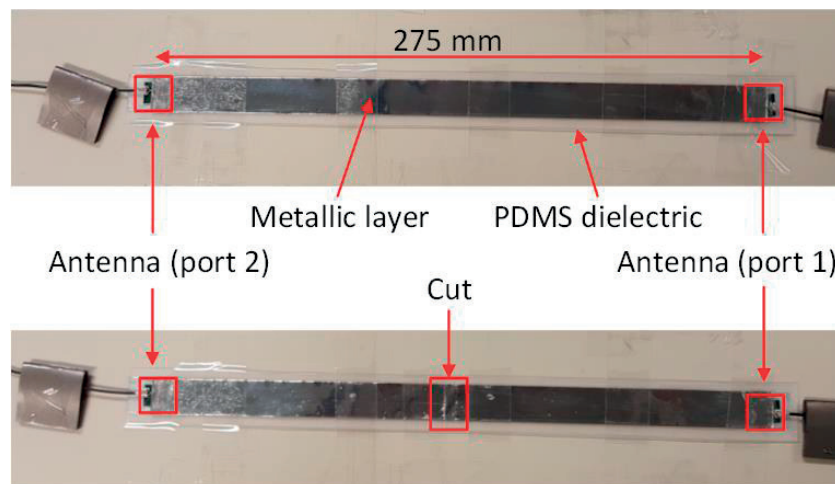


Figure 6.6: Examples of the used waveguide samples, 275 mm long waveguide (up) and the same waveguide with a cut in the middle (down).

coupling. The full test setup is shown in Fig. 6.7.

The s-parameters of all the measured samples are shown in Fig. 6.8. The reflection coefficient (S_{11}) shows good characteristics in all cases and is close to or below -10 dB around 2.45 GHz. The measured antenna resonance frequency roughly coincides with the simulated value. The differences compared to the simulated S_{11} curve mainly come from the different geometry of the tested samples. Other non-ideal effects are present as well, for example the thickness of the samples is not ideally constant, there might be air trapped between the conductive tape and the PDMS, the antenna is not ideally placed in the vertical sense (not exactly in the middle between the two metallic layers) etc. In addition, only a single antenna case is evaluated in the simulation. The presence of the second antenna will influence the reflection coefficient, particularly in the shortest sample, since it is in the near field of the transmit antenna, but also in other cases (although as the distance increases this effect should diminish). For the three cases where the waveguide is not damaged, transmission coefficient indicates relatively small losses, mainly caused by the antenna impedance mismatch. Looking at the small variation of results for the 120 mm and 275 mm samples it is expected that increasing the waveguide

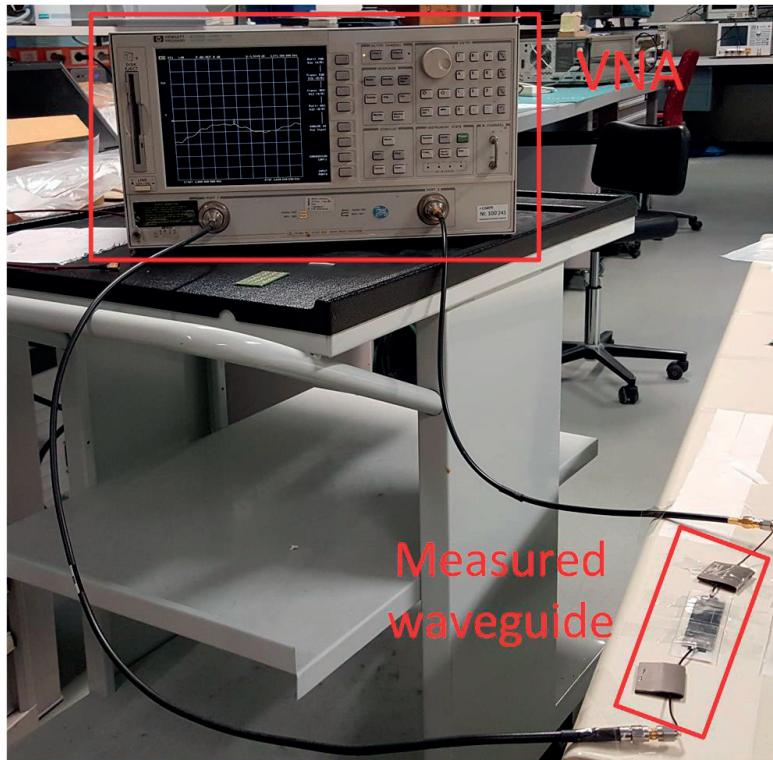


Figure 6.7: Test setup with the VNA and the implemented waveguide prototype.

length beyond this point does not introduce significant additional losses, and that the concept could be extended to distances of several meters. In this case the test samples are limited by the size of available PDMS sheets. Additional samples with larger width of the metallic plates (approximately 30 mm) were also measured, and they exhibited transmission coefficient lower by 1-2 dB. Since in this case the waveguide is roughly twice as wide as the antenna, this could imply that part of the energy located in the waveguide is not collected by the receiving antenna resulting in reduced energy available on the receiver side. The given example highlights the fact that waveguide geometry must be carefully optimized together with the antenna in order to obtain a good performance.

The transmission coefficient of the sample with a fissure in the metallic layer shows somewhat higher losses. The discontinuity in the metallic layer is likely causing reflections in the waveguide, resulting in reduced system efficiency, however, the energy transfer is still possible. If the metal traces were used to supply dc power to the node, such fissure would break the circuit and completely disconnect the sensor node. In this case the only consequence is the efficiency degradation, but the system remains functional, and increased losses can be compensated by increasing the transmitted power. All the results at 2.45 GHz are summarized in Tab. 6.1, together with the available power at the output, as a percentage of the transmitted power.

To gain insight into the expected overall efficiency of the proposed system (not accounting for the transmitter efficiency), efficiency of rectifiers and rectennas reported in literature is shown in Fig. 6.9. A note should be taken regarding the efficiency in the two cases. Rectenna efficiency takes into account both antenna and rectifier efficiency, meaning that losses due to antenna mismatch are taken into account. Rectifier efficiency assumes perfect antenna match, and therefore the overall efficiency reported for standalone rectifiers will decrease when antenna is added. The rectennas and rectifiers

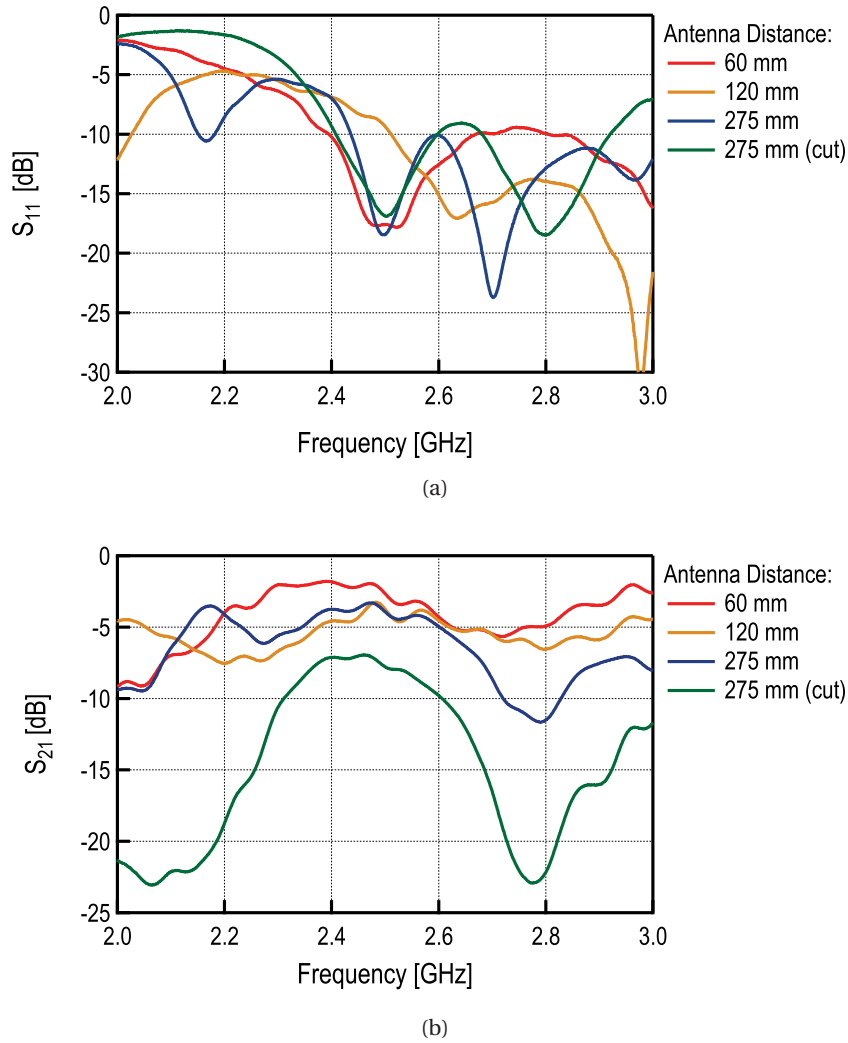
Figure 6.8: S-parameters for different antenna distances: (a) S_{11} and (b) S_{21} .

Table 6.1: Available output power

Distance [mm]	S_{21} [dB]	Available power [%]
60	-1.8	66.1
120	-3.2	47.8
275	-3.3	46.8
275 (cut)	-7	20.0

reported here are intended for energy harvesting, they were designed for free space, line of sight scenarios, but can nevertheless be used for rough efficiency estimation. For our application the focus is mainly on received power in the range from -5 dBm to 20 dBm. For that range the expected efficiency varies between 60 % and 80 %. For the shortest sample, the expected estimated efficiency should be between 40.7 % and 52.9 %. For the longest waveguide sample the efficiency should stay between 28 % and 37.4 %. Even if the metallic layer is damaged, the minimum expected efficiency should still remain above 12 % and could go up to 16 %.

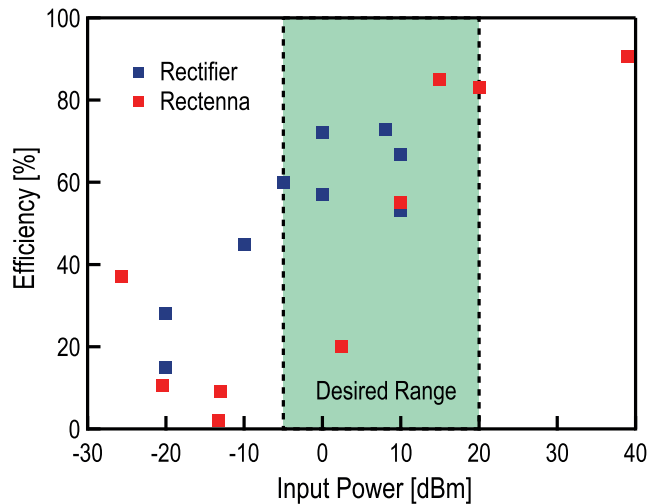


Figure 6.9: Reported efficiency of implemented rectifiers and rectennas at 2.4 GHz [18].

The proposed solution provides means of remote powering via guided propagation through a flexible, stretchable waveguide structure. The low loss waveguide structure enables efficient powering via EM energy, and therefore batteryless operation of sensors and actuators, reliable operation, lower production cost and higher configurability and flexibility. To truly enable batteryless operation, the radio on the sensor node must be able to work in the presence of a strong signal used for supplying power to the sensor nodes. In this case a narrowband signal at 2.4 GHz would be used to supply power to the nodes. As shown in the previous section the implemented FM-UWB receivers can still work in the presence of a 3 dBm, 2.4 GHz interferer. If power is provided by a 3 dBm signal at the receiver input, then available output power of the rectenna (assuming 60 % efficiency) would be 1.2 mW which is more than enough to supply the FM-UWB transceiver described in the previous section. The assumption here is that other components of the sensor node consume significantly less power than the radio.

6.5 Summary

The powering solution presented here is contactless and wireless, in the sense that there are no contacts required to power the nodes or to connect them. The metallic layers are still needed for the waveguide structure that enables high efficiency. The focus of the work is on a proof of concept used for powering a single node. Although a rather simplistic case, it demonstrates the feasibility of the proposed concept. The targeted system requires a more complex waveguide shape and consists of several sensor nodes that all need to be powered. This case remains a topic for future research. The irregularly shaped waveguide poses many new challenges that would inevitably cause more losses and lower overall efficiency. It would have to be optimized carefully with the antenna and the rectifier in order to achieve good performance. Higher frequencies could be considered for the proposed powering solution as well. Increasing the frequency would allow to decrease the size of antenna and the width of the waveguide, consequently also allowing to reduce the size of sensor nodes. Problem with increasing the frequency is that efficiency of the rectifier typically drops, which will result in lower system efficiency. The final choice of the waveguide geometry, frequency of operation and antenna size will be a trade-off between different demands and the exact system specification, that may vary with application.

References

- [1] A. Hirsch, H. O. Michaud, A. P. Gerratt, S. de Mulatier, and S. P. Lacour, “Biphasic metal films: Intrinsically stretchable biphasic (solid–liquid) thin metal films (adv. mater. 22/2016),” *Advanced Materials*, vol. 28, no. 22, pp. 4506–4506, 2016.
- [2] K. Jung, Y. H. Kim, E. J. Choi, H. J. Kim, and Y.-J. Kim, “Wireless power transmission for implantable devices using inductive component of closed-magnetic circuit structure,” in *2008 IEEE International Conference on Multisensor Fusion and Integration for Intelligent Systems*, Aug. 2008, pp. 272–277.
- [3] S. Y. Hui, “Planar wireless charging technology for portable electronic products and Qi,” *Proceedings of the IEEE*, vol. 101, no. 6, pp. 1290–1301, June 2013.
- [4] X. Lu, D. Niyato, P. Wang, D. I. Kim, and Z. Han, “Wireless charger networking for mobile devices: fundamentals, standards, and applications,” *IEEE Wireless Communications*, vol. 22, no. 2, pp. 126–135, Apr. 2015.
- [5] J. O. Mur-Miranda, G. Fanti, Y. Feng, K. Omanakuttan, R. Ongie, A. Setjoadi, and N. Sharpe, “Wireless power transfer using weakly coupled magnetostatic resonators,” in *2010 IEEE Energy Conversion Congress and Exposition*, Sep. 2010, pp. 4179–4186.
- [6] M. C. and A. H., “Design issues in radio frequency energy harvesting system,” *Sustainable Energy Harvesting Technologies - Past, Present and Future*, Dec. 2011.
- [7] H. Nishimoto, Y. Kawahara, and T. Asami, “Prototype implementation of ambient rf energy harvesting wireless sensor networks,” in *2010 IEEE Sensors*, Nov. 2010, pp. 1282–1287.
- [8] M. Piñuela, P. D. Mitcheson, and S. Lucyszyn, “Ambient RF energy harvesting in urban and semi-urban environments,” *IEEE Transactions on Microwave Theory and Techniques*, vol. 61, no. 7, pp. 2715–2726, July 2013.
- [9] X. Zhang, H. Jiang, L. Zhang, C. Zhang, Z. Wang, and X. Chen, “An energy-efficient ASIC for wireless body sensor networks in medical applications,” *IEEE Transactions on Biomedical Circuits and Systems*, vol. 4, no. 1, pp. 11–18, Feb 2010.
- [10] C. R. Valenta, M. M. Morys, and G. D. Durgin, “Theoretical energy-conversion efficiency for energy-harvesting circuits under power-optimized waveform excitation,” *IEEE Transactions on Microwave Theory and Techniques*, vol. 63, no. 5, pp. 1758–1767, May 2015.
- [11] X. Shao, B. Li, N. Shahshahan, N. Goldsman, T. S. Salter, and G. M. Metzger, “A planar dual-band antenna design for rf energy harvesting applications,” in *2011 International Semiconductor Device Research Symposium (ISDRS)*, Dec. 2011, pp. 1–2.
- [12] J. M. Barcak and H. P. Partal, “Efficient rf energy harvesting by using multiband microstrip antenna arrays with multistage rectifiers,” in *2012 IEEE Subthreshold Microelectronics Conference (SubVT)*, Oct 2012, pp. 1–3.
- [13] S. Oh and D. D. Wentzloff, “A -32 dBm sensitivity RF power harvester in 130 nm CMOS,” in *2012 IEEE Radio Frequency Integrated Circuits Symposium*, June 2012, pp. 483–486.
- [14] A. Dolgov, R. Zane, and Z. Popovic, “Power management system for online low power RF energy harvesting optimization,” *IEEE Transactions on Circuits and Systems I: Regular Papers*, vol. 57, no. 7, pp. 1802–1811, July 2010.
- [15] C. Peters, J. Handwerker, D. Maurath, and Y. Manoli, “A sub-500 mV highly efficient active rectifier for energy harvesting applications,” *IEEE Transactions on Circuits and Systems I: Regular Papers*, vol. 58, no. 7, pp. 1542–1550, July 2011.
- [16] G. Papotto, F. Carrara, and G. Palmisano, “A 90-nm CMOS threshold-compensated RF energy harvester,” *IEEE Journal of Solid-State Circuits*, vol. 46, no. 9, pp. 1985–1997, Sept 2011.
- [17] T. Le, K. Mayaram, and T. Fiez, “Efficient far-field radio frequency energy harvesting for passively

Chapter 6. Efficient Contactless Waveguide Power Transfer

- powered sensor networks,” *IEEE Journal of Solid-State Circuits*, vol. 43, no. 5, pp. 1287–1302, May 2008.
- [18] C. R. Valenta and G. D. Durgin, “Harvesting wireless power: Survey of energy-harvester conversion efficiency in far-field, wireless power transfer systems,” *IEEE Microwave Magazine*, vol. 15, no. 4, pp. 108–120, June 2014.
- [19] S. Shrestha, S.-K. Noh, and D.-Y. Choi, “Comparative study of antenna designs for RF energy harvesting,” *International Journal of Antennas and Propagation*, Jan. 2013.
- [20] V. Kopta, J. Farserotu, and O. Vorobyov, “System and method for remote powering at least one sensor or actuator from a RF power source,” May 4 2017, US Patent App. 15/336,955.
- [21] —, “System and method for remote powering at least one sensor or actuator from a RF power source,” May 3 2017, EP Patent App. EP20,150,192,228.
- [22] A. Nathan *et al.*, “Flexible electronics: The next ubiquitous platform,” *Proceedings of the IEEE*, vol. 100, no. Special Centennial Issue, pp. 1486–1517, May 2012.
- [23] D. Pozar, *Microwave Engineering*. Wiley, 2004.
- [24] J. Farserotu, J. Baborowski, J. D. Decotignie, P. Dallemagne, C. Enz, F. Sebelius, B. Rosen, C. Antfolk, G. Lundborg, A. Björkman, T. Knieling, and P. Gulde, “Smart skin for tactile prosthetics,” in *2012 6th International Symposium on Medical Information and Communication Technology (ISMICT)*, Mar. 2012, pp. 1–8.
- [25] A. Vorobyov, V. Kopta, J. R. Farserotu, and C. C. Enz, “Efficient through-waveguide wireless power transfer for body area networks,” in *2012 IEEE Biomedical Circuits and Systems Conference (BioCAS)*, Oct. 2017.

7 Conclusion

The development and implementation of a low power wireless transceiver for short range communications is the central topic of this work. Although the motivation comes primarily from the *WiseSkin* project, aiming to provide wireless connectivity between sensor nodes in an artificial skin, the implemented FM-UWB radio could find broader use in WBANs, targeting different applications (e.g. health monitoring). The emphasis is mainly on the reduction of power consumption, seeking to provide a solution that will not significantly affect the autonomy of the existing battery in the prosthetic arm. To achieve that, the approach investigated here leverages short distance between the nodes and trades sensitivity to conserve energy. Although improvements were made, narrowband radios still have the edge, at least when it comes to power and sensitivity.

The FM-UWB, however, provides some interesting capabilities that may not be apparent at first. Some of them were implemented and highlighted throughout the preceding chapters, one example being the multi-user communication. To cope with the increasing number of nodes, and improve scalability, the implemented radio provides the sub-carrier FDMA capability, allowing multiple nodes to communicate simultaneously in the same RF band. Although the concept itself has been suggested previously, this is the first time a full receiver chain that supports SC-FDMA was characterized. Another good characteristic of FM-UWB was confirmed in practice, namely tolerance to reference clock frequency offset. This capability could eventually result in a radio with zero external components, and is in fact one of the biggest advantages compared to narrowband radios that still need a quartz resonator. Finally, the FM-UWB is known to be reliable in frequency selective channels and in the presence of interferers. Inherent robustness to narrowband interferers demonstrated in this work eliminates the need for sharp external filters, again providing means for high degree of miniaturization.

Initially, the reduction of power consumption was primarily driven by the desire to maintain a negligible impact on the autonomy of the prosthetic arm. There is another motivation - removing the power supply connection, cutting the final wire. Further improvements and reduction of the consumption of the radio could one day allow to use energy harvested from the environment to power the nodes, but the implemented radio already achieves a level low enough to enable supplying power via a dedicated RF narrowband signal, while simultaneously using the FM-UWB signal for communication. Wires, initially intended for supplying dc power to the sensor nodes, serve as a waveguide and prevent

electromagnetic energy from escaping, allowing to achieve relatively good efficiency of the wireless power transfer. Although the principle was validated here, more effort is needed for the realization of this fully contactless system, which for now remains a potential topic for future research.

7.1 Summary of Achievements

As discussed previously, when it comes to power consumption narrowband receivers inevitably have the advantage. The FM-UWB receiver simply cannot achieve the same sensitivity for a given power consumption, but it brings other benefits to the table. The work presented here continues the trend of lowering the power of FM-UWB transceivers, as indicated in Fig. 7.1. The implemented single-ended AZ-IF receiver further narrows the gap between the narrowband and wideband receivers, but it does so at the cost of a lower sensitivity. The second implemented quadrature AZ-IF receiver consumes slightly more than the first version, the difference coming from the baseband circuits, mainly the sharp baseband channel filter, needed to remove the adjacent sub-carrier signals. As shown in Chapter 5, the achieved consumption levels, combined with good interference tolerance, already make it possible to power the radio without contact, via electromagnetic waves. If the trend continues, the goal of using other energy harvesting sources might become a reality.

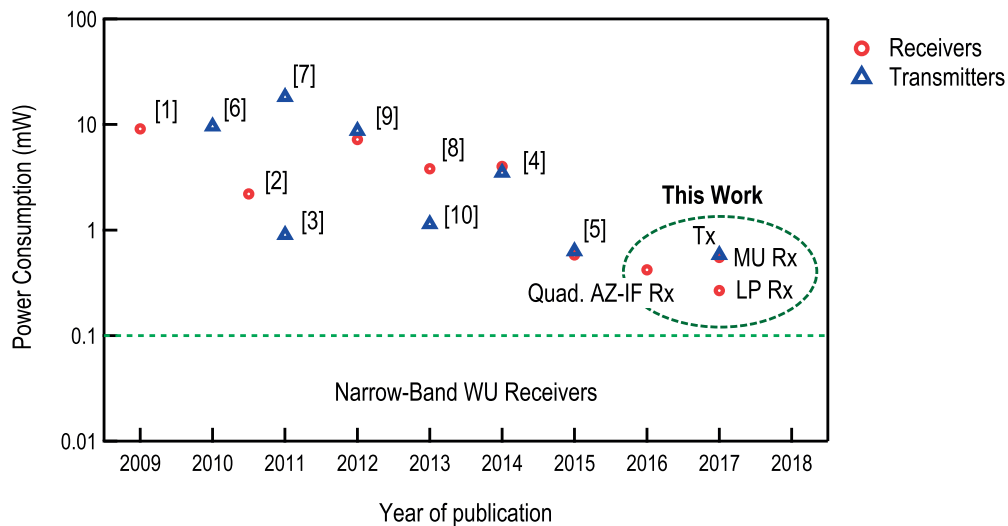


Figure 7.1: Power consumption evolution of implemented FM-UWB transmitters and receivers.

The trade-off between sensitivity and power consumption, for different implementations of FM-UWB receivers is shown in Fig. 7.2. The RF delay line demodulator consumes the most, but still provides the best sensitivity performance, and in addition it should be able to support multi-user communication [1]. The super regenerative architecture [2, 3], achieves considerable power savings, and relatively good sensitivity, but loses the capability to distinguish multiple FM-UWB signals. Finally, the two architectures proposed here are targeting short range communications, and can therefore withstand lower sensitivity in order to further reduce the power requirements and provide the multi-user capability.

The core of the work focuses on the implementation of an ultra low power FM-UWB transceiver. The

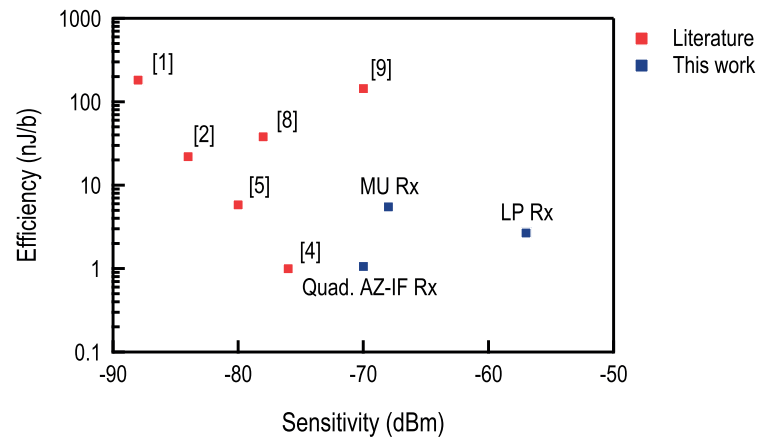


Figure 7.2: Power consumption vs. sensitivity of implemented FM-UWB receivers.

design process started with the exploration of options and capabilities of the FM-UWB modulation. The second step was the study of transmitter and receiver architectures that would yield the best performance for the given application. In the last step, abstract block diagrams were transformed into electronic circuits that implemented the desired functions. The journey, from the concept on a piece of paper to the real “live” silicon chip, brought many challenges but also resulted in some interesting inventions and ideas. The most important ones are summarized here:

- The FM-UWB modulation, originally proposed by Gerrits is a combination of the low modulation index BFSK (at baseband) and the large modulation index frequency modulation (at RF). The concept was first extended to include other baseband modulation types such as MFSK, BPSK and MPSK. Here a multi-channel transmission is proposed, using a sum of several orthogonal sub-carrier signals to modulate the carrier. The concept allows simultaneous transmission in the same frequency band to multiple receivers and is demonstrated through experiments in Chapter 4.
- The approximate zero-IF architecture is introduced as a modification of the uncertain IF narrowband receiver. The quadrature approximate zero-IF receiver allows to save power while preserving enough linearity to allow simultaneous demodulation of multiple input FM-UWB signals. The single-ended version of the receiver further simplifies its architecture reaching the record low power consumption, but loses sensitivity and loses the capability to distinguish multiple FM-UWB users.
- Aside from power consumption the implemented transceiver is the first full FM-UWB transceiver that provides the multi-user capability. In this case four channels with a 100 kb/s data rate are available for simultaneous communication. High tolerance to large reference frequency offsets is demonstrated, allowing to integrate the full transceiver without the need for an external high-Q resonator, or any other off-chip components. High resilience to out of band interferers enables reliable communication and provides means of powering the transceiver wirelessly using a narrowband signal at 2.4 GHz (although other frequencies could also be used).
- Electronic circuits have been a topic of research for a long time, making it rather difficult to innovate and discover truly new topologies. Most of the used circuits are adaptations and minor modifications of already existing solutions. The two more notable blocks that brought some

innovation in this work are the baseband N-path channel filter and the low power DCO. The use of an N-path filter in the baseband allows to easily implement a tunable, high-Q bandpass filter, with relatively low power consumption and simple control. Although N-path filters have been out there for some time, they have never been used in a low power and low frequency application such as this one. Implementing the DCO as a stack of a ring oscillator and a frequency multiplier allowed to run the oscillator at one third of the actual frequency, allowing it to reduce consumption. This was one of the key innovations that led to such low overall consumption of the single-ended approximate zero-IF receiver.

- The use of the existing flexible and stretchable waveguide structure to supply power to the sensor nodes is proposed. Metallic layers at the top and bottom of the PDMS layer conserve the electromagnetic energy within the waveguide, enabling relatively good achievable efficiency. The proposed powering scheme improves reliability and eases manufacturing, therefore lowering the production cost and complexity.

7.2 Future Work

Throughout the research conducted here opportunities to take different paths have appeared. Unfortunately, as it is usually the case, time and resources are limited, and one must limit the scope of the work, making it impossible to look into all of them. A short list of possible future research directions is given here, also pointing out some missing pieces that would better round up the work described in the dissertation:

- The implemented FM-UWB receivers had a rather poor noise performance, the reason being that the first block of the receiver is an active mixer with quite a high noise figure. This approach was chosen simply because it doesn't require a full LO swing, allowing to save some power on the oscillator side. The oscillator together with the active mixer, however dominates the receiver consumption, and instead of investing that power for the active mixer perhaps it would have been better spent on increasing the oscillator output swing. This approach could be combined with a passive mixer that consumes no power, and was proven to achieve lower noise figure. The overall performance could potentially be improved in this way.
- Four SC-FDMA channels, with a maximum data rate of 100 kb/s, were used for this transceiver, somewhat limiting its scope of use. The future implementations could address increased data rates (1 Mb/s already demonstrated) and higher number of channels, and might use higher sub-carrier frequencies to achieve that.
- The concept of multi-channel transmission was proven to work, but it was only implemented using the available test equipment. The concept could be transferred to silicon, with the idea to implement a low power transmitter capable of transmitting data to multiple receivers at once. Other modifications of the original FM-UWB modulations might be possible as well, Chirp-UWB being one of them [4], and could address different applications.
- The FM-UWB transmitter presented here achieves only a slight improvement in terms of consumption and efficiency compared to the state of the art. The architecture itself is quite similar to the one from [5], and the said improvement is simply a result of circuit optimization. The question remains whether there is a way to make the whole design more efficient. The effort should mainly be put into optimizing the power amplifier together with the preamplifier, as the two are currently the bottleneck.

- Although a full transceiver has been implemented a number of blocks are needed to provide a complete, fully functional radio that could be integrated into a bigger system. The first block missing is the received signal strength indicator (RSSI), that could provide information about the level of the received signal (usually needed at the protocol level) or be used as a part of the automatic gain control loop. Another feature, usually required by the protocol, is the link quality indicator (LQI), that provides the information about the modulation accuracy. The two are used at the protocol level to assess the channel condition and assure reliable communication, and are present in most commercially available narrowband radios. Digital baseband circuits that would provide the interface for the microcontroller and handle data packets should also be implemented to provide a fully functional transceiver that can easily be interfaced by a microcontroller.
- The concept of wireless powering through a waveguide was barely touched upon. Although the feasibility of such approach is demonstrated, there is a long way to go before this system could become a reality. Design and optimization of a rectenna that would convert the RF energy into dc, and a power management unit that would provide supply for the node remain to be done as a part of future research. Other parameters of the system should be investigated as well. In this work 2.4 GHz frequency was used (antenna was designed for the available 2.4 GHz radio used for the prototype), but switching to higher frequencies could provide means to reduce the antenna size. At the same time higher frequencies make the rectifier design more challenging, and the question of optimal frequency remains. Finally, in this work radio and powering are completely separated, but seeing the small amount of losses present in the channel, perhaps a different approach for communication would yield better results. The same channel could be used to provide both data and power, and backscattering technique, widely used in RFID tags, could replace a transmitter on the sensor nodes, allowing to further reduce power consumption.

References

- [1] Y. Zhao, Y. Dong, J. F. M. Gerrits, G. van Veenendaal, J. Long, and J. Farserotu, "A Short Range, Low Data Rate, 7.2 GHz-7.7 GHz FM-UWB Receiver Front-End," *IEEE Journal of Solid-State Circuits*, vol. 44, no. 7, pp. 1872–1882, July 2009.
- [2] N. Saputra and J. Long, "A Short-Range Low Data-Rate Regenerative FM-UWB Receiver," *IEEE Transactions on Microwave Theory and Techniques*, vol. 59, no. 4, pp. 1131–1140, Apr. 2011.
- [3] —, "A Fully-Integrated, Short-Range, Low Data Rate FM-UWB Transmitter in 90 nm CMOS," *IEEE Journal of Solid-State Circuits*, vol. 46, no. 7, pp. 1627–1635, Jul. 2011.
- [4] F. Chen, Y. Li, D. Liu, W. Rhee, J. Kim, D. Kim, and Z. Wang, "9.3 A 1mw 1mb/s 7.75-to-8.25ghz chirp-UWB transceiver with low peak-power transmission and fast synchronization capability," in *Solid-State Circuits Conference Digest of Technical Papers (ISSCC), 2014 IEEE International*, Feb. 2014, pp. 162–163.
- [5] N. Saputra and J. R. Long, "A Fully Integrated Wideband FM Transceiver for Low Data Rate Autonomous Systems," *IEEE Journal of Solid-State Circuits*, vol. 50, no. 5, pp. 1165–1175, May 2015.
- [6] B. Zhou, R. He, J. Qiao, J. Liu, W. Rhee, and Z. Wang, "A low data rate FM-UWB transmitter with-based sub-carrier modulation and quasi-continuous frequency-locked loop," in *2010 IEEE Asian Solid-State Circuits Conference*, Nov. 2010, pp. 1–4.
- [7] B. Zhou, H. Lv, M. Wang, J. Liu, W. Rhee, Y. Li, D. Kim, and Z. Wang, "A 1mb/s 3.2-4.4 ghz reconfig-

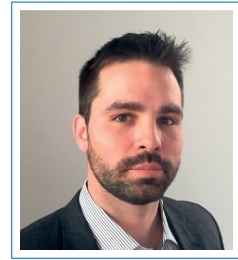
Chapter 7. Conclusion

- urable FM-UWB transmitter in 0.18 μm CMOS,” in *2011 IEEE Radio Frequency Integrated Circuits Symposium (RFIC)*, June 2011, pp. 1–4.
- [8] F. Chen, W. Zhang, W. Rhee, J. Kim, D. Kim, and Z. Wang, “A 3.8-mW 3.5-4-GHz Regenerative FM-UWB Receiver With Enhanced Linearity by Utilizing a Wideband LNA and Dual Bandpass Filters,” *IEEE Transactions on Microwave Theory and Techniques*, vol. 61, no. 9, pp. 3350–3359, Sep. 2013.
- [9] B. Zhou, J. Qiao, R. He, J. Liu, W. Zhang, H. Lv, W. Rhee, Y. Li, and Z. Wang, “A Gated FM-UWB System With Data-Driven Front-End Power Control,” *IEEE Transactions on Circuits and Systems I: Regular Papers*, vol. 59, no. 6, pp. 1348–1358, Jun. 2012.
- [10] F. Chen, Y. Li, D. Lin, H. Zhuo, W. Rhee, J. Kim, D. Kim, and Z. Wang, “A 1.14mw 750kb/s FM-UWB transmitter with 8-FSK subcarrier modulation,” in *2013 IEEE Custom Integrated Circuits Conference (CICC)*, Sep. 2013, pp. 1–4.

Vladimir Kopta

Curriculum Vitae

Pierre-de-Vinglé 20
2000 Neuchâtel
Switzerland
☎ +41 78 736 2893
✉ vladimir.kopta@epfl.ch



Experience

- Nov. 2017–
–Present **CSEM**
R&D Engineer
- Wireless and integrated systems division
- Jul. 2013–
–Present **EPFL/CSEM**
Doctoral assistant
- Worked on a *WiseSkin Nano-Tera* project (<http://www.nano-tera.ch/projects/353.php>) as a part of a multi-disciplinary team
 - Research focus on low-power UWB wireless transceivers, designed a 4 GHz, low-power FM-UWB receiver and transceiver in 65 nm CMOS technology
- Sep. 2012–
–Jun. 2013 **CSEM**
Internship/Master's thesis
- Contributed to the design of a 2.4 GHz, low-power polar transmitter compatible with the IEEE 802.15.6 standard for body area networks in 65 nm CMOS technology

Education

- 2013–Pres. **Ecole Polytechnique Fédérale de Lausanne**
Ph.D. in Electrical and Electronic Engineering
- 2011–2013 **Ecole Polytechnique Fédérale de Lausanne**
MS in Electrical and Electronic Engineering, *GPA: 5.68/6*
- Recipient of the EPFL Scholarship of Excellence
- 2007–2011 **Belgrade University, School of Electrical Engineering**
BS in Electrical Engineering and Computer Science, *GPA: 9.96/10*
- Graduated from the department of Electronics as top of the class
 - Recipient of the scholarship for young talents

Skills

- Languages ◦ English (fluent) ◦ French (working proficiency) ◦ Serbian (native)
- Training ◦ PLLs, Clock & Data Recovery ◦ Techniques for Handling Noise and Variability in Analog Circuits ◦ Ultra-Low-Voltage RF Circuits for IoT ◦ High-Speed Data Converters ◦ Management of Innovation and Technology Transfer
- Teaching ◦ Advanced Analog and RF IC design I & II ◦ Receivers for Wireless Communications ◦ Systems Engineering ◦ Fundamentals of Electrical Engineering (LAB).

Extra-curricular activities and interests

- Reviewer ◦ Reviewed articles for IEEE MTT-S journals and IEEE conferences.
- Volunteer ◦ Workshop on Advances in Analog Circuit Design 2015.
◦ European Solid State Circuits Conference 2016.
- Sports ◦ Former ice-hockey player, played for U18 national team of Serbia and Montenegro in 2005.
◦ Practicing: skiing, skating, running (ran two Lausanne half-marathons), scuba-diving (PADI open water diving license), karate

Publications

1. V. Kopta and C. C. Enz, "A 100 kb/s, 4 GHz, 267 μ W fully integrated low power FM-UWB Transceiver with Multiple Channels," in *Proceedings of the IEEE Custom Integrated Circuits Conference (CICC)*, Apr. 2018.
2. V. Kopta, J. Farserotu, and C. Enz, "FM-UWB: Towards a Robust, Low-Power Radio for Body Area Networks," *Sensors*, vol. 17, no. 5, 2017.
3. V. Kopta, D. Barras, and C. C. Enz, "An Approximate Zero IF FM-UWB Receiver for High Density Wireless Sensor Networks," *IEEE Transactions on Microwave Theory and Techniques*, vol. 65, no. 2, pp. 374–385, Feb 2017.
4. V. Kopta, D. Barras, and C. C. Enz, "A 420 μ W, 4 GHz Approximate Zero IF FM-UWB Receiver for Short-Range Communications," in *2016 IEEE Radio Frequency Integrated Circuits Symposium (RFIC)*, May 2016, pp. 218–221.
5. V. Kopta, R. Thirunarayanan, F. Pengg, E. L. Roux, and C. Enz, "A 2.4-GHz Low Complexity Polar Transmitter Using Dynamic Biasing for IEEE 802.15.6," in *2015 IEEE International Symposium on Circuits and Systems (ISCAS)*, May 2015, pp. 1686–1689.
6. V. Kopta, E. L. Roux, F. Pengg, and C. Enz, "A 2.4 GHz Low Power Polar Transmitter for Wireless Body Area Network Applications," *Analog Integrated Circuits and Signal Processing*, vol. 81, no. 3, pp. 657–666, 2014.
7. V. Kopta, F. Pengg, E. L. Roux, and C. Enz, "A 2.4 GHz Low Power Polar Transmitter for Wireless Body Area Network Applications," in *2013 IEEE 11th International New Circuits and Systems Conference (NEWCAS)*, June 2013, pp. 1–4.
8. A. Vorobyov, V. Kopta, J. R. Farserotu, and C. C. Enz, "Efficient through-waveguide wireless power transfer for body area networks," in *IEEE Biomedical Circuits and Systems Conference (BioCAS)*, Oct. 2017.
9. J. Farserotu, J. D. Decotignie, J. Baborowski, P. N. Volpe, C. R. Quirós, V. Kopta, V. Koch, H. Huang, T. Li, C. Enz, S. Lacour, H. Michaud, R. Martuzzi, and C. Antfolk, "Tactile Prosthetics in WiseSkin," in *2015 Design, Automation Test in Europe Conference Exhibition (DATE)*, March 2015, pp. 1695–1697.
10. C. Antfolk, V. Kopta, J. Farserotu, J. D. Decotignie, and C. Enz, "The WiseSkin Artificial Skin for Tactile Prosthetics: A Power Budget Investigation," in *2014 8th International Symposium on Medical Information and Communication Technology (ISMICT)*, April 2014, pp. 1–4.
11. V. Kopta, J. Farserotu, and O. Vorobyov, "System and method for remote powering at least one sensor or actuator from a rf power source," Oct. 28 2016, US Patent App. 15/336,955, European Patent App. EP3163715.

